



UNIVERSIDAD DE CASTILLA-LA MANCHA
Departamento de Mecánica Aplicada e Ingeniería de Proyectos
Escuela de Ingeniería Industrial y Aeroespacial de Toledo

TESIS DOCTORAL

**Complexity of the structural response of fibre
reinforced polymer matrix composites**

Autor: Sergio Horta Muñoz

Directora: María del Carmen Serna Moreno

Toledo, marzo de 2020

The present work has been co-funded by the Junta de Comunidades de Castilla-La Mancha (JCCM) and the European Social Fund (ESF) under research grant SBPLY/16/180501/000263 and by the Ministerio de Economía y Competitividad (MINECO) of Spain under the research project DPI2016-77715-R.

This research was conducted in part during the author's visit to Ghent University, Belgium, which was co-funded by University of Castilla-La Mancha and European Regional Development Fund (ERDF).

© Sergio Horta Muñoz

Without written permission of the author it is forbidden to reproduce or adapt in any form any part of this publication.

This document should be printed double-sided in DIN B5 size.

Formatted with \LaTeX

Complexity of the structural response of fibre reinforced polymer matrix composites

A Thesis by
Sergio Horta Muñoz

presented for the degree of
Doctor of Philosophy
in
Science and Technologies
applied to Industrial Engineering

supervised by
Prof. Dr. María del Carmen Serna Moreno

at
University of Castilla-La Mancha
Continuum Mechanics, Structures and
Materials Engineering Group
Department of Applied Mechanics and Projects Engineering
School of Industrial and Aerospace Engineering of Toledo (Spain)

*A mi familia, sin su apoyo
nada de esto sería posible.*

Bis vincit qui se vincit in victoria
Publius Syrus

Agradecimientos

Y llegó la hora de agradecer a las personas que han acompañado este camino tedioso pero a la vez bonito (y siempre con una sonrisa) que lleva a la conclusión de esta Tesis, que más que un trabajo, definiría una etapa de la vida y un cambio de mentalidad, y que sin duda me ha hecho madurar. Allá va la lista de agradecimientos, y pido perdón si me dejo a alguien por el camino:

En primer lugar agradecer con el mayor de los agradecimientos posible a la directora y tutora (y sin duda coautora) de este trabajo, M^a Carmen, cuya ayuda se hace indispensable, por su enorme dedicación, apoyo, consejo, tiempo invertido, y sobre todo, entusiasmo plasmado en esta tesis. Espero que este agradecimiento no sea recibido como el típico de cortesía hecho a los supervisores de una tesis, sino que quede claro que es un sincero agradecimiento a una dedicación no sólo profesional sino también personal, que va más allá de una *simple* dirección de tesis.

También quisiera agradecer a Juan José López Cela, por permitirme y motivarme a realizar la tesis en su grupo de investigación, por ayudarme a tener otro punto de vista del trabajo realizado.

Sin salir de nuestra universidad, no podría falta el agradecimiento a los compañeros y amigos, investigadores, profesores, técnicos y estudiantes, principalmente de la ETSII-CR, pero extensible a toda la UCLM. Reconocer sobre todo el apoyo de Pablo y Juan Luis por su ayuda, por su experiencia y disposición. No me olvido de José Miguel, quien como codirector de TFM marcó mi inicio al mundo de la investigación y cuyos consejos y entusiasmo han sido de gran valor para ver el valor más importante de la investigación. También agradecer el recibimiento y el apoyo tan importante para estos últimos meses, en los que la tesis *se hace cuesta arriba*, de los compañeros de la EIIA-To: David, Arantxa, Reyes, Luis, Jesús, Carlos, Damián . . .

No podría falta el agradecimiento a la gente que me acompañó durante la estancia en Gante: David (y a su familia por la cariñosa acogida en tierras extranjeras), Ruben, Vikram, Arada, Ivan, Fran... Y por supuesto al Prof. Wim Van Paepegem por recibirme amablemente en su grupo y permitirme aprovechar los recursos y conocimientos desarrollados en el *Mechanics of Materials and Structures (MMS) research group*.

Gracias a mis amig@s, los de aquí y los de allá, los de siempre, por esos buenos ratos. No puedo dejar de mencionar a Diego, Carlos, Sara, Tobajas, Pablo L., Víctor... con un especial agradecimiento a Álex, compañero de piso y compañero de "locuras" del doctorado, por esos *braulios* y *touchdowns* que arreglaban los días malos que a veces tiene la investigación.

Y por último, no podría olvidarme de mi familia, a la cual dedico mi más cariñoso agradecimiento por todo su amor y comprensión, por su apoyo y consejo. Sois la razón de que haya llegado hasta aquí y sea lo que soy, y espero haceros sentir orgullosos de este trabajo. Y ahora sí, finalizo con una tierna reseña al pequeño de la familia, Mario, que desde su inocencia aporta una especial ilusión y ánimo por llevar este trabajo a buen puerto.

Abstract

The structural application of fibre reinforced polymer (FRP) composites has meant a revolution in mechanical properties, making the most of strength and stiffness at a lower weight than traditional structural materials. This is leading to the gradual replacement of structural components with the aim of environmental, economical and safety advantages in sectors where mechanical properties are critical, such aerospace industry.

The heterogeneity and anisotropy of these composite materials lead to a intricate mechanical behaviour, which requires a change in the very basics of characterization and modelling of continuum mechanics. In this way, the topics of damage and failure have been widely addressed by the scientific community from different analytical, numerical and experimental approaches.

However, there is still great uncertainty in the mechanical behaviour of composite structures when load states are complex. This doctoral thesis deals with the study of the behaviour of carbon fibre reinforced polymeric material (CFRP) laminates, obtained by stacking unidirectional continuous fibre plies. It deepens in stacking sequences of industrial interest, namely angle-ply, with highly non-linear behaviour associated to different damage mechanisms and plasticity.

The response of different laminates is analysed in a wide range of loading conditions, including quasi-static uniaxial and multiaxial characterization. This is performed via standardized testing, including tensile, compressive and flexural loading, up to advanced non-standardized tests such as cruciform biaxial testing.

This study is approached from the analytical, numerical and experimental fields, discussing the effectiveness of different approaches and proposing new analytical models for the design of laminates validated through experimental testing. Different numerical analyses are also performed using the Finite Element Method (FEM) which allows to describe the appearance and evolution of different damage mechanisms and geometry instabilities, following a “cost-effective” methodology (in other words, simulations with low computational cost).

The results obtained from the different perspectives and loading scenarios allow to offer recommendations for testing and characterizing the mechanical behaviour of FRP laminates, addressing in detail the non-isotropic behaviour of the lamina and laminate.

Resumen

La aplicación estructural de materiales compuestos de matriz polimérica reforzada con fibra (FRP) ha significado una revolución desde el punto de vista de las propiedades mecánicas, elevando los límites de resistencia y rigidez con un peso menor que los materiales estructurales tradicionales. Esto está llevando a la sustitución, al menos parcial, de componentes estructurales con el objetivo de conseguir mejoras en sostenibilidad ambiental, económicas y de seguridad en sectores donde las propiedades mecánicas son críticas, como la industria aeroespacial.

La heterogeneidad y la anisotropía de estos materiales compuestos conducen a un complicado comportamiento mecánico, que requiere una redefinición de los conceptos básicos de caracterización y modelado de su respuesta mecánica. Por ello, los conceptos de daño y fallo han sido ampliamente abordados por la comunidad científica desde diferentes enfoques analíticos, numéricos y experimentales.

Sin embargo, todavía existe una gran incertidumbre en el comportamiento mecánico de las estructuras compuestas cuando los estados de carga son complejos. Esta tesis doctoral aborda el estudio del comportamiento de los laminados de material polimérico reforzado con fibra de carbono (CFRP), obtenidos mediante el apilado de capas de fibra continua unidireccional. Se profundiza en secuencias de apilamiento de interés industrial, principalmente *angle-ply*, con un comportamiento altamente no lineal asociado a diferentes mecanismos de daño y plasticidad.

La respuesta de diferentes laminados se analiza sometida a diversos escenarios de carga, incluidos estados de carga cuasiestáticos uniaxiales y multiaxiales. Entre ellos se engloban desde ensayos estándar de tracción, compresión y flexión, hasta ensayos no estandarizados, como es el caso de los ensayos biaxiales con probetas cruciformes.

Este estudio se aborda desde los campos analítico, numérico y experimental, discutiendo la efectividad de diferentes enfoques y proponiendo nuevos modelos analíticos para el diseño de laminados, validados mediante evidencias experimentales. También se realizan diferentes análisis numéricos utilizando el Método de los Elementos Finitos (FEM) que permite describir la aparición y evolución de diferentes mecanismos de daño e inestabilidades geométricas, siguiendo una metodología que prima la sencillez del modelo (en otras palabras, simulaciones con bajo coste computacional).

Los resultados obtenidos mediante las diferentes metodologías y bajo los distintos escenarios de carga permiten ofrecer recomendaciones para ensayar y caracterizar la respuesta y el fallo mecánico de los laminados FRP, abordando en detalle el comportamiento no isótropo de la lámina y del laminado.

Contents

Abstract	i
Resumen	iii
Contents	v
List of figures	ix
List of tables	xvii
List of Abbrevations	xix
1 Introduction	1
1.1 Scientific and industrial context	1
1.2 State of the art	4
1.2.1 Pseudo-ductility in angle-ply laminates	4
1.2.2 Biaxial testing on composite materials	7
1.2.3 Failure theories	13
1.2.4 Damage modelling	17
1.3 Objectives	18
1.4 Summary of the contents	20
2 Experimental, analytical and numerical frameworks	23
2.1 Material and experimental equipment	23

2.1.1	Lamina characteristics and laminate preparation	23
2.1.2	Experimental facilities	25
2.2	Analytical framework	28
2.2.1	Classical Laminated Plate Theory	28
2.3	Numerical modelling	34
2.3.1	Hashin’s Damage Model	34
2.3.2	Ladevèze’s Damage Model	40
3	Mechanical response under uniaxial loading	49
3.1	Uniaxial tensile testing	49
3.1.1	Cross-ply laminates	51
3.1.2	Angle-ply laminates	51
3.2	Uniaxial compressive testing	59
3.3	Numerical modelling of the non-linear response of angle-ply laminates under uniaxial loading	62
3.3.1	Parameter identification for Hashin’s Damage Model	62
3.3.2	Material parameter identification for Ladevèze’s model	68
3.3.3	Results obtained with Ladevèze’s model for different angle-ply laminates	72
3.3.4	Effects of the geometry and element type	76
4	Flexural response of angle-ply laminates	81
4.1	Analytical framework	81
4.2	Pseudo-ductility in bending of $\pm 45^\circ$ symmetrical angle-ply laminates	87
4.2.1	Analysis of flexural response considering different tensile and compressive elastic moduli	87

4.2.2	Experimental bending characterization of pseudo-ductile effects on angle-ply laminates	90
4.2.3	Optimization of stacking sequences	94
5	Assessment of laminates under biaxial loading	97
5.1	General aspects of the analysis of cruciform biaxial testing	98
5.1.1	Design and preparation of cruciform specimens	98
5.1.2	Numerical modelling of non-linear effects on biaxial tests	101
5.1.3	Numerical elastic estimation of stresses in biaxial zone	104
5.2	Elastic analytical approach to biaxial stress	105
5.2.1	Representation of uniaxial and biaxial states on Mohr's Circle	110
5.3	Tensile-Tensile biaxial tests on cruciform specimens	112
5.3.1	Biaxial tensile loading on cross-ply laminate	112
5.3.2	$\pm 45^\circ$ laminate under Tensile-Tensile biaxial loading	115
5.4	Analysis of the buckling initiation on biaxially compressed laminated plates	125
5.4.1	Bending-twisting coupling effect on buckling critical load	125
5.4.2	β -Coefficients approach for thin plates	129
5.4.3	Buckling analysis of biaxially compressed cruciform specimens	133
5.5	$\pm 45^\circ$ laminate under Compressive-Compressive biaxial loading	137
5.6	Tensile-Compressive biaxial testing of $\pm 45^\circ$ laminate	140
5.7	Evaluation of internal damage via phased-array ultrasonic inspection	143
6	Conclusions and future works	147
6.1	Conclusions	147

6.1.1	Uniaxial characterization and damage numerical modelling of laminates	147
6.1.2	Bending and pseudo-ductility in angle-ply laminates	148
6.1.3	Buckling in laminated plates and cruciform specimens	149
6.1.4	Biaxial testing on cruciform specimens in FRP laminates	150
6.2	Future research lines	151
Bibliography		175
A Scientific production		177
A.1	Publications in peer-reviewed international journals indexed in the Journal Citation Reports	177
A.2	Publications in national journals	177
A.3	Contributions to international conferences	178
A.4	Contributions to national conferences	178
A.5	Intellectual property	179
A.6	Recognitions	180

List of figures

1.1	Schematic representation of damage mechanisms induced in a composite laminate by low velocity impact [7] and (b) compressive loading [8].	2
1.2	Carbon fibre global demand (*Estimations made at 11/2018). Shown in a reconstructed edition [14].	3
1.3	Examples of aircraft relevant for composite industry: (a) Airbus A350 XWB [17] and (B) Boeing 787 Dreamliner [18].	4
1.4	Uniaxial tensile tests results for different angle-ply laminates, depicting applied stress against longitudinal and transverse strains. Reproduction based on [9].	5
1.5	Biaxial testing methodologies: (a) Off-axis uniaxial and (b) Cruciform test.	8
1.6	FEM simulations for different specimen geometries: (a) Principal strain [51] and (b) Principal stress [77].	11
1.7	(a) Modified ARCAN jig [110] and (b) ISO20337 fixture [113].	13
1.8	Matrix cracking modes collected by Puck’s failure criteria [142].	16
1.9	Theoretical inelastic response obtained with damage and plasticity model. Reproduction based on [21,155].	18
2.1	Fabrication of laminates: (a) Hand lay-up laminate in vacuum bag and (b) hot platen press.	24
2.2	Examples of specimens: UD plates for ultrasonic characterization and tensile tabbed coupons.	24
2.3	MICROTEST MAEFH triaxial electromechanical testing machine.	25
2.4	Strain measurement equipment applied in quasi-static testing: (a) Foil strain gauge, (b) Axial extensometer and (c) StrainMaster DIC system.	26

2.5	Phased array ultrasonic inspection: (a) Olympus OmniScan®SX, (b) C-Scan setup including transducer and position encoder [164] and (c) inspection of a cruciform specimen (S-Scan mode visualized in screen).	27
2.6	Laminate and ply notation and coordinate systems: Principal material directions (blue) and global coordinate system (red).	29
2.7	Theoretical evolution of elastic properties predicted through CLPT for different stacking sequences: (a) Angle ply $[\pm\theta]_S$ and (b) $[(0 + \theta)/(90 + \theta)]_S$.	32
2.8	Ply and laminate elastic properties at η -direction plotted against ϕ . $+45^\circ$ ply elastic modulus, $[\pm 45]_{2S}$ apparent extensional and flexural modulus.	33
2.9	Deformation under bending for cross-ply laminates: $[0/90]_S$ (left) and $[90/0]_S$ (right). Reproduction based on [165].	33
2.10	Representation of insensitivity opposed sign shear in principal directions. Adapted from [166].	36
2.11	Hashin's damage model evolution, reinterpreted from [130].	37
2.12	Planar representation of isotropic hardening, supposing $\sigma_{22} = 0$.	45
2.13	Representation of damage law combined with plasticity. Stress-strain evolution is also reported in right axis for clarification.	46
2.14	Representation of strain results considering linear and non-linear strain relations in the Ladevèze script, compared with Abaqus results including the UMAT.	48
3.1	Dimensions of uniaxial tensile test coupon (in mm).	50
3.2	$[0/90]_S$ and $[90/0]_S$ uniaxial tensile testing.	52
3.3	Quasi-static uniaxial tensile test of different angle-ply configurations. Low stress-strain levels are zoomed in the subfigure.	53
3.4	Estimation of fibre reorientation in uniaxially tensile tested angle-ply laminates.	54
3.5	Uniaxial tensile test results for different angle-ply configuration, depicting $\sigma_{xx} - \epsilon_{xx}$ (right side) and $\sigma_{xx} - \epsilon_{yy}$ (left side).	55

3.6	Uniaxially tensile tested $[\pm 45]_{2S}$: (a) Top view depicting matrix crack and permanent deformation and (b) side view of matrix cracking in internal plies.	55
3.7	Uniaxial tensile tested specimens of $[\pm 33.7]_{2S}$ (above) and $[\pm 56.3]_{2S}$ (below) laminates, including 100x microscopic magnifications.	56
3.8	Uniaxial tensile tested $[\pm 67.5]_{2S}$ specimen illustrating brittle matrix cracking.	56
3.9	Stress and strain components in principal directions for uniaxial tensile tests: (a) $[\pm 33.7]_{2S}$ and (b) $[\pm 56.3]_{2S}$	57
3.10	Representation of LUR stress-strain response. Red path indicates the unload, while blue line describes the reloading cycle.	57
3.11	Quasi-static and LUR test of $[\pm 45]_{2S}$ laminate: (a) extensometer strains and (b) strain gauge measures.	58
3.12	Modified ASTM D695 fixture: (a) positioning of stabilizing base on testing machine, (b) side view with short gauge length specimen and (c) long gauge length specimen exhibiting invalid failure mode.	60
3.13	Uniaxial compressive tested $[90]_8$ laminates: (a) End crushing of untabbed specimen and (b) tabbed coupons and (c) Fracture angle.	60
3.14	Dimensions of uniaxial compressive test coupons (in mm).	61
3.15	Compressive uniaxial response of $[0]_4$, $[90]_4$, $[\pm 45]_{4S}$ and $[\pm 45]_S$ laminates. Subfigure is included to better visualization of small strain range.	62
3.16	Flowchart for Hashin's damage model calibration.	64
3.17	$[\pm 45]_{2S}$ uniaxial tensile loading results from Hashin's model including reorientation: (a) numerical stress-strain compared to experimental curves and (b) damage initiation indexes and variables evolutions.	66
3.18	$[\pm 45]_{4S}$ uniaxial compressive loading results from Hashin's model: (a) experimental and numerical stress-strain and (b) evolution of energies on the simulation.	66
3.19	Hashin's damage model and experimental results for angle-ply uniaxially tensile tested laminates: (a) $[\pm 56.3]_{2S}$ stress-strain results, (b) $[\pm 56.3]_{2S}$ damage evolutions, (c) $[\pm 33.7]_{2S}$ stress-strain results and (d) $[\pm 33.7]_{2S}$ damage evolutions.	67

3.20	LUR tests for calibration of Ladevèze’s model: (a) $[\pm 45]_{2S}$ laminate and (b) $[\pm 67.5]_{2S}$	68
3.21	Fitting for the Ladevèze’s damage evolution law.	71
3.22	Evolution of plastic law, expressed in terms of effective shear stress against accumulated plastic strain.	72
3.23	Fitting for the shear-transverse damage interaction.	73
3.24	Ladevèze’s numerical model and experimental results for angle-ply tensile tested laminates: (a) $[\pm 45]_{2S}$ LUR test, (b) detail of initial response of $[\pm 45]_{2S}$ and (c) $[\pm 67.5]_{2S}$	74
3.25	Ladevèze’s numerical model and experimental results for angle-ply tensile tested laminates: (a) $[\pm 33.7]_{2S}$ and (b) $[\pm 56.3]_{2S}$	75
3.26	Stress-strain results of the modified parameter identification.	75
3.27	Schematization of the different applied element types, nodes (blue circles), degrees of freedom and lay-up definitions: (a) Shell 2D, b (b) Continuum Shell with one element through thickness, (c) Continuum element with one element for each ply thickness and solid element representation.	77
3.28	Tabbed coupon model applied on simulations. Red and blue faces represent the tied to the reference points, corresponding in colour, where displacement BCs and gripping loads are applied. Representation adapted from [193].	78
3.29	Comparison of ϵ_{xx} contour from Hashin’s damage model (above) and experimental via DIC, for three different stages: (a) Prior to plateau, (b) plateau stage and (c) stiffening stage before failure.	79
3.30	DIC photography of the $[\pm 45]_{2S}$ specimen after failure.	80
4.1	3-point bending numerical results for E_f computation: (a) Normalized moduli vs D_{ratio} and (b) Flexural moduli vs N , with $[\pm 45]_{NS}$	85
4.2	ϵ_{xx} and σ_{xx} profiles caused by bending moment on a material with different tensile and compressive elastic moduli. Reproduction based on [132].	88
4.3	Schematization of the homogenised section technique: (a) original cross-section and (b) homogenised for $E = E_t$. Adapted from [168]. . .	88

4.4	Images of the three-point bending test of ± 45 symmetric laminate: (a) Arrangement of DIC system and triaxial testing machine and (b) Detail of specimen during test, showing high damage accumulation due to matrix cracking and delaminations.	90
4.5	ϵ_{xx} distributions for the midspan cross-section in linear and non-linear stages: (a) $[\pm 45]_{6S}$ and (b) $[+45_2 - 45_2]_{3S}$ [168].	91
4.6	Stress strain response at four different through-thickness positions (defined at Fig. 4.2) at the midspan cross-section: (a) $[\pm 45]_{6S}$ and (b) $[+45_2 - 45_2]_{3S}$ [168].	92
4.7	SEM fractographies for $[\pm 45]_{6S}$ laminate: (a) damage initiation and (b) damage evolution [168].	93
4.8	SEM fractographies for $[+45_2 - 45_2]_{3S}$ laminate: (a) damage initiation and (b) damage evolution [168].	93
4.9	Matrix crack angles reflecting permanent deformation at the inferior ply: (a) $[+45 - 45]_{6S}$ and (b) $[+45_2 - 45_2]_{3S}$ [168].	94
4.10	Evolution of P/b against strain gauge measurements in x and y directions [168].	94
5.1	Geometries of central zone of biaxial cruciform specimens (same scale): (a) Geometry <i>A</i> , (b) Geometry <i>B</i> and (c) Geometry <i>C</i>	98
5.2	Biaxial T-T geometry <i>A</i> specimens: (a) $[0/90]$ instrumented and tabbed specimen and (b) Detail of the tapered gauge zone for a $[\pm 45]$	99
5.3	$\pm 45^\circ$ biaxial cruciform specimens: (a) T-C (upper) and C-C (bottom) specimens after CNC milling and (b) C-C specimen after tab gluing.	100
5.4	Plot of force in perpendicular direction during $[0, 90]_S$ biaxial tensile-tensile test, zooming the maximum difference of forces.	100
5.5	Testing facility during the realization of a T-T biaxial test: (a) Top-view showing DIC system and (b) detail of the instrumented specimen during testing.	101
5.6	Comparison of strain measurement in $[\pm 56.3]_S$ biaxial tensile-tensile test.	102
5.7	Schematization of the thickness reduction in the biaxial gauge zone, exemplifying a $[\pm 45]_{2S}$ reduced to $[\pm 45]_S$	102

5.8	Finite element mesh for the T-C biaxial test simulation (with one SC8R element through thickness) for 0.5 mm element size: (a) 3D representation of the full mesh and (b) 2D detail of the gauge zone.	103
5.9	Analytical curve depicting relation between stress and strain biaxial ratios under linear elastic response of the material. Experimentally produced ratios are also included as marking points. (a) Different symmetrical angle-ply sequences, (b) Detailed plot for $[\pm 45]$ symmetrical, (c) Detailed plot for $[\pm 33.7]_{NS}$ and (d) $[0/90]_{NS}$	109
5.10	3D Mohr's circles depicting the apparent laminate stresses for: (a) Compressive uniaxial test, (b) C-C 1/1 biaxial test and (c) T-C pure biaxial test.	111
5.11	Numerical and experimental results for the biaxial tensile test of the cross-ply laminate: (a) Apparent stress-strain response in gauge zone and (b) Applied force against strains in tapered region.	113
5.12	DIC observations of the biaxially loaded cross-ply laminate, previous (left) and after (right) the apparition of debonding in the stepped thickness transition: (a) Photographies and (b) ϵ_{xx} contour plots.	114
5.13	Numerical contour plot for the matrix tensile damage variable (d_{mt}) from the simulation of $[0/90]$ biaxial tensile test. The represented state correspond to a load step higher than the experimental apparition of the debonding.	115
5.14	Failure of the cross-ply biaxially loaded specimen: (a) Specimen after tests and (b) initiation of matrix cracking at the corners.	115
5.15	Biaxial stress-strain curves for T-T-A45-1: (a) Position A of strain gauges and (b) Position B of strain gauges. Dashed lines symbolise the elastic estimation for the centre stresses after initiation of non-linearities.	116
5.16	Normalized applied force-time plot for a pure T-T biaxial test showing small deviations in force regularization. Force data to virtualize the test is obtained from this plot.	117
5.17	Stress-strain results from simulations for pure T-T biaxial test including force deviations. For easier comparison, experimental average stress-strain is also plotted. Green and orange rectangles allow comparison with Fig. 5.16.	118
5.18	Failure of a T-T biaxially tested $\pm 45^\circ$ symmetrical laminate: (a) 1/1 ratio failure and (a) detail of fracture surface.	119

5.19	Biaxial T-T test over geometry <i>A</i> cruciform specimen under $P_y^a/P_x^a = 1.2/1$ (T-T-A45-1.2): (a) Force-time plot and (b) experimental and numerical stress-strain curves in gauge zone.	120
5.20	Numerical and experimental stress-strain responses for biaxially tensile tested laminates: (a) T-T-B45-1.5 and (b) T-T-C45-0.5.	120
5.21	Failure of a T-T biaxially tested $\pm 45^\circ$ symmetrical laminate: (a) T-T-B45-1.5 and (b) T-T-C45-0.5.	121
5.22	Experimental and numerical stress-strain plots at tapered region from biaxially tensile $[\pm 56.3]_S$ laminate: (a) T-T-56-1 and (b) T-T-56-3.	122
5.23	Experimental and numerical stress-strain plots at longitudinal direction of arms from biaxially tensile $[\pm 56.3]_S$ laminate: (a) T-T-56-1 and (b) T-T-56-3. Left figures represent <i>x</i> -direction arm and right figures represent <i>y</i> -direction arm.	123
5.24	Photographies of biaxially tensile tested specimens of $[\pm 56.3]_S$ laminate: (a) T-T-56-1 and (b) T-T-56-3.	124
5.25	DIC contour plots for ϵ_{xx} under $P_x^a = 3$ kN: (a) T-T-56-1 and (b) T-T-56-3.	125
5.26	Schematization of a buckling mode for a in-plane biaxially loaded plate, representing the example of $m = 3$ and $n = 1$	126
5.27	Buckling load regarding bending-twisting coupling ratio.	128
5.28	Buckling critical stress for a rectangular specially orthotropic plate under biaxial pure stress ($ \sigma_{xx} = \sigma_{yy} $): (a) C-C and (b) T-C.	132
5.29	Buckling modes for different laminates with same geometry and BCs: (a) $[\pm 45]_{2S}$, (b) $[\pm 45]_{4S}$, (c) $[\pm 45]_{12S}$ and (d) $[-45/ + 45_2/ - 45/ + 45/ - 45_2/ + 45]_S$	133
5.30	3D schematic representation of the geometry, BCs and applied forces for the linear 2D buckling simulations on cruciform specimen: (a) C-C and (b) T-C. Dashed lines represent the u_z constrained faces supposed for the anti-buckling jig.	134
5.31	Region of elastic stability for a $[\pm 45]_S$ laminate, comprising at the upper part of the bifurcation curve, compared with the Tsai-Wu failure criterion in the biaxial plane [218].	136
5.32	C-C biaxial testing: (a) Experimental facility including the fixture and (b) detail of the contact surface.	138

5.33	Stress-strain response in biaxially loaded zone of the C-C test, including numerical and experimental curves. DIC and strain gauge measurements in the central zone in both specimens are included.	139
5.34	Out-of-plane displacement maps at the biaxially loaded zone obtained via DIC during C-C biaxial test of $[\pm 45]_S$ with anti-buckling jig: (a) 3D surface and (b) 2D representation.	139
5.35	C-C biaxially tested $\pm 45^\circ$ symmetrical laminate, showing the buckling of the biaxially loaded zone.	140
5.36	Comparison of ϵ_{xx} contours in the linear behaviour for the T-C biaxial test on $\pm 45^\circ$ laminate: numerical (left) and DIC (right)	140
5.37	Shear response observed by means of T-C biaxial test with and without utilising the anti-buckling fixture. Both tests are performed for a $[\pm 45]_{4S}$ laminate, reduced to $[\pm 45]_S$ in the gauge section.	141
5.38	Failure of biaxially T-C tested $\pm 45^\circ$ symmetrical laminate: (a) due to misalignment of the cruciform specimen without the anti-buckling fixture and (b) adequate failure mode.	142
5.39	ϵ_{xx} strain contour plots obtained from simulation with Hashin's PDM and via DIC for T-C biaxial test after onset of non-linearities.	142
5.40	Phased-array inspection of the $\pm 45^\circ$ T-T cruciform specimen after 1/1 biaxial test (above), and numerical contour for matrix tensile damage variable d_{mr} at a point close to maximum load (below). The inspected region (ROI) is schematized at the right side.	143
5.41	Phased-array inspection of the $\pm 45^\circ$ T-C cruciform specimen after biaxial test. The inspected region (ROI) is schematized at the right side.	144
5.42	Phased-array inspection of the $\pm 45^\circ$ C-C cruciform specimen after biaxial test (above), and numerical contour for matrix compressive damage variable d_{mc} at a point close to maximum load (below). The inspected region (ROI) is schematized at the right side.	145

List of tables

2.1	Equivalent stress and displacement relations for damage evolution in Hashin's model.	38
3.1	Tensile and shear properties of M21E/IMA-12K lamina [168].	50
3.2	Ultrasonic identification of M21E/IMA-12K elastic properties.	50
3.3	Tensile properties of cross-ply laminates.	51
3.4	Uniaxial tensile testing of different angle-ply laminates.	53
3.5	Compressive properties of M21E/IMA-12K lamina.	61
3.6	Experimental and analytical compressive estimates tensile elastic properties of $[\pm 45]_{4S}$ laminate.	62
3.7	Hashin's parameter identification for angle-ply laminates. Note this values are obtained for a characteristic length $L_c = 1 \text{ mm}$	65
3.8	Materials properties applied on Ladevèze's model.	69
3.9	Elastic constants relating stress between global and principal directions.	70
3.10	Comparison of different approaches for meshing. Same scenario is tested: uniaxial tensile $[\pm 45]_{2S}$ coupon with 2.5 mm element size (in plane) under 2.5 mm applied displacement. Total number of nodes and DOFs are included. All simulations were run in an eight core Intel I7-7700 processor with 16 Gb PC4-17000 RAM.	78
4.1	Simulations performed for flexural modulus estimation.	85
4.2	Numerical results for flexural modulus estimation and bending stiffness values.	86
4.3	Experimental observations and analytical predictions for the $[\pm 45]_{6S}$ and $[+45_2 / -45_2]_{3S}$ bending specimens [168].	91

5.1	Description of the totality of biaxially tested loading ratios, specimen geometries and laminates. It includes the applied forces and the resultant elastic stress and strain ratios obtained in the biaxially loaded zone.	103
5.2	Tensile apparent elastic properties obtained by means of CLPT.	108
5.3	Compressive apparent elastic properties obtained by means of CLPT.	108
5.4	Ply elastic properties for comparison in numerical models (named as “Modified properties”).	128
5.5	Numerical results for flexural modulus estimation and bending stiffness values.	129
5.6	Analytical and numerical estimations of the bifurcation stress and the corresponding buckling mode in isotropic rectangular thin-plates. The analytical methodology of the β -coefficients is utilised [218].	131
5.7	Estimations of the bifurcation stress and the corresponding buckling mode in square thin-plates of a $[+45 - 45]_S$ laminate. The analytical methodology of the β -coefficients is utilised [218].	132
5.8	Numerical results of the bifurcation values, the corresponding buckling modes and the compressive stress in the central region in $\pm 45^\circ$ angle-ply laminates just before the instability [218].	135
5.9	$[\pm 45]_S$ averaged strengths obtained via uniaxial tensile and compressive characterization and biaxial T-T testing.	136

List of Abbreviations

BBA	B uilding B lock A pproach
BCs	B oundary C onditions
C-C	C ompression- C ompression biaxial test
CDM	C ontinuum D amage M echanics
CFRP	C arbon F ibre R einforced P olymer
CLPT	C lassical L aminated P late T heory
CNC	C omputer N umerical C ontrol
DIC	D igital I mage C orrelation
DOF	D egree of F reedom
FEM	F inite E lement M ethod
FPF	F irst P ly F ailure
FRP	F ibre R einforced P olymer
GFRP	G lass F ibre R einforced P olymer
LEFM	L inear E lastic F racture M echanics
LUR	L oading- U nloading- R eloading
NF	N eutral F ibre
PDM	P rogressive D amage M odel
ROI	R egion of I nterest
SEM	S canning E lectron M icroscopy
SOAPL	S pecially orthotropic a ngle- p ly laminate
T-C	T ension- C ompression biaxial test
T-T	T ension- T ension biaxial test
UD	U nidirectional
UMAT	U ser subroutine to define mechanical m aterial behaviour
WWFE	W orld- W ide F ailure E xercise
XFEM	e Xtended F inite E lements M ethod

Chapter 1

Introduction

*“The science of today is
the technology of tomorrow.”*

Edward Teller, *The Legacy of Hiroshima* (1962), 146.

1.1 Scientific and industrial context

Fibre reinforced polymer (FRP) composites have provided an alternative to consider when optimizing structural designs in which mechanical properties are demanding and weight is a critical design factor [1]. These materials can contain different kinds of fibre (usually glass, carbon or aramid) with high strength and stiffness embedded in a polymer matrix that provides ease of forming and handling of the resultant material.

In the last few years many studies have sought to increase the use of thermoplastic polymers [2] and there are expectations of replacing thermoset composites [3] due to the advantages they provide in forming and recyclability. However, most composites employ thermosetting matrices because of their higher mechanical properties. Among them, the toughened epoxy resins have gained large acceptance in primary aerospace structures, for example [4].

The combination of two materials with a very different nature causes a complex mechanical response of the material, that can be approached from two different points of view. Firstly, the presence of fibres with a certain orientation produces an anisotropy inherent to the lamina of reinforced material, leading to a mechanical response dependent on the direction. Secondly, the heterogeneity and great difference in properties of the constituents of composites causes the appearance of different failure modes [5], schematized in Fig. 1.1. Particularly, when a FRP laminate is under load the polymer matrix can develop cracks, the layers can delaminate, or the fibres can separate from the matrix and fail. This damage leads to a localized or global failure of the composite, which involves many possible modes of failure [6].

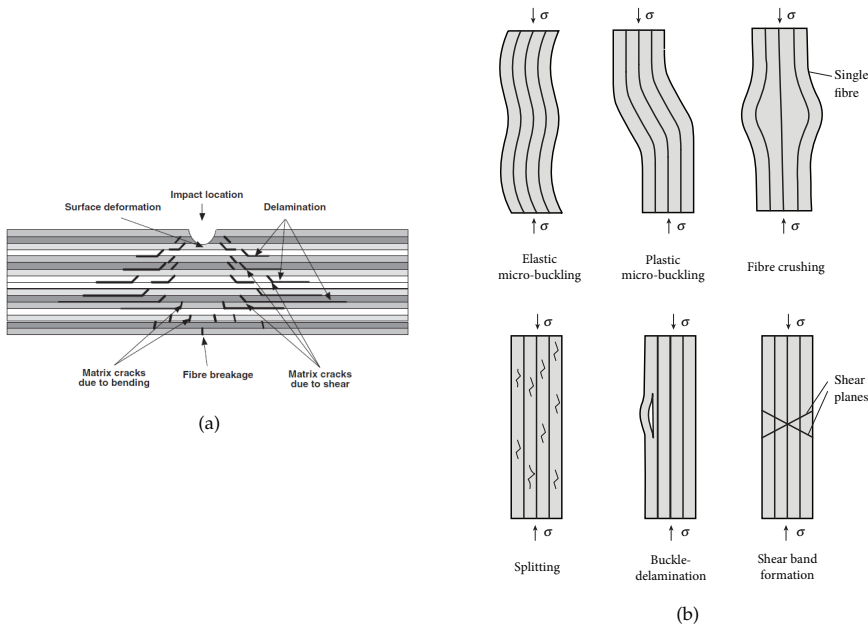


Figure 1.1: Schematic representation of damage mechanisms induced in a composite laminate by low velocity impact [7] and (b) compressive loading [8].

The variety of arrangements, configurations and manufacturing methods for FRP laminates existing today leads designers to consider endless possibilities to increase structural efficiency. As a matter of summary, fibres could be arranged as discontinuous random reinforcement (chopped strand mat, most typical of glass fibre and lower cost applications), unidirectional (UD) continuous fibre or multidirectional woven fabrics. Although the latter could have some advantages dealing with delamination, laminates obtained by lay-up of UD plies offer the optimal in-plane strength and stiffness due to the bigger possibilities in stacking sequences.

Traditional aspects such as stiffness and strength or criteria such as stability under different load situations should be taken into account. Besides, energy absorption or delay of the damage initiation (or monitored appearance) could be tuned via laminate modification, as well as the ability to alter the mechanisms of initial failure [9–12]. In this sense, the influence of the different constituents over the apparent response of the material has been deeply analysed, as local phenomena like fibre kinking, fibre-matrix debonding or matrix shear yielding have a decisive effect in the overall response [13].

Moreover, a brief economical analysis of the FRP market justifies the increasingly high scientific and industrial interest in this field. The “Composites Market Report

2018” [14] shows not only a steady growth in the demand for fibre-reinforced composite materials in recent years (Fig. 1.2), but also includes a series of strong indicators supporting the positive outlooks. It stands out the continuous investment of fibre producers, increasing their plant capacities and investment in R&D. As a matter of example, in the last few years the scientific and industrial communities made a special effort on the development of well known thin-ply laminates, by means of implementing advanced fibre manufacturing techniques [15].

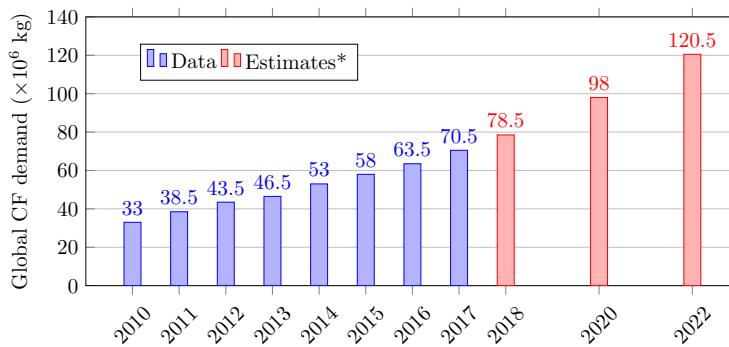


Figure 1.2: Carbon fibre global demand (*Estimations made at 11/2018). Shown in a reconstructed edition [14].

The inclusion of fibre-reinforced polymer matrix composites wherever structural efficiency is at a premium is reflected on the newest families of passenger aircraft, e.g. Airbus A350 XWB and Boeing 787 (Fig. 1.3). Although FRP have been applied decades before the first flight of the mentioned models, these both aircraft families and specially the former, suppose an impressive growth in the application of Carbon Fibre Reinforced Polymer (CFRP). The weight percentage of composite in Airbus A350 XWB reached around 50% of the total weight of the aircraft, including large fuselage and wing components. Not only wide-body twin-engine passenger aircraft apply composite materials in their primary structures, but also some smaller narrow-bodies aircraft such as Airbus A220 are making the most of these materials [16].

In summary, there is a increasing trend in the industrial use of FRP, but today there is still some uncertainty and need of developing know-how about this materials, in order to optimise their design and application. In the case of laminates composed by UD plies, they are mostly utilised in applications with high structural requirement, which makes necessary a complete knowledge of their mechanical response in complex loading situations.



Figure 1.3: Examples of aircraft relevant for composite industry: (a) Airbus A350 XWB [17] and (b) Boeing 787 Dreamliner [18].

1.2 State of the art

1.2.1 Pseudo-ductility in angle-ply laminates

Angle-ply laminates, and specially $\pm 45^\circ$ orientations, arouse great interest due to the possibility of obtaining multiaxial stress states in the lamina. Specifically, the uniaxial test of $\pm 45^\circ$ symmetric laminates constitutes a standard for characterizing the shear properties of the lamina by means of a uniaxial tensile test [19]. For many years the response of these laminates has been analysed in detail from the numerical, analytical and experimental points of view [9, 20–31]. This is due to the appearance of an interesting shear-driven phenomenon, resulting in a highly non-linear stress-strain behaviour, with high yielding and damage accumulation, altogether with fibre reorientation towards the loading direction.

This phenomenon, named pseudo-ductility, has awakened a considerable interest due to the capacity to avoid the inherent brittle behaviour of FRP laminates. This abrupt, and probably catastrophic, failure of FRP composite is usually compensated by conservative design limits, which hinders component manufacturers from fully exploiting their excellent mechanical properties. High performance ductile or pseudo-ductile composites delivering safe failure mechanisms similar to plasticity and strain hardening typical from metals are therefore of significant interest [9, 10, 29, 32].

This concern is reflected in one of the largest research projects that aims to increase ductility in composite materials is the HiPerDuCT [33], headed by the University of Bristol and the Imperial College London. The scope of this project is to look

for alternatives of manufacturing composite material with a ductile or pseudo-ductile behaviour, which could be obtained by using different angle-ply laminates (Fig. 1.4) [9, 29, 34], fragmentation of plies [10, 35], “brick and mortar” interphase [36, 37] and hybridisation of thin-ply [11, 32, 38–41]. Furthermore, different sort of testing has been performed to analyse the possibilities of pseudo-ductile composites, such as the response under high strain rates [41] or the notch insensitivity [11, 42].

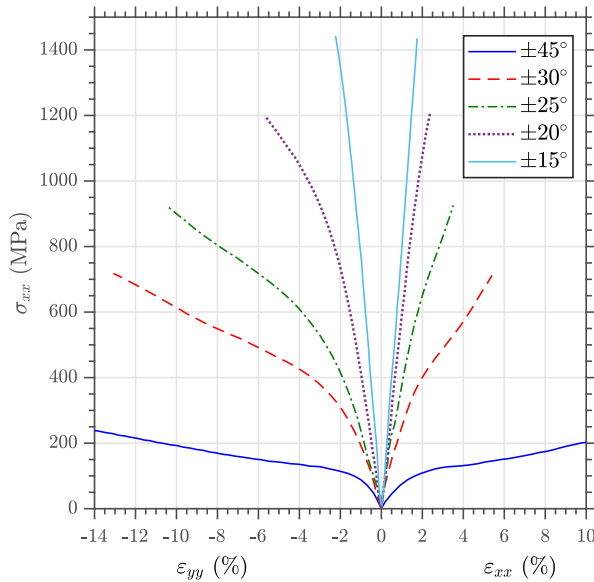


Figure 1.4: Uniaxial tensile tests results for different angle-ply laminates, depicting applied stress against longitudinal and transverse strains. Reproduction based on [9].

Most of these tests depict a similar stress-strain behaviour: a first *almost* linear elastic region is observed, followed by a plateau in which the stress keeps almost at a constant value while plastic strain increases rapidly, reaching values of shear strain up to 10-40% depending on the specific composite. Consequently a fibre re-orientation appears, with measured values up to 14° approximately [9], which it is promoted by shear yielding of the polymer matrix. Then, a third well-differentiated region appears, similar to a hardening effect with an increase of stress until final failure of the specimen.

A detailed analysis of the damage and failure mechanisms on $[\pm 45]_{2S}$ laminates was performed by Sket et al. [26] via X-ray tomography. Matrix cracking was firstly detected in the outer plies at the end of the linear region previous to the plateau. Afterwards, the crack density increases rapidly reaching a saturation level in the outer plies at the end of the plateau. Close to the final failure of the specimen, the density of cracks in the inner plies gets even higher than in the outer plies. The matrix cracking mechanism is not the only failure mode, but during the third region

edge delamination appears and propagates unstably producing the final failure of the laminate.

The previously mentioned works about pseudo-ductility in angle-ply laminates focus on the uniaxial tensile testing, which leads to a combined shear and normal stress state in the lamina. There are few examples of the study of this phenomenon under different loading scenario in the scientific literature. The study of Cui et al. [43] highlights the interest in applying compressive uniaxial test to $\pm 45^\circ$ laminates, as it was previously proven that tension test lead to significant fibre reorientation (also named as “fibre scissoring”). As fibre get more aligned with the loading axis, the shear stress increase and this results in the overestimation of shear stress [20, 21], which it is of concern as this test is standardized for shear characterization [19]. Cui et al. proved that the opposite trend is observed, i.e. compressive testing promotes fibre reorientation away from loading direction. Another important remark from this study is that the commercial software based on the Finite Element Method (FEM) Abaqus does not update the fibre orientation when shear strain is present, which lead to wrong calculations of the constitutive relations. Additionally, higher maximum stresses are measured when increasing strain rate, in agreement with other results for tensile testing [41]. These strain rate effects explain the contribution of the matrix to the pseudo-ductile behaviour, as fibre still behaves as brittle constituent.

Another work of interest, although not directly associated with pseudo-ductility, is performed by Fedulov et al. [44]. In this study, the influence of non-linear elastic shear stiffness phenomena on damage and failure is analysed. The constitutive behaviour of the material is modelled through a Progressive Damage Model (PDM), obtaining good results when the non-linear shear material model is applied. However, it is not clear that this is due to the non-linear shear behaviour that appears since the beginning of the test. The authors note that another work with thermoplastic matrix [45] demonstrated that the ply shear modulus drop is explained neither by intra- or inter-ply matrix cracking nor by changing the degree of crystallization of the polymer. In this last work it is indicated that perhaps it could be related to viscoelastic phenomena or degradation of the matrix-fibre interface.

Herakovich et al. [21] proposed a numerical modification of the Ladevèze mesoscale model in order to account fibre rotation due to large shear strain response of $[\pm 45]_S$ laminates. Additionally, they compared the numerical results considering fibre rotation and change in cross-sectional area with experimental evidences, proving the importance of these effects in the analysis of this laminate configuration. Van Paepegem et al. [22, 23] also studied the non-linear shear stress-strain response, in this case with GFRP $[\pm 45]_{2S}$ laminates, proving that there is an important decrease in the secant shear modulus while permanent shear strain is also very large. Be-

sides, these experimental evidences were addressed with a numerical FEM model, proposing the calibration of a phenomenological model consisting in an exponential evolution of damage and plastic shear strain.

Apart from these non-linear phenomenon affecting angle-ply laminates, the choice of stacking sequences with layer orientations at $\pm 45^\circ$ is common in real applications, due to thermal factors that can affect the curing of the laminates [46]. Although angle-ply stacking sequence may not be optimal in terms of properties such as stiffness and strength, these orientations facilitate some design aspects, as obtaining quasi-isotropic laminates. Another important advantage of this laminate sequence is the high torsional stiffness they provide [47]. Even when applying biaxial and triaxial fabric laminates, angle-ply configurations are widely used in industrial applications such wind turbine blades [48] due to the last reason.

1.2.2 Biaxial testing on composite materials

The large increase in the structural use of this laminates mentioned above has generated great scientific interest in the study of its mechanical behaviour. In real applications such as the aerospace or the wind turbine sectors, examples of the use of laminates, structures submitted to multidirectional loads are found frequently. Due to the geometry and load disposition, these may be analyzed as a plane stress situation, where the significant stresses are the two normal and the in-plane shear components (i.e. out-of-plane components of the stress tensor are negligible).

When analysing UD laminates, a clear definition of multiaxiality should be provided [49]: an *external* (or apparent) multiaxiality is achieved if the material coordinate system is aligned with the global one and loads are applied in multiple directions; conversely if fibres form an angle with global/load coordinate system, the stress state results in a combination of *external* and *internal* multiaxiality.

For instance, an easily performed and quite common multiaxial test is the off-axis uniaxial test (schematised in Fig. 1.5a), with a laminate consisting of a stack of UD plies oriented at a certain degree θ regarding loading direction [50]. Therefore, laminate behaves as a single lamina and due to the different orientation between principal and global direction, an *internal* multiaxial stress state appears where the three in-plane components are non zero. The respective stress ratios, however, depend on the fibre orientation angle and cannot be selected at will [51].

Another example of multiaxial test, in this case producing an *external* multi-axiality, is the biaxial test via application of loading in two perpendicular in-plane

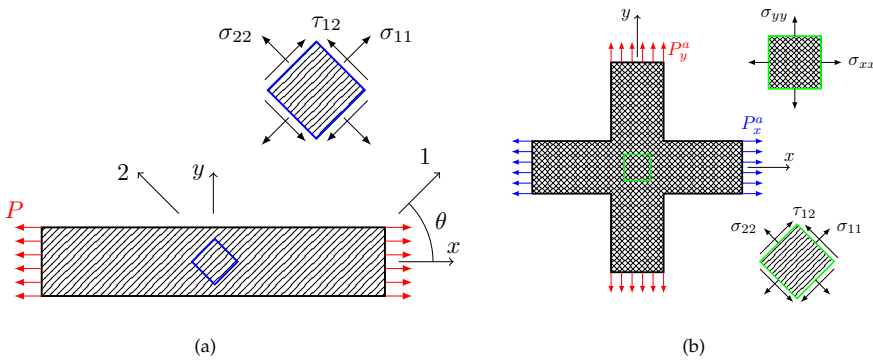


Figure 1.5: Biaxial testing methodologies: (a) Off-axis uniaxial and (b) Cruciform test.

directions over a cruciform specimen, as depicted in Figure 1.5b.

Although for the uniaxial case there are regulations for the characterization of the material and a large number of experimental results, there is not yet a standardized procedure in the multiaxial characterization of laminates under externally loading in multiple directions. Therefore the experimental results regarding multiaxial stress/strain states are limited to a small range of loading ratios and stacking sequences. In the absence of failure criteria applied to composite materials, Hinton, Soden and Kaddour promoted in 1991 the initiative of *First World-Wide Failure Exercise* (WWFE-I), in order to create theoretical predictions for the damage and failure of composites, at the same time validated with multiaxial testing data [52–55]. Analysing certain laminate configurations established by Hinton and Soden [52], recommendations were obtained for the design and multiaxial characterization of these materials [55].

Among the conclusions of these studies, Soden et al. [55] emphasize that, despite obtaining a large amount of experimental data, it seemed to be a limited number of studies where a wide range of different loading ratios were applied to an specific laminate. In addition, the majority of WWFE experimental results derive from tests with tubular specimens, which present certain difficulties, such as determining the initial failure and problems to obtain the geometry of these specimens.

Although multiaxial testing has been performed for many years [56–58], in the last two decades many methods have been extensively developed to assess multiaxial mechanical characteristics. The predominance of tubular tests during the WWFEs that require a certain combination of tensile/torsion loads and stacking sequences to reach different biaxial loading ratios [49] has already been referenced. Currently, it seems that this type of test is postulated as a suitable solution in multi-

axial fatigue tests [49,59–61].

Nevertheless other authors [51] point out how such tests with tubular specimens can lead to certain inconveniences. Listing a number of these: the presence of radial stresses could be not negligible, the properties of plane plates and tube shells are not directly comparable (e.g. this could be easily related to the curvature of fibres), and specimens in the form of thin-walled tubes can experience instability phenomena when subjected to compression or torsion.

Comparing the results on tubes with those obtained for the off-axis plies of multidirectional flat laminates, it was concluded that crack initiation and propagation phenomena are consistent under *internal* and *external* biaxial loading conditions, provided that the local stress state is the same [49]. Conversely, Cai et al. [62] pointed out certain differences between cruciform biaxial and off-axis testing. Especially when applying failure criteria, the results obtained for the interaction coefficients between the different loading directions (explained in next section of this document) are more precise in the case of the cruciform biaxial testing.

Following the WWFEs studies, cruciform specimens begin to be used more frequently in biaxial testing. This type of test consists in the direct application of tensile and/or compressive loads in the two in-plane perpendicular directions, so that it is possible to easily obtain the desired ratio of biaxial stress/strain, acting on the applied force/displacement rates in both directions. However, among its main drawbacks are the obtention of the cruciform geometry and the uniqueness of the testing machines [63].

Deepening into the state of the art of cruciform specimens biaxial testing, some of the most discussed lines of research when designing the test procedure are collected. Part of the following works deal with characterization of metals, note that anisotropy of some metals (i.e. rolled thin plates [64]) arouse also interest on multiaxial characterization.

- **Clear definition of the requirements needed to achieve a successful biaxial test:** There is a general agreement on the requirements that allow to define a correct biaxial test [51, 65]: (i) maximization of the region of uniform biaxial strain, (ii) minimization of the shear strains in the biaxially loaded test zone, (iii) minimization of the strain concentrations outside the test zone, (iv) specimen failure in the biaxially loaded test zone, and (v) repeatable results.
- **Design of testing facility:** One of the main problems to address when performing biaxial tests is the uniqueness and complexity of biaxial testing facilities. Several authors detailed the requirements to be fulfilled by these ma-

chines, inter alia having a sufficiently rigid frame to maintain the alignment of the specimens under reaction forces [63]. Besides, synchronization between actuators is critical to maintain the necessary loading ratios, as well as to prevent mismatches due to certain misalignment or slippage of the gripping system. There are some test machines with only two mobile actuators, fixing the opposite ones, although this option causes a distortion of the specimen, leading to erroneous results [65]. The most commonly used solution in biaxial test systems with cruciform specimens is the application of a closed-loop servo control using force transducers feedback signals [51, 63, 66]. Due to the cost of the aforementioned equipment, some authors have proposed devices to adapt uniaxial machines [67–71], transferring the uniaxial load to the two perpendicular directions of the plane. However, these solutions usually pose misalignment problems, lack of balance between opposing actuators and limitations in the applicable load ratio.

- **Cruciform specimen geometry optimization:** several authors have performed simulations using **FEM**, as reflected in Fig. 1.6 [51, 72–77]. Smits et al. [51, 72] investigated the effects of biaxial stress states on the failure of Glass Fiber Reinforced Polymer laminates (**GFRP**), and determined a specific geometry for biaxial testing working with $[(\pm 45/0)_4/\pm 45]_T$ lay-up. Combining the **FEM** and experimentation, they optimized a cruciform-shape geometry with a reduction in central thickness, maximizing the failure strain and promoting breakage in the study region. This solution has been taken as a reference for most subsequent works in composite biaxial testing. The analysis of the effect of geometric discontinuities and a comparison of the modelling of geometry with 2D and 3D elements was performed by Lamkanfi et al. [78, 79]. It is shown in the conclusions how both numerical solutions offer similar results far away from discontinuities, highlighting the influence central zone tapering on the heterogeneity of the strain fields in the gauge region. Nevertheless, these studies agree with the inevitable concentration of stress/strain at the corners of the cruciform specimen when applying tensile-tensile or compressive-compressive loading, no matter the geometry chosen to reduce the influence of these.

Moreover, Serna Moreno and López Cela [77] carried out numerical simulations, combined with experimental results (illustrated in Fig. 1.6b), to demonstrate the need for a change in the width of the specimen arms in order to adapt the arms maximum load to the biaxial stress ratio, thus preventing premature failure out of the gauge region. This result is further demonstrated with numerical simulations based on the eXtended Finite Element Method **XFEM** [80–82]. These studies also demonstrate the need for thickness reduction in the central zone to maximize stresses/strains in the biaxially loaded zone, validating also the ability to obtain homogeneous strain states in the gauge zone of the speci-

men. Finally, the simulations carried out in [83] demonstrate how the tensile-compressive stress state favours the strain concentration in the biaxially loaded region.

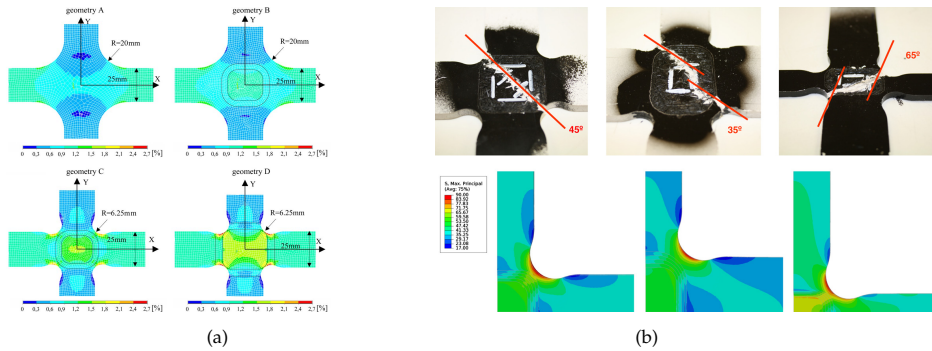


Figure 1.6: FEM simulations for different specimen geometries: (a) Principal strain [51] and (b) Principal stress [77].

- Manufacturing method influence:** The reasoned thickness reduction in the central zone can be achieved by different methods, such as tabbing [84–86] or CNC milling [71, 74, 77, 80, 87, 88]. In the work of Ramault et al. [73, 74] was demonstrated as similar test specimens made by machined tabs resulted in lower values of failure loads, due to the debonding of the tabs. Therefore, the milling option is preferable, although damage generated by machining should be minimised.
- Data acquisition techniques:** strain gauges are still in application due to their simplicity and precision, yet the application of the Digital Image Correlation DIC technique for measuring full field strains [89–91] stands out. The problem comes when estimating the stresses produced in the biaxially loaded area. In this sense, coefficients indicating the ratio of applied force that reaches the gauge section have been defined from analytical estimations [92] or by means of FEM simulations [77]. The drawback of this solution is that they are based on linear elastic analysis, so the range of application is limited until the appearance of material non-linearities. A similar alternative is embodied in the work of [87], where stresses are obtained from the measurement of strains in combination with the constitutive equations of the material, which is also limited to the elastic behaviour. Another option also included in this work is the combination of numerical simulations and experimental measurement to perform an inverse calculation of the material stiffness, further detailed in [93].
- Fatigue and stress concentrations in cruciform specimens:** other studies in the field of biaxial testing seek to study phenomena related to geometric discontinuities, such as the case of open hole discontinuity [86, 94–97]. There is

also interest in examining the effect of multiaxial loads on fatigue life of composites [98–100].

The problem of biaxial characterization is not limited to the scientific-academic sector. In recent years, some efforts have been made for different research and normalization centres in order to look for a industrialization of this kind of testing [96, 97, 101]. Complex testing fixtures and facilities are proposed for a more detailed studied of phenomenon surrounding multiaxiality, not only in composites, but also of high interest relating metal plasticity [102, 103].

Regarding commercialization of biaxial testing, in recent years different biaxial generic test machines have appeared, unlike the unique machines made ex professo from the scientific studies previously mentioned in this section. Known manufacturers of test equipment have launched machines with different application ranges, from the testing of thin textile, biomaterial or polymer membranes to testing machines for high strength materials such as metal alloys and composites [104–106]. Among the most outstanding features of these equipments is the need for high rigidity, as well as the electronic control of the load-displacement application, highlighting the mid-point control systems as a distinguishing feature.

With regard to the regulatory framework, today it is still not possible to find standards for biaxial characterization in composite materials. However, ISO developed recently a standard for the characterization of metal alloys via cruciform biaxial testing [107].

In recent years there are several authors pushing biaxial characterization through (modified) ARCAN fixtures [99, 108–111] and other tests somehow similar to biaxial tension-compression (T-C) for the obtention of shear properties (Fig. 1.7b) [112]. The ARCAN method is more similar to the cruciform test, since a flat specimen is subjected to biaxial states, but with the particularity of a specific jig that allows certain combined tension/compression + shear ratios to be introduced using a uniaxial test machine (Fig. 1.7a). Despite simplifying the specimen geometry and the necessary test facility, the limitation of this test is again the impossibility of obtaining any state of biaxial loading, as it depends on applied force vector decomposition.

In summary, many biaxial studies have been performed in past years in order to characterize the biaxial strength and failure modes under different ratios, mostly tensile-tensile. Despite of this, biaxial strength characterization of tensile-tensile (T-T) loaded specimens still awakes uncertainty in the scientific community, due to the difficulties of obtain a pristine failure mode due to stress concentrations, edge effects and damage promoted by tapered specimens [114]. Few studies detail the mech-

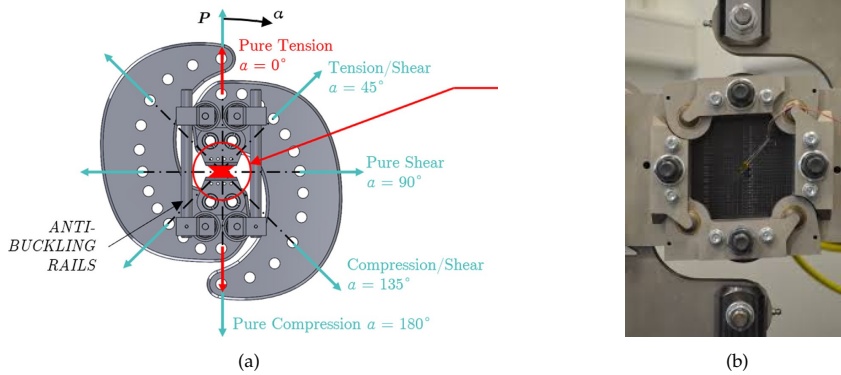


Figure 1.7: (a) Modified ARCAN jig [110] and (b) ISO20337 fixture [113].

anisms of non-linearities due to plasticity and damage evolution observed under multiaxial loading [89, 110, 115], while these works allow to establish the limits in which the biaxial tests are feasible [116]. This research line will be emphasized in the present Thesis.

On a separate issue, some studies tried to experiment with triaxial testing, without any significant progress due to the even greater complexity [117–120]. Welsh and Adams [63, 121] attempted to triaxially test cruciform specimens by means of attachments glued to the central region of the specimen. The authors reported that through-thickness compression was insensitive to in-plane loading in a cross-ply laminate, and the attempts of test out-of-plane tensile strength were unsuccessful due to attachment debonding. Additionally, a Second World-Wide Failure Exercise (WWFE-II) [122–124] was performed in order to test the failure theories under triaxial stress states. Among the conclusions of this exercise, promoters remark that the proposed twelve failure theories provided very different results, which also needed to be modified with the data from the multiaxial experimental testing, and that raise very different opinions about the failure under hydrostatic pressure.

1.2.3 Failure theories

The first aspect to consider when talking about failure theories is the lack of a clear definition of the *failure*, as the promoters of the WWFE noticed. In fact, Hinton et al gave an ambiguous definition of the failure [52]: “as the point at which the structure or component ceases to fulfil its function”. After this, the trend is to speak of the so-called First Ply Failure (FPF), defining mathematical expressions for a failure index (F) which represents initiation when it reaches 1. This FPF does not usually represent the true failure of the laminate, since after the first load drop, de-

pending on the laminate, there will be a progressive stiffness degradation that can largely delay the total failure of the laminate.

The first failure theories for composite materials originated in the 60-70s as adaptations of existing theories for metals applied to anisotropic materials. Some of this non-physically based models with greater impact and validity in FRP are the Tsai-Hill and Tsai-Wu criteria. These models are based on a mathematical expression which predicts failure, sometimes interpolating a few experimental points [125]. They are also called phenomenological criteria, as they do not attempt to predict which failure mode is taking place.

Tsai-Hill failure criteria is based on a modified distortion energy principle coming from the quadratic Hill yield criterion [126] applied to the case of the orthotropic lamina by Tsai [127], and expressed in Eq. 1.1 for plane-stress case.

$$f = \frac{\sigma_{11}^2}{S_{11}^2} - \left(\frac{\sigma_{11}\sigma_{22}}{S_{22}^2} \right) + \frac{\sigma_{22}^2}{S_{22}^2} + \frac{\tau_{12}^2}{S_{12}^2} \quad (1.1)$$

where S_{ii} represent the failure strength in i -direction. The Tsai-Wu semi-empirical interactive failure criterion [128] had an important acceptance, showing itself as one that gave a better results during the WWFE, and it has been implemented in different commercial codes of FEM such as ANSYS [129] or Abaqus [130]. However, it has led to a large number of discussions and oppositions due to its lack of mode-differentiating character. This criterion has the advantage of its most general anisotropic approach, based on single quadratic tensorial expression accounting for all possible failure modes observed in experiments (Eq. 1.2), while including the possibilities of different tensile and compressive strengths (represent by superscripts t and c respectively), typical of composites [131–133].

$$\begin{aligned} f &= F_1\sigma_{11} + F_2\sigma_{22} + F_{11}\sigma_{11}^2 + F_{22}\sigma_{22}^2 + F_6\sigma_{12}^2 + 2F_{12}\sigma_{11}\sigma_{22} \\ F_1 &= \frac{1}{S_{11}^t} - \frac{1}{S_{11}^c}; & F_{11} &= \frac{1}{S_{11}^t S_{11}^c} \\ F_2 &= \frac{1}{S_{22}^t} - \frac{1}{S_{22}^c}; & F_{22} &= \frac{1}{S_{22}^t S_{22}^c} \\ F_6 &= \frac{1}{S_{12}^2} \end{aligned} \quad (1.2)$$

However, there is still one coefficient F_{12} which has not yet been specified above. The interaction coefficient F_{12} is expressed in Eq. 1.3, where σ_b represents the biaxial strength in a T-T biaxial test. Given the difficulties in conducting this type of tests and the lack of standardized testing procedure, different proposals have been done

in order to estimate this coefficient.

$$F_{12} = \frac{1}{2\sigma_b^2} \left[1 - \left[\frac{1}{S_{11}^t} + \frac{1}{S_{11}^c} + \frac{1}{S_{22}^t} + \frac{1}{S_{22}^c} \right] \sigma_b + \left[\frac{1}{S_{11}^t S_{11}^c} + \frac{1}{S_{22}^t S_{22}^c} \right] \sigma_b^2 \right] \quad (1.3)$$

Tsai and Wu insisted that the failure envelope must be an ellipsoid and hence remains closed [128]. According to analytic geometry, this condition offers some constraints on F_{12} but the constraints are given as ranges. If plane stress hypothesis is assumed, then the condition for ellipsoid is $F_{12}^2 < F_{11}F_{22}$, which still generates a wide range of possibilities. A proposal of Tsai [134] is to consider that: $F_{12} = -\frac{1}{2}\sqrt{F_{11}F_{22}}$. This value is included in the aforementioned range. Besides, the Tsai-Wu equation particularized for an isotropic material with equal tensile and compressive strengths applying this factor is equivalent to von Mises's criteria. Another proposal found in literature for this interaction factor is to make it equal to zero [135], arguing the difficulty of obtaining a representative biaxial failure. Some authors [136] explain that this consideration can produce adequate results when the shear stresses are not zero.

Regarding physically-based failure criteria, the most basics models are based on maximum stress (Eq. 1.4) and maximum strain (Eq. 1.5). The basics of these models explain that failure occurs if one stress/strain exceeds the corresponding allowable quantity. In this sense, for an orthotropic material, different equations should be proposed for each material direction under tension and compression.

$$f = \max \left(\frac{\sigma_{ij}^k}{S_{ij,ult}^k} \right) \text{ where } i, j = 1, 2, 3 \text{ and } k = t, c \quad (1.4)$$

$$f = \max \left(\frac{\varepsilon_{ij}^k}{\varepsilon_{ij,ult}^k} \right) \text{ where } i, j = 1, 2, 3 \text{ and } k = t, c \quad (1.5)$$

Subsequently, the Hashin-Rotem failure criteria [137,138] has gained wide acceptance in the scientific and engineering community on the field of fibrous composites, being one of the first physically-based models for anisotropic materials, developed in parallel to Puck's failure theory [139,140]. Both criteria are based on a collection of expressions based on strengths of different failure modes, which unquestionably includes at least part of the range of failure modes that may exist in FRP. They include the fibre and matrix, tensile and compressive failure modes, with Puck adding the

matrix failure mode due to inclined plane fracture, the so-called “mode C” (Fig. 1.8), therefore producing more accurate results under compressive stresses. Both criteria have inspired considerable research in failure-mode oriented criteria [125, 141].

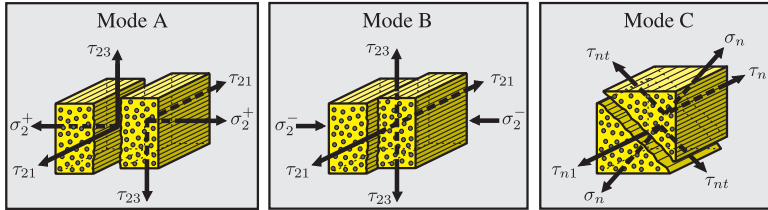


Figure 1.8: Matrix cracking modes collected by Puck’s failure criteria [142].

Starting from the concept of the Hashin-Rotem and Puck theories, many failure-mode oriented criteria were proposed. Most of these were evaluated during the WWFEs. As a summary of the three exercises, the recent publication [1] collects 30 design tools (in other words, failure theories and damage models) that provide good results. However, none of them is capable of giving a closed solution to the problem of composites failure, at least within a range of $\pm 10\%$ of the failure strength/strain. In addition, the promoters of the WWFEs recommend the use of different criteria or tools according to the application, but this solution is not at all attractive to engineers who design composites structures. Other relevant conclusions of these exercises for the present Thesis is that the application of multiaxial states that generate large deformations remains a challenging problem for the current models, and that there is also no consensus in the scientific community on the progression of laminate damage.

Moreover, it should be noted that the $[\pm 45]_S$ laminate is one of the proposed stacking sequences in the WWFE [143], along with three quasi-isotropic laminates that combine layers at $\pm 45^\circ$. Regarding the failure envelope, for the angle-ply laminate it was concluded that all the predictions showed an enhancement in the strength under both biaxial tension-tension (T-T) and biaxial compression-compression C-C. Besides, authors noted there was a broad agreement between the majority of the theories, with a factor of 2 between the largest and lowest strength predictions in the pure (C-C) biaxial.

Currently it seems that the generalized trend in the application of failure theories is the criteria originated at NASA Langley Research Center (LaRC). Dávila et al. [144, 145] proposed the first version of this criterion under plane stress conditions, namely LaRC03, which was later extended to three-dimensional stress states by Pinho et al. [146], defining the LaRC04. Afterwards, the formulation relating the compression matrix failure was improved [147], leading to the current version of the criterion,

LaRC05 (further detailed in [148, 149]).

1.2.4 Damage modelling

In the previous section some of the most applied failure theories for composite materials have been defined. In addition, it has been commented that these criteria only define the stress/strain state in which the first material failure occurs (the so-called **FPF**). However, it must be understood that, in a general approach, the material is considered to behave linearly elastic for lower loads, this implies assuming that all interfaces between plies and between fibre and matrix are perfectly bonded.

When large loads are applied, the failure criteria allow us to define when the first microstructural damage appears, which results in a progressive degradation of the material properties, and therefore, a non-linear behaviour of the material. These damages are ideally posed as a diffuse phase of damage in the form of microcracks or microvoids that will be extended with the increase in stress/strain up to initiation of macroscopic crack and catastrophic failure [150–152]. These models consider that the damage can only increase or remain constant over time, thus resulting in a progressive degradation of stiffness, hence the name of Progressive Damage Model (**PDM**). The damage is usually symbolised with the variable d , accounting the percent loss of initial undamaged modulus E_0 , as illustrated in figure 1.9.

The first works found in bibliography regarding the field of Continuum Damage Mechanics (**CDM**) are those from Kachanov [153] and Rabotnov [154]. They applied the continuum damage to the study of the creep phenomenon on metals. Over the next two decades, these models are generalized to more general cases of isotropic materials under different states of multiaxial loading. The first major advance in the application of the **CDM** to the **FRP** composites comes from the hand of Ladevèze et al. [155], proposing a mechanical behaviour model for an *elementary* ply based on the general theory of anisotropic damage that Ladevèze previously formulated in [156]. This model, in addition to the development of a basis for later **PDM** approaches, is still of great application today [21, 157] and has been implemented in commercial **FEM** codes [158]. It collects the mechanisms of damage via matrix microcracking and fibre/matrix debonding, using variables called associated thermodynamic forces (based on the derivation of the damaged strain energy) coupled with a plasticity model with isotropic hardening. The evolution of the damage together with the plasticity generates an inelastic behaviour that is schematized in the Fig. 1.9.

Ladevèze’s model is a mesoscale composite damage theory because it considers that the damage is uniform in the thickness of each layer. It also considers the dif-

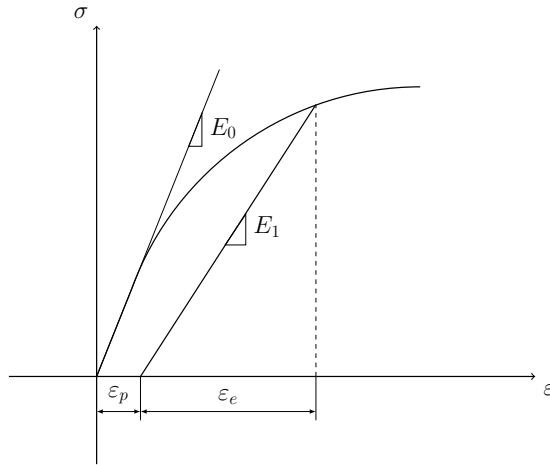


Figure 1.9: Theoretical inelastic response obtained with damage and plasticity model. Reproduction based on [21,155].

ference in tensile and compressive failures, assuming that the transverse cracks are closed under compressive loading, and therefore suppressing compressive damage in the transverse direction. On the other hand, it assumes the predominant brittle behaviour in the fibre direction, so that it applies a criterion of instantaneous complete degradation when the allowed associated forces are reached. The formulation, characteristics and limitations of this and other damage models will be described in detail in Chapter 2.

Another damage formulation, simpler but less methodical, is the Ply Discount Method [4], also denominated Post-First-Ply-Failure analysis [159]. This method consists on the traditional ply stress calculation based on Classical Laminated Plate Theory (CLPT), combined with some failure criterion in order to predict FPF. Then, it reduces the moduli in the failed ply (usually the transverse modulus E_2 and the in-plane shear modulus G_{12} , supposing matrix cracking), recalculate ply stresses, increase the load, test for second ply failure, and so on until “last ply failure” is predicted.

1.3 Objectives

The complexity of the mechanical response of FRP composites, with the presence of different non-linear effects, dependence on the stacking sequence and drastic variances that arise in damage and failure modes makes necessary to develop the

comprehension of multiaxial loading effects. This mechanical characterization has been developed through different standardized tests, some of these slightly modified. Furthermore, non-standardized tests are performed to provide an intermediate level characterization (Element/Structural Tests level) in a design step following the Building Block Approach (BBA), typical of the certification process of a composite aero-structure [160].

In parallel, numerical simulations at the macro and mesoscale level are needed for the evaluation of the elastic response of the laminate, its stability, and the prediction of the initiation and evolution of the damage by means of different existing models for fibrous composites. Although failure under multiaxial loading will be also analysed, this PhD Thesis does not consist of a compendium of tests where failure of numerous laminates under any loading states is collected, but rather an in-depth study of the problematic and complexity of the multiaxial loading states in laminates, trying to bring to light the need for a consensus standardization of the biaxial test applied to FRP laminates.

Following the motivation and knowledge explained in this chapter, a series of objectives have been proposed for this Thesis, in accordance with those of the research project DPI2016-77715-R (*Estructuras de materiales compuestos ante cargas multiaxiales*) in which the present work has been framed.

- Conduct a study from the analytical, numerical and experimental fields, thus allowing the validation of different models and their extrapolation to load situations beyond those carried out experimentally. A methodology based on the ideas of Virtual Testing is pursued, trying to minimize the number of experimental tests necessary to characterize the response of the material under multiaxial loading scenarios.
- Analyse different configurations of CFRP laminates composed of epoxy prepreg laminae reinforced with UD continuous carbon fibre. Symmetrical stacking sequences of industrial interest are chosen, deepening in the case of angleply due to the presence of highly non-linear behaviour related to shear stresses.
- Perform experimental tests that include from the basic characterization of the mechanical properties of the UD lamina to the response of non-standard tests with different ratios of tensile and compressive biaxial loads as well as bending tests.
- Discuss the validity of biaxial testing at different loading ratios, taking into account the geometry and stacking sequence of the specimen to be tested. It is worth highlighting the debate about the capacity of these tests in the failure

strength characterization, although the primary objective of these testing campaigns is the study of the mechanical response prior to the failure, with emphasis on the initiation and evolution of the non-linear behaviour of the material. In this sense, it will be necessary to design a new biaxial test methodology for compressive loading.

- Develop numerical simulations based on **FEM** which allow a correct evaluation of the initiation and evolution of the damage in the experimental tests carried out. In this context, the evaluation of the apparent response of the laminate under flexural loads and buckling instability should be analysed, as well as the characterization of the initiation of non-linear behaviour associated with damage and plasticity at the mesomechanical level. For the latter, the ability to model large structures under any stress/strain state with a relatively low computational cost will be sought, proposing alternatives at the meso- and macro-mechanical level.
- Compare the experimental results with the predictions of different analytical models. The **CLPT**, theoretical failure criteria existing in the literature, such as Hashin, Ladevèze and Tsai-Wu, as well as analytical models that estimate the influence of the bending-twisting couplings will be applied for this purpose.
- Carry out an overall comparison among the apparent behaviour of angle-ply laminates under uniaxial and multiaxial loads of different nature. This aspect seeks to make the reader aware of the importance of the correspondence between the properties determined by standard characterization of the material and the actual response considering the geometries and load scenarios frequently present in composite structures. For instance, up to date pseudo-ductility phenomenon has been analysed mostly under uniaxial loading. These previous works aim to take advantage of this non-linear behaviour to avoid catastrophic failure of **FRP** but they do not cope with the fact that most real applications are not uniaxially loaded.

1.4 Summary of the contents

This doctoral dissertation is composed of six chapters. The aspects discussed in each chapter are briefly described below:

Chapter 1 posed an introduction and contextualisation of the scope of the Thesis.

Chapter 2 depicts the main characteristics of the numerical, analytical and experimental tools that are applied throughout the following chapters. This includes the

properties of the material, the facilities and test methodologies used to ensure the reproducibility of the results shown in this document. Besides, the formulation of the analytical models and the software applied are detailed in this chapter.

Chapter 3 is based on the characterization of the uniaxial behaviour of the lamina and some laminates of interest, developing tension, compression and cyclic quasi-static tests, which are also applied to calibrate and validate numerical and analytical models.

Chapter 4 describes the response of angle-ply laminates under flexural loading. The non-linear behaviour caused by the so-called pseudo-ductility, its relation with bending-twisting coupling terms and analytical models considering the different behaviour under tension and compression are highlighted.

Chapter 5 focuses on the biaxial testing over **FRP** laminates, showing a wide variety of tensile and compressive loading scenarios on cruciform specimens. Special attention is given to tests including compressive loading, performing a detailed analysis of the buckling of laminated plates. From the numerical point of view, special emphasis is made on the basic ideas of the **PDMs** applied to the highly non-linear behaviour of the uniaxially and biaxially tested angle-ply laminates.

Chapter 6 brings together the results obtained through the different approaches described in the previous chapters. Then it summarizes the most relevant results of all the work developed, opening a discussion on the methodologies used, their applicability and scope. From these conclusions it is possible to draw potential future lines of research that collect the knowledge base expounded in this document and will allow to expand the understanding of the complexity of the mechanical response of **FRP** laminates.

Finally, **Appendix A** lists the publications in the form of journal papers and communications in national and international conferences to which this doctoral thesis has led up to the moment of the completion of this document.

Chapter 2

Experimental, analytical and numerical frameworks

*“Each material has its specific characteristics
which we must understand if we want to use it...”*

Each material is only what we make of it”

Ludwig Mises van der Rohe

From his inaugural address at the Illinois Institute of Technology, 1938.

This chapter will first describe all the facilities used in the experimental characterization of the material, from the point of view of the manufacturing, testing and analysis of the test specimens. Then, the analytical framework applied during the rest of chapters is exposed, with a predominance of the use of Classical Laminated Plate Theory (CLPT). Finally, the main characteristics of the utilised software and numerical damage models are detailed.

2.1 Material and experimental equipment

2.1.1 Lamina characteristics and laminate preparation

The work performed throughout this Thesis has focused on the characterization of an epoxy matrix reinforced with intermediate modulus carbon fibres from the company Hexcel[®]. This comes in the form of prepreg rolls with commercial designation M21E/34%/UD268/IMA-12K, kindly provided by Airbus Group, with a theoretical cured ply thickness of 0.25 mm.

The material is kept at a temperature of -21°C until use, when it is extracted from the freezer to temper it. Once it reaches a temperature that allows its handling, the UD tape is cut to the desired dimensions for the laminate and stacked using the

hand lay-up technique. The laminae are stacked following the desired lamination sequence and subsequently a peel-ply, a perforated release film and a breather layer cloth are respectively placed in order to absorb the excess of epoxy resin during curing. The previous assembly is introduced in a vacuum bag to proceed to cure (Fig. 2.1a). Although this material is mainly prepared for autoclave processing, it is possible to imitate these conditions by means of a hot platen press, although this entails a geometric limitation. In this case, every laminate manufactured in the present work consist of flat plates. The curing was carried out in a Fontijne Presses LabEcon 300 hot platen press (Fig. 2.1b), applying the curing cycle recommended by the prepreg manufacturer [161].

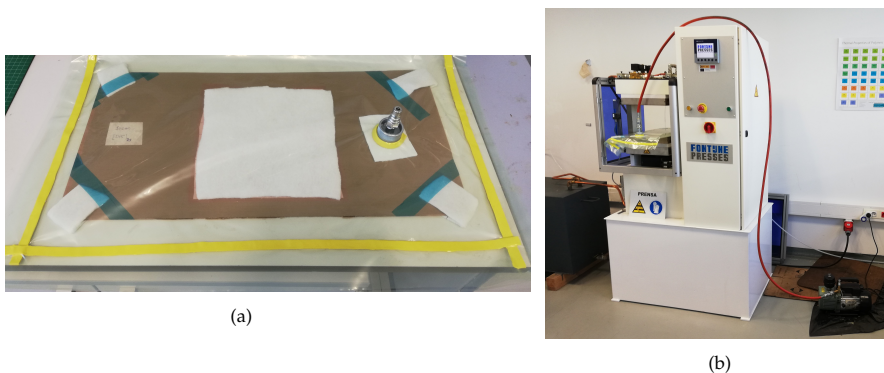


Figure 2.1: Fabrication of laminates: (a) Hand lay-up laminate in vacuum bag and (b) hot platen press.

The cured laminates are extracted from the vacuum bag once the cycle is finished, and they are afterwards cut or machined with the necessary geometry for each test, as exemplified in Fig. 2.2. The dimensions of every specimen are measured, and defective specimens (i.e. damaged during processing) are discarded for testing.

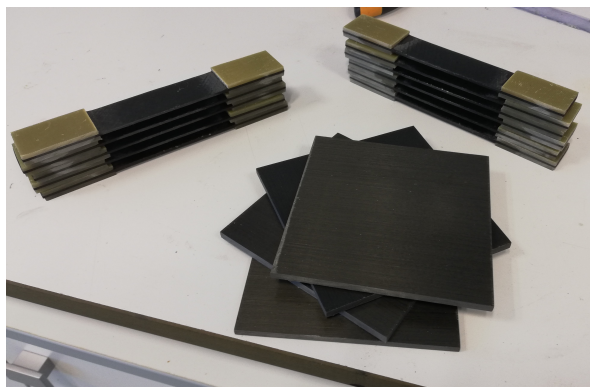


Figure 2.2: Examples of specimens: UD plates for ultrasonic characterization and tensile tabbed coupons.

2.1.2 Experimental facilities

Triaxial testing machine

For consistency of results, every quasi-static test performed in this Thesis (uniaxial/biaxial, tension/compression and bending) was performed in a MICROTTEST MAEFH electromechanical triaxial testing machine (Fig. 2.3). It has six closed-loop synchronized actuators equipped with pneumatic grip jaws. Each actuator is driven by an electric motor, whose position is controlled by an encoder while 5kN and 50 kN force transducers are utilised to register the applied force. The maximum applicable load is 50 kN per actuator, with a total travel of each pair of actuators of 100 mm. In the explanation of every sort of test, the specific procedure followed for the preparation and the fixtures applied will be described.

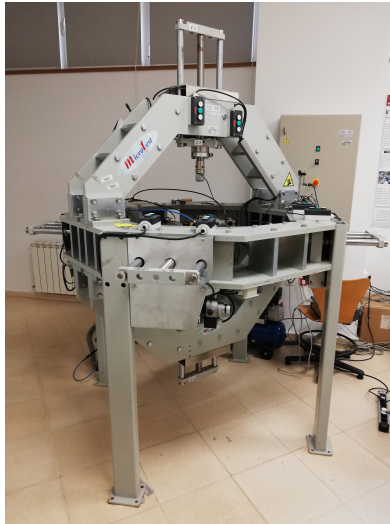


Figure 2.3: MICROTTEST MAEFH triaxial electromechanical testing machine.

Strain acquisition

In order to obtain a precise measurement of the mechanical behaviour of the material in certain points or regions of interest (ROI), different strain measurement techniques are used, depending on the geometry and the necessary results:

- Foil strain gauges, from company KYOWA® (Fig. 2.4a). Depending on the requirements of the specific test, uniaxial or rosette strain gauges have been

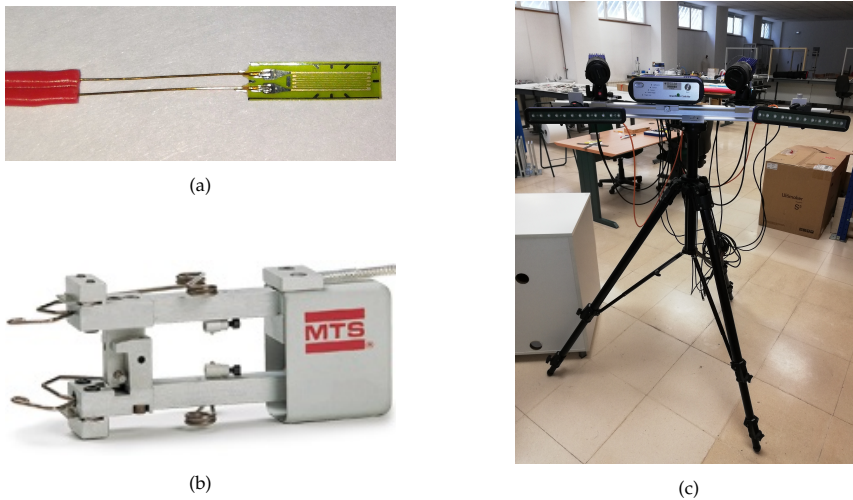


Figure 2.4: Strain measurement equipment applied in quasi-static testing: (a) Foil strain gauge, (b) Axial extensometer and (c) StrainMaster DIC system.

applied, all of them in a quarter bridge configuration connected to the KYOWA PCD-300B acquisition instrument. Although high precision measurement in a small area can be obtained through this method, the principal inconvenient is the limited range of acquisition, which in the case of this equipment is 2% strain.

- A contact axial extensometer MTS 634.12F-54 (Fig. 2.4b), which allows to measure strain with a lower accuracy but in a wider range (-10 to 50% strain) in a gage length of 25 mm.
- A 3D Digital Image Correlation DIC system (Fig. 2.4c), namely LaVision StrainMaster and consisting of two cameras, LED illumination and a controller, that allows a non-contact visual acquisition of full displacement and strain fields over the surface of the specimen. The methodology requires the application of a speckle pattern (usually a black and white dots pattern obtained by spray painting).

Then, a constant frequency acquisition and post-processing of the images is performed by means of the commercial software Davis. The images are discretized into square subsets of a defined number of pixels, and the cross-correlation algorithm tracks the pattern of grey level within each subset. A Least Square Matching method is applied for correlating subsequent frames, in combination with a shape function that accommodates pattern transformations like stretch and rotation. The local displacement is computed where the pattern matching presents a maximum. Repeating this across the entire image for all subsets yields a full field map of displacements, differentiating from them the

strains [162]. The 3D DIC system requires a calibration for each test in order to find the cameras position and orientation in space with respect to the specimen.

Phased Array ultrasound

Phased array technique presents some advantages compared to the conventional methodology based on single-element probes, such as the reduction of the number of transducers to be used in an inspection, the ability to examine areas with curvature and complex geometric variations, and better precision in the measurement of the defect size and position [163].

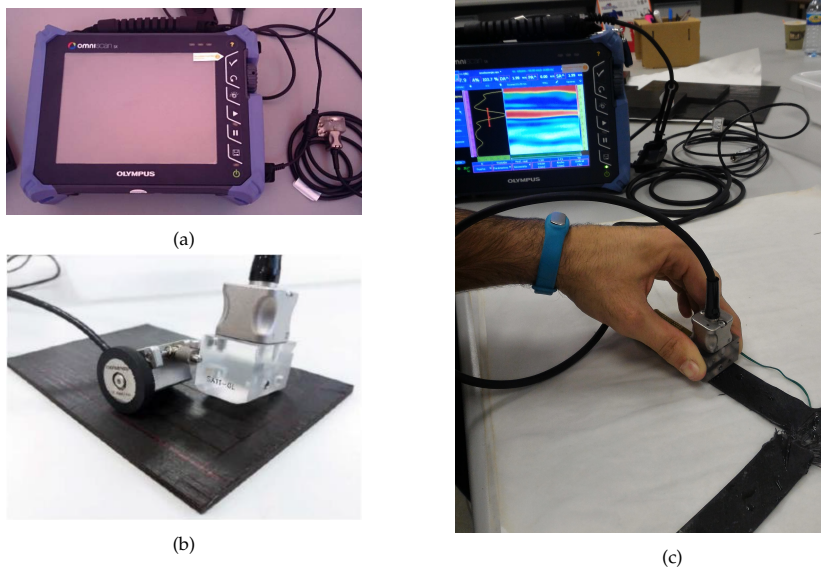


Figure 2.5: Phased array ultrasonic inspection: (a) Olympus OmniScan® SX, (b) C-Scan setup including transducer and position encoder [164] and (c) inspection of a cruciform specimen (S-Scan mode visualized in screen).

The scanning is performed via reflection methodology (pulse-echo mode), as the transducer send pulsed waves which reflect when colliding with an interface such as the bottom of the specimen or a defect within the object. The diagnostic machine displays the amplitude of the intensity of the reflected wave and the distance of the interference measured through the arrival time.

Phased array ultrasonic inspections were performed using the Olympus OmniScan SX equipment with a phased-array transducer of 64 elements at 5 MHz (Fig. 2.5a). This equipment has the capacity to simultaneously perform S-Scan, B-Scan and C-Scan. The B-Scan is based on the time between the pulse and the reflection

echo and the speed of propagation of the waves in the material to determine the through-thickness depth where the defect is located. With the C-Scan it is possible to generate a two-dimensional image of wave attenuation and therefore dimensioning the in-plane size and position of the damage in the thickness of the laminate. To ensure continuity of the medium where the waves propagate, the specimens are wetted superficially or submerged in a water container, generating a continuous layer of water between specimen and transducer. The emission frequency has been set to 5 MHz and the measurement of the position when performing the C-Scan is collected by a mini wheel encoder with resolution of 12 steps/mm (Fig. 2.5b).

Data acquisition requires the calibration of propagation velocity, attenuation, and acoustic impedance, which can vary amongst different materials. The calibration was performed before inspection using a stepped block technique, consisting on an M21E/IMA-12K laminate with three different thicknesses. Three calibration steps were required: propagation velocity, wedge delay and sensitivity. Calibration requires the use of a pattern with the same material of the specimen tested to reproduce the same conditions of attenuation and wave propagation. After calibration, the instrument can recognize defects in the material by measuring the amplitude of the discontinuity echo [164].

2.2 Analytical framework

2.2.1 Classical Laminated Plate Theory

This Thesis includes a work with different laminate sequences, obtained by stacking layers reinforced with unidirectional fibre in different orientations. The most frequently used methodology to estimate the effect of the orientation and position of the layers on the laminate structural behaviour is the CLPT. Its fundamentals are briefly explained in this subsection, summarizing the main ideas of this analytical theory exposed in most of the books about mechanics of composites [165–167].

The CLPT is an extension of Kirchoff-Love thin plate theory to account for laminated composite plates. This theory, limited to the elastic behaviour and small displacements, is based on the following kinematic assumptions [167]:

- straight cross-sections normal to the mid-surface remain straight and normal to the mid-surface after deformation. This implies zero transverse shear strains ε_{xz} and ε_{yz} .

- the thickness of the plate does not change due to deformation. This results in neglecting transverse normal strain ϵ_{zz} .

A sketch of the dimensions and coordinate systems necessary to understand the subsequent formulation is depicted in Fig. 2.6. This notation is kept throughout the whole document. A global reference system is defined with the xyz axes parallel to the loading directions. For each of the UD plies, due to its orthotropic behaviour and possible change of orientation, a local coordinate system is defined. This system corresponds to the principal directions of the lamina, where axis 1 is aligned with the direction of the fibres, axis 2 is the in-plane perpendicular to the fibre and axis 3 is normal to the lamina. The angle θ represents the fibres orientation at each ply with respect to x -axis.

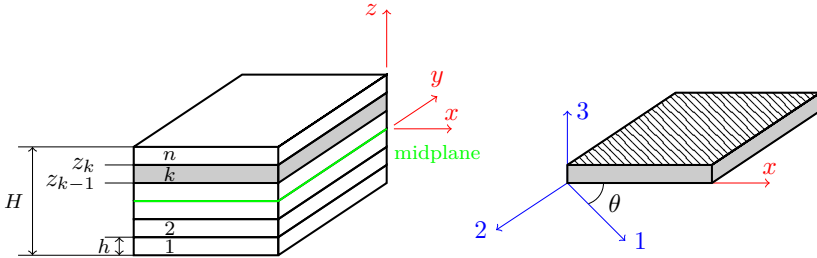


Figure 2.6: Laminate and ply notation and coordinate systems: Principal material directions (blue) and global coordinate system (red).

It is necessary for the subsequent analysis to define the relationship between the stress/strain components in the principal and global directions, which is easily obtained by applying a rotation matrix $[T]$, as set out in Eq. 2.1. The same approach is extensible to the strain tensor components (as tensorial shear strain ϵ_{xy} is utilized).

$$\begin{aligned}
 \begin{bmatrix} \sigma_{11} \\ \sigma_{22} \\ \tau_{12} \end{bmatrix} &= [T] \cdot [\sigma]_{xyz} = \\
 &= \begin{bmatrix} \cos^2(\theta) & \sin^2(\theta) & 2 \sin(\theta) \cos(\theta) \\ \sin^2(\theta) & \cos^2(\theta) & -2 \sin(\theta) \cos(\theta) \\ -\sin(\theta) \cos(\theta) & \sin(\theta) \cos(\theta) & \cos^2(\theta) - \sin^2(\theta) \end{bmatrix} \begin{bmatrix} \sigma_{xx} \\ \sigma_{yy} \\ \tau_{xy} \end{bmatrix} \quad (2.1)
 \end{aligned}$$

The reverse transformation, from principal to off-axis coordinates, is obtained

using the inverse transformation matrix $[T]^{-1}$. Besides, it is still required to establish the stress-strain relations for a lamina in principal directions. With the aim to apply the Generalized Hooke Law, expressed in tensorial form in Eq. 2.2 or in its inverse form (Eq. 2.3), compliance tensor $[S]$ is defined for an orthotropic material (Eq. 2.4). Note that the stiffness tensor $[C]$ can be computed as the inverse of $[S]$.

$$[\sigma]_{123} = [C][\varepsilon]_{123} \quad (2.2)$$

$$[\varepsilon]_{123} = [S][\sigma]_{123} \quad (2.3)$$

$$[S] = \begin{bmatrix} \frac{1}{E_1} & -\frac{\nu_{21}}{E_2} & -\frac{\nu_{31}}{E_3} & 0 & 0 & 0 \\ -\frac{\nu_{12}}{E_1} & \frac{1}{E_2} & -\frac{\nu_{32}}{E_3} & 0 & 0 & 0 \\ -\frac{\nu_{13}}{E_1} & -\frac{\nu_{23}}{E_2} & \frac{1}{E_3} & 0 & 0 & 0 \\ 0 & 0 & 0 & \frac{1}{G_{23}} & 0 & 0 \\ 0 & 0 & 0 & 0 & \frac{1}{G_{13}} & 0 \\ 0 & 0 & 0 & 0 & 0 & \frac{1}{G_{12}} \end{bmatrix} \quad (2.4)$$

Continuing with the development of the CLPT, it is necessary to consider the plane stress hypothesis. This is not only due to a mathematical simplification, but also seeks to collect the usual form of structural behaviour of FRP laminates [166]. Under this consideration, the constitutional relations are simplified in Eq. 2.9.

$$\begin{bmatrix} \sigma_{11} \\ \sigma_{22} \\ \tau_{12} \end{bmatrix} = \begin{bmatrix} Q_{11} & Q_{12} & Q_{16} \\ Q_{12} & Q_{22} & Q_{26} \\ Q_{16} & Q_{26} & Q_{66} \end{bmatrix} \begin{bmatrix} \varepsilon_{11} \\ \varepsilon_{22} \\ \gamma_{12} \end{bmatrix} \quad (2.5)$$

where the Q_{ij} are the so-called reduced stiffnesses for a plane stress state, which are derived from the stiffness tensor $[C]$ (the inverse of the compliance matrix expressed in Eq. 2.4). These matrices can be expressed in a global reference system by applying the transformation matrices previously defined (Eq. 2.1), resulting in Eq. 2.6.

$$[\bar{Q}] = [T]^{-1}[Q][T]^{-T} \quad (2.6)$$

where \bar{Q}_{ij} represents the reduced stiffness transformed to xyz coordinate system.

Finally, considering the assumptions previously stated, it is possible to express in Eq. 2.7 the apparent behaviour of the laminate as the relation between the in-plane force resultants (N) and the moment resultants (M) per unit length with the in-plane strains (ϵ) and curvatures (κ) at the mid-plane (superscript 0 refers to mid-surface).

$$\begin{bmatrix} N_x \\ N_y \\ N_{xy} \\ M_x \\ M_y \\ M_{xy} \end{bmatrix} = \begin{bmatrix} A & B \\ B & D \end{bmatrix} \begin{bmatrix} \epsilon_{xx}^0 \\ \epsilon_{yy}^0 \\ \gamma_{xy}^0 \\ \kappa_x^0 \\ \kappa_y^0 \\ \kappa_{xy}^0 \end{bmatrix} \quad (2.7)$$

where the *laminate stiffness matrix* $[ABD]$ is divided into four submatrices of 3×3 , which are calculated using the Eq. 2.8. The A_{ij} represent extensional stiffnesses, B_{ij} are bending-extension coupling stiffnesses and D_{ij} are bending stiffnesses.

$$\begin{aligned} A_{ij} &= \sum_{k=1}^n \bar{Q}_{ijk} (z_k - z_{k-1}) \\ B_{ij} &= \frac{1}{2} \sum_{k=1}^n \bar{Q}_{ijk} (z_k^2 - z_{k-1}^2) \\ D_{ij} &= \frac{1}{3} \sum_{k=1}^n \bar{Q}_{ijk} (z_k^3 - z_{k-1}^3) \end{aligned} \quad (2.8)$$

It is also of interest to particularize this result for each ply, so that it is possible to determine the stress state of each lamina in global directions through the strains and curvatures of the middle-surface as expressed in Eq. 2.9.

$$\begin{bmatrix} \sigma_{xx} \\ \sigma_{yy} \\ \sigma_{xy} \end{bmatrix} = \begin{bmatrix} \bar{Q}_{11} & \bar{Q}_{12} & \bar{Q}_{16} \\ \bar{Q}_{12} & \bar{Q}_{22} & \bar{Q}_{26} \\ \bar{Q}_{16} & \bar{Q}_{26} & \bar{Q}_{66} \end{bmatrix} \begin{bmatrix} \epsilon_{xx}^0 + z\kappa_x^0 \\ \epsilon_{yy}^0 + z\kappa_y^0 \\ \epsilon_{xy}^0 + z\kappa_{xy}^0 \end{bmatrix} \quad (2.9)$$

Additionally, it should be noted that the elastic properties of the lamina under tension and compression may be different [131, 132]. This entails a deviation of the neutral fibre and a difference of properties between the compressive and tensile regions of the laminate, having accounted for the necessary modifications of the CLPT under simultaneous tension and compression due to bending in [168]. This Thesis will take into account the difference in tensile and compressive properties when the CLPT is applied depending on the loads that dominate the test to analyse.

From the stiffness matrices defined in Eq. 2.8 the apparent elastic properties of the laminates are defined, as the laminate elastic modulus in x and y directions (Eq. 2.10), the in-plane shear modulus (Eq. 2.11), the apparent Poisson's ratio (Eq. 2.12) and the apparent flexural modulus in x -direction (Eq. 2.13).

$$E_{xx} = \frac{1}{a_{11}H} \quad (2.10)$$

$$G_{xy} = \frac{1}{a_{66}H} \quad (2.11)$$

$$\nu_{xy} = -\frac{a_{12}}{a_{11}} \quad (2.12)$$

$$E_{flex,x} = \frac{12}{d_{11}H^3} \quad (2.13)$$

where the terms a_{ij} and d_{ij} refer to the inverse of the $[A]$ and $[D]$ stiffnesses matrices. The evolutions of the above elastic properties for some laminates of interest for this Thesis are depicted in Fig. 2.7.

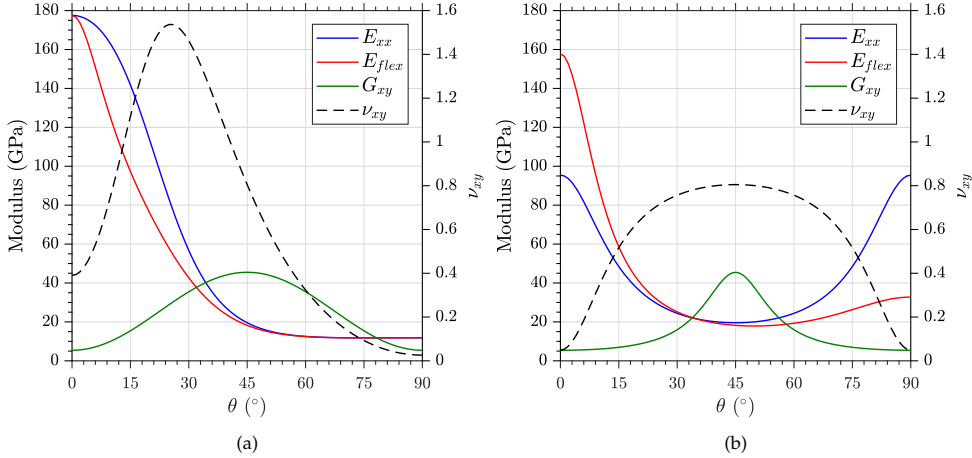


Figure 2.7: Theoretical evolution of elastic properties predicted through CLPT for different stacking sequences: (a) Angle ply $[\pm\theta]_S$ and (b) $[(0+\theta)/(90+\theta)]_S$.

The results obtained for the cases of laminates $[0/90]_{NS}$ and $[\pm 45]_{NS}$ are of special interest for biaxial loading conditions. Those laminates exhibit equal extensional properties in both directions ($A_{11} = A_{22}$), in addition to a lack of shear-extensional couplings ($A_{16} = A_{26} = 0$). This resembles the behaviour of the so-called extensionally quasi-isotropic laminates, but these also require a non-fulfilled third condition associated with the in-plane shear stiffness: $2A_{66} = A_{11} - A_{12}$.

In Fig. 2.8, the extensional and flexural modulus for a ply oriented at 45° and for the $[\pm 45]_{2S}$ laminate are represented versus the angular direction ϕ , in order to better illustrate the properties of interesting stacking sequences for this Thesis. Note that the same result can be obtained for a $[0/90]_{2S}$ cross-ply laminate rotating the polar plot -45° .

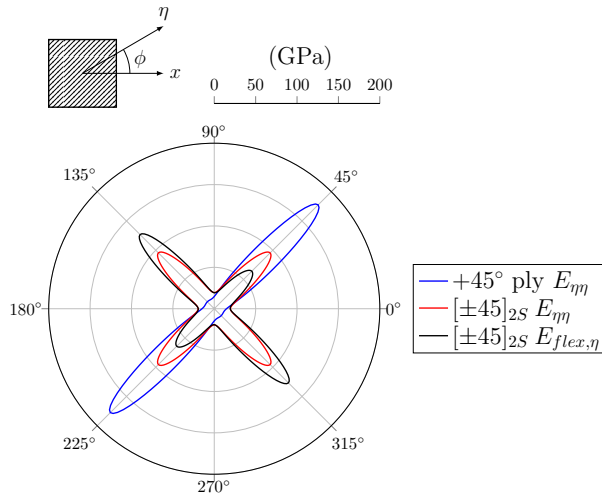


Figure 2.8: Ply and laminate elastic properties at η -direction plotted against ϕ . $+45^\circ$ ply elastic modulus, $[\pm 45]_{2S}$ apparent extensional and flexural modulus.

This figure allows to visualize the same apparent extensional and bending response for the laminate at 0° and 90° directions, while a difference is observed between the E_f at $+45^\circ$ and -45° , which is explained by the alignment of the fibres at the outermost ply. In other words, at 45° the laminate resembles the $[0/90]_{2S}$ configuration, which allow an easier visualization of the difference in flexural stiffness, schematized in Fig. 2.9.

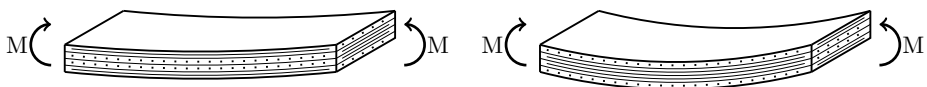


Figure 2.9: Deformation under bending for cross-ply laminates: $[0/90]_S$ (left) and $[90/0]_S$ (right). Reproduction based on [165].

2.3 Numerical modelling

All the numerical simulations are performed using the **FEM** commercial software Abaqus/Standard 2019. In order to compare the computational cost, all simulations shown in this Thesis have been performed in an eight core Intel I7-7700 processor with 16 Gb PC4-17000 RAM. The orthotropic properties of the lamina are assigned through the values of elastic moduli, Poisson's ratios and strengths in the principal directions of the ply, differentiating in tensile and compressive properties depending on the specific loading scenario to model. Besides, it must be noted that mesh sensitivity studies have been carried out for all the models used, until achieving consistent results. In the different sections dealing with the numerical analyses, the specific geometry, type of element and boundary conditions will be detailed.

In addition to the linear static simulations, this work highlights the use of progressive damage models **PDM**, which have been implemented also in MATLAB scripts to perform checks and calibrations without the need to generate and solve time-consuming numerical models. In this section the two damage models used in the simulations are introduced, that is, the one based on the Hashin's criterion and the Ladevèze's mesomodel.

2.3.1 Hashin's Damage Model

In this subsection, the main characteristics of the Progressive Damage Model (**PDM**) for fibre-reinforced composites implemented in the **FEM** software Abaqus will be defined [130]. The initial choice of this damage model is based on practical criteria, since it is already implemented in a software of wide industrial and scientific use, while resulting in a low computational cost as it will be shown below. Hereinafter we will denominate it *Hashin's Damage Model*, because the initiation of the damage is given by the failure criteria of Hashin-Rotem [137,138], while the evolution of the damage is defined in terms of damaged energy release rates through a generalization of the ideas exposed in previous studies from Camanho et al. [169] and Matzenmiller et al. [170]. Note that energetic evolutions are the most frequent approach when dealing delamination and debonding phenomena [171].

Damage initiation based on Hashin's failure criteria

The Hashin-Rotem criteria propose two failure mechanisms: one based on the failure of the fibre and the other on the matrix failure, distinguishing in both cases

between tension and compression. The first failure mechanism is governed by the fibre-direction stress, both in tensile (Eq. 2.14) and compressive (Eq. 2.15), while the Abaqus implementation of these criteria additionally allows to include the interaction of shear stresses through the material parameter α in the tensile fibre mode.

$$f_{ft} = \left(\frac{\widehat{\sigma}_{11}^t}{S_{11}^t} \right)^2 + \alpha \left(\frac{\widehat{\tau}_{12}}{S_L} \right)^2 \quad (2.14)$$

$$f_{fc} = \left(\frac{\widehat{\sigma}_{11}^c}{S_{11}^c} \right)^2 \quad (2.15)$$

Note that subscripts f , m , t , and c mean fibre, matrix, tensile and compressive, respectively. S_{11}^c represents the longitudinal compressive strength, S_{22}^t represents the transverse tensile strength, S_L is the in-plane longitudinal shear strength and f are the damage initiation indexes, which are applied to active each damage mode when $f = 1$. $\widehat{\sigma}_{ii}$ and $\widehat{\tau}_{12}$ are the components of the effective stress tensor, which represent the stress acting over the damaged area that effectively resists the internal forces and can be computed as Eq. 2.16.

$$[\widehat{\sigma}]_{12} = \begin{bmatrix} \frac{1}{1-d_f} & 0 & 0 \\ 0 & \frac{1}{1-d_m} & 0 \\ 0 & 0 & \frac{1}{1-d_s} \end{bmatrix} [\sigma]_{12} \quad (2.16)$$

where d_i are damage variables defined below. Similarly to other PDMs, damage is considered irreversible, i.e. $d_i \geq 0$ at any moment, and damage variables must be in the range $0 \leq d_i \leq 1$. The second damage mode is governed by the transverse and shear stresses, as collected in Eqs. 2.17 and 2.18. The matrix failure is represented by a quadratic function of transversal and shear stresses. Note that the material is insensitive in principal directions to the shear stress direction (illustrated in Fig. 2.10), so the terms related to the first power of the shear stress are neglected [138], leading to Eqs. 2.17 and 2.18.

$$f_{mt} = \left(\frac{\widehat{\sigma}_{22}^t}{S_{22}^t} \right)^2 + \left(\frac{\widehat{\tau}_{12}}{S_L} \right)^2 \quad (2.17)$$

$$f_{mc} = \left(\frac{\widehat{\sigma}_{22}^c}{2S_T} \right)^2 + \left[\left(\frac{S_{22}^c}{2S_T} \right)^2 - 1 \right] \frac{\widehat{\sigma}_{22}^c}{S_{22}^c} + \left(\frac{\widehat{\tau}_{12}}{S_L} \right)^2 \quad (2.18)$$

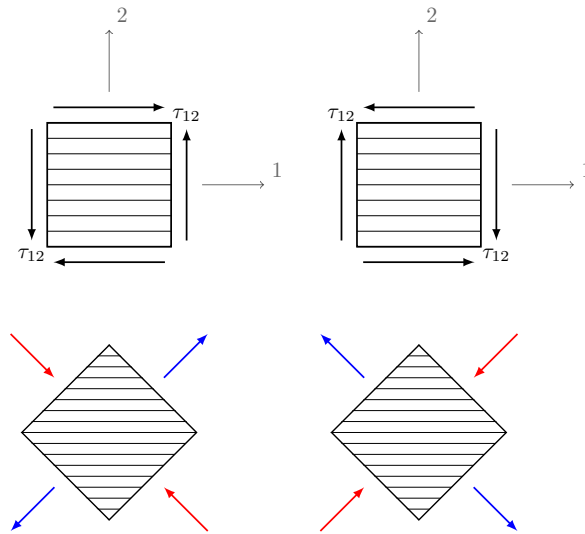


Figure 2.10: Representation of insensitivity opposed sign shear in principal directions. Adapted from [166].

where S_T represents the shear strength transverse to the lamina, which is assumed to correspond to S_{23} . An analysis of the possibilities and limitations of these failure criteria must be conducted. On the one hand, authors do not distinguish matrix and interface failure, that is, a single mode of matrix cracking due to transverse and shear stresses is collected, without specifying whether the mechanisms of these failures are due to matrix cracking or fibre-matrix debonding. Nor are delaminations collected because it is a model oriented to a **UD** lamina. Although the formulation of Hashin [137] reflects a state of 3D stresses, the model that has extended the most and is included in the previous equations assumes that plane stress is the predominant state in the layer.

Furthermore, París [141] stated that the most serious issues with this criteria comes from the interaction between stresses. Above all, author highlights the fact of involving an out-of-plane shear strength (S_T) that does not match a failure criterion based on a state of plane stress. In this regard, it should be noted that Hashin seemed to include the shear failure mode typically observed under compression of the pure matrix, as other criteria such as LaRC05 address the compressive mode with the transverse shear. Therefore, it looks correct to include the effect of out-of-plane shear strength (the component related to the matrix-dominant shear strength S_{23}) in the matrix compressive mode. Also it should be noted that this transverse intralaminar strength appears in Eq. 2.18 multiplied by two, which is related to the rotation of a maximum shear stress state, easily visualized using Mohr circles for a state of pure in-plane compression (see discussion of Section 5.2.1).

Progressive stiffness degradation based on energy release rates

Subsequently, it is necessary to define the evolution of damage, which is also addressed with four independent modes corresponding to the initiation ones. The evolution law implemented in the Abaqus PDM [130] has been schematized in Fig. 2.11 for better clarification. Up to the point of damage initiation (point A in Fig. 2.11) the model requires that the behaviour of the undamaged material is linearly elastic. If a damage initiation criterion is fulfilled, the evolution of damage is represented as a loss of stiffness, measured through the damage variables d_{kl} (computed with Eqs. 2.19 and 2.20). These variables represent the ratio of stiffness loss, therefore the stiffness tensor for the damaged material is modified as Eq. 2.21.

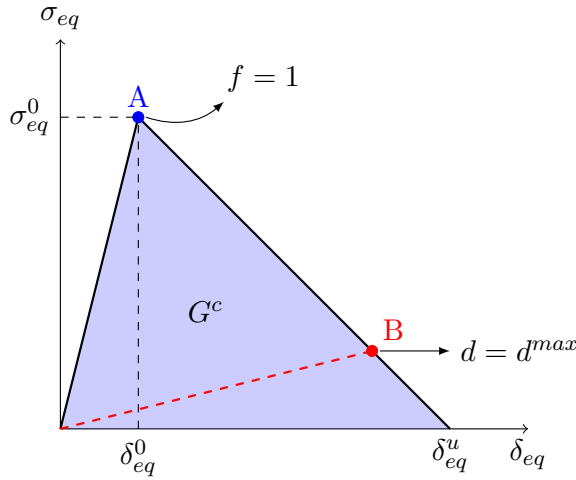


Figure 2.11: Hashin's damage model evolution, reinterpreted from [130].

$$d = \frac{\delta_{eq}^u (\delta_{eq} - \delta_{eq}^o)}{\delta_{eq} (\delta_{eq}^u - \delta_{eq}^o)} \quad (2.19)$$

$$d_s = 1 - (1 - d_{ft})(1 - d_{fc})(1 - d_{mt})(1 - d_{mc}) \quad (2.20)$$

$$C_d = \frac{1}{D} \begin{bmatrix} (1 - d_f)E_1 & (1 - d_f)(1 - d_m)v_{12}E_1 & 0 \\ (1 - d_f)(1 - d_m)v_{21}E_1 & (1 - d_f)(1 - d_m)E_2 & 0 \\ 0 & 0 & D(1 - d_s)G_{12} \end{bmatrix} \quad (2.21)$$

where D is expressed in Eq. 2.22. Then, the damage variables are calculated for each mode as a relation of equivalent displacements. The equivalent stress and displacement at any point of the damage evolutions can be computed using the equations collected in Table 2.1. The maximum equivalent displacement (δ_{eq}^u), i.e. the one associated to the maximum damage, is calculated as the equivalent displacement that produces an energy dissipated to failure (integral of the equivalent stress-displacement curve) equal to the G^c defined in each studied mode.

$$D = 1 - (1 - d_f)(1 - d_m)v_{12}v_{21} \quad (2.22)$$

Table 2.1: Equivalent stress and displacement relations for damage evolution in Hashin's model.

Damage mode	Equivalent displacement	Equivalent stress
Fibre tension	$L_c \sqrt{\langle \epsilon_{11} \rangle^2 + \alpha \epsilon_{12}^2}$	$\frac{\langle \sigma_{11} \rangle \langle \epsilon_{11} \rangle + \alpha \tau_{12} \epsilon_{12}}{\delta_{eq}/L_c}$
Fibre compression	$L_c \langle -\epsilon_{11} \rangle$	$\frac{\langle -\sigma_{11} \rangle \langle -\epsilon_{11} \rangle}{\delta_{eq}/L_c}$
Matrix tension	$L_c \sqrt{\langle \epsilon_{22} \rangle^2 + \epsilon_{12}^2}$	$\frac{\langle \sigma_{22} \rangle \langle \epsilon_{22} \rangle + \tau_{12} \epsilon_{12}}{\delta_{eq}/L_c}$
Matrix compression	$L_c \sqrt{\langle -\epsilon_{22} \rangle^2 + \epsilon_{12}^2}$	$\frac{\langle -\sigma_{22} \rangle \langle -\epsilon_{22} \rangle + \tau_{12} \epsilon_{12}}{\delta_{eq}/L_c}$

where L_c is the characteristic element length and the symbol $\langle \rangle$ represents the Macaulay brackets operator, defined as:

$$\langle x \rangle = \frac{x + |x|}{2} \quad (2.23)$$

Furthermore the ultimate point of the damage evolution (represented as point B in Fig. 2.11) can be numerically modified by establishing a limit in the degradation of the stiffness, through an element internal variable named maximum degradation (d^{max}).

As reflected in the Abaqus documentation, the definition of the damage evolution in terms of equivalent stress-displacement is due to alleviate mesh dependency during material softening [130]. This is achieved by means of defining a characteristic length L_c which in the case of 2D elements it is equal to the square root of the area of the reference surface. Some preliminary analyses of the effect of the damage model parameters revealed that the appearance of L_c could be detrimental in case of modelling with irregular meshes. Although the results of these simulations are not included in the Thesis, it was observed that Abaqus assigns a single characteristic length to the whole model and therefore the capacity of damage evolution for elements with different sizes varies (unless energy release rates are adapted for spe-

cific element sizes). For this reason, meshes with uniform element size are pursued during the analyses performed with the Hashin's damage model. Additionally, it should be remarked that energy release rates defined in Abaqus are dependent on the element size, and this implies that they must be modified proportionally to the change of the element when refining mesh.

Effect of large strain and fibre reorientation

In literature it is described that angle-ply laminates, and specially the stacking sequences consisting on $\pm 45^\circ$ layers, show a high strain and fibre reorientation. Therefore, these effects must be considered when making a correct identification of the numerical parameters based on the experimental behaviour, where the tensile tested $[\pm 45]_{2S}$ laminate is studied in detail.

This analysis of the so-called pseudo-ductile effect in angle-ply laminates has been previously addressed in the literature. The work of Yuan et al. [172] talks about the effect of considering the fibre reorientation on a model based on the Tsai-Hill criterion, where the angle variation is measured experimentally on the images obtained with a DIC system. Another similar study [21] consists on an approach to damage and permanent deformation modelling of laminates ± 45 using the Ladevèze's model. Herakovich et al. estimate the reorientation of the fibre by means of an equation which includes the ratio of ϵ_{xx} and ϵ_{yy} , while considering the change of cross-sectional width in the computation of the apparent stress from the experimentally measured force. The variation of the area is appreciable due to the large deformations achieved, linked to the high apparent Poisson's ratio of the laminate.

When conducting our identification of the model parameters, an alternative identification is proposed considering the effect of the reorientation of the fibre and the change of area similar to [151], which is named with the acronym *FR*. In our case, the variation of angle is estimated directly in the numerical model using Eq. 2.24. Thus, observing the formulation of the Hashin's PDM, the effect of this reorientation rests on the constitutive equation relating stress and strain in global coordinates (Eq. 2.21), where it is necessary to update the value of Q_θ for each iteration, as the angle θ is continuously reduced under tensile loading. Although there are no direct measurements of the cross-section over each instant of the test, an estimation of the area based on the strain measurement is proposed, so that the true section (A') can be estimated using Eq. 2.25. Note that the approximation of $\nu_{xy} = \nu_{xz}$ is considered.

$$\Delta\theta = \theta - \arctan\left(\frac{\tan(\theta) + \epsilon_{yy}}{1 + \epsilon_{xx}}\right) \quad (2.24)$$

$$A' = b't' = bt(1 + \varepsilon_{yy})^2 \quad (2.25)$$

Then, experimental apparent longitudinal stress σ_{xx} is computed as the quotient of the applied force and the instantaneous section A' . Likewise other authors propose corrections for large strain based on the longitudinal strain measurement [43]. This estimation relies on the fact that the longitudinal and transverse strain are constantly related, but our experimental observations results in the opposite, that is, a drastic change of the transverse/normal strain ratio (see Fig. 3.5).

2.3.2 Ladevèze's Damage Model

The phenomenological model from Ladevèze [155] presents an evolution of the matrix damage in the form of ply stiffness reduction based on associated forces, combined with an isotropic hardening plasticity law. This PDM for an elementary ply has been afterwards developed in [173, 174], seeking an extension at the full meso-scale level by introducing mechanisms such as interlaminar damage (delamination).

Material properties identification for this model requires the realization of tests in principal directions (0° and 90°), as well as Load-Unload-Reload (LUR) tests on laminates $[\pm 45]_{2S}$ and $[\pm 67.5]_{2S}$, since these allow characterization of the shear behaviour (similar to that proposed in ASTM D3518 [19]), as well as the interaction between shear and transverse stress. This calibration strategy has been used by other authors [21, 175] with good results. The LUR tests allow simultaneous measurement of the evolution of the damage and plasticity, since the different cycles provide the values of loss of stiffness and permanent deformation.

The original implementation of the model does not distinguish tensile and compressive damage modes, but it may be applied in each situation using either tensile or compressive properties as appropriate. With this model, the already commented phenomenology existing in angle-ply laminates will be described in detail. Unlike the Hashin's model, this considers plasticity and damage, so that more realistic results are expected, although the complexity of the model is higher. However, it must be borne in mind that the phenomenology of the model is limited, and therefore, it may be too conservative given certain damage mechanisms not contemplated in the original formulation of the model. For example, in the work of Le et al. [176], it is demonstrated how the model should be readjusted to adequately reproduce the behaviour of laminates involving extensive splitting.

It is important to highlight two reference works applying this PDM. On the one

hand, the PhD Thesis of Sevenois [177] describes a successful fitting of the experimental results with the Ladevèze's model in different angle-ply laminates. However, it should be noted that the behaviour of the laminates studied in this work produce a lower non-linearity than that exhibited under the same conditions by the M21E/IMA-12K material, reaching much lower failure strains, and without describing a re-stiffening effect. Thus, the model discussed did not require the consideration of fibre reorientation, being the same negligible. In other words, the study of Sevenois focuses on diffuse damage, which will be followed by matrix microcracking (stages defined in [174]), in which the loss of stiffness occurs very gradually without exhibiting macroscopic failures.

On the other hand, the work of Herakovich et al. [21] also uses the Ladevèze's model for the characterization of the non-linear tensile behaviour of the $\pm 45^\circ$ laminate. In this case, the response achieved exhibits a high capacity of damage and permanent deformation due to shear, thus producing a high reorientation of the fibres towards the loading directions (*scissoring effect*). However, it should be noted that the damage and plasticity produced in the first stage (apparently linear compared to the rest of the behaviour) is ignored in the modelling, thus focusing on the stress-strain plateau.

In a similar way to what has been done with the Hashin's model, the way to proceed in this section will combine the use of the previously mentioned LUR tests, with a MATLAB script that collects the equations of the Ladevèze's model. Subsequently, having identified the model parameters for the M21E/IMA-12K prepreg, a UMAT user subroutine is applied in Abaqus/Standard to be able to model the damage and plasticity of the proposed tests. It should be noted that the subroutine for Ladevèze's model and the script were developed by researchers from the *Mechanics of Materials and Structures* research group at Ghent University, whose results were shown in previous works [157, 177].

Damage kinematics

The model considers the in-plane behaviour of an orthotropic lamina as collected in Eq. 2.26.

$$S = \begin{bmatrix} \frac{H(\sigma_{11})}{(1-d_1)E_1^0} + \frac{H(-\sigma_{11})}{E_1^0} & \frac{-\nu_{12}}{E_1^0} & 0 \\ \frac{-\nu_{12}}{E_1^0} & \frac{H(\sigma_{22})}{(1-d_2)E_2^0} + \frac{H(-\sigma_{22})}{E_2^0} & 0 \\ 0 & 0 & \frac{1}{(1-d_{12})G_{12}^0} \end{bmatrix} \quad (2.26)$$

where the Heaviside step function ($H(x)$), defined in Eq. 2.27, is applied to difference the tensile and compressive damage mechanisms. Therefore, note that if $\sigma_{11} < 0$ no damage in fibre direction is considered (the same applies to transverse direction). This idea, consistent with other damage models, is based on the assumption that cracks are propagated under tensile stresses, while compressive stresses are supposed to close the cracks, then recovering the initial stiffness [155].

$$H(x) = \begin{cases} 0 & \text{for } x < 0 \\ 1 & \text{for } x \geq 0 \end{cases} \quad (2.27)$$

Then, the strain energy density, considering a linear response of the damaged stress-strain, could be expressed as 2.28.

$$E = \frac{1}{2}[\sigma][\varepsilon] \quad (2.28)$$

Having defined the damaged compliance matrix (Eq. 2.26), it is possible to replace the strains in order to express the strain energy only in terms of stresses, resulting in Eq. 2.29.

$$E = \frac{1}{2} \left[\frac{\langle \sigma_{11} \rangle^2}{(1-d_1)E_1^0} + \frac{\langle -\sigma_{11} \rangle^2}{E_1^0} + \frac{\langle \sigma_{22} \rangle^2}{(1-d_2)E_2^0} + \frac{\langle -\sigma_{22} \rangle^2}{E_2^0} + \right. \\ \left. -2 \frac{\nu_{12}^0 \sigma_{11} \sigma_{22}}{E_1^0} + \frac{\tau_{12}^2}{(1-d_{12})G_{12}^0} \right] \quad (2.29)$$

where the MacAuley operator $\langle \cdot \rangle$ was defined in Eq. 2.23; d_1 , d_2 and d_{12} represent the damage variables in fibre, transverse and in-plane shear direction, respectively. Again, these are scalar values in the range $0 \leq d_i \leq 1$. Following that, the evolution of this energy as a function of the damage variables is computed in Eqs. 2.30.

$$Y_{d_i} = \frac{\partial E_D}{\partial d_i} = \frac{\langle \sigma_{ii} \rangle^2}{(1-d_i)E_i^0} \quad \text{for } i = 1, 2 \quad (2.30a)$$

$$Y_{d_{12}} = \frac{\partial E_D}{\partial d_{12}} = \frac{\tau_{12}^2}{2(1-d_{12})G_{12}^0} \quad (2.30b)$$

where Y_d are the so-called thermodynamic associated forces, which are somehow analogous to energy release rates, similarly to the G^c in the Hashin's damage model. Following Ladevèze and Le Dantec formulation, a equivalent associated force Y_{eq} combining the shear and transverse forces is defined in Eq. 2.31. In this expression, b_L is the parameter regulating the shear and transverse interaction. Note that this is not present in Hashin's model, but conversely a fibre-shear interaction was controlled by means of coefficient α .

$$Y_{eq} = Y_{d_{12}} + b_L Y_{d_2} \quad (2.31)$$

Using the equivalent thermodynamic force, the damage laws can be written as Eqs. 2.32.

$$d_{12} = \begin{cases} \frac{\sqrt{Y_{eq}} - \sqrt{Y_0}}{\sqrt{Y_C}} & \text{if } d_2 < 1 \text{ and } d_{12} < 1 \text{ and } Y_{d_{12}} < Y_{12S} \\ 1 & \text{otherwise} \end{cases} \quad (2.32a)$$

$$d_2 = \begin{cases} b' d_{12} & \text{if } d_2 < 1 \text{ and } d_{12} < 1 \text{ and } Y_{d_2} < Y_{C'} \\ 1 & \text{otherwise} \end{cases} \quad (2.32b)$$

where the values of Y_0 , Y_C , $Y_{C'}$, Y_{12S} and b' are material parameter to be determined from experimental tests. Detailing these parameters, the quotient Y_0/Y_C represent the initiation thermodynamic force, i.e. the necessary energy/damage rate to start stiffness degradation, while $1/Y_C$ is the slope of the damage law expressed as d_i versus $\sqrt{Y_{eq}}$. Besides, Y_C and $Y_{C'}$ are the parameters collecting the maximum degradation of shear and transverse moduli, respectively. Finally, b' relates in-plane transverse and shear damage, then coupling both evolutions. Continuing the analogy with Hashin's model, Eq. 2.20 shows that shear damage was directly associated to fibre and matrix damage, not considering a possible softer interaction between damage modes.

These two equations represent the transverse and shear damage mechanisms. A third considered mechanism is fibre breakage, but in this case a brittle failure criterion is defined (Eq. 2.33), which implies an instantaneous degradation of the stiffness in the fibre direction when a the value of Y_{d_1} reach the fibre failure associated force Y_T . Note that this assumption, combined with the linear elastic behaviour in longitudinal direction, is equivalent to a maximum stress criterion resulting in failure when $\sigma_{11} = S_{11}$.

$$d_1 = \begin{cases} 0 & \text{if } Y_{d_1} < Y_T \\ 1 & \text{otherwise} \end{cases} \quad (2.33)$$

To sum up, note that the main characteristic of Ladevèze's damage model is the inclusion of energy-related parameters in both the initiation and evolution of damage, but if the behaviour is elastic up to damage initiation and brittleness dominates fibre and transverse direction may lead to similar results that stress-based criteria. The most relevant differences lie in permanent deformation and the interaction with shear component, where the non-linear behaviour is expected to be better fitted by the thermodynamic force criteria.

Plasticity in Ladevèze's model

Different studies with approaches from micro- and mesomechanical points of view [13, 34, 110, 175, 178, 179] shown that shear in polymers induces an inelastic deformation. In the case of FRP, in addition, the premature initiation of fibre-matrix debonding, due to the low strength existing in the fibre-matrix interface, also generates a sliding and subsequent friction of the fibres with the matrix. This inelastic behaviour can be collected with the use of plasticity models, although this will be named as evolution of permanent strain (ϵ_p) because the described phenomenology is not only plastic.

Briefly introducing the basics of plasticity, when a certain stress is reached, a non-recoverable deformation appears in the material, generally causing a more pronounced increase in strain with respect to the level of stress. The starting point is given by the so-called yielding criterion, an equation expressed as a function of the stress tensor. This collects the surface in the stress space which defines the boundary between the elastic and plastic behaviour of the material. Without going into detail of the different plasticity criteria existing in literature (more information can be found on [126, 180, 181]), we focus on the case of an isotropic hardening rule. This implies that the yield surface expands proportionally in all directions when yield stress is exceeded, which can be schematized as Fig. 2.12.

The approach from Ladevèze's decouples the damage evolution from the evolution of permanent strain by defining an effective stress ($\bar{\sigma}$) and an effective permanent strain rate ($\dot{\bar{\epsilon}}_p$), which are related to damaged stresses and strains through the expression 2.34.

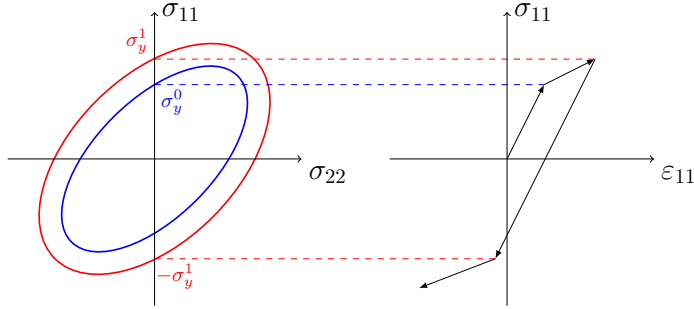


Figure 2.12: Planar representation of isotropic hardening, supposing $\sigma_{22} = 0$.

$$Tr[\tilde{\sigma}\tilde{\epsilon}_p] = Tr[\sigma\epsilon_p] \quad (2.34)$$

where $Tr[\]$ is the trace of the tensor. The effective term refers to the equivalent undamaged stress and strain, which are computed as expressed in Eqs. 2.35 and 2.36, highlighting the necessity of defining the tensile and compressive differently due to the hypothesis of no damage under compressive loads.

$$\begin{bmatrix} \tilde{\sigma}_{11} \\ \tilde{\sigma}_{22} \\ \tilde{\tau}_{xy} \end{bmatrix} = \begin{bmatrix} \frac{\langle \sigma_{11} \rangle}{1-d_1} + \langle -\sigma_{11} \rangle \\ \frac{\langle \sigma_{22} \rangle}{1-d_2} + \langle -\sigma_{22} \rangle \\ \frac{\tau_{12}}{1-d_{12}} \end{bmatrix} \quad (2.35)$$

$$\begin{bmatrix} \epsilon_{11p}^{\tilde{}} \\ \epsilon_{22p}^{\tilde{}} \\ \epsilon_{12p}^{\tilde{}} \end{bmatrix} = \begin{bmatrix} \langle \epsilon_{11p}^{\tilde{}} \rangle (1-d_1) + \langle -\tilde{\epsilon}_{11p} \rangle \\ \langle \epsilon_{22p}^{\tilde{}} \rangle (1-d_2) + \langle -\tilde{\epsilon}_{22p} \rangle \\ \epsilon_{12p}^{\tilde{}} (1-d_{12}) \end{bmatrix} \quad (2.36)$$

This decoupling of damage and permanent strain should be appropriately understood. Although effective components are defined in order to give a correct formulation, this does not mean plasticity and damage evolve independently. To clarify this concept, a representation of a damage evolution law obtained with the Ladevèze's model is shown in Fig. 2.13. This figure reflects how the damage law is almost stopped (in terms of stress) by the yielding evolution. This limitation is quite relevant, as a high permanent strain rate is related to a reduction of the damage rate, which may complicate the calibration of the model. Continuing with the definition of the permanent strain, the plastic yield function is defined as expressed in Eq. 2.37.

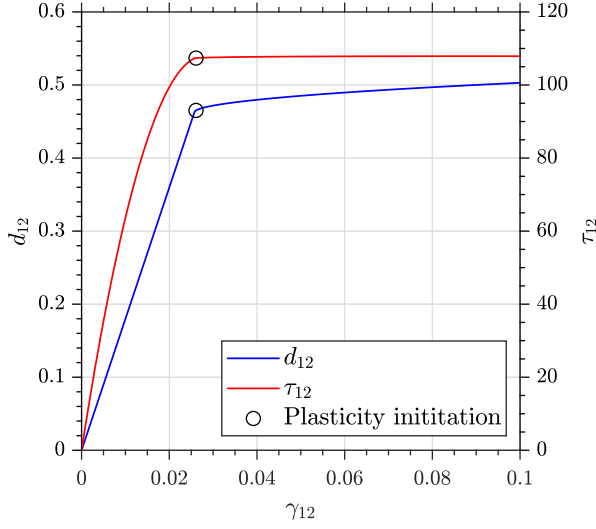


Figure 2.13: Representation of damage law combined with plasticity. Stress-strain evolution is also reported in right axis for clarification.

$$f = \sqrt{\tilde{\sigma}_{12}^2 + a_L^2 \tilde{\sigma}_{22}^2} - R(p) \quad (2.37)$$

Again an interaction coefficient a_L between transverse and shear components is included. Notice fibre stress has no effect on the yielding function. $R(p)$ is the isotropic hardening law as function of the accumulated permanent strain (p), chosen initially to be a power function expressed in Eq. 2.38.

$$R(p) = \beta p^{\alpha_L} - R_0 \quad (2.38)$$

where β and α_L are material parameters to be determined experimentally and R_0 represents the initial plastic threshold. Besides, regarding the fibre direction the model assumes that the permanent strain is negligible, as UD plies generally show no inelastic strain in this direction. The yielding conditions are in consequence written as Eq. 2.39.

$$\begin{bmatrix} \tilde{\varepsilon}_{1p} \\ \tilde{\varepsilon}_{2p} \\ \tilde{\varepsilon}_{12p} \end{bmatrix} = \begin{bmatrix} 0 \\ a_L^2 \dot{p} \frac{\tilde{\sigma}_2}{R(p)} \\ \frac{1}{2} \dot{p} \frac{\tilde{\sigma}_1^2}{R(p)} \end{bmatrix} \quad (2.39)$$

Finally, the accumulated plastic strain rate is obtained combining Eqs. 2.37 and 2.39, resulting in Eq. 2.40.

$$\dot{p} = \begin{cases} \sqrt{(2\varepsilon_{12p}^{\tilde{}})^2 + \frac{1}{a_L^2}(\varepsilon_{2p}^{\tilde{}})^2} & \text{if } \dot{p} \geq 0 \\ 0 & \text{if } \dot{p} < 0 \end{cases} \quad (2.40)$$

The adequate implementation of the material model in the implicit solver through the **UMAT** was already verified by comparing the results of uniaxial strain loading on a single element to the results of the analytical implementation (see [177]). However, comparing them in the case of uniaxial tensile stress on the $[\pm 45]_{2S}$ when using the original script, it was found that the global-principal strain relations initially included were formulated linearly. That is, as input to the code, the γ_{12} strain is used, but the application of the model equations requires defining the normal components, so the relations of the **CLPT** were used for the uniaxial stress case, resulting in the Eqs. 2.41 and 2.42.

$$\varepsilon_{11} = \varepsilon_{22} = \frac{4(E_1^0 - E_2^0 v_{12}^0)G_{12}^0}{E_1^0(E_1^0 + E_2^0 + 2E_2^0 v_{12}^0)} \varepsilon_{12} \quad (2.41)$$

$$\varepsilon_{33} = -\frac{(v_{23}E_1^0 + v_{12}^2 E_2^0)\varepsilon_{22} + (1 + v_{23})v_{12}E_1^0 \varepsilon_{11}}{E_1^0 - v_{12}^2 E_2^0} \quad (2.42)$$

Nevertheless, these equations entail the error of assuming an elastic relations between the strains, so their application in highly non-linear cases (either by damage, plasticity or combination of both) involves an important error in the computation of 1 and 2 strain components. These equations must be corrected taking into account degradation and inelastic deformations, resulting in Eqs. 2.43 and 2.44.

$$\varepsilon_{11el} = \varepsilon_{22el} = \frac{4(E_1^D - E_2^D v_{12}^D)G_{12}^D}{E_{11}^D(E_1^D + E_2^D + 2E_2^D v_{12}^D)} \varepsilon_{12el} \quad (2.43)$$

$$\varepsilon_{33} = -\frac{(v_{23}E_1^D + v_{12}^2 E_2^D)\varepsilon_{22} + (1 + v_{23})v_{12}E_1^D \varepsilon_{11}}{E_1^D - v_{12}^2 E_2^D} \quad (2.44)$$

where $E_i^D = (1 - d_i)E_i^0$, $G_{12}^D = (1 - d_{12})G_{12}^0$, and the subscript *el* represents elastic (strain).

Therefore, the result of comparing the subroutine in Abaqus with the original implementations of the model script and the non-linear implementation are illustrated in Fig. 2.14, where it is checked how the original implementation of the Ladevèze's model resulted in wrong estimations of the fibre strain. Although not plotted, this extends to matrix direction. Note that the difference between the UMAT and the non-linear script is explained due to the latter only assumes a theoretical approach on a single element submitted to the imposed pure strain conditions, while the UMAT is applied on the coupon FEM model, and therefore stress concentrations alter the results compared to the pristine formulation of the script.

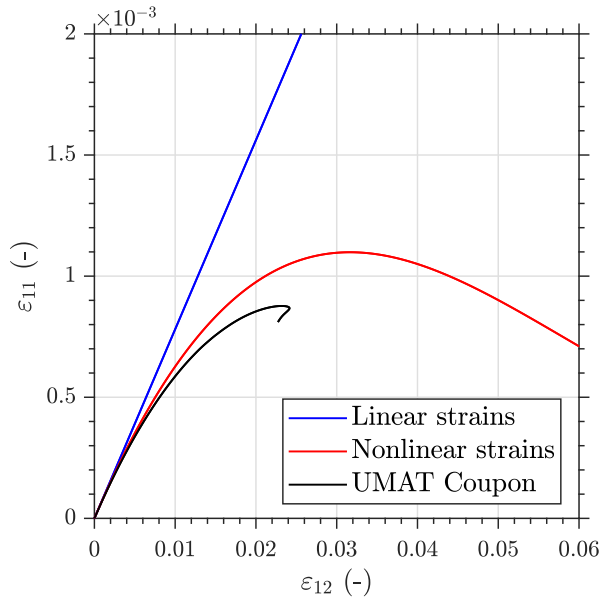


Figure 2.14: Representation of strain results considering linear and non-linear strain relations in the Ladevèze script, compared with Abaqus results including the UMAT.

Chapter 3

Mechanical response under uniaxial loading

*“Today’s scientists have substituted mathematics for experiments,
and they wander off through equation after equation,
and eventually build a structure which
has no relation to reality.”*

Nikola Tesla.

Experimental testing is needed to know the response of the material and its properties. Even in the case of numerical modelling, a minimum of tests that provide material properties as well as data for the calibration and validation of the numerical models are required, therefore explaining the necessity of a detailed uniaxial characterization of the material. Moreover, the highly non-linear mechanical response of angle-ply laminates under uniaxial loading due to the shear-dominated permanent strain and damage makes necessary a detailed study of different orientations of fibre in angle-ply laminates. This is added to the fact that composites exhibit a different behaviour when they are submitted to tension or compression.

3.1 Uniaxial tensile testing

In general, a methodology similar to that proposed in ASTM D3039 [182] has been followed, with rectangular prismatic specimens to which GFRP tabs are glued at the ends, protecting the gripping region, applying an epoxy adhesive Araldite® 2000. The tests have been performed under quasi-static conditions, applying a constant control of displacement rate. The dimensions applied on these tests are depicted in Fig. 3.1, in which the thickness of the laminate can be estimated as $0.25n$ (mm), where n represents the total number of plies. Every test performed includes the use of strain gauges and DIC in order to accurately acquire the strains in the top and bottom surfaces of the specimen. The specimens are fixed on the pneumatic

grips, attached to the electromechanical actuators equipped with 50 kN load cells, and displacement is applied up to final failure of the laminate. The loading rate is adapted to the stiffness of the laminate, taking as reference a displacement rate of 1.5 mm/min for the $[\pm 45]_{2S}$ laminate under tensile loading.

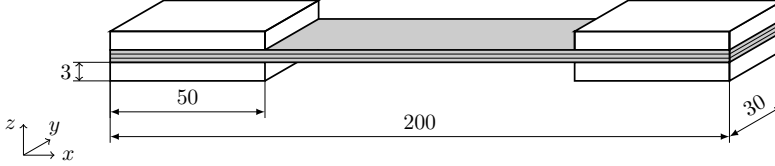


Figure 3.1: Dimensions of uniaxial tensile test coupon (in mm).

The experimental characterization of the lamina properties in principal directions under tensile and shear loads is collected in the Table 3.1, which collect the results from previous works [168].

Table 3.1: Tensile and shear properties of M21E/IMA-12K lamina [168].

E_1 (GPa)	$E_2 = E_3$ (GPa)	$\nu_{12} = \nu_{13}$	$G_{12} = G_{13}$ (GPa)	G_{23} (GPa)
177.56 ± 5.73	11.84 ± 1.05	0.39 ± 0.01	5.42 ± 0.14	3.1
ν_{23}	σ_{11}'' (MPa)	σ_{22}'' (MPa)	τ_{12}'' (MPa)	
0.36	2600.9 ± 121.5	56.07 ± 2.12	91.18 ± 3.25	

Additionally, in order to verify the previous values, aninsonification process for characterization of the elastic properties was carried out by researchers from the *Mechanics of Materials and Structures* (MMS) research group at Ghent University, having described the followed methodology in a previous work [183]. This process has the main advantage of allowing the characterization of the elastic properties of the material in all directions with a single UD laminate through ultrasounds. Specifically for the characterization of the M21E/IMA-12K, a $[0]_{24}$ laminate was used, and its outcomes are summarized in Table 3.2.

Table 3.2: Ultrasonic identification of M21E/IMA-12K elastic properties.

E_1 (GPa)	$E_2 = E_3$ (GPa)	$G_{12} = G_{13}$ (GPa)	G_{23} (GPa)
152.03	10.81	7.37	3.34
ν_{12}	ν_{13}	ν_{23}	
0.392	0.51	0.371	

Comparing with the conventional methodology of characterization of the tensile properties (Table 3.1), good agreement in E_2 and G_{23} and Poisson's ratios is obtained. The large difference (14.3%) in the longitudinal modulus E_1 could be due to

a small misalignment of the fibre on the insonicated specimen, while the disagreement (35.9%) in the in-plane shear modulus G_{12} could be related to two reasons. On the one hand, the ultrasound characterization can be influenced by viscoelastic effects, as the insonication produces high strain rate in the material, and then the epoxy matrix may behave stiffer [183]. On the other hand, as it will be detailed below, the shear modulus varies greatly in a small strain range, which can lead to a large dispersion of this property according to the stress-strain range considered to compute it.

3.1.1 Cross-ply laminates

For this work, the tests of $[0/90]_S$ and $[90/0]_S$ cross-ply laminates are also of interest, in order to analyse the effect on the apparent strength of the laminate as a function of 0° ply position in cross-ply laminates. The failure strength and strains from these tests are collected in Table 3.3. While the in-plane elastic properties of these two laminates are expected to be equivalent as it is demonstrated by the slope of the experimental curves (Fig. 3.2), the apparent strength of the laminate (determined as $\sigma_{xx} = \frac{P}{A}$, where P is the applied load and A the initial cross-section) is affected by a stacking sequence effect, showing a lower failure load in the case of lay-ups with 0° laminae in the outer layers. It is also observed how a first failure of the laminate $[0/90]_S$ occurs at a stress of 757.86 ± 9.9 MPa, with a remarkable stiffness drop. This conclusion is related to the premature matrix tensile failure of the 90° plies, which in the case of being clustered around the laminate midplane, promote crack propagation and result in the internal failure of the laminate, so 0° plies are left isolated in the top and bottom of the $[0/90]_S$ lay-up.

Table 3.3: Tensile properties of cross-ply laminates.

Laminate	ϵ_{xx}^u	σ_{xx}^u (MPa)
$[0/90]_S$	0.0132 ± 0.0002	1111.24 ± 106.19
$[90/0]_S$	0.0156 ± 0.0007	1430.94 ± 51.91

3.1.2 Angle-ply laminates

In order to analyse the non-linear response and the pseudo-ductile effects in angle-ply laminates, testing on different sequences of interest was carried out. Particularly, the $[\pm 45]_{2S}$ laminate maximizes the shear stress component, and therefore the non-linear effects, while the $[\pm 67.5]_{2S}$ laminate is suggested by Ladevèze et al. [155] because it allows to identify the interaction between transverse tension and shear

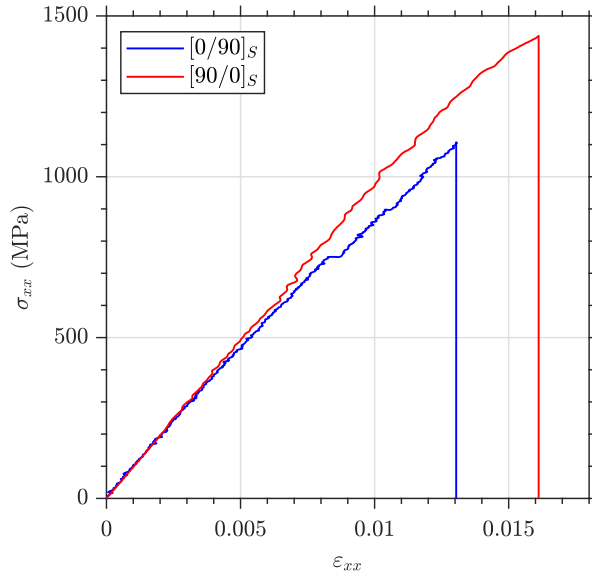


Figure 3.2: $[0/90]_S$ and $[90/0]_S$ uniaxial tensile testing.

while reducing results dispersion. The laminates $[\pm 56.3]_{2S}$ and $[\pm 33.7]_{2S}$ have been chosen because they correspond with the angles formed by the diagonal of a rectangle of base 1 and height 1.5. This fact is related to the geometric variation of the cruciform specimens that will be explained in the Chapter 5.

For these tests, a large number of alternating layers has been avoided, limiting the laminate to 8 plies, since it has been proven in previous works that size-scale effects greatly affects the non-linear evolution of these stacking sequences due to pseudo-ductile effects. Specifically, a high number of alternating layers in a sublaminate level technique generates greater pseudo-ductile effects, while ply clustering leads to a more elastic and brittle behaviour [168,184].

In Fig. 3.3 the results obtained from the tensile tests on angle-ply laminates are plotted. First, it is noteworthy the large difference between the laminate $\pm 45^\circ$ and the rest of the angle-ply sequences, showing maximum normal strain close to 10 % for the $\pm 45^\circ$, exhibiting large strain at a constant stress. Laminates with orientations greater than 45° show predominantly brittle linear behaviour, without experiencing clear pseudo-ductile effects. This can be explained by the reduction of the stress/strain shear component and a predominance of stresses in the matrix direction, generating a tensile failure before producing a shear-driven matrix plasticity. The laminate $\pm 33.7^\circ$ does experience a certain non-linearity, therefore expecting a certain reorientation of the fibre. The averaged results for the tests of these angle-ply laminates are shown in Table 3.4, including the analytical estimates obtained using

the CLPT for comparison.

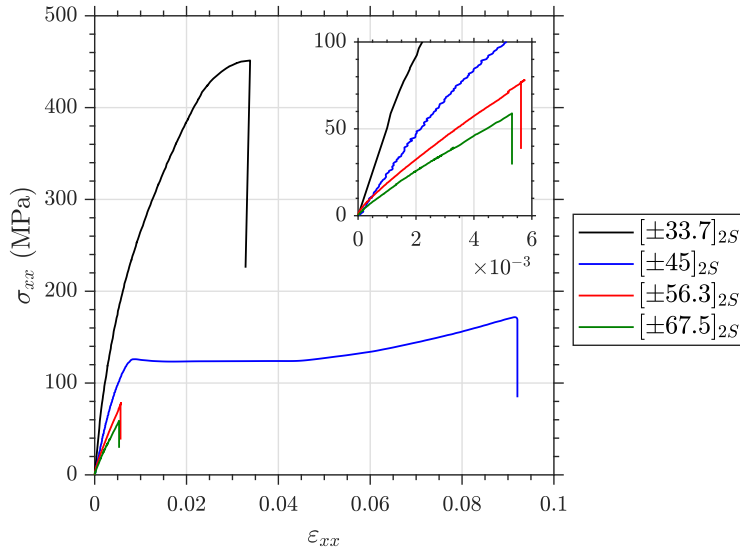


Figure 3.3: Quasi-static uniaxial tensile test of different angle-ply configurations. Low stress-strain levels are zoomed in the subfigure.

Table 3.4: Uniaxial tensile testing of different angle-ply laminates.

Laminate	Experimental			Analytical (CLPT)	
	S'_{xx} (MPa)	E_{xx} (GPa)	ν_{xy}	E_{xx} (GPa)	ν_{xy}
$[\pm 33.7]_{2S}$	440.6 ± 29.1	42.15 ± 1.98	1.34 ± 0.06	41.07	1.34
$[\pm 45]_{2S}$	182.4 ± 6.5	19.18 ± 0.41	0.81 ± 0.01	19.59	0.81
$[\pm 56.3]_{2S}$	78.5 ± 6.3	15.68 ± 0.31	0.40 ± 0.01	12.78	0.42
$[\pm 67.5]_{2S}$	63.7 ± 6.5	12.40 ± 0.85	0.19 ± 0.01	11.91	0.18

It is proven that the experimental values agree with the theoretical estimations, except for the elastic modulus of the $[\pm 56.3]$ laminates, for which theory underestimate this property, possibly due to a bigger stress transfer to the fibre than the theoretically expected.

An important phenomenon concerning the pseudo-ductile behaviour is the fibre reorientation. For the purpose of adequately illustrating those effects, the variation of the fibre angle has been estimated through the Eq. 2.24 and the result is depicted in Fig. 3.4, plotted against the normal strain normalized with the ultimate strain for each test. This reorientation can be also analysed by visualizing the ϵ_{xx} and ϵ_{yy} evolutions together, as represented for the $\pm 45^\circ$ and $\pm 67.5^\circ$ in Fig. 3.5. It is verified that when non-linearity is high (i.e. in the plateau stage) there is no constant relation between the two strain components since, for instance in the $\pm 45^\circ$ laminate, the

initial Poisson's ratio is 0.8 but ϵ_{yy}^u exceeds ϵ_{xx}^u .

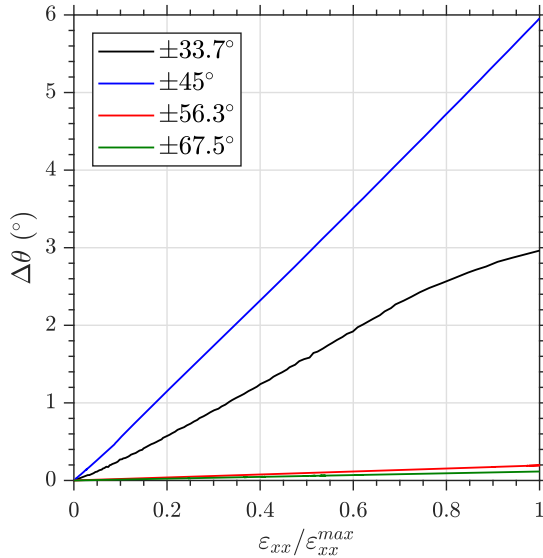


Figure 3.4: Estimation of fibre reorientation in uniaxially tensile tested angle-ply laminates.

Additionally, note that the state of stress in each lamina of angle-ply laminates is a combination of the normal and shear stresses σ_{11} , σ_{22} and τ_{12} . The standard ASTM D3518 [19] details the use of the laminate $\pm 45^\circ$ for shear characterization even when shear stress is combined with the other normal components. Normally, these considerations would lead to the rejection of this test geometry for shear characterization [185]. However, the shear stress-strain responses of many composite laminae are non-linear and exhibit strain-softening characteristics. Thus, although the in-ply *internal* biaxial state of stress likely causes the measured value of shear strength to be lower than the true value, the reduction may be small because of the non-linear stiffness degradation. Therefore, the $[\pm 45]_{NS}$ tensile shear test method may often be reliable in determining lamina shear modulus and strength. Apart from the elastic properties and ultimate strength, the $\pm 45^\circ$ laminate provides a clear value for drastic change in the response (i.e. the initiation of the plateau), which is usually named as yielding strength, but it should not be confused with the phenomenon of plasticity in metals. For the tensile tested $[\pm 45]_{2S}$ laminated it takes a value of $\sigma_{xx} = 124.2 \pm 4.2$ MPa, which in ply shear stress is equivalent to $\tau_{12} = 62.1 \pm 2.1$ MPa.

Finally, the optical observation of the test specimens allows a better understanding of the behaviour of the ply depending on the failure modes achieved. In the case of the $\pm 45^\circ$ test (Fig. 3.6) the specimen shows a significant reduction of the cross section, also showing in some of the specimens a necking zone due to the location of the permanent shear strain in the weakest section (i.e. near the end-tabs due to

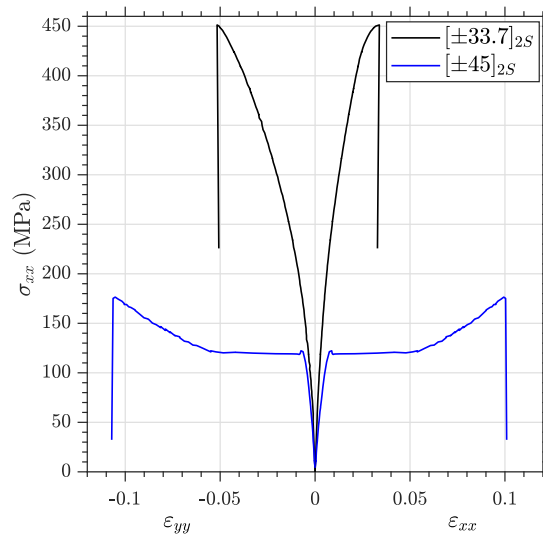


Figure 3.5: Uniaxial tensile test results for different angle-ply configuration, depicting $\sigma_{xx} - \varepsilon_{xx}$ (right side) and $\sigma_{xx} - \varepsilon_{yy}$ (left side).

the stress concentration generated by the change in the specimen's section). A high permanent reorientation of the fibres is observed under the naked eye. Clearly the initial failure of the material is caused by matrix cracks, which appear first in the central layers (Fig. 3.6b), deriving in cracks that completely travel through the cross-section, following the shear direction parallel to the fibre alternating for each ply. It is also possible to observe some degree of fibre breakage near the main crack, as well as delaminations of the two outer layers in this same region, associated to the final stage of the laminate failure.

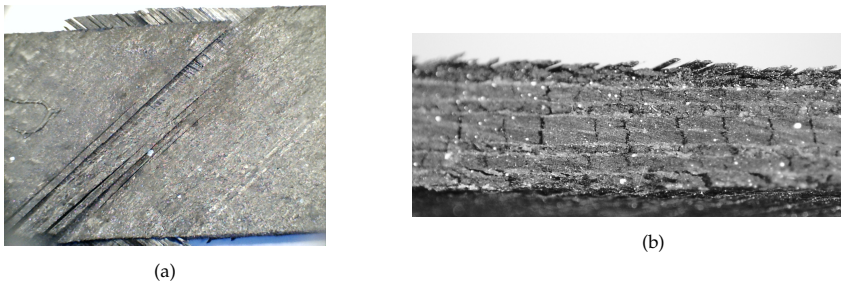


Figure 3.6: Uniaxially tensile tested $[\pm 45]_{2S}$: (a) Top view depicting matrix crack and permanent deformation and (b) side view of matrix cracking in internal plies.

Studying now the other cases of angle-ply laminates (Fig. 3.7), first the $[\pm 33.7]_{2S}$ laminate shows a similar pattern of failure, with a lower permanent deformation, but with a reorientation of fibres also visible at the macroscopic level. The microscopic observation reveals a higher fibre breakage density, as it is understandable due to the

higher longitudinal stress (see Fig. 3.9), although it does not reach the fibre strength values due to pure tension. Compressive stress/strain on the transversal direction (observe red line in Fig. 3.9a) points to a shear dominated failure over the matrix. Regarding the laminate $[\pm 56.3]_{2S}$, the reduction of the longitudinal and shear stresses reveals a failure more dominated by the σ_{22} component (promoting tensile matrix crack), although certain similarities are still appreciated with the failure mode of $\pm 45^\circ$ but at a much lower degree. In this sense, several matrix microcracks are observed in the areas close to the main crack.

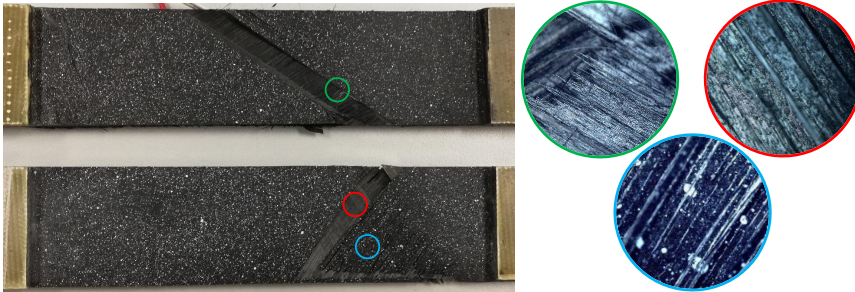


Figure 3.7: Uniaxial tensile tested specimens of $[\pm 33.7]_{2S}$ (above) and $[\pm 56.3]_{2S}$ (below) laminates, including 100x microscopic magnifications.

Finally, $\pm 67.5^\circ$ laminate presents a clear and brittle tensile matrix failure, showing neither signs of damage in the longitudinal direction nor plastic behaviour of the material, as illustrated in Fig. 3.8.

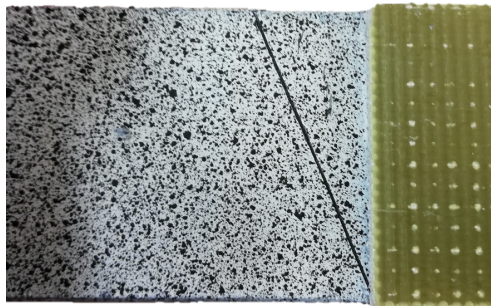


Figure 3.8: Uniaxial tensile tested $[\pm 67.5]_{2S}$ specimen illustrating brittle matrix cracking.

Loading-Unloading-Reloading

In order to measure the capacity of plastic deformation and the progressive degradation of the polymer-based material, cyclic tests have been carried out on the laminates $[\pm 45]_{2S}$ and $[\pm 67.5]_{2S}$. The damage and plasticity of the lamina can be quan-

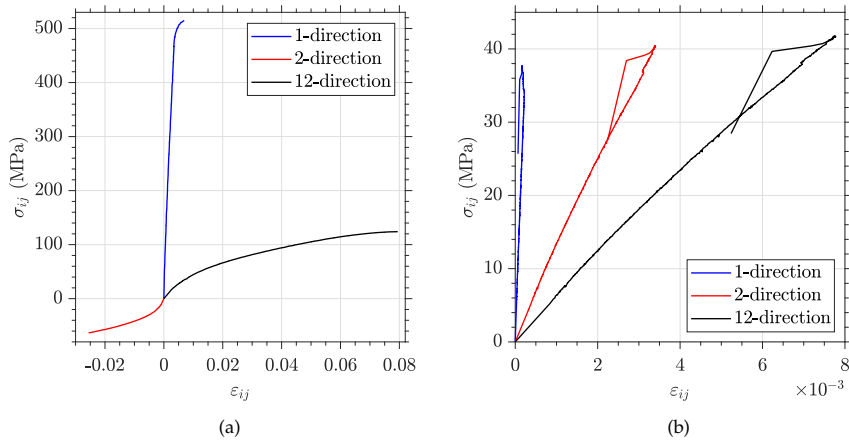


Figure 3.9: Stress and strain components in principal directions for uniaxial tensile tests: (a) $[\pm 33.7]_{2S}$ and (b) $[\pm 56.3]_{2S}$.

tified by applying load cycles up to a predefined value, almost complete discharge and recharge to a higher load/deformation value. The parameters which could be measured through this Loading-Unloading-Reloading (**LUR**) are schematized in Fig. 3.10. Note that the difference in energies between the unload (red) and reload (blue) curves represents the hysteresis of the material due to irreversible thermodynamic processes [186].

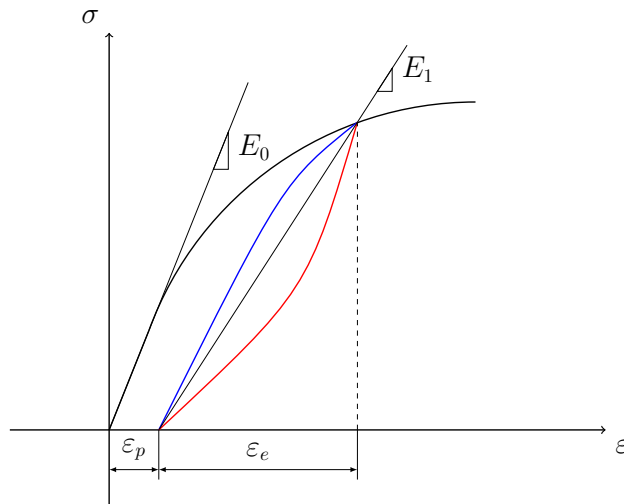


Figure 3.10: Representation of **LUR** stress-strain response. Red path indicates the unload, while blue line describes the reloading cycle.

The results of the application of this test to the $[\pm 45]_{2S}$ laminate produces a stress-strain curve for the studied material depicted in Fig. 3.11, where it is shown that the

quasi-static test represents the envelope of the cyclic test. Note that strain gauges can only collect the behaviour under small strains (Fig. 3.11b), so the axial extensometer and DIC are applied to measure the strains of higher magnitude. Analysing in detail the response of the material, the evolution of the three stages typically observed in laminates with pseudo-ductile behaviour can be described. First, there is an evolution with diffuse damage and some plastic strain (sometimes obviated by its apparent linearity with respect to the rest of the test [21, 27]). In literature this is associated with possible viscoelastic effects of the material or matrix-fibre interface failure [44, 45]. The plateau in which most of the deformation occurs, and therefore a high energy absorption, which entails an important shear yielding, combined with a great degradation of the material stiffness. This produces different surface cracks (shear cusps) as well as internal matrix cracking [25, 26]. Finally, the high fibre re-orientation and the matrix plasticity lead to a third stage where damage apparently ceases (the damage of the matrix actually progresses but the fibres increase the load bearing capacity) while the plastic deformation continues to grow until the failure produced by matrix cracking and delamination. The outcomes of these tests are further analysed in Section 3.3.2.

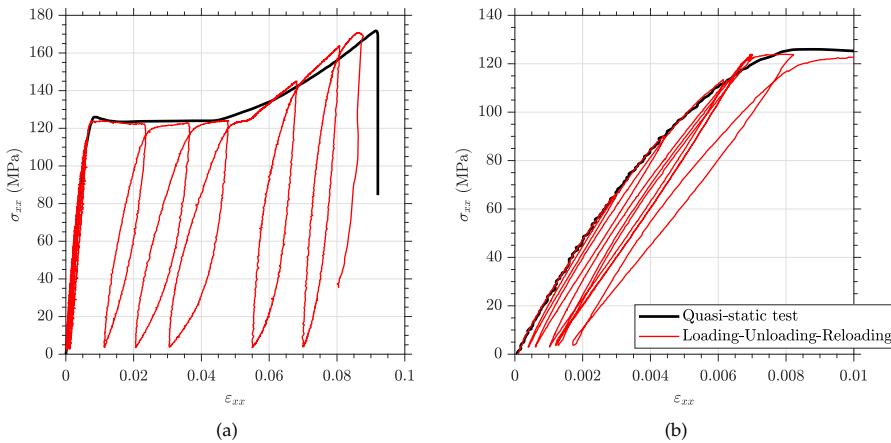


Figure 3.11: Quasi-static and LUR test of $[\pm 45]_{25}$ laminate: (a) extensometer strains and (b) strain gauge measures.

Nevertheless, it must be emphasized the difficulty of carrying out LUR cycles over this laminate. The usual way to proceed in LUR tests is to establish the levels of applied force to be achieved at each unloading-reloading loop. However, the appearance of a plateau in which the stress decreases slightly prevents the cycles from being load controlled. This test required the definition of an ad hoc test control program, which was developed using the interface *LabView*. Therefore, the methodology followed required to divide the test into 3 stages. A first zone in which the force control allows to establish the limits of each cycle as percentages of the plateau initiation stress (i.e. yielding strength), a displacement control of the plateau stage to

avoid an uncontrolled application of force, and a last force control to ensure again the unloading stresses of cycles prior to failure. This difficulty is added to the presence of *necking* effects in the vicinity of the end-tab, due to the inevitable stress concentration. The combined measurement with foil strain gauges, axial extensometer and DIC allowed control of the tests and the recording of local effects on the specimen.

3.2 Uniaxial compressive testing

With regard to standard uniaxial compressive tests, it is important to take into account the high complexity of these tests, specially when pursuing a complete characterization of stiffness and strength in principal directions of the material. This reasoning explains why there is not a unique recommended standard for compressive characterization of laminates, but different types of tests could be found [187]. These procedures involve changes in specimen geometry and the application of different jigs, with the aim of stabilizing against buckling [188–190]. Some tests have the disadvantage of involving shear stresses [189, 191], so we opt for the Modified D695 standard testing, also similarly included in the ISO14126 normative [190]. It should be noted that the anti-buckling device of these regulations has undergone several modifications throughout its history, some not included up to date in international standards (for instance the so-called Modified D695, also found as the Boeing Specification Support Standard BSS 7260 [192]). These modifications include jigs and specimens with and without end-tabs, liberating a central gauge section and allowing direct measurement of strain. However large unconstrained gauge zone can lead to premature failure strength due to buckling instability.

For this work, a jig based on the Modified D695 standard was designed ad-hoc, including a stabilizing base that facilitates the alignment of the test system (Fig. 3.12a), a parameter of critical relevance in compressive testing. In order to perform adequate strain measurement, a window that allows visual inspection for the application of DIC system is proposed. Additionally, the instrumentation with strain gauges on the opposite side of the specimen permits controlling the appearance of instabilities, in other words, the presence of curvatures due to buckling is reflected in opposite sign strain measurements on each of the instrumentalized surfaces.

Additionally, different specimen geometries were tested in order to obtain proper failure modes, while reducing undesired stress components in the tab-gauge zone transition [193, 194]. Some trials with not-tabbed rectangular specimens, as well as with the 1 mm thickness GFRP end-tabs, produced inadequate failure modes (crushing of the loading face in Fig. 3.13a). Although the use of tabs has been extensively

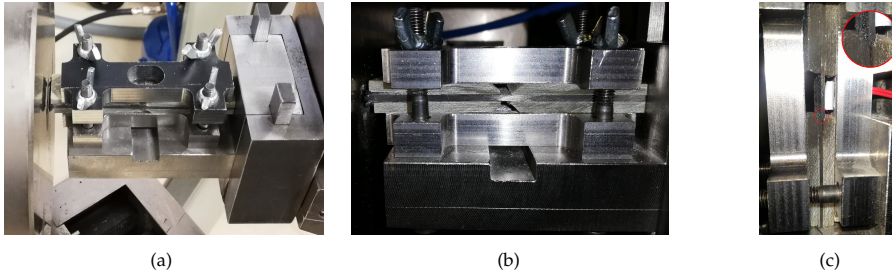


Figure 3.12: Modified ASTM D695 fixture: (a) positioning of stabilizing base on testing machine, (b) side view with short gauge length specimen and (c) long gauge length specimen exhibiting invalid failure mode.

discussed in literature for producing lower strength in compressive tested specimen [193, 195], the best results obtained in this testing campaign were obtained using coupons with 3 mm thickness end-tabs. For instance, the failure mode obtained when compressive testing in transverse direction are shown in Fig. 3.13b. Note that interlaminar shear failure in inclined plane is obtained, in agreement with fracture angle theoretically estimated for typical FRP composite [139, 147].

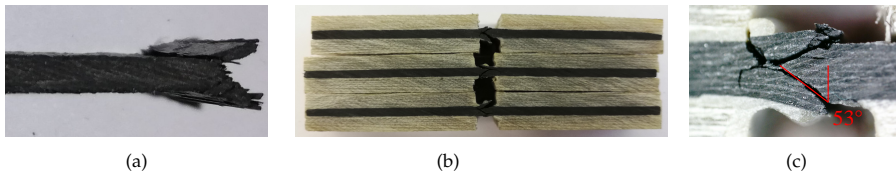


Figure 3.13: Uniaxial compressive tested $[90]_s$ laminates: (a) End crushing of untabbed specimen and (b) tabbed coupons and (c) Fracture angle.

Trials were also carried out with different free lengths between the tool and compression plates in order to minimize the unconstrained distance to reduce the possibility of buckling, but allowing a correct application of the load. The dimensions of the coupon with better performance are depicted in Fig. 3.14. Following the comments of the Modified ASTM D695, two types of tests are necessary to determine stiffness and strength, consisting on reducing the gauge length (l_g) to 12 and 4.75 mm respectively. Besides, test are carried out placing the specimen in the fixture between cylindrical compressive plates, and displacement is applied under constant velocity, where a quasi-static rate of 1.5 mm/min is applied.

The results of the compressive properties characterization in material principal directions are shown in the Table 3.5. The value for S_{11}^c shows the higher dispersion and is well below the values observed in literature for CFRP UD laminae, finding for example $S_{11}^c = 1560.2$ MPa in a similar prepreg [161]. This is related to the high strength of the fibre which complicates to reach compressive failure before the ap-

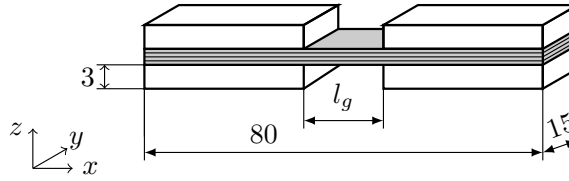


Figure 3.14: Dimensions of uniaxial compressive test coupons (in mm).

partition of buckling. Nevertheless, pure longitudinal compressive mechanisms are not relevant for the scope of this Thesis, and therefore the exact value of S_{11}^c is not necessary.

In order to obtain shear properties, a methodology similar to that described for tensile tests has been followed, in which the shear properties of the lamina have been estimated from the test of a $\pm 45^\circ$ symmetric laminates. Trials with different number of plies (8 and 16 plies) reveals that the $[\pm 45]_{4S}$ postpone the apparition of instabilities in the specimen due to a lower slenderness of the specimen (see Fig. 3.15), while increasing the pseudo-ductile effects due to higher number of alternating plies.

Table 3.5: Compressive properties of M21E/IMA-12K lamina.

E_1 (GPa)	$E_2 = E_3$ (GPa)	$\nu_{12} = \nu_{13}$	$G_{12} = G_{13}$ (GPa)
132.99 ± 11.74	9.14 ± 0.10	0.19 ± 0.01	5.46 ± 0.42
S_{11}^c (MPa)	S_{22}^c (MPa)	S_{12} (MPa)	
628.5 ± 74.6	172.3 ± 6.7	82.4 ± 5.2	

By testing the $\pm 45^\circ$ lay-up is also possible to study its non-linear behaviour under compressive loading, observing qualitatively the same stages as in the tensile tests. Similar initial and plateau stages are developed, but a lower re-stiffening before failure is observed as fibre reorientation is not contributing to the rigidity at loading direction. In Fig. 3.15 the comparison of the response in the three principal directions is shown, which gives an idea of the brittle elastic behaviour also existing in compression in the longitudinal and transverse directions, while a large permanent deformation still appears of the matrix due to shear strain effects.

Once again, it is verified that the elastic properties of the laminate can be estimated using the CLPT, in this case by introducing the compressive properties (Table 3.5) into the ply stiffness matrix (Q). The comparison of these analytical predictions with the results obtained experimentally are shown in Table 3.6.

3.3. NUMERICAL MODELLING OF THE NON-LINEAR RESPONSE OF ANGLE-PLY LAMINATES UNDER UNIAXIAL LOADING

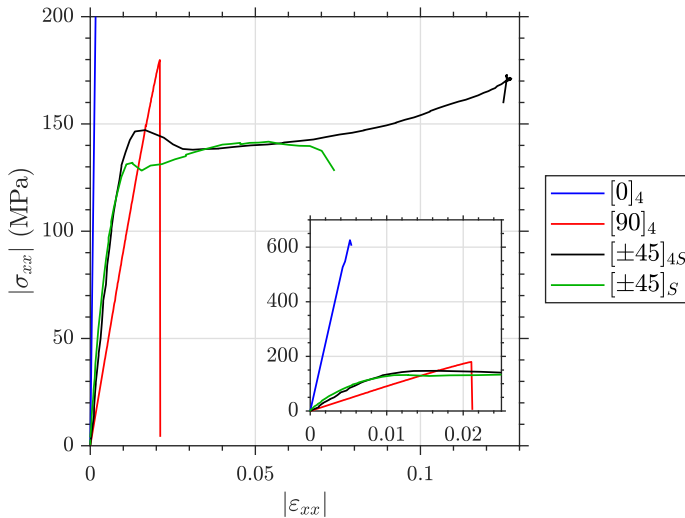


Figure 3.15: Compressive uniaxial response of $[0]_4$, $[90]_4$, $[\pm 45]_{4S}$ and $[\pm 45]_S$ laminates. Subfigure is included to better visualization of small strain range.

Table 3.6: Experimental and analytical compressive estimates tensile elastic properties of $[\pm 45]_{4S}$ laminate.

	$E_{xx} = E_{yy}$ (GPa)	ν_{xy} (GPa)
Experimental	18.41 ± 0.54	0.88 ± 0.03
CLPT	18.89	0.74

3.3 Numerical modelling of the non-linear response of angle-ply laminates under uniaxial loading

This section aims to numerically simulate the gradual loss of stiffness associated with pseudo-ductility which leads to a highly energetic damage evolution process. Then, the two PDM models described in Chapter 2 are applied to this end. Firstly, the calibration of the material parameters related to damage and permanent strain is required. Afterwards, the capacity of both models is validated with different angle-ply and loading conditions. Besides, the influence of the numerical modelling strategy, that is, the use of element with different constitutive formulation, is analysed.

3.3.1 Parameter identification for Hashin’s Damage Model

In this section, the values of the numerical parameters (α , G_{kl}^c and d^{max}) necessary to apply the damage model are proposed to be calculated based on the experimen-

tal results obtained from the uniaxial testing. A similar methodology is conducted in [196]. Apart from the already defined material parameters, the most important to control the evolution of the damage are the damage energy release rate (G_{kl}^c , where kl refers to the four damage modes defined above), which represent the area under the equivalent stress-displacement curve (Fig. 2.11). Some remarks about these parameters are necessary to correctly understand the operation of this model. First of all, when talking about the energy release rate, these values associated with the propagation of in-plane damage modes should not be confused with values such as fracture energy, which can be measured by crack opening testing. This idea is also highlighted in the work of Barbero et al. [196], where it is shown that the energy of this Hashin's damage model does not correspond to that of interlaminar damage. As these energy release rates cannot be obtained from literature, an alternative requires a fitting of the stress-strain curves obtained experimentally.

This process of obtaining parameters has been carried out using a non-linear multivariate optimization based on the trust-region reflective algorithm [197]. This material parameter identification seeks to reflect the great damage absorption capacity existing in the case of angle-ply laminates due to the pseudo-ductile effect, which is unrelated to the brittle linear elastic behaviour of the lamina in principal directions. Once these parameters are fitted, the material model is applied to a more complex stress state, the analysis of the biaxial testing. Then this Thesis attempts to collect the modelling of a laminate in which damage and plasticity are combined, so that both phenomena are included in the stiffness degradation. This idea is observed similarly in other works found in literature, for instance, Laux et al. [110] modelled the shear behaviour of UD composites applying a plasticity model without addressing the effects of stiffness degradation. In other words, on the contrary to the approach of this Thesis to associate non-linearities only to damage, Laux et al. proposed to fit the high shear strain just with a yielding model.

This leads to the fact that, in the case of studying the response to cyclic loads, the Hashin's model is inadequate by itself, since it fits neither the permanent deformation nor the instantaneous damage. However, it allows us to provide a greater level of understanding of what happens in testing with biaxial loading states, and also to predict the stress-strain relations in other states not achieved in the laboratory.

The model parameter identification for Hashin's PDM is performed implementing the equations of Section 2.3.1 in a MATLAB script and performing an optimization of the parameters which cannot be measured experimentally. This process is summarized in the flowchart depicted in Fig. 3.16. Note the script implemented in MATLAB imitates the PDM included in Abaqus, so that it has been possible to verify that the result of both codes coincides when working with a single finite element

3.3. NUMERICAL MODELLING OF THE NON-LINEAR RESPONSE OF ANGLE-PLY LAMINATES UNDER UNIAXIAL LOADING

submitted at similar boundary conditions.

The results of the material parameter identifications for different uniaxial tensile and compressive tests on the angle-ply laminates shown in the previous sections are summarized in Table 3.7. In order to better illustrate the parameter calibrations, the numerical stress-strain response together with the experimental curves utilised are shown in Figs. 3.17, 3.18 and 3.19.

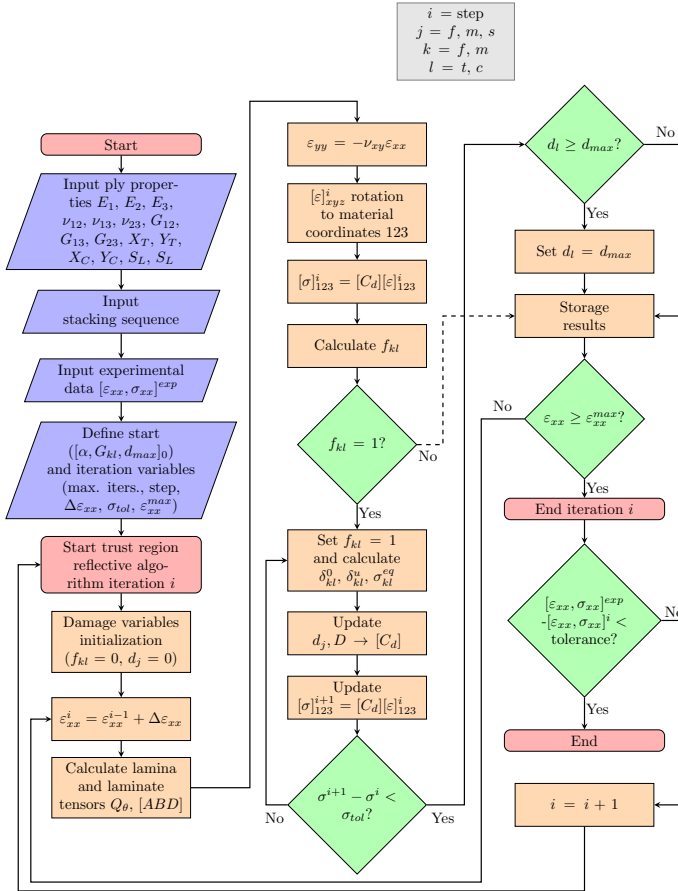


Figure 3.16: Flowchart for Hashin's damage model calibration.

Analysing the data collected in Table 3.7, it is important to point out that the identification of energy release rates does not provide exact values, but rather guides the order of their magnitude, fitting with the experimental observations. This result agrees with the conclusions of the study from Barbero et al. [196], which reported a high insensitivity of the results to the energy release rates, even with different GFRP laminates.

Regarding the case of $[\pm 45]_{2S}$, Fig. 3.17 depicts two calibration of parameters. On the one hand, the experimental data obtained using the engineering strain ($\sigma_{xx} = P/A_o$) is used to determine the parameters of the Hashin's damage model as implemented in Abaqus. On the other hand, the experimental curve considering the true stress ($\sigma_{xx} = P/A_i$, where A_i means instantaneous cross-section) is fitted with the Hashin's PDM considering fibre reorientation (*FR*). The difference between both approaches proceeds from the fact that a bigger stiffness is achieved when *FR* is considered, compared to the former implementation. Therefore it makes necessary to increase the shear component to failure (related to α). Besides, more matrix stiffness degradation (through a higher d^{max} and a lower G_{mt}^c) is required to compensate for the stiffening at the loading direction given by the reorientation. For both identifications, it should be noted that the energy release rate assigned to the fibre mode has little relevance in the results, since the stiffness in fibre direction will only degrade when the failure stress is reached, which is controlled with the interaction parameter α . Subsequently, a brittle failure is observed, and the G_{ft}^c controls the slope of the final drop.

Table 3.7: Hashin's parameter identification for angle-ply laminates. Note this values are obtained for a characteristic length $L_c = 1 \text{ mm}$.

Laminate & test	α	G_{mt}^c (N/mm)	G_{mc}^c (N/mm)	G_{ft}^c (N/mm)	G_{fc}^c (N/mm)	d^{max}
$[\pm 45]_{2S}$ tensile	0.34	1200	—	5000	—	0.91
$[\pm 45]_{2S}$ tensile (<i>FR</i>)	0.53	3000	—	5000	—	0.95
$[\pm 45]_{4S}$ compressive	—	—	1000	—	5000	0.94
$[\pm 56.3]_{2S}$ tensile	—	230	—	—	—	1
$[\pm 33.7]_{2S}$ tensile	0.22	—	100	3000	—	0.68

Note values are given only for the damage modes actually involved in each simulation. It is worth remembering that *FR* refers to the calibration of the model considering both fibre reorientation and change in cross-sectional area.

The compressive identification of the $\pm 45^\circ$ laminate (Fig. 3.18) results in similar values compared with the tensile one, what it was expected as the apparent response of the laminate under tensile and compressive loading is analogous due to the shear-dominated response. Higher strains are achieved in the case of compressive loading, however it should be pointed out that fibre reorientation in this loading scenario is not contributing to stiffening. As noted by Cui et al. [43], this reorientation of the fibre away from the loading direction should contribute to determine the shear

3.3. NUMERICAL MODELLING OF THE NON-LINEAR RESPONSE OF ANGLE-PLY LAMINATES UNDER UNIAXIAL LOADING

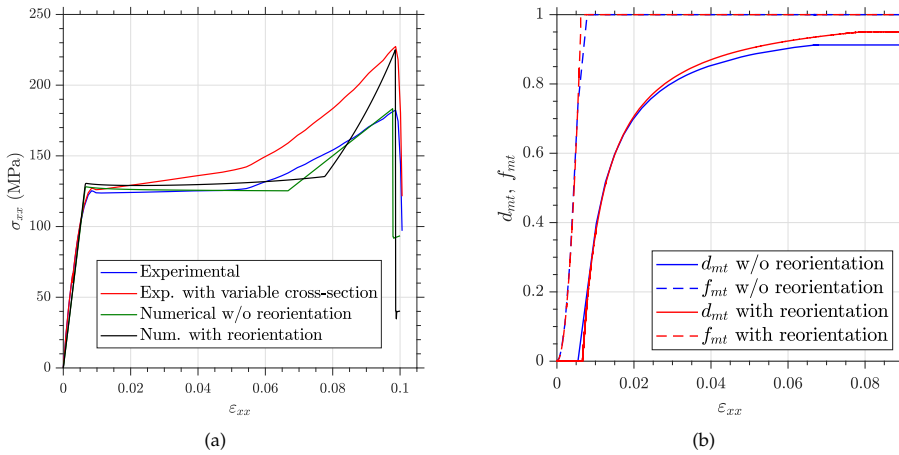


Figure 3.17: $[\pm 45]_{2S}$ uniaxial tensile loading results from Hashin’s model including reorientation: (a) numerical stress-strain compared to experimental curves and (b) damage initiation indexes and variables evolutions.

response, because it allows a better interpretation of the lamina shear behaviour in comparison to the one obtained from tensile test.

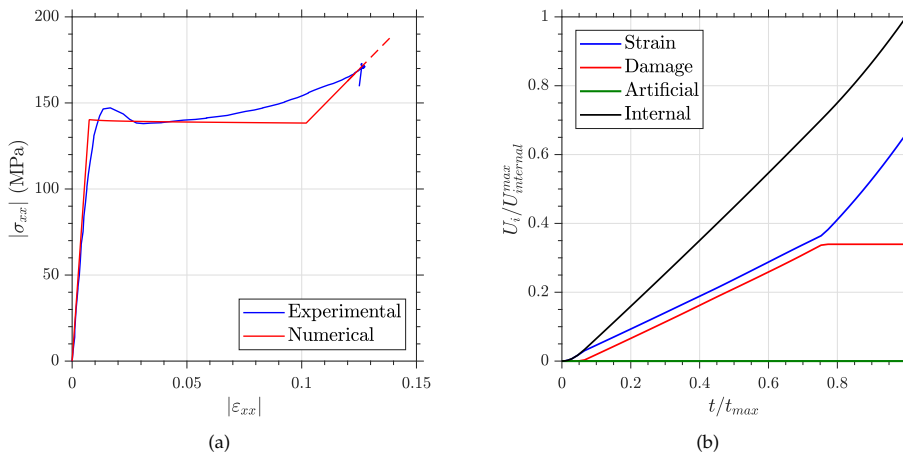


Figure 3.18: $[\pm 45]_{4S}$ uniaxial compressive loading results from Hashin’s model: (a) experimental and numerical stress-strain and (b) evolution of energies on the simulation.

Additionally, Fig. 3.18b depicts for the compressive loading case the energies (U) involved in the simulation in order to check the correct adequacy of the identified parameters once they are included in the Abaqus model. The values of strain, damage, artificial and internal energies have been normalized with the maximum internal energy for better comparison (as internal energy is the sum of all the others [130]). The strain energy is due to the accumulation of elastic stress and strain. The damage

energy is related to the stress-strain appearing after the damage initiation criterion is fulfilled ($f = 1$) up to the maximum degradation. Besides, it is observed how the damage energy for this test is quite similar to the strain energy up to the point in which maximum degradation of the matrix mode is reached. The negligible value of artificial energy reflects that there is little need of viscous regularization in order to achieve convergence of these simulations.

With regard to the other angle-ply sequences included in the Table 3.7, the identifications results in much lower energy release rates. In the case of $[\pm 56.3]_{2S}$, the linear brittle failure of this lay-up (Fig. 3.19a) explains the lowest value of the table for G_{mt}^c , as higher importance of the damage and failure in matrix direction is observed due to the high angular mismatch between fibre and loading direction, thus fibre modes have no effect in the damage and failure.

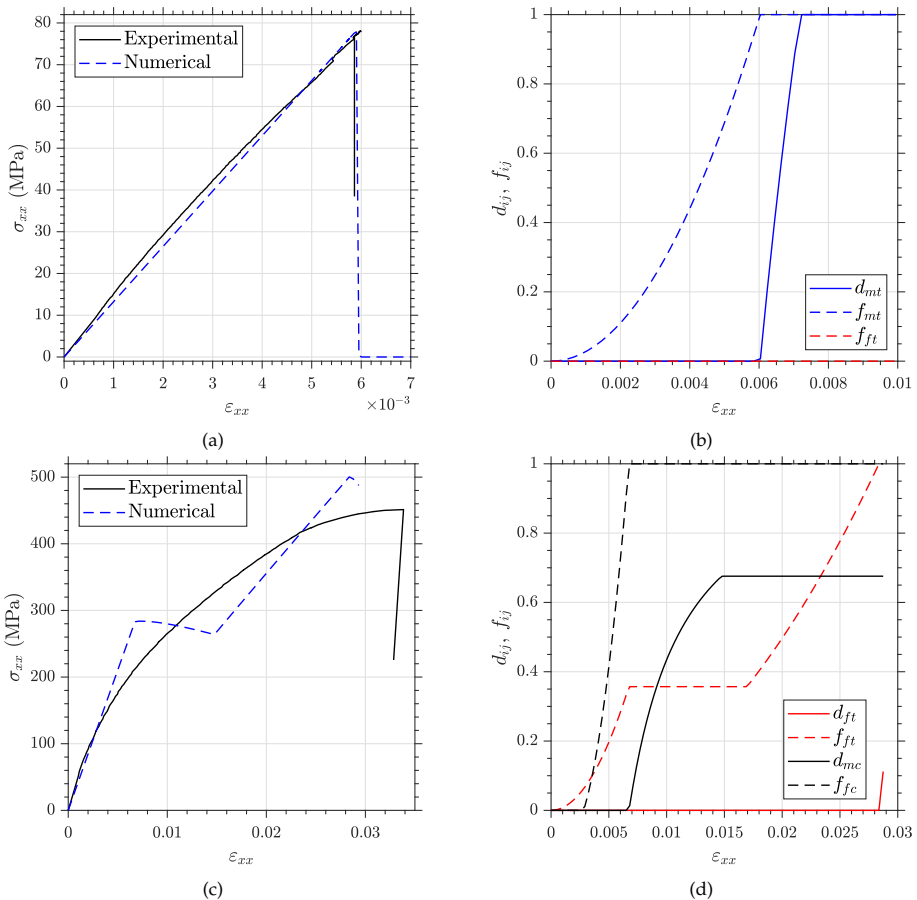


Figure 3.19: Hashin's damage model and experimental results for angle-ply uniaxially tensile tested laminates: (a) $[\pm 56.3]_{2S}$ stress-strain results, (b) $[\pm 56.3]_{2S}$ damage evolutions, (c) $[\pm 33.7]_{2S}$ stress-strain results and (d) $[\pm 33.7]_{2S}$ damage evolutions.

Regarding the $[\pm 33.7]_{2S}$, the effects are just the opposite. The reduction of the angle between x and 1 directions result in a higher influence of the fibre tensile mode (representing the final failure), but the lower strength of the matrix and the effect of shear stress promotes the damage initiation on the matrix compressive mode (Fig. 3.19d).

3.3.2 Material parameter identification for Ladevèze's model

As performed in other studies [155, 175, 177], 0° , 90° , $\pm 45^\circ$ and $\pm 67.5^\circ$ symmetrical laminates stacking sequences allow to calibrate the material properties defined for the Ladevèze's model. The last two laminates develop a full in-plane state of stress (σ_{11} , σ_{22} , τ_{12}), maximizing the shear component for the case of $[\pm 45]_{2S}$ and preferring the $[\pm 67.5]_{2S}$ to other possibilities due to reduction of scattering of the results [155]. Fig. 3.20 shows the results of all the LUR tests that provide the data for the computations performed in this section. Note that the parameter identification that it is explained in this section aims to fit the evolution of the first region, whose results are summarised in Table 3.8. After that, another identification considering the whole dataset (including the plateau and re-stiffening stages of the $[\pm 45]_{2S}$) will be detailed.

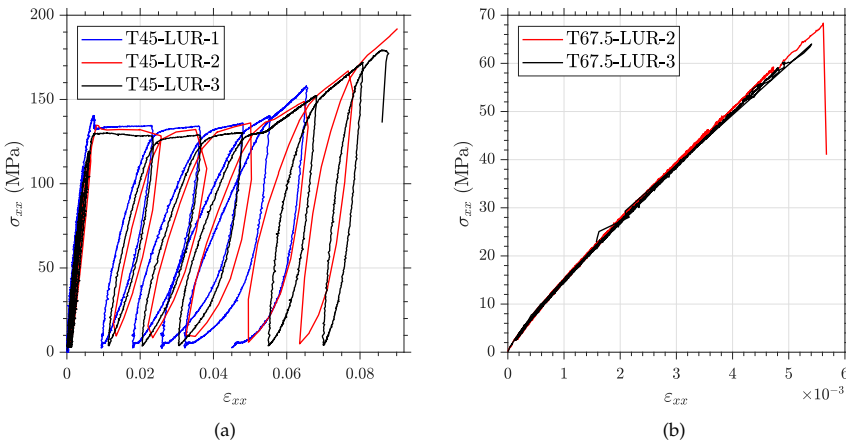


Figure 3.20: LUR tests for calibration of Ladevèze's model: (a) $[\pm 45]_{2S}$ laminate and (b) $[\pm 67.5]_{2S}$.

The results previously shown for tensile uniaxial testing of $[0]_2$, $[90]_2$ and $[\pm 45]_{2S}$ laminates allow to determine all the elastic properties necessary for the model (collected in Table 3.1), and also supply enough data to compute the thermodynamic forces related to maximum degradation of fibre, shear and transverse moduli, which are calculated applying Eqs. 2.30. Regarding the undamaged transverse modulus (E_2^0) and the in-plane shear modulus G_{12}^0 , these should be recalculated as the trans-

Table 3.8: Materials properties applied on Ladevèze's model.

E_1 (GPa)	177.56	R_0 (MPa)	0
E_2^0 (GPa)	13.07	α_L	0.476
G_{12}^0 (GPa)	7.76	β (MPa)	1494.6
G_{23} (GPa)	3.1	Y_C (MPa)	4
ν_{12}	0.39	Y_0 (MPa)	0.04
ν_{23}	0.36	Y_T (MPa)	19.05
a_L	0	$Y_{C'}$ (MPa)	6.92
b_L	0	Y_{12S} (MPa)	4.93
b'	0.628	Y_{22} (MPa)	0.10

verse stress-strain curve for the $[\pm 67.5]_{2S}$ and the shear stress-strain for the $[\pm 45]_{2S}$ depicts non-linearity at the very beginning of the curves (Fig. 3.20). This is due to the premature initiation of damage and permanent strain in these test.

Firstly, it is necessary to compute the lamina stress and strain tensor in principal directions. While strains are measured experimentally in x , y and xy directions and can be easily rotated applying a transformation matrix (Eq. 3.1), experimental data is only available for σ_{xx} . Therefore, applying CLPT is possible to relate (by means of elastic relations) the principal direction stress tensor, resulting in the expressions collected in Eqs. 3.2 and 3.3.

$$\begin{cases} \varepsilon_{11} = \varepsilon_{xx} \sin^2(\theta) + \varepsilon_{yy} \cos^2(\theta) \\ \varepsilon_{22} = \varepsilon_{xx} \cos^2(\theta) + \varepsilon_{yy} \sin^2(\theta) \\ \gamma_{12} = 2(\varepsilon_{xx} - \varepsilon_{yy}) \cos(\theta) \sin(\theta) \end{cases} \quad (3.1)$$

$$\begin{cases} \sigma_{11} = s \sigma_{xx} \\ \sigma_{22} = s' \sigma_{xx} \\ \sigma_{12} = s'' \sigma_{xx} \end{cases} \quad (3.2)$$

$$\begin{cases} s = \cos^2(\theta) + 2 \sin(\theta) \cos(\theta) \left(\frac{\overline{Q_{16} - \nu_{xy} \overline{Q_{26}}}}{E_{xx}} \right) \\ s' = \sin^2(\theta) - 2 \sin(\theta) \cos(\theta) \left(\frac{\overline{Q_{16} - \nu_{xy} \overline{Q_{26}}}}{E_{xx}} \right) \\ s'' = -\sin(\theta) \cos(\theta) + (\cos^2(\theta) - \sin^2(\theta)) \left(\frac{\overline{Q_{16} - \nu_{xy} \overline{Q_{26}}}}{E_{xx}} \right) \end{cases} \quad (3.3)$$

The results for the application of these expressions to the $\pm 45^\circ$ and $\pm 67.5^\circ$ lami-

3.3. NUMERICAL MODELLING OF THE NON-LINEAR RESPONSE OF ANGLE-PLY LAMINATES UNDER UNIAXIAL LOADING

nates are gathered in Table 3.9. Tensile properties of the M21E/IMA-12K (Table 3.1) have been utilised.

Table 3.9: Elastic constants relating stress between global and principal directions.

Laminate	s	s'	s''
$[\pm 45]_{NS}$	0.5	0.5	-0.5
$[\pm 67.5]_{NS}$	0.174	0.826	-0.354

Having defined all the required linear elastic material properties and the limiting thermodynamic forces, the following step consists on calibrating the remaining material parameters regarding the damage and permanent strain initiation and evolution. This is performed by means of the $[\pm 45]_{2S}$ and $[\pm 67.5]_{2S}$ LUR testing. At least two loops are programmed in each of the three main stages of the test in order to supply enough data for identification.

Damage and permanent strain will be evaluated for each of the proposed cycles. Observing the scheme in Fig. 3.10, it is easy to understand the calculation of permanent strain, working in terms of shear component, while the damage will be estimated from the degradation of stiffness (Eq. 3.4).

$$d_{12} = 1 - \frac{G_{12}^i}{G_{12}^0} \quad (3.4)$$

where G_{12}^i represents the stiffness of each of the cycles, estimated as the slope between the start points of the unload and reload. In order to fit the evolution of damage, it is necessary to find the relation between the equivalent thermodynamic force Y_{eq} and the shear damage d_{12} . Since the effect of thermodynamic force (and damage) in the transverse direction is assumed negligible, the equivalent force is simplified as Eq. 3.5.

$$Y_{eq} \approx Y_{d_{12}} \quad (3.5)$$

In this way, it is straightforward to replace the previous result in the equation for the evolution of damage (Eq. 2.30), resulting in Eq. 3.6.

$$d_{12} = \frac{\sqrt{Y_{d_{12}}} - \sqrt{Y_0}}{\sqrt{Y_C}} \quad (3.6)$$

Now it is possible to represent the experimentally obtained values in Fig. 3.21, collecting a total of three representative tests. By proposing a least square fit of the form of Eq. 3.6, the values of Y_0 and Y_C can be determined.

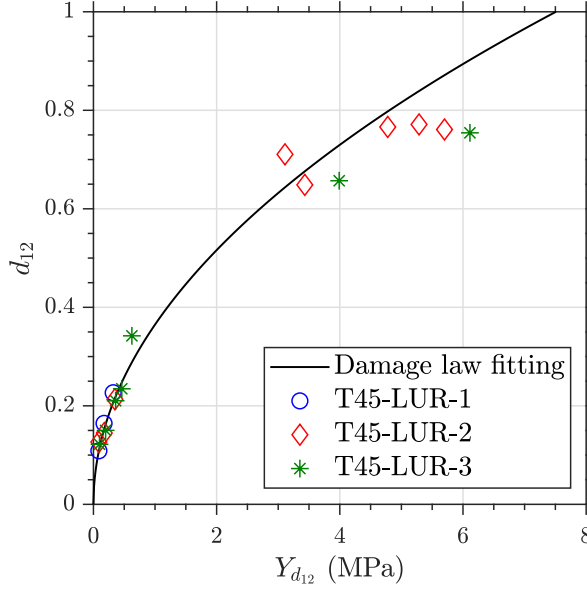


Figure 3.21: Fitting for the Ladevèze's damage evolution law.

Note that the proposed fitting is in good agreement with the data corresponding to lowest damage level (that is, the data related to the loops previous to the plateau), but the fit overestimates the damage at highest level of thermodynamic force, as damage measured data seems to get constant around a 70% degradation of the initial shear modulus. However, the exponential damage law proposed by Ladevèze cannot collect this abrupt change of damage rate.

Having identified the evolution of damage, we proceed to calibrate the isotropic hardening plasticity model. For this, it is necessary to first define the accumulated permanent strain, expressed as Eq. 3.7.

$$p = \int_0^{\varepsilon_{12p}} 2(1 - d_{12})d\varepsilon_{12p} \quad (3.7)$$

In order to simplify the calculation of the plasticity law, an assumption is made, supposing damage is negligible for $\varepsilon_{12p} = 0$. Then, Eq. 2.37 is rewritten as Eq. 3.8.

$$\frac{\sigma_{12}}{1 - d_{12}} = R_0 + \beta p^{\alpha_L} \quad (3.8)$$

After these definitions, again a least squares fitting could be proposed between the effective tension $\tilde{\tau}_{12}$ and the accumulated permanent deformation p , in order to obtain the material parameters R_0 , β and α_L . The results of this fitting are shown in Fig. 3.22

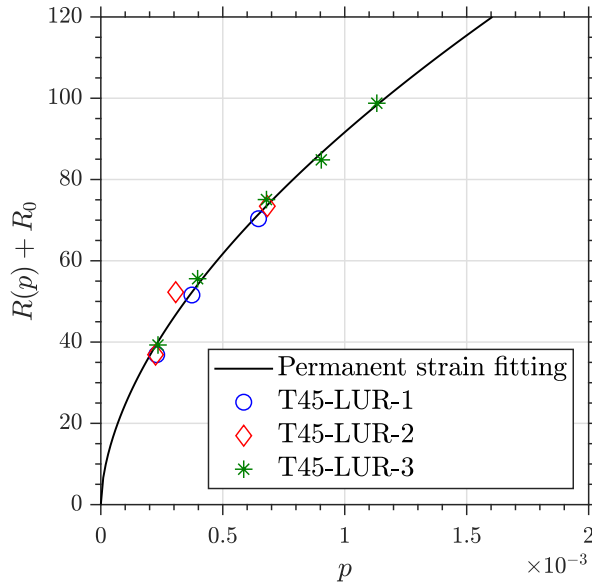


Figure 3.22: Evolution of plastic law, expressed in terms of effective shear stress against accumulated plastic strain.

Finally, only the parameters controlling the shear-transverse interaction (a_L , b_L and b') are to be determined. These are obtained from the $[\pm 67.5]_{2S}$ LUR uniaxial tensile test (see Fig. 3.20b), through the fitting of the experimental evolution of the shear and transverse damage as plotted in Fig. 3.23. In this case, three cycles are performed, controlling them in terms of applied stress. Note that an almost linear and brittle behaviour is observed in these tests, with little damage and permanent strain evolutions. Then, for this material a_L and b_L are considered approximately zero in the parameter identification.

3.3.3 Results obtained with Ladevèze's model for different angle-ply laminates

After the calibration of the material parameters is performed and the correct operation of the subroutine is checked, other numerical simulations for model verification are conducted. The cases that have been used to calibrate the model are shown in the Fig. 3.24. Regarding the $[\pm 45]_{2S}$ laminate, this calibration of parame-

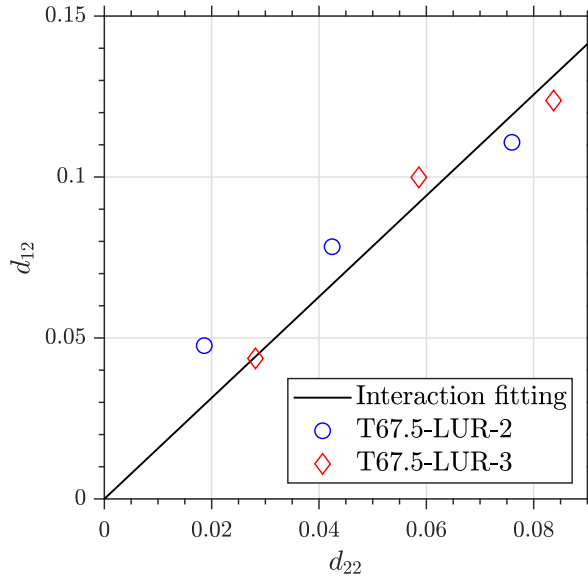


Figure 3.23: Fitting for the shear-transverse damage interaction.

ters demonstrates to collect with good agreement the initial region (Fig. 3.24b), but is not able to follow the behaviour under large strain at constant stress (Fig. 3.24a).

With regard to the $[\pm 67.5]_{2S}$ laminate, the numerical results are closer to the experimental, although the former is completely linear compared to a certain non-linearity of the experimental results, which leads us to think that the calibration of the parameters a_L and b_L should be further analysed.

Finally, the capacity of the simulation to model tests that have not been part of the calibration is verified, using the cases of $[\pm 56.3]_{2S}$ and $[\pm 33.7]_{2S}$ laminates (Fig. 3.25). Similarly to the Hashin's model, the quasi-linear behaviour of the laminate $[\pm 56.3]_{2S}$ is reflected in the Ladevèze's material model, but failing to collect the smooth degradation of the material in the last stage prior to final failure of the laminate. In addition, the results of this model overestimate the stress and strain by 16% and 10.5%, respectively. It must be taken into account that this laminate continues to experience an important shear component (see Fig. 3.9b), but the transverse stress reaches values very close to the shear stress, so that a failure by matrix cracking will be expected to arise before reaching the starting point of the shear-induced matrix yielding.

The application of the Ladevèze's model to the laminate $[\pm 33.7]_{2S}$ under uniaxial tensile stress originates a behaviour marginally similar to the experimental response, obtaining an adequate failure strain, but at an strength value overestimated by 26%. The lack of LUR tests in this laminate impedes drawing more detailed con-

3.3. NUMERICAL MODELLING OF THE NON-LINEAR RESPONSE OF ANGLE-PLY LAMINATES UNDER UNIAXIAL LOADING

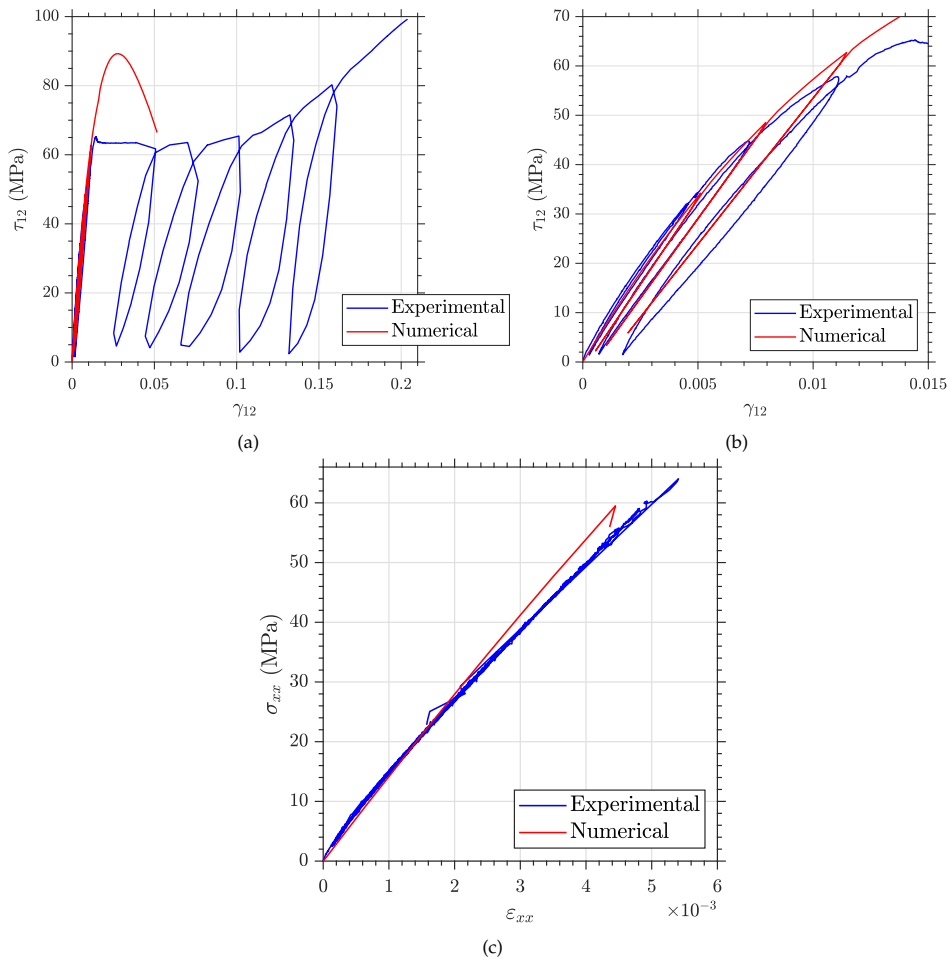


Figure 3.24: Ladevèze’s numerical model and experimental results for angle-ply tensile tested laminates: (a) $[\pm 45]_{2S}$ LUR test, (b) detail of initial response of $[\pm 45]_{2S}$ and (c) $[\pm 67.5]_{2S}$.

clusions about whether it is due to the evolution of damage or plasticity, since the shear stress/strain are quite high (see Fig. 3.9a), promoting the two non-linear mechanisms in a similar manner to $\pm 45^\circ$ lay-up. However, the stress component in the direction of the fibres is quite high, hence explaining the high values of σ_{xx} achieved without allowing large permanent deformation.

Finally, it is important to highlight that other parameter identifications were analysed in order to fit the complete shear non-linear behaviour, following the same methodology explained above. These were performed by means of proposing modifications of the plasticity law in order to cause a great evolution of permanent strain during the plateau, but then the increase in damage becomes negligible (see Fig. 3.26). In other words, even if trying to calibrate the curve by collecting all the load-

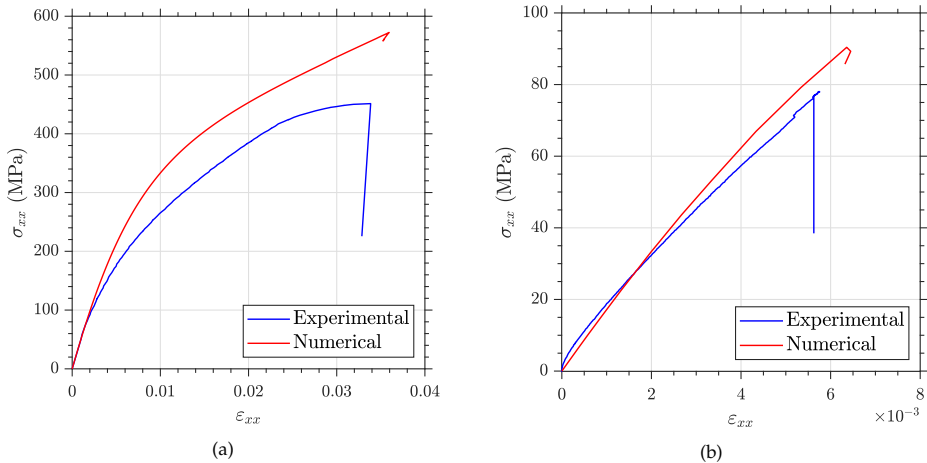


Figure 3.25: Ladevèze’s numerical model and experimental results for angle-ply tensile tested laminates: (a) $[\pm 33.7]_{2S}$ and (b) $[\pm 56.3]_{2S}$.

unload-reload cycles (including those of the plateau and the stiffening zone before final failure), it is observed that the experimental stress-strain curve is not accurately estimated.

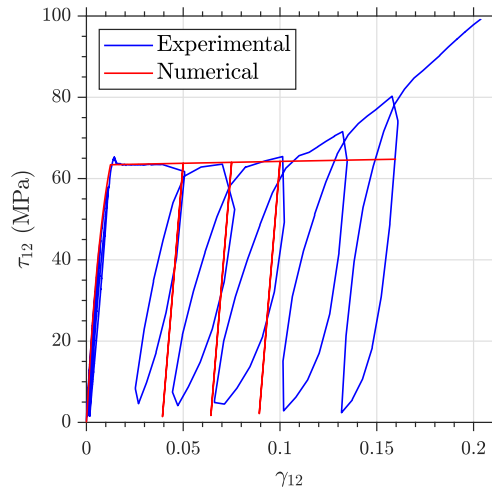


Figure 3.26: Stress-strain results of the modified parameter identification.

If one observes the equations that define Ladevèze’s model and the experimental values reached, it can be stated that it is not possible to collect the measured damage and plasticity values, as the mathematical functions for the evolution cannot fit the experimental data set. Damage greater than 0.5 is measured experimentally, but in the Ladevèze’s model this would imply a drop in the stress curve, which does not agree with the tests. In addition, when plasticity starts, the damage cannot progress

at the same rate than experimentally monitored, as the stress does not increase beyond the yielding point.

3.3.4 Effects of the geometry and element type

Regarding the implementation of these damage models in Abaqus, an important observation is that Hashin's damage model only considers the case of plane or shell elements, since the damage constitutive law is defined for the case of plane stress. Some remarks about the results obtained depending the element type are detailed in [196], concluding that S8R and S8R5 shell elements offer identical solutions, while S4 and S4R linear elements overestimate the stiffness degradation. On the other hand, Ladevèze's **UMAT** is implemented for a 3D constitutive material model, and therefore only solid elements considering the six components of the stress/strain tensors must be utilised.

The main characteristics of the numerical model for the different simulations representing the uniaxial tests are described below. In all cases, models that collect the complete geometry of the laminates have been used, not resorting to symmetry **BCs** (except with regard to the laminate midplane) because the analysis of angle-ply laminates does not allow imposing symmetry conditions with respect to the global coordinate system. In this way, the **BCs** are based on preventing the longitudinal displacement of one end of the specimen and applying a constant or tabular (in case of **LUR** tests) displacement simulating the actuator at the opposite end.

An analysis of the meshing techniques was performed in order to corroborate the possible use of different element types. Starting with a basic model in which the geometry defined in 2D (Fig. 3.27a) is dimensioned with the width and length of the specimen (200×30 mm), an S8R shell element with internal definition of the laminate (namely *Composite Layup*) is applied. The formulation of these elements means that the result is uniform throughout the specimen, that is, they do not suffer concentration effects in the boundary conditions.

Similarly to the previous one, a 3D geometry is meshed by means of Continuum Shell SC8R elements, with a plane formulation similar to the shell. Two different meshing methodologies are applied with this element: a single element through laminate thickness or an element thickness equal to ply thickness, as shown in Fig. 3.27c.

Finally, a more realistic model (Fig. 3.28) is proposed in order to obtain numerical results more similar to the experimental tests. This entails modelling the complete

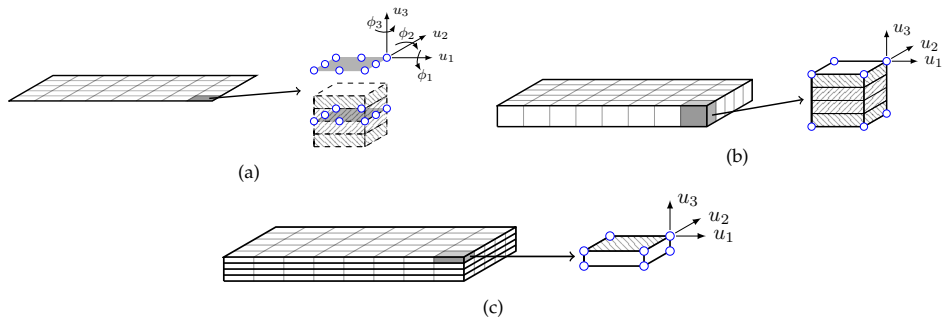


Figure 3.27: Schematization of the different applied element types, nodes (blue circles), degrees of freedom and lay-up definitions: (a) Shell 2D, b (b) Continuum Shell with one element through thickness, (c) Continuum element with one element for each ply thickness and solid element representation.

specimen including the **GFRP** end-tabs, as schematized in Fig. 3.1. Due to its low influence on the results obtained, the material model of the tabs is simplified to a linear elastic isotropic behaviour with typical properties of a **GFRP** quasi-isotropic laminate: $E = 22 \text{ GPa}$ and $\nu = 0.12$.

This model is meshed with either SC8R continuum shells or C3D8 solid elements (thickness equal to 0.25 mm, i.e. theoretical thickness of cured ply). Therefore, this model allows to reproduce adequately the strain states caused by the geometric change of the specimen in the vicinity of the end-tab [193].

Regarding the **BCs**, they are described on *Reference Points* tied to the different surfaces of the specimens with constraint equations, following the methodology explained in [193] and schematized in Fig. 3.28. Each layer is modelled separately, assigning the orientation of the material, and tie constraints are introduced between all layers and tabs. In the RP-1 all the degrees of freedom (**DOFs**) are fixed, while in the RP-2 the z and y translations are constrained and longitudinal displacement is applied in x direction. Vertical nodal loads of 15 kN (equivalent to 10 MPa pressure over the tab surface) are applied on RP-3 and RP-4, tied to the tabs external surfaces, representing the gripping force. By means of this set of restrictions in the form of equations, the directionality of the load is guaranteed and the introduction of loads and displacements is simplified.

The results of the different approach in terms of computational cost are collected in Table 3.10. Regarding the different approaches applied to the Hashin's damage model, it is concluded that the evolution observed when using the S8R element or the single through thickness SC8R is oversimplifying the evolution of damage in the specimen. In other words, the constitutive behaviour and the apparent response of the laminate for these models is similar to the case of the full coupon modelled with one element representing each ply in thickness, but geometric effects such stress

3.3. NUMERICAL MODELLING OF THE NON-LINEAR RESPONSE OF ANGLE-PLY LAMINATES UNDER UNIAXIAL LOADING



Figure 3.28: Tabbed coupon model applied on simulations. Red and blue faces represent the tied to the reference points, corresponding in colour, where displacement BCs and gripping loads are applied. Representation adapted from [193].

concentrations and edge effects are obviated in both simpler models. Then, the technique applied for the rest of simulations concerning the Hashin’s damage model are performed with the SC8R including one element per ply through thickness (Fig. 3.27b). The comparison in terms of computation time with the Ladevèze’s model reveal a much higher cost for the latter, mainly due to a more difficult convergence of the results as damage and plasticity are simultaneously computed.

Additionally, the use of cohesive interfaces between the layers was also analysed, seeking to model the possible delamination due to interlaminar shear stresses. The idea of allowing decohesion of plies was believed to release the shear strain of differently oriented plies, in order to allow the reorientation of the lamina. However, debonding started at the specimen edges in the vicinity of the end-tabs, as a result of edge effects and geometric concentration, but progression of this debonding was unstable. For this reason, these results have not been included in this document. Furthermore, experimental evidences prove that delamination in tensile tested angle-ply laminates is related only to the final failure of the laminate, after matrix cracking dominate the stiffness degradation of the material [25, 26, 43].

Table 3.10: Comparison of different approaches for meshing. Same scenario is tested: uniaxial tensile $[\pm 45]_{2S}$ coupon with 2.5 mm element size (in plane) under 2.5 mm applied displacement. Total number of nodes and DOFs are included. All simulations were run in an eight core Intel I7-7700 processor with 16 Gb PC4-17000 RAM.

	Shell-2D S8R	Hashin		Ladevèze
		Continuum shell SC8R (1 through thickness)	Continuum shell SC8R (1 per ply thickness)	Solid CS8R
CPU time (s)	97	146	922	3546
Nodes	2106	2106	17468	17468
Variables	6318	6318	52400	52400

Finally, the ε_{xx} strain contours obtained numerically (with Hashin's *PDM*) and experimentally at same load level for the uniaxial tensile tested $[\pm 45]_{2S}$ laminate are shown in Fig. 3.29. The three well distinguished stages are represented, and the agreement between experimental and numerical results is again well illustrated. Please note that undamaged regions (in blue) are corresponding to the tabbed sections. In the case of experimental observations, the map is limited to the Region of Interest *ROI* that can be recorded by the assembly of the cameras of the *DIC* system to the triaxial testing machine. The second image displays how there is an offset of the maps, since the necking predicted by the Hashin's model in the midspan of the specimen occurs experimentally closer to the concentrations near the edge of the end-tabs. Fig. 3.30 shows an image taken by one of the cameras of the *DIC* system just after failure of the laminate where this offset of the damage accumulation is represented by the off-centred fracture surface (at the top right of the image).

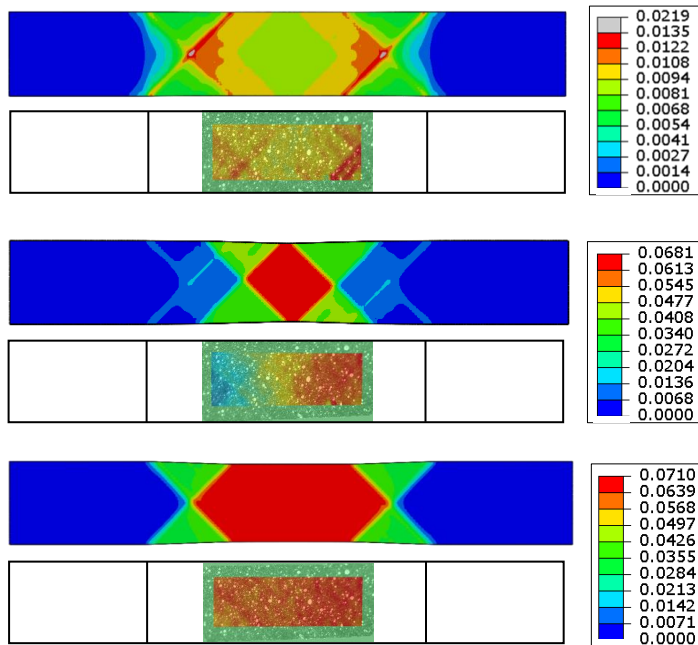


Figure 3.29: Comparison of ε_{xx} contour from Hashin's damage model (above) and experimental via *DIC*, for three different stages: (a) Prior to plateau, (b) plateau stage and (c) stiffening stage before failure.

Note that when strain-localization/necking is enabled due to the specimen geometry and boundary conditions, softening can obviously occur through the development of macroscopic shear bands. If the re-stiffening capability is sufficient to delocalize the deformation, the shear bands thicken and the sample re-hardens as a whole [198], as it is visualized in the bottom contours in Fig. 3.29.

3.3. NUMERICAL MODELLING OF THE NON-LINEAR RESPONSE OF ANGLE-PLY LAMINATES UNDER UNIAXIAL LOADING

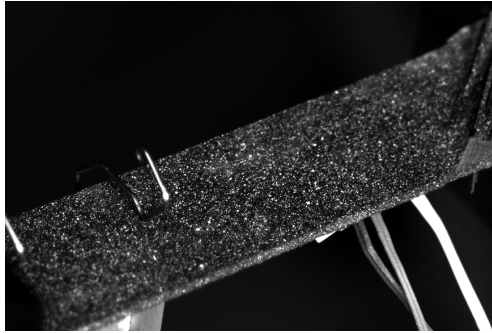


Figure 3.30: DIC photography of the $[\pm 45]_{2S}$ specimen after failure.

Chapter 4

Flexural response of angle-ply laminates

*“There is no such thing as a composite material.
There is an infinity of composite materials.
You can’t test an infinity of specimens.
The way out is calculation.”*

Zvi Hashin, 2012 Laureate of the Franklin Institute in Mechanical Engineering.

This chapter will detail the flexural response of laminates principally from an analytical approach, although validated with numerical simulations and experimental testing. The case of angle-ply laminates, mainly those formed by a combination of plies oriented at $\pm 45^\circ$ is emphasized. Two methodologies are applied in order to study the laminate apparently working as a beam or plate. In this way, a predominantly uniaxial state approach (at least in terms of dominant normal stress) and a multiaxial approach can be achieved, again investigating the presence of non-linear effects that may affect the response of the material, i.e. pseudo-ductility, as well as the appearance of different mechanisms of damage and failure in these materials, the effects of orthotropy and couplings.

4.1 Analytical framework

Based on the Euler-Bernoulli beam theory, the Eqs. 4.1 and 4.2 represents the maximum stress and strain produced in a simply supported beam with load applied in the midspan. From these expressions, it is direct to derive the flexural elastic modulus (Eq. 4.3).

$$\sigma_f = \frac{M_z b}{I_y 2} = \frac{3PL}{2bH^2} \quad (4.1)$$

$$\varepsilon_f = \frac{6wH}{L^2} \quad (4.2)$$

$$E_f = \frac{L^3 m}{4bH^3} \quad (4.3)$$

where m is the force-displacement ($P - w$) slope at the linear elastic region. Note these expressions are the ones applied in the standards for experimental characterization of the flexural stiffness in FRP, the ASTM D7264 [199]. At this point, an observation is to be made about the study of the structural behaviour of laminates. The CLPT precisely addresses the mechanical response of laminated plates, and emphasis should be placed on the concept of working with plates. The normative for flexural testing [199] focuses on characterizing the behaviour of monodimensional structures (beam type), with a length greater than the cross-sectional dimensions. However, the behaviour of a laminate must be approached from the mechanics of plates, due to its orthotropy of properties and the frequent application of these materials in two-dimensional structures, as explained in the introductory chapter of this document.

Besides, the use of E_f in the analysis of composite materials raises many simplifications frequently omitted. In the first place, this flexural modulus starts from an approach based on the hypothesis that the material has elastic moduli equal under tension and compression, which is not usually applicable in polymeric matrix materials, and even less in FRP composites [132, 133, 168]. This issue is further detailed in the next section.

On the other hand, it is known that certain stacking sequences, as in the case of $[\pm 45]_{NS}$, have bending-twisting couplings, which may vary depending on the number of layers. In other words, a $[\pm 45]_{NS}$ laminate in which the number of plies is modified present different values of experimentally measured flexural modulus [184, 200]. This approach is debatable as we are assuming that a property that in principle is associated with the material differs simply by changing the number of layers.

Moreover, this can be taken to another extreme, which is to vary the dimensions of the specimen's geometry. When analysing thicker beams, the value of E_f increases (even in the range of slender beams, as thicker beams will require a correction due to shear). Therefore different values for the flexural modulus are measured, which is contradictory to the concept of modulus as a material property independent of

geometry.

In order to bring to light the importance of correctly addressing the flexural behaviour of laminates, an analysis of the bending response of laminated plates has been performed. Considering equilibrium in a plate subjected to transverse distributed load $p(x, y)$ and specifying for the case of angle-ply symmetrical lay-ups, the governing differential equation (Eq. 4.4) is obtained [166].

$$D_{11}\partial_{xxxx}w + 4D_{16}\partial_{xxxy}w + 2(D_{12} + 2D_{66})\partial_{xyyy}w + 4D_{26}\partial_{xyyy}w + D_{22}\partial_{yyyy}w = p(x, y) \quad (4.4)$$

where e.g. $\delta_{xxxy}w$ symbolises abbreviated notation for $\frac{\partial^4 w}{\partial x^3 \partial y}$, and w is the displacement perpendicular to the laminate plane. The appearance of D_{16} and D_{26} multiplied by cross partial derivatives makes impossible to obtain an analytical closed-form solution to the partial differential equations. Based on the previous equation, a flexural stiffness ratio (D_{ratio}) has been defined in Eq. 4.5, which relates the magnitude of the couplings (considering $D_{16} = D_{26}$) with the primary bending stiffnesses.

$$D_{ratio} = \frac{D_{16}}{D_{11} + D_{22} + 4 \cdot D_{66} + 2 \cdot D_{12}} \quad (4.5)$$

Then, it is necessary to define a laminate configuration referenced in literature, the *specialy orthotropic laminated plates*. According to the definition of [165, 166], these are laminates in which only the terms $A_{11}, A_{12}, A_{22}, A_{66}, D_{11}, D_{12}, D_{22}$ and D_{66} are non-zero. In other words, these are laminates with neither bending-torsional couplings nor shear-extensional. Although the formulation developed by [166] for these specific laminates was originally intended for cross-ply sequences, it is possible to obtain the characteristics of these with angle-ply laminates with specific distributions of alternating layers. These laminates are hereafter referenced as *specialy orthotropic angle-ply laminate* (SOAPL). Based on what is defined above, the mathematical requirements to define these laminates are shown in Eq. 4.6. Note that the orthotropic behaviour of the ply implies shear-extensional couplings are null in material directions ($Q_{16} = Q_{26} = 0$).

$$\begin{aligned}
A_{16} &= \sum_{k=1}^N \bar{Q}_{16k} (z_k - z_{k-1}) = 0 \\
D_{16} &= \sum_{k=1}^N \bar{Q}_{16k} (z_k^3 - z_{k-1}^3) = 0 \\
A_{66} &= \sum_{k=1}^N \bar{Q}_{66k} (z_k - z_{k-1}) = 0 \\
D_{66} &= \sum_{k=1}^N \bar{Q}_{66k} (z_k^3 - z_{k-1}^3) = 0
\end{aligned} \tag{4.6}$$

Due to the symmetry of the stiffness matrices, the rest of the terms involved in this approach (A_{26} , D_{26} , A_{62} , D_{62}) are also null if the above conditions are met. As an example of this specific laminate configuration we find the sequence $[-45/+45_2/-45/+45/-45_2/+45]_S$. This stacking sequence will be the reference for the calculations and simulations performed from now on that involve the [SOAPL](#).

Specially orthotropic laminates are interesting because of the simplification of the calculations they provide having $D_{16} = D_{26} = 0$. However this does not imply that bending-twisting or extensional-shear couplings are not of interest in certain structures, for example airplane wings or wind turbine blades, in order to optimize the aeroelasticity of these structures [201, 202]. An interesting study developing the full space of laminates composed of 0° , 90° , $+45^\circ$ and -45° oriented plies with all possible extension-shear and/or bending-twisting coupling was developed in a series of articles by York et al. [203, 204].

Therefore, a closed solution of coupling effects in bending of laminated composites is limited to specially orthotropic laminates (ruled by the Eq. 4.7) based on the theory proposed in [166].

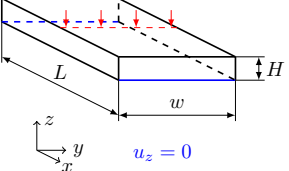
$$D_{11} \partial_{xxx} w + 2(D_{12} + 2D_{66}) \partial_{xyy} w + D_{22} \partial_{yyy} w = p(x, y) \tag{4.7}$$

The objective of this section is to understand how it is possible to correct the value of the flexural modulus defined in a traditional way to isolate the effect of bending-twisting couplings.

Static linear numerical simulations have been performed in order to validate the analytical expressions. The geometry described in Table 4.1 is modelled in Abaqus/Standard with S8R shell elements (eight nodes, reduced integration), in which the different laminate sequences are defined internally to the element, by utilising the *Composite Layup* module. Regarding the material model, tensile properties of the M21E/IMA-12K lamina (Table 3.1) have been utilised to define an elastic orthotropic ply material model. For each of the three geometries described at the right part of

the Table 4.1, the four laminate sequences have been modelled, resulting in a total of 12 different simulations.

Table 4.1: Simulations performed for flexural modulus estimation.

	Laminate	h (mm)	L (mm)	w (mm)	H (mm)
		$[\pm 45^\circ]_S$	0.25	300	5
	$[\pm 45^\circ]_{4S}$	0.0625	200	10	1
	$[\pm 45^\circ]_{12S}$	0.0208	30	10	1
	SOAPL	0.0625			

In these simulations, whose results are depicted in Fig. 4.1 and shown in Table 4.2, it is demonstrated how the flexural modulus (E_f), defined according to the Eq. 4.3, varies by geometric and lay-up sequence changes. Note that different colours in the figure represent geometric changes, while different ordinates are related to each of the four studied sequences. Besides, Fig. 4.1a represent the value of E_f in the vertical axis normalized with the case of the SOAPL laminate, in order to illustrate the reduction of stiffness regarding the laminate free of bending-twisting couplings.

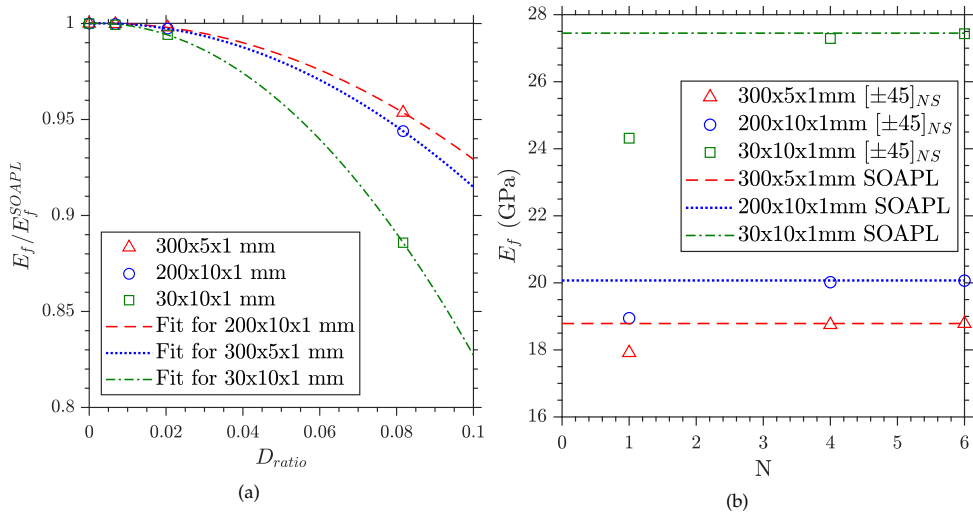


Figure 4.1: 3-point bending numerical results for E_f computation: (a) Normalized moduli vs D_{ratio} and (b) Flexural moduli vs N , with $[\pm 45]_{NS}$.

The fact that there is a change in the values of E_f is easily intelligible from the theoretical point of view, since we are trying to collect the behaviour of a laminated plate with an equation based on a beam model (Eq. 4.3), obviating the in-plane lamina effects due to the monodimensional approximation.

Table 4.2: Numerical results for flexural modulus estimation and bending stiffness values.

Laminate	D_{11} (Nm)	D_{16} (Nm)	D_{ratio}	$L \times w \times h$ (mm)	E_{flex} (GPa)
[$\pm 45^\circ$] _S	3.4924	1.9401	0.08169	300x5x1	17.915
				200x10x1	18.946
				30x10x1	24.315
[$\pm 45^\circ$] _{4S}	3.4924	0.485	0.02042	300x5x1	18.75
				200x10x1	20.019
				30x10x1	27.289
[$\pm 45^\circ$] _{12S}	3.4924	0.162	0.00681	300x5x1	18.783
				200x10x1	20.065
				30x10x1	27.432
SOAPL	3.4924	0	0	300x5x1	18.787
				200x10x1	20.071
				30x10x1	27.449

Although a closed solution has not been reached in this Thesis, the fittings shown in Fig. 4.1 illustrate how it is possible to estimate these effects based on the calculation of the flexural laminate stiffness matrix $[D]$ via CLPT.

Summarizing the ideas developed in this section, it is necessary to bear in mind that the definition of flexural modulus based on Eq. 4.3 for its application in laminates does not provide a value independent of the number of plies due to the behaviour of laminated plate. This becomes even more visible in the case of laminates with couplings, so the comparison between specimens with different configuration is not direct and requires a detailed analysis.

This idea was already postulated by Reddy [167], however the classical definition of flexural modulus is currently used as described in the bending testing standards for composites. This value would be the one that would approximate to a greater extent a slender specimen. Nevertheless, the reduction of span and the increase of cross-section apparently rise the value of flexural modulus, by moving away from the definition of laminated beam [167].

It should also be noted that the SOAPL laminate has the maximum flexural modulus (considering the definition of Eq. 4.3) for each specimen geometry. Although it has already been pointed out that the E_f can lead to confusion due to its dependence with the geometry, it can be certainly concluded that the SOAPL laminate leads to

reduce the displacement under a certain load in comparison with any other arrangement of alternating plies with the same orientation.

4.2 Pseudo-ductility in bending of $\pm 45^\circ$ symmetrical angle-ply laminates

4.2.1 Analysis of flexural response considering different tensile and compressive elastic moduli

Some authors have already defined analytical models to take into account the different tensile and compressive behaviour of composites [131–133,205]. These models are based on the modification of the classical theory of Navier-Bernoulli beams and on the CLPT. All these works agree on the importance of taking into account these differences in elastic properties when analysing the results of bending tests, applicable not only to FRP, but also to unreinforced polymers [206]. Insausti et al. [207] demonstrated how these analytical models could be validated through numerical methodologies, considering the deviation of the neutral fibre (NF) and the different elastic moduli.

The approach from Serna Moreno et al. [132,133], namely the homogenized section technique, is based on the Navier-Bernoulli bending theory, which application for a three-point bending test is gathered in Eqs. 4.1-4.3, but considering a different tensile (E_t) and compressive (E_c) elastic moduli of the material. This results in a deviation of the NF, and different tensile and compressive stresses and strain at the top and bottom faces, as schematized in Fig. 4.2. Imposing equilibrium of horizontal forces in the cross-section, it is possible to deduce an expression that relates both moduli with the thicknesses of the areas subjected to tension (t) and compression (c), as shown in Eq. 4.8.

$$\lambda = \frac{E_c}{E_t} = \left(\frac{t}{c}\right)^2 \quad (4.8)$$

In order to determine the distribution of stresses in the cross-section of the specimen, which we assume rectangular of width b and thickness H , we start from the hypothesis of assigning a material behaviour throughout the section equal to the tensile elastic modulus E_t , hence the denomination of homogenized section. By assigning the same response, the balance of internal forces is maintained by modifying

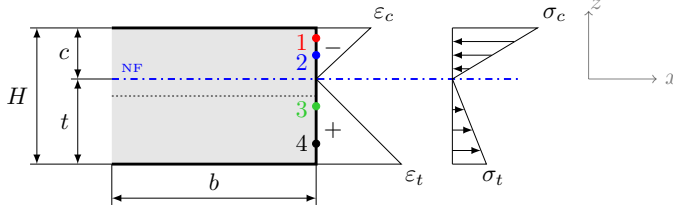


Figure 4.2: ε_{xx} and σ_{xx} profiles caused by bending moment on a material with different tensile and compressive elastic moduli. Reproduction based on [132].

the dimensions of the compressed region, specifically its width, which is now considered to be b' (see Fig. 4.3). The equilibrium is posed again, in this case by matching the forces of the compressed region before and after the modification, obtaining that $b' = b/\lambda$. Then, it is possible to define the second moment of area for the modified cross-section, which results in the Eq. 4.9.

$$I_y = \frac{b(t^3 + \lambda c^3)}{3\lambda} \quad (4.9)$$

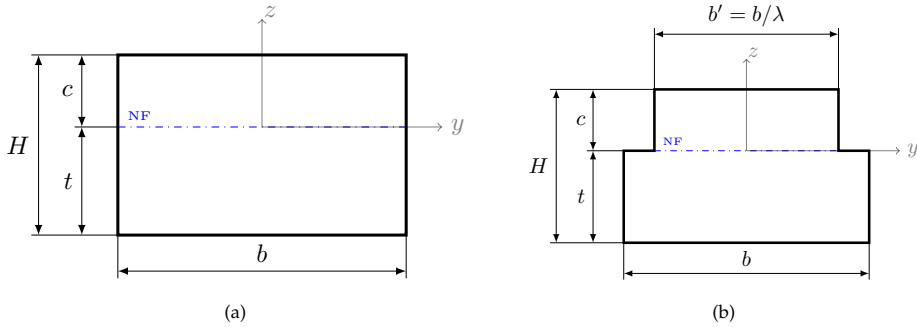


Figure 4.3: Schematization of the homogenised section technique: (a) original cross-section and (b) homogenised for $E = E_t$. Adapted from [168].

By applying the homogenised section inertia it is possible to define the maximum tensile and compressive stresses, which are summarized in the Eqs. 4.10 and 4.11.

$$\sigma_t = \frac{1}{\lambda} \frac{M_y}{I_y} t = \frac{3PL}{4bH^2} \frac{1 + \sqrt{\lambda}}{\sqrt{\lambda}} \quad (4.10)$$

$$\sigma_c = -\frac{M_y}{I_y} c = -\frac{3PL}{4bH^2} (1 + \sqrt{\lambda}) \quad (4.11)$$

It must be taken into account that the deviation of the neutral fibre also implies that the maximum interlaminar shear stress is offset by the same distance d , and then it must be calculated by means of the Eq. 4.12 [132].

$$\tau_{xz} = \begin{cases} \frac{3P}{4bH} \left[1 - \left(\frac{z}{c} \right)^2 \right] & \text{for } 0 \leq z \leq c \\ \frac{3P}{4bH} \left[1 - \left(\frac{z}{t} \right)^2 \right] & \text{for } -t \leq z \leq 0 \end{cases} \quad (4.12)$$

After obtaining the expressions for the computation of maxima laminate stresses it is possible to propose a criterion that includes the specimen failure mode according to its slenderness, or more specifically its thickness. This will allow us to estimate the number of layers which lead to a failure due to intralaminar opening at the neutral fibre or a breakage due to maximum normal stresses. Although the deviation of the NF results in greater maximum compressive stress than tensile, the tensile strength of the material at 45° is small enough compared to that of compression so that the failure is firstly expected on the most tensioned face. Therefore, a criterion based on maximum stress is set out in Eq. 4.13, where the flexural failure represents the matrix tensile crack, while if the predominant stress is the interlaminar shear result in delamination or interlaminar shear opening.

$$\begin{aligned} \frac{H}{L} < \frac{S_{13}(1+\sqrt{n})}{S'_{45^\circ} \sqrt{\lambda}} & \text{ Flexural failure} \\ \frac{H}{L} > \frac{S_{13}(1+\sqrt{n})}{S'_{45^\circ} \sqrt{\lambda}} & \text{ Interlaminar shear failure} \end{aligned} \quad (4.13)$$

where S'_{45° is the tensile strength at 45° of the fibre direction.

Regarding the elastic linear analysis of the laminated plate by means of the CLPT considering the different tensile and compression response, the formulation described in Section 2.2.1 is modified considering that the reference plane corresponds to the NF deviated from the midplane and the in-plane stiffness matrix of the lamina is modified as it appears in Eq. 4.14. Therefore, through this technique it is possible to analyse simultaneously the response under tension and compression of the material when it is subjected to a bending moment.

$$[Q]_k = \begin{bmatrix} \frac{E_1^\chi}{1-\nu_{12}\nu_{21}} & \frac{\nu_{21}E_1^\chi}{1-\nu_{12}\nu_{21}} & 0 \\ \frac{\nu_{12}E_2^\chi}{1-\nu_{12}\nu_{21}} & \frac{E_2^\chi}{1-\nu_{12}\nu_{21}} & 0 \\ 0 & 0 & 2G_{12} \end{bmatrix} \quad \text{with } \chi = \begin{cases} t & \text{for } z < 0 \\ c & \text{for } z > 0 \end{cases} \quad (4.14)$$

Then it is proposed to apply this analysis to the flexural response of $\pm 45^\circ$ symmetrical laminates. In this way, the pseudo-ductile effects on a laminate subjected to tensile and compressive strains in different positions are investigated. Besides, the study of two laminates with similar linear responses allows analysing the effect of the increase in bending-twisting couplings due to ply blocking. The laminates chosen are $[\pm 45]_{6S}$ and $[+45_2 / -45_2]_{3S}$, so that it is possible to obtain specimens of the same thickness, but with apparent layer thickness duplicated (i.e. ply clustering).

4.2.2 Experimental bending characterization of pseudo-ductile effects on angle-ply laminates

The flexural response of these two laminates are studied by means of three-point bending tests, performed using the triaxial testing machine with a flexural fixture attached (Fig. 4.4a). The approximately $40 \times 10 \times 5.5$ mm cuboid specimens are simply supported on a 25 mm span and vertically loaded in the mid section under a constant quasi-static displacement rate of 0.3 mm/min.

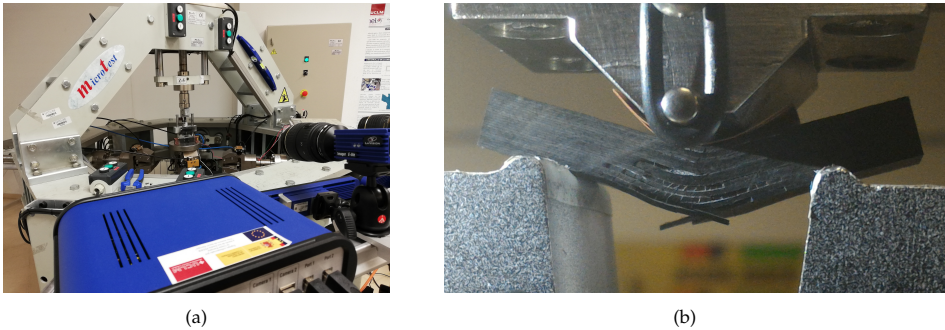


Figure 4.4: Images of the three-point bending test of ± 45 symmetric laminate: (a) Arrangement of DIC system and triaxial testing machine and (b) Detail of specimen during test, showing high damage accumulation due to matrix cracking and delaminations.

For both lay-ups, matrix microcracking and subsequent delamination are expected to be the mechanisms of damage initiation and propagation respectively (see Fig. 4.4b). However, the ply clustering is reflected in a double effective ply thickness and Linear Elastic Fracture Mechanics (LEFM) points that the energy necessary to propagate a crack via delamination is inversely proportional to the characteristic size of the crack. Therefore, configuration $[\pm 45]_{6S}$ is expected to require more energy to propagate the damage through delamination, as the effective ply thickness is inferior than the case of $[+45_2 / -45_2]_{3S}$ stacking sequence. This should be reflected in lower failure strain for the latter.

Fig. 4.5 depicts the strain distribution of the midspan cross-section obtained via

the measurement of the specimen side surface with DIC system during flexural testing. The deviation of the NF from the midplane is measured as the the position of transition from negative to positive strain at an intermediate load level of $P/b = 175$ N/mm (results are shown in Table 4.3), and then the strain distributions are corrected such as $z = 0$ corresponds to the NF. Note that Fig. 4.5 illustrates how the neutral fibre is further deviated with a higher load, as the most tensioned plies are damaged and therefore the NF rises to fulfil the force balance at the cross-section. Then, the values of t and c can be extrapolated from these plots. Note that for similar load levels (260 N/mm and 230 N/mm respectively), both laminates depict quite different strain profiles, as the $[\pm 45]_{6S}$ is still fitted by a linear regression, while $[+45_2 / -45_2]_{3S}$ is better fitted with a non-linear profile (a quadratic least square regression is proposed as example in Fig. 4.5b), which is related to the higher damage accumulation on the bottom plies for this lay-up, even at a slightly lower load level regarding the equivalent plot for the $[\pm 45]_{6S}$ laminate.

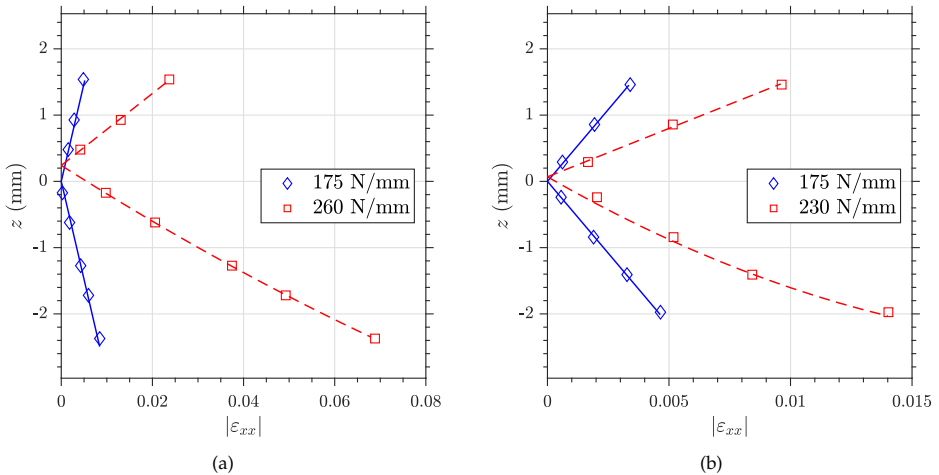


Figure 4.5: ε_{xx} distributions for the midspan cross-section in linear and non-linear stages: (a) $[\pm 45]_{6S}$ and (b) $[+45_2 / -45_2]_{3S}$ [168].

Table 4.3: Experimental observations and analytical predictions for the $[\pm 45]_{6S}$ and $[+45_2 / -45_2]_{3S}$ bending specimens [168].

Laminate	Experimental measurements		Proposed estimations via homogenised section technique		
	t (mm)	c (mm)	λ	$E'_{\pm 45^\circ}$ (GPa)	$E^c_{\pm 45^\circ}$ (GPa)
$[\pm 45]_{6S}$	2.97 ± 0.04	2.53 ± 0.04	1.37 ± 0.03	18.01 ± 1.13	24.95 ± 1.74
$[+45_2 / -45_2]_{3S}$	2.97 ± 0.01	2.53 ± 0.01	1.37 ± 0.02	18.61 ± 1.82	25.62 ± 2.30

Fig. 4.6 illustrates the stress-strain curves for both laminates at different z -positions

of the midspan cross-section, obtained thanks to the combination of the DIC strain distributions and the homogenised section technique. The stress-strain responses are plotted for four reference points, two of them placed on the tensile region and the other in the compressive region, as schematized in Fig. 4.2, in order to represent the state of differently loaded plies. Please note that stresses are calculated by means of expressions deriving from a linear elastic analysis (Eqs. 4.10 and 4.11 particularized for each z -position), so non-linear evolutions are included as approximated estimations.

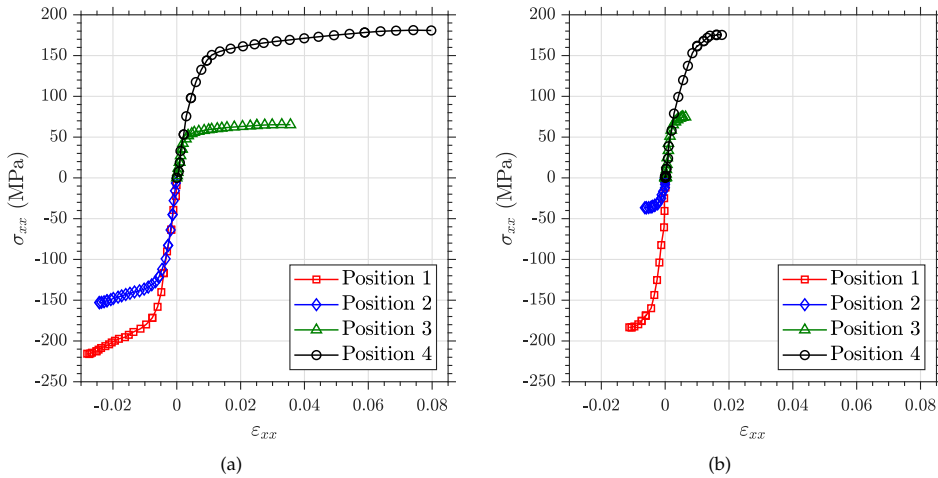


Figure 4.6: Stress strain response at four different through-thickness positions (defined at Fig. 4.2) at the midspan cross-section: (a) $[\pm 45]_{6S}$ and (b) $[+45_2 - 45_2]_{3S}$ [168].

Some conclusions are drawn from the observation of these figures. Firstly, both laminates present a similar elastic slope, as it is expected from the theoretical point of view, and they are in agreement with the $E_{\pm 45^\circ}^t$ and $E_{\pm 45^\circ}^c$ collected in Table 4.3. Secondly, different degrees of pseudo-ductility is observed depending on the vertical position, with the highest non-linearities achieved in the tensile region (i.e. the bottom face of the specimen following notation on Fig. 4.2). It is noteworthy the difference of permanent strains achieved in the different laminates, reflecting the highest damage accumulation capability of the $[\pm 45]_{6S}$ stacking configuration.

Moreover, the microscopic observations via Scanning Electron Microscopy (SEM) of the flexural tested specimens help to better illustrate the mechanisms involving damage initiation and propagation. The application of Eq. 4.13 leads to the inequality $0.22 < 0.88$ for the studied laminates, so flexural failure is expected in both lay-ups. The SEM images (Figs. 4.7a and 4.8a) clearly show how the initiation of the damage is produced due to tensile matrix cracking of the bottommost ply. Note that in the case of the $[+45_2 - 45_2]_{3S}$ sequence, the ply blocking helps crack propagation between laminae with same orientation of fibres, while with regard to the $[\pm 45]_{6S}$

is observed in Fig. 4.7b that crack needs to move through the interlaminar surface, therefore requiring a higher energy for damage evolution, not only due to delamination as posed above, but also because crack migration in the interfaces of adjacent plies with change of fibre orientation. This mechanism of crack migration additionally promotes the delamination of all the plies in the $[+45 - 45]_{6S}$, while the other analysed sequence present most delaminations between each two layers (Fig. 4.8b).

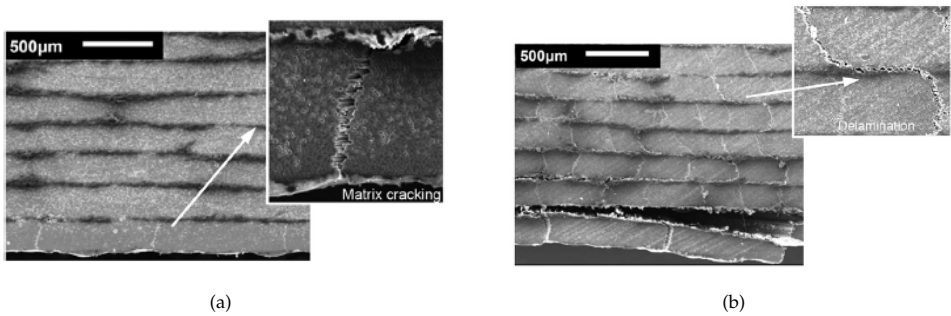


Figure 4.7: SEM fractographies for $[\pm 45]_{6S}$ laminate: (a) damage initiation and (b) damage evolution [168].

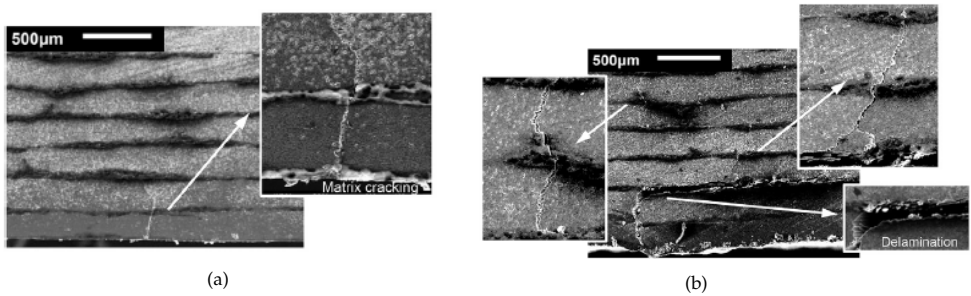


Figure 4.8: SEM fractographies for $[+45_2 - 45_2]_{3S}$ laminate: (a) damage initiation and (b) damage evolution [168].

The observation of the bottom face of both laminates helps also to assess the degree of pseudo-ductility achieved, in this case related to the permanent strain after failure and the corresponding fibre reorientation. An estimation of the angle of the fibre at the tensile cracked surface of the specimens is shown in Fig. 4.9. This optical observation agrees with the strain values measured over this face by means of a strain gauge rosette, whose results are plotted in Fig. 4.10. The much lower ϵ_{yy} measured for $[+45_2 - 45_2]_{3S}$ matches with the conclusion of a much smaller fibre permanent reorientation with regard to the $[\pm 45]_{6S}$ laminate.

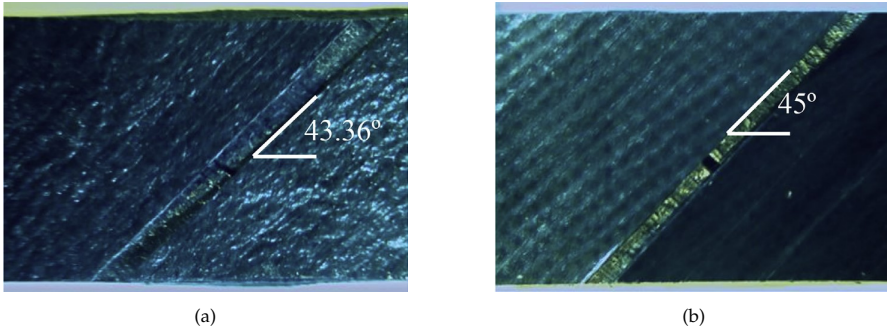


Figure 4.9: Matrix crack angles reflecting permanent deformation at the inferior ply: (a) $[+45 - 45]_{6S}$ and (b) $[+45_2 - 45_2]_{3S}$ [168].

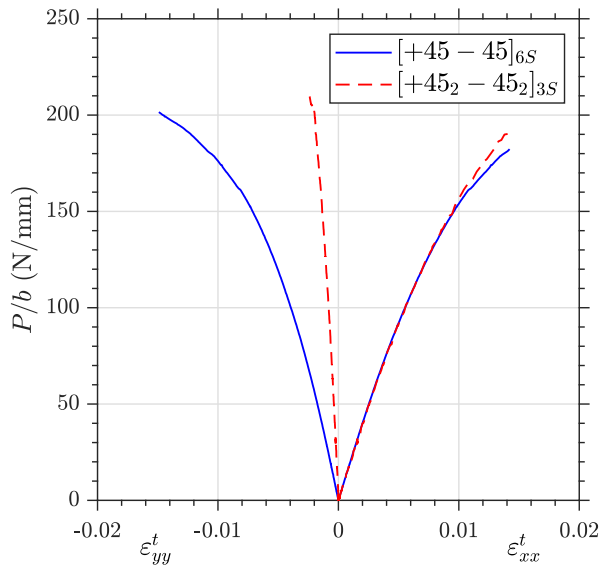


Figure 4.10: Evolution of P/b against strain gauge measurements in x and y directions [168].

4.2.3 Optimization of stacking sequences

Finally, all the previous analysis and discussion of results has shown how it is possible to obtain different degrees of pseudo-ductile effects in laminates with a similar elastic response, but that nevertheless pose different magnitudes of membrane-flexural couplings, where the laminate obtained by ply blocking entails a greater B_{16}/B_{11} ratio, which implies a greater development of in-plane shear strains, and therefore seems to lead to a less ductile behaviour.

An optimization of the symmetric lamination sequence with layers oriented to $\pm 45^\circ$ is proposed. The optimization seeks to minimize the effects of coupling, which are to be measured according to the ratios D_{16}/D_{11} and B_{16}/B_{11} (please take into account that for laminates with layers at $\pm 45^\circ$, it is true that the terms 16 and 26 are equal for the stiffness submatrices A , B and D). In addition, the optimization includes a term referring to the laminate total thickness, in order to avoid too thick laminates. In this way, a cost function to be minimized is defined in Eq. 4.15. Details on the implementation of the mathematical problem are further detailed in [168].

$$\text{Cost} = \left| \frac{D_{16}}{D_{11}} \right|_{scaled} + \left| \frac{B_{16}}{B_{11}} \right|_{scaled} + 0.1H_{scaled} \quad (4.15)$$

The result of this optimization yields several results, in which we focus on the first two minima. Specifically, the first minimum is the laminate $[-45/+45_2/-45/+45/-45_2/+45]_S$ and the second is $[-45+45_2-45+45]_S$. Note that the condition of balanced laminate was not obligated in the algorithm, so that the last laminate results unbalanced.

Chapter 5

Assessment of laminates under biaxial loading

*“Computer simulations are really just virtual time machines . . .
Computer modeling is a kind of time machine,
and it lets us see the future . . . perhaps even
billions of years into the future.”*

Edmond Kirsch (fictitious), *Origin*, Dan Brown.

The development of experimental tests together with analytical and numerical models in the previous chapters has resulted in a detailed knowledge of the response and failure under predominantly uniaxial loading on different laminate sequences, mainly angle-ply. This background allows to analyse now with greater understanding the biaxial tests on cruciform specimens performed in this chapter.

In the first place, the **CLPT** is particularized for biaxial testing, in order to permit foreseeing the apparent elastic response obtained in the different trials, also providing analytical values which serve as validation of the results obtained numerically and experimentally. Different loading states on diverse laminates are studied from a combination of the last two approaches, starting with the **T-T** loading cases in several ratios and on laminates with different degrees of non-linearity. Subsequently, the analysis of biaxial tests under compressive loads in one or both directions is proposed, for which a buckling study on laminated plates is developed beforehand. The outcome of this study entails modifications to the test method which allow postponing the instability of the cruciform specimen when submitted to compressive loads. Subsequently, the main results of **T-C** and **C-C** tests on symmetrical $\pm 45^\circ$ laminates are shown. The examination of various loading ratios in different quadrants of the $\sigma_{xx} - \sigma_{yy}$ stress space permit the evaluation of failure theories.

5.1 General aspects of the analysis of cruciform biaxial testing

This section is meant to describe the main characteristics common for all the biaxial experimental and numerical tests performed in this chapter.

5.1.1 Design and preparation of cruciform specimens

Starting from the experimental characterization, the specimen's design follows the geometry used in previous studies [77, 80, 208]. Adaptation of the dimensions is required depending on specific tests, that is, when testing force ratios different to 1/1 (the notation to designate biaxial tests hereinafter follows the ratio of applied forces P_x^a / P_y^a) a change of the arms' width is proposed in order to maintain a lower level of stresses in the arms. First of all it is necessary to define the different characteristics of the T-T tests carried out on the $[\pm 45]_S$ laminate. The work of Serna Moreno and López Cela [77] concluded the need to adapt specimen geometry to the applied load ratio to avoid premature arm failure. Thus, in Fig. 5.1 the three geometries analysed for this laminate are collected. Furthermore, the length of the arms in the tensile loaded directions is chosen to be as long as the manufacturing process and the testing machine allow in order to avoid undesired stress concentrations close to the biaxially loaded zone, while for the compressive directions the arms' length must be reduced to prevent them from buckling.

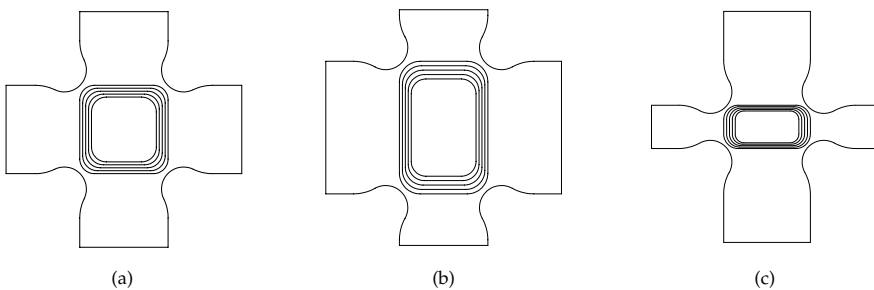


Figure 5.1: Geometries of central zone of biaxial cruciform specimens (same scale): (a) Geometry A, (b) Geometry B and (c) Geometry C.

In order to obtain the geometry of the cruciform biaxial specimen (Fig. 5.2), a computer numerical control (CNC) milling is performed over a square laminated plate. The accuracy of this process is critical in order to obtain the desired thickness reduction of the biaxially loaded zone, without introducing damage to the specimen. After machining, specimens are measured to check that thickness of the central

gauge zone correspond to the theoretical laminate thickness. Regarding the degree of thickness reduction, some preliminary linear elastic simulations were performed in order to assess the minimum thickness ratio (defined as arm to centre thickness ratio) necessary to obtain an adequate failure mode. Nevertheless, stress concentrations in the **T-T** and **C-C** ratios close to 1/1 are unavoidable. Additionally, an analysis of the effect of thickness ratio on compressive loaded specimens is to be described in Section 5.4.3. Moreover, note that thicknesses ratio (t_r) must be an integer (N) in order to obtain arm and centre laminates consisting on stacking sequences with the form $[]_{NS}$, which is reduced to the minimum stacking sequence ($[]_S$) at the gauge zone.

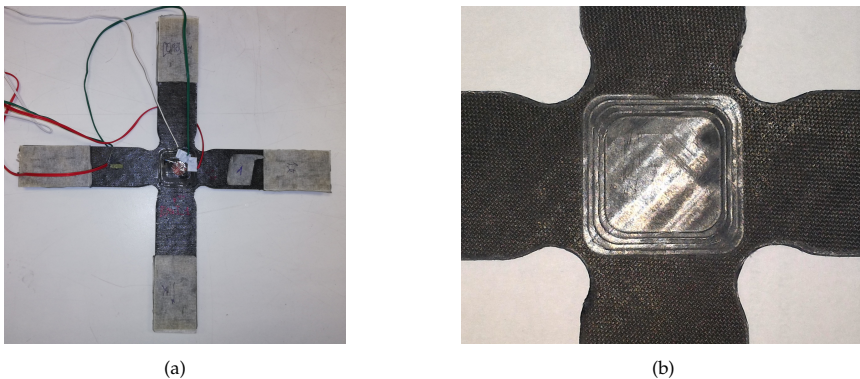


Figure 5.2: Biaxial **T-T** geometry *A* specimens: (a) $[0/90]$ instrumented and tabbed specimen and (b) Detail of the tapered gauge zone for a $[\pm 45]$.

After machining and dimensioning, 3 mm thick **GFRP** tabs are glued to the end of the arms (see Fig. 5.3), following the same procedure described in the uniaxial characterization. The width of the tabs is equal to the arms' width, while the length is chosen to be 50 mm, corresponding to the maximum gripping length of the pneumatic actuators.

Regarding the testing procedures, there is a general tendency to control the tests based on the application of quasi-static loads by means of setting the applied displacement rate δ^a . This generally implies a safer control of the test and helps maintaining a constant strain rate when stiffness degradation appears. However, in the biaxial tests carried out in this Thesis, the control of applied force rate \dot{P}^a is utilised due to the interest in maintaining the proposed biaxial stress ratio. After different trials, it was proven that the displacement control may bring difficulties to ensure the ratio, taking into account the requirement of synchronization among four actuators acting simultaneously on a specimen in which, depending on the stacking sequence, severe changes in the local material stiffness arise. Fig. 5.4 shows how a load ratio applied in perpendicular directions is maintained with a maximum deviation of 2

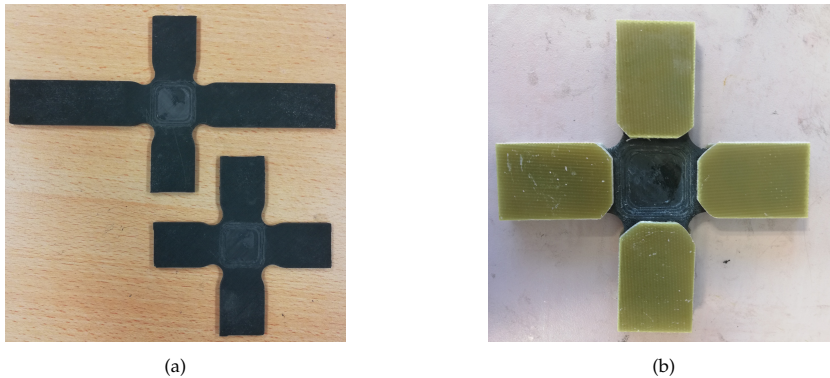


Figure 5.3: $\pm 45^\circ$ biaxial cruciform specimens: (a) T-C (upper) and C-C (bottom) specimens after CNC milling and (b) C-C specimen after tab gluing.

%, which is generally given at low loads due to the effects of material loading (observed in other kind of testing and usually named as “toe region”). This aspect is critical when it comes to obtaining representative results of the sought multiaxial ratio. The magnitude of the loading rates are adapted to the strength of the laminate, taking as reference a load rate of 20 N/s for the $\pm 45^\circ$ laminate under tensile loading.

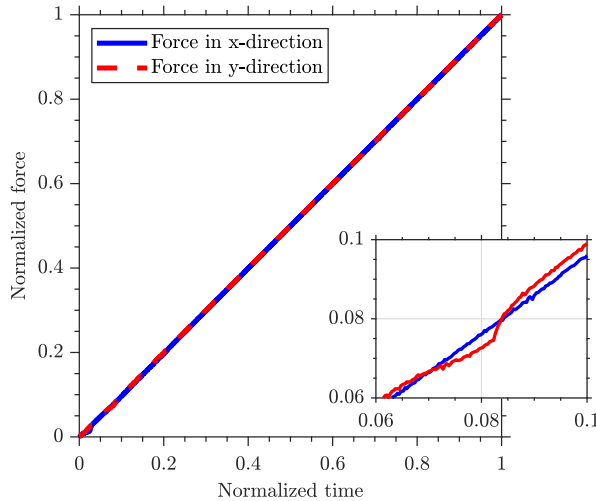


Figure 5.4: Plot of force in perpendicular direction during $[0, 90]_s$ biaxial tensile-tensile test, zooming the maximum difference of forces.

All the methods of instrumentation described in Chapter 2 have been applied to biaxial tests, whenever the assembly of the test and the dimensions of the specimen allow it, as shown in Fig. 5.5a. All the tests carried out involve the simultaneous movement of the four actuators in the horizontal plane of the triaxial machine equipped with 50 kN force transducers. The biaxial specimen (see Fig. 5.5b) is

painted with a black and white speckle pattern on the upper face for the application of the DIC technique on the surface that is observable from the cameras. Besides, a strain gauge rosette is placed on the central point of the bottom face of the specimen, consisting on three strain gauges oriented at 0° , 45° and 90° with respect to one of the loading axes. Moreover, uniaxial gauge and axial extensometer are placed in perpendicular arms of the cruciform specimen. In this way, measures can be collected in the centre (variables that are named with the *centre* superscript), as well as measurements on the arms of the specimen (called with the *arm* superscript).

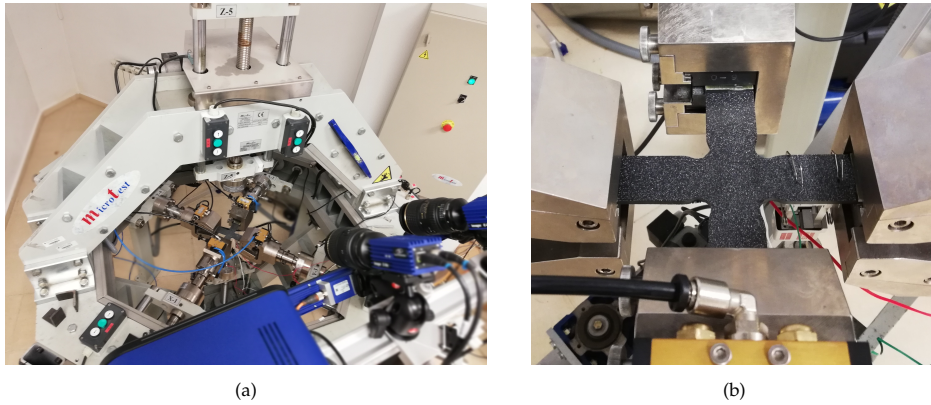


Figure 5.5: Testing facility during the realization of a T-T biaxial test: (a) Top-view showing DIC system and (b) detail of the instrumented specimen during testing.

Finally, in order to demonstrate the correct alignment and synchronization of the testing machine, Fig. 5.6 illustrates an example of strain measurements recorded by the two acquisition systems applied to biaxial testing. Note that the measurements only differ after a strain level of 2% because of the saturation of the strain gauge recorder. A practically identical data record is shown by both techniques, even in an intricate test due to the simultaneous presence of tensile and compressive strains, therefore validating the applicability of both strain acquisition methodologies.

5.1.2 Numerical modelling of non-linear effects on biaxial tests

Regarding the numerical model applied to the simulation of the biaxial tests, the discussion of the element type for the application of the Hashin's damage models (Section 3.3.4) led to the conclusion of accurate and low computational cost for the modelling with a single SC8R element through thickness. Note that this methodology also simplifies the definition of the model geometry, as it is not required to model each lamina. The stepped transition of the tapered central zone is modelled as the actual specimen, with the same ply thickness reduction for each one of the

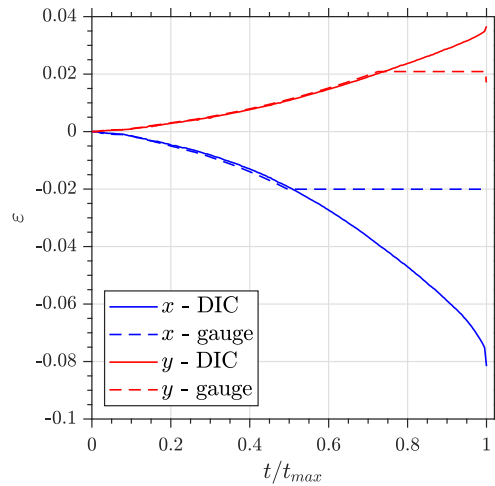


Figure 5.6: Comparison of strain measurement in $[\pm 56.3]_s$ biaxial tensile-tensile test.

steps (Fig. 5.7).

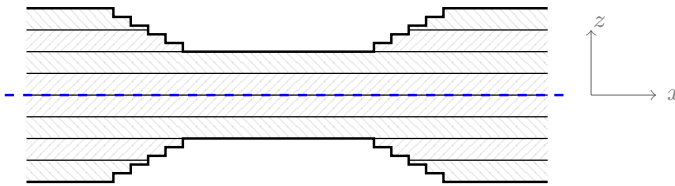


Figure 5.7: Schematization of the thickness reduction in the biaxial gauge zone, exemplifying a $[\pm 45]_{2s}$ reduced to $[\pm 45]_s$.

The same length of arms has been modelled in all the simulations, since the apparent behaviour of the specimen is not affected providing that a minimum length of the arms is considered in order to allow the correct development of the stresses flow between the predominately uniaxially and biaxially loaded regions. As a large geometry (only reduced thanks to the symmetry with respect to midplane laminate) on which a non-linear material model is analysed, the computational cost of the simulation is reduced by avoiding the modelling of end-tabs, since there is no experimental evidence of an effect of tabs on the response or failure of the cruciform specimen. Critical concentrations are found in the thickness-reduced area and in the filleted corners, however a uniform element size in the $x - y$ plane has been chosen for the entire model (as shown in Fig. 5.8), in order to avoid inconsistencies on the energy release rates of different elements.

Regarding the implementation of the Hashin's PDM, the material parameters collected in Tables 3.1, 3.5 and 3.7 are applied to the simulation, considering the

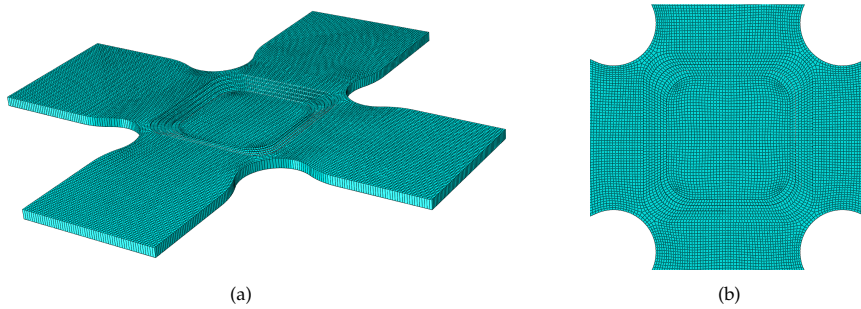


Figure 5.8: Finite element mesh for the T-C biaxial test simulation (with one SC8R element through thickness) for 0.5 mm element size: (a) 3D representation of the full mesh and (b) 2D detail of the gauge zone.

laminate to be tested. The tensile or compressive properties are chosen for the T-T and C-C respectively, while the T-C test is modelled using the tensile elastic properties, while a combination of the tensile and compressive parameters for the Hashin's PDM is utilised.

To conclude the description exposed in this section, Table 5.1 includes a list of all the biaxial tests analysed experimentally and numerically throughout this chapter. In the following sections these tests will be further detailed, referring them in the manner shown in the second column of the table. Please consider that the difficulty and cost associated to obtain the biaxial specimens make it necessary to focus the study on few particular ratios, from which the response for other loading ratios not experimentally tested is extrapolated by numerical and analytical modelling.

Table 5.1: Description of the totality of biaxially tested loading ratios, specimen geometries and laminates. It includes the applied forces and the resultant elastic stress and strain ratios obtained in the biaxially loaded zone.

Geometry	Designation	Laminate		P_x^a / P_y^a	$\sigma_{xx}^c / \sigma_{yy}^c$	$\epsilon_{xx}^c / \epsilon_{yy}^c$
		Arm	Centre			
A, T-T	T-T-A45-1	$[\pm 45]_{2S}$	$[\pm 45]_S$	1/1	1/1	1/1
	T-T-A45-1.2			1/1.2	1/1.36	-1/2.77
B	T-T-B45-1.5	$[\pm 45]_{2S}$	$[\pm 45]_S$	1.6/1	2.26/1	1.76/-1
C	T-T-C45-0.5	$[\pm 45]_{2S}$	$[\pm 45]_S$	0.4/1	0.38/1	-0.61/1
A, T-C	T-C-45-1	$[\pm 45]_{4S}$	$[\pm 45]_S$	1/-1	1/-1	1/-1
A, C-C	C-C-45-1	$[\pm 45]_{4S}$	$[\pm 45]_S$	-1/-1	-1/-1	-1/-1
A, T-T	T-T-090-1	$[0/90]_{4S}$	$[0/90]_S$	1/1	1/1	1/1
B	T-T-56-1			1.6/1	3.63/1	2.75/-1
	T-T-56-2	$[\pm 56.3]_{2S}$	$[\pm 56.3]_S$	1/6	-1/5.55	-1/0.63
	T-T-56-3			1/8	-1/4.55	-1/0.61

5.1.3 Numerical elastic estimation of stresses in biaxial zone

One of the issues concerning the application the biaxial test with cruciform specimens is the measurement of the stress state in the biaxially loaded area. Different techniques have been proposed in literature either directly applying a constitutive material model to the experimentally measured biaxial strains, or a correction parameter is combined with the applied load, which should include the effect of the geometry and material of the specimen [77, 80]. Other authors defined a similar parameter, namely *bypass correction factor*, basing their definition in the fact that not all the applied force is contributing to the stress on the central zone [92].

Both techniques involve a similar limitation. If we choose to consider the constitutive behaviour of the material known, it may be correct in the elastic region, but it is difficult to foresee with certainty that a non-linear model adequately fits the response of the material under biaxial loads. If we opt for applying a coefficient over the applied force, a numerical simulation, usually using the elastic case, is required, then limiting again the range of application of this factor. In this Thesis the last methodology is applied, following the description in the works from Serna Moreno et al. [77, 80], in which by means of elastic linear simulations of the cruciform specimen subjected to the specific state applied in each test, a factor ψ_i is determined. Then, ψ_i relates the force applied at the end of the arm to the force in the central section for each loading direction (x and y), so that from this parameter it is possible to estimate the stress in the central gauge section following the Eq. 5.1.

$$\sigma_{ii}^{centre} = \frac{P_i^a}{\psi_i A_i} \quad (5.1)$$

It is necessary to emphasize that this factor must be calculated for each material, stacking sequence, load ratio and geometry of the cruciform specimen tested, and that it is only valid to estimate the stress as long as the specimen maintains the linear elastic response globally. It will be shown in the following sections how this factor collects accurately the linear state response by comparing the stress-strain state obtained experimentally with the analytical predictions from the CLPT. However, ψ_i generally overestimates the stress at the gauge zone when non-linearities appear at some point in the specimen. For this reason, the estimation of stresses in the biaxial gauge zone is limited to the elastic range in the following figures, and they are accompanied with the applied force evolution to describe the complete response up to failure.

5.2 Elastic analytical approach to biaxial stress

As mentioned in the state of the art about biaxial testing, literature agrees with a *strengthening effect* of the materials when these are under some **T-T** and **C-C** biaxial stress states regarding the uniaxial case. The analysis of the stress tensors allows a theoretical discussion about the strength of the material under multiaxial loading states, taking into account that the failure is promoted by the deviatoric part of the stress tensor. In the case of biaxial loads of the same module and sign, the volumetric part of the tensor increases and consequently the deviatoric decreases, which explains the fact that the **T-T** and **C-C** biaxial tests lead to greater strength values. On the contrary the **T-C** describes a more premature failure related to a higher deviatoric stress tensor.

Ergo a stiffening effect of the **T-T** and **C-C** biaxial state may be also expected, as the multiaxial loading is related to the stiffness of the laminated plate in both directions. This can be easily verified in an analytical way, determining the stress-strain relation under a biaxial state. Let us propose a simple case, that of isotropic material with same tensile and compressive moduli due to the simplicity of its constitutive relations (Eq. 5.2). Assuming the plane stress case, the expression is simplified to Eq. 5.3.

$$\begin{bmatrix} \varepsilon_{xx} \\ \varepsilon_{yy} \\ \varepsilon_{zz} \\ \gamma_{xy} \\ \gamma_{xz} \\ \gamma_{yz} \end{bmatrix} = \frac{1}{E} \begin{bmatrix} 1 & -\nu & -\nu & 0 & 0 & 0 \\ -\nu & 1 & -\nu & 0 & 0 & 0 \\ -\nu & -\nu & 1 & 0 & 0 & 0 \\ 0 & 0 & 0 & 2+2\nu & 0 & 0 \\ 0 & 0 & 0 & 0 & 2+2\nu & 0 \\ 0 & 0 & 0 & 0 & 0 & 2+2\nu \end{bmatrix} \begin{bmatrix} \sigma_{xx} \\ \sigma_{yy} \\ \sigma_{zz} \\ \tau_{xy} \\ \tau_{xz} \\ \tau_{yz} \end{bmatrix} \quad (5.2)$$

$$\begin{bmatrix} \varepsilon_{xx} \\ \varepsilon_{yy} \\ \varepsilon_{zz} \\ \gamma_{xy} \end{bmatrix} = \frac{1}{E} \begin{bmatrix} 1 & -\nu & 0 \\ -\nu & 1 & 0 \\ -\nu & -\nu & 0 \\ 0 & 0 & 2+2\nu \end{bmatrix} \begin{bmatrix} \sigma_{xx} \\ \sigma_{yy} \\ \tau_{xy} \end{bmatrix} \quad (5.3)$$

If we assume now the case of pure **T-T** biaxial stress (equivalent to the pure **C-C** state, i.e. $\sigma_{xx} = \sigma_{yy} = \sigma_b$), the tensorial expression is simplified to the equation 5.4. Note that isotropy of the material implies also that $\varepsilon_{xx} = \varepsilon_{yy} = \varepsilon_b$.

$$\varepsilon_b = \frac{\sigma_b}{E}(1 - \nu) \quad (5.4)$$

A linear relation between biaxial stress and strain is obtained, and the constant that relates these two parameters hereafter is called *apparent biaxial elastic modulus* (E_{biax}), whose value for the case of **T-T** and **C-C** biaxial state can be computed using the Eq. 5.5.

$$E_{biax}^{T-T} = E_{biax}^{C-C} = \frac{E}{1 - \nu} \quad (5.5)$$

Proceeding similarly for the case of pure **T-C** biaxial stress ($\sigma_b = \sigma_{xx} = -\sigma_{yy}$), a similar expression relating the biaxial stress-strain is obtained (Eq. 5.6).

$$E_{biax}^{T-C} = \frac{E}{1 + \nu} = 2G \quad (5.6)$$

Analysing both biaxial moduli, it is verified that in the case of loads in the same direction, an apparent stiffening of the material is obtained for a positive Poisson's ratio. On the other hand, the apparent stiffness under **T-C** is inferior to the material Young's modulus (again considering $\nu > 0$) and equal to $2G$. This last result is not surprising because the **T-C** test, as it will be further discussed in Section 5.2.1, it is equivalent to a pure shear test, with the factor 2 associated with the conversion between engineering (γ_{xy}) and tensorial shear strain (ε_{xy}).

This formulation E_{biax} can be extrapolated to **FRP** laminates, assuming the same hypothesis of pure biaxial stress. The stiffness tensor of the laminate could be obtained through the **CLPT** (Eq. 2.8) as the extensional matrix $[A]$ is divided by the laminate thickness H , resulting in the constitutive relation expressed in Eq. 5.7. Please remind that the following σ_{ij} are the apparent stresses over the laminate (i.e. the average of all the ply stresses).

$$\begin{bmatrix} \sigma_{xx} \\ \sigma_{yy} \\ \sigma_{xy} \end{bmatrix} = \frac{1}{H} \begin{bmatrix} A_{11} & A_{12} & A_{16} \\ A_{12} & A_{22} & A_{26} \\ A_{16} & A_{26} & A_{66} \end{bmatrix} \begin{bmatrix} \varepsilon_{xx} \\ \varepsilon_{yy} \\ \gamma_{xy} \end{bmatrix} \quad (5.7)$$

If the idea of the formulation of an isotropic E_{biax} is extended to laminated structures composed of orthotropic plies, the previous equation could be simplified by

assuming the hypothesis of pure biaxial stress state ($\sigma_{xx} = \sigma_{yy} = \sigma_b$), developing the Eq. 5.8.

$$\sigma_b = \frac{1}{H}(A_{11}\epsilon_{xx} + A_{12}\epsilon_{yy} + A_{16}\gamma_{xy}) \quad (5.8)$$

We found that in this case an E_{biax} cannot be obtained for any laminate, as the extensional elastic response in x and y directions may be different ($A_{11} \neq A_{22}$). In other words, a state of biaxial 1:1 stress would not be equivalent to the 1:1 strain ratio. Assuming the simplifications of pure extensional loadings (cancelling the terms of coupling in the extensional stiffness matrix $[A]$) or lack of shear strain, the biaxial state is defined by the Eqs. 5.9 and 5.10.

$$\sigma_{xx} = \frac{1}{H}(A_{11}\epsilon_{xx} + A_{12}\epsilon_{yy}) \quad (5.9)$$

$$\sigma_{yy} = \frac{1}{H}(A_{12}\epsilon_{xx} + A_{22}\epsilon_{yy}) \quad (5.10)$$

Thus, the identification of an elastic constant that relates σ_b and ϵ_b is indeed possible for laminates with $A_{11} = A_{22}$. With these restrictions, it is still possible to define a biaxial apparent elastic modulus for the cases of symmetrical and balanced $0^\circ/90^\circ$ and $\pm 45^\circ$ lay-ups, which are to be discussed in the experimental testing. Making the x and y strains and stresses in Eqs. 5.9 and 5.10 equal, it is straightforward to derive the expressions for the biaxial T-T (expression again equivalent for C-C) and T-C cases, resulting in the Eqs. 5.11 and 5.12, respectively.

$$E_{biax}^{T-T} = E_{biax}^{C-C} = \frac{A_{11} + A_{12}}{H} \quad (5.11)$$

$$E_{biax}^{T-C} = \frac{A_{11} - A_{12}}{H} \quad (5.12)$$

Because of the interest for this Thesis, the Eq. 5.11 is particularized for the case of a symmetric and balanced $\pm 45^\circ$ laminate, resulting in $E_{biax}^{T-T} = E_1 \left[\frac{1+2\nu_{21} + \frac{\nu_{21}^2}{\nu_{12}}}{2(1-\nu_{12}\nu_{21})} \right]$.

The result of the biaxial moduli for the cross-ply and $\pm 45^\circ$ angle-ply laminates are shown in the Tables 5.2 and 5.3. To facilitate comparison the uniaxial elastic properties obtainable by CLPT are also collected in these tables.

Table 5.2: Tensile apparent elastic properties obtained by means of CLPT.

Laminate	E_{xx}^t (GPa)	E_{yy}^t (GPa)	G_{xy} (GPa)	ν_{xy}	E_{biax}^{T-T} (GPa)
$[0/90]_{NS}$	95.44	95.44	5.42	0.054	100.34
$[\pm 45]_{NS}$	19.57	19.57	45.50	0.81	100.34

It should be noted that the apparent biaxial modulus is higher in both cases than the uniaxial elastic module, also emphasizing that for the laminate $\pm 45^\circ$ it is approximately five times greater than the uniaxial elastic modulus. In other words, a laminate which apparently does not provide a high rigidity in the loading direction because it has the highest loading-fibre angle mismatch results in a laminate with large extensional stiffness when it is subjected to a biaxial state. This reinforces the idea of studying laminates from the point of view of the plate when submitted to multiaxial loading. Note that E_{biax}^{T-T} has the same value for the cross-ply laminate. This can be explained as the application of pure T-T biaxial state generate an apparent stress and strain tensor equivalent in any direction of the plane (this is further discussed in Section 5.2.1), then explaining that the apparent in-plane biaxial stiffness of both laminates is the same.

When determining the apparent biaxial elastic modulus under tension-compression, an issue appears due to the simultaneity charges of opposite sign, since the approach of the CLPT does not allow the simultaneous consideration of the tensile and compressive properties in principal directions. However, in the case of the laminate $\pm 45^\circ$, it is given that $E_{biax}^{T-C} = 2G_{12} = 10.44$ GPa, which is independent of the sign of the forces. In addition, it can be concluded that in other stacking sequences, E_{biax}^{T-C} is equivalent to the apparent shear modulus rotated 45° , i.e. in the case of the 0/90 laminate, $E_{biax}^{T-C} = 2G_{xy}^{[\pm 45]}$.

Table 5.3: Compressive apparent elastic properties obtained by means of CLPT.

Laminate	E_{xx}^c (GPa)	E_{yy}^c (GPa)	G_{xy} (GPa)	ν_{xy}	E_{biax}^{C-C} (GPa)
$[0/90]_{NS}$	71.20	71.20	5.42	0.024	72.98
$[\pm 45]_{NS}$	18.89	18.89	34.76	0.74	72.98

Additionally, by dividing both Eqs. 5.9 and 5.10, the space of possible biaxial stress-strain ratios could be easily visualized (Eq. 5.13) and represented for any stacking sequence with negligible shear-extensional couplings, e.g. angle-ply and cross-ply balanced laminates. Therefore, in Figs. 5.9a, 5.9b and 5.9c some angle-ply stacking sequences of interest for the experimental biaxial tests are plotted, while Fig. 5.9d

illustrates the same result for $0^\circ/90^\circ$ symmetrical cross-ply laminates. Additionally biaxial ratios proposed for testing in Table 5.1 are also represented for posterior discussion of results.

$$\frac{\sigma_{xx}}{\sigma_{yy}} = \frac{\frac{\varepsilon_{xx}}{\varepsilon_{yy}} A_{11} + A_{12}}{A_{22} + \frac{\varepsilon_{xx}}{\varepsilon_{yy}} A_{12}} \quad (5.13)$$

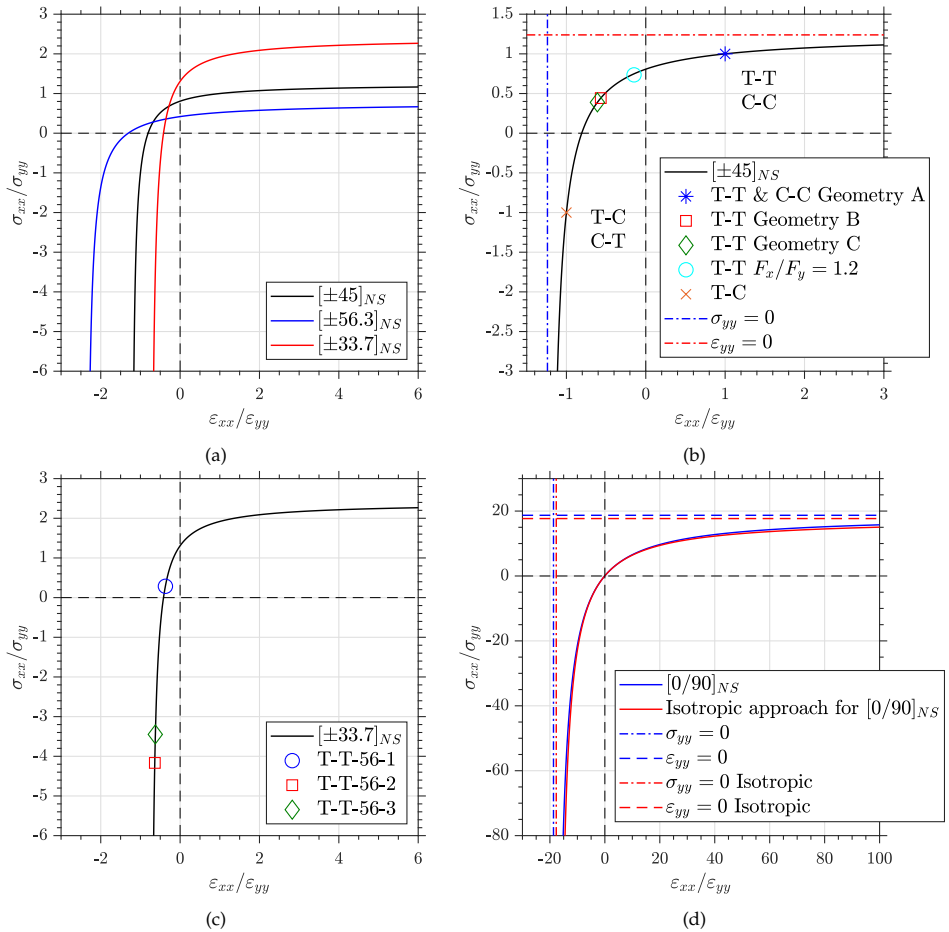


Figure 5.9: Analytical curve depicting relation between stress and strain biaxial ratios under linear elastic response of the material. Experimentally produced ratios are also included as marking points. (a) Different symmetrical angle-ply sequences, (b) Detailed plot for $[\pm 45]_{NS}$, (c) Detailed plot for $[\pm 33.7]_{NS}$ and (d) $[0/90]_{NS}$.

Observing the Fig. 5.9, some remarks should be highlighted. First, the interaction of the stress and strain spaces results in some *alternate* biaxial states. That is, tensile-tensile stress ratios may not result in T-T strain ratios. Secondly, in Figs. 5.9b and 5.9d, the uniaxial stress and strain values are represented, highlighting the asymp-

otic behaviour of this curves. In other words, there is an abrupt change when getting closer to uniaxial ratios, which may suppose difficulties to obtained ratios far from the $\pm 1 / \pm 1$ depending on the machine synchronization control. In order to better illustrate this idea, let us assume that a $\sigma_{xx} / \sigma_{yy} = 15$ is pursued in the cross-ply laminate, then a deviation of 1% in this stress ratio suppose a 5.3% difference in the strain ratios (from 75.58 to 79.56), reflecting the complexity in achieving some ratios from an analytical approach.

Furthermore, a simplification used in the previous figures should be pointed out to clarify the scope of this plots. In order to assign numerical values, the tensile properties for M21E/IMA-12K lamina (in Table 3.1) are utilised. Therefore, tensile dominated ratios are expected to be consistent with these theoretical curves, while some slight deviations are predicted for the compressive dominated ones.

Finally, the similarities in extensional behaviour between loading directions of cross-ply laminates are illustrated in Fig. 5.9d. Note that the term quasi-isotropy is avoided for failing to fulfil the requirement expressed by the expression: $2A_{66} = A_{11} - A_{12}$. The agreement is visualized comparing the curve obtained from the CLPT, (Eq. 5.8), with the results of the consideration of apparent isotropic behaviour of the laminate, represented by the red lines in Fig. 5.9d. This curve comes from using the estimation of the tensile apparent properties for the cross-ply laminate (Table 5.2) in the Eq. 5.3.

This conclusion could not be applied to the case of $\pm 45^\circ$ symmetric angle-ply laminates due to the value of apparent laminate Poisson's ratio, which is higher than the theoretical range for isotropic materials ($\nu_{xy} = 0.81 > 0.5$, Table 3.4).

5.2.1 Representation of uniaxial and biaxial states on Mohr's Circle

With the purpose of creating a better idea of the multiaxial state of the tests carried out in this Thesis, it is possible to use the graphic tool of Mohr circles. Starting from a simpler case, a uniaxial stress state is described. Specifically, if the apparent stress state obtained in the uniaxial compressive test is represented in 3D Mohr's circles (Fig. 5.10a), it is checked that this state generates, in a similar way to the uniaxial tensile test, a maximum shear stress at 45° , both in the xy and xz plane. In this way, the compressed specimens will experience a failure dominated by these tangential components in both planes, so that fractures with angles close to 45° in those two planes are expected, which actually corresponds to the cracks observed in experimental testing.

This same idea can be studied in the case of the biaxial pure compression test, whose 3D Mohr's circle is represented in Fig. 5.10b. In this case, the laminate resultant stress state in any direction of the specimen plane (xy) is equivalent to the biaxial C-C state. However, if we consider for instance the case of the $[\pm 45]_S$ laminate, the Mohr's circle for each lamina does not correspond with the laminate: although in ply it is also true that $\sigma_{xx} = \sigma_{yy}$, the shear stress τ_{xy} are not zero locally to each ply, but these are equal in module in all layers and with opposite signs, what yields a zero resultant of shear stress for the laminate.

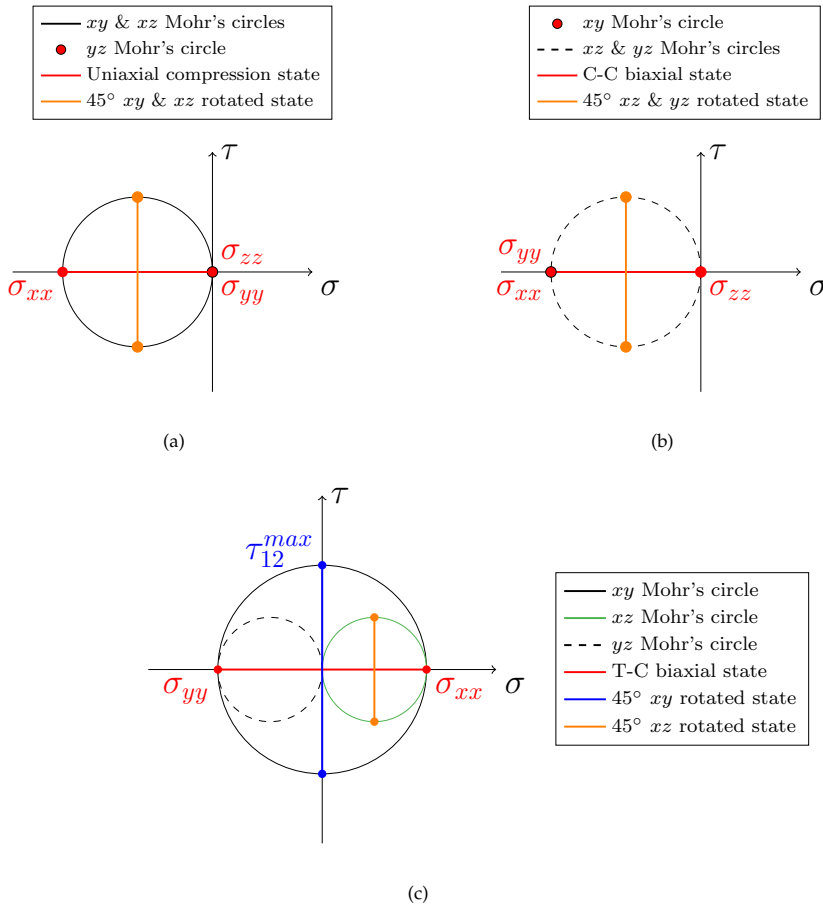


Figure 5.10: 3D Mohr's circles depicting the apparent laminate stresses for: (a) Compressive uniaxial test, (b) C-C 1/1 biaxial test and (c) T-C pure biaxial test.

Nevertheless, it is possible to find a maximum out-of-plane shear stress in any plane that forms 45° with respect to the plane xy . In this way, one would expect that the failure obtained in this test describes fractures that correspond to these planes. However, in experimental tests it will be verified that the cracks obtained do not

clearly show these failure modes. This is explainable due to the small thickness of the laminate in the central area of the biaxial specimen, hindering the appearance of out-of-plane cracks, and also combined with the curvature produced by the buckling.

Finally, thanks to the representation of the Mohr's circles for the T-C test (Fig. 5.10c), it is verified that in a 45° rotation in xy -plane the maximum shear stress is obtained. Furthermore, the case of equal tension and compression results in **pure shear** component [83]. If a laminate composed by $\pm 45^\circ$ plies is considered, then the pure shear stress (not strain because $\varepsilon_{zz} \neq 0$) is obtained in principal directions of the lamina, making this test extremely appropriate for shear characterization.

5.3 Tensile-Tensile biaxial tests on cruciform specimens

In this section, the analysis of all the laminates submitted to biaxial tension-tension loads is detailed. As shown in Table 5.1, this includes different laminates, specimen geometries and loading ratios. Specifically, the 1/1 ratio of the cross-ply laminate has been considered due to its demonstrated mostly linear behaviour according to the previously detailed uniaxial tensile tests. Because of its greater presence of non-linear effects, four loading ratios for $\pm 45^\circ$ symmetrical angle-ply have been analysed. Apart from the pure T-T loading ratio, a 1/1.2 helps to understand how a small deviation with respect to the former ratio may lead to a quite different response. Besides, the study of two ratios in combination with geometries following them helps to understand the importance of a correct adaptation of the cruciform specimen. Finally, a $\pm 56.3^\circ$ laminate introduces the issue of a different elastic and non-linear response in the two loading directions.

5.3.1 Biaxial tensile loading on cross-ply laminate

The study of the $[0/90]_S$ laminate raises three important characteristics regarding its response and failure. First, the extensional stiffness in the x and y directions are identical from a theoretical point of view. Secondly, the behaviour is quasi-linear until the failure (as shown in Fig. 3.2). Finally, this same graph shows how there is an important difference in tensile strength between the 0/90 and 90/0 lay-ups, so that if the arms follow these same sequences, one loading direction exhibits a lower strength than the other one. Therefore, an undesirable failure (if considering biaxial strength characterization) out of the gauge zone is promoted.

For this stacking sequence, no special considerations apart from the overall char-

acteristics of the biaxial tests described in Section 5.1 need to be considered regarding the experimental testing procedure or the numerical analysis. The only difference with the rest of biaxially tensile laminates is the use of a higher thickness reduction ratio $N = 4$ (i.e. the laminate in the arms is $[0/90]_{4S}$), in order to compensate the directional strength dependencies described in the previous paragraph.

Therefore, Fig. 5.11 depicts the results for the apparent response of this laminate under T-T from the numerical and experimental approaches. In Fig. 5.11a, the experimental stress computed with the Eq. 5.1 is plotted against the strain measured with the strain gauge rosettes placed on the tapered region, in combination with the stresses and strains directly measured on the gauge zone in the Hashin's PDM numerical simulations. As a first observation, an important different between both approaches is depicted, although both estimations show an slope in agreement with the apparent biaxial elastic modulus (analytical value shown in Table 5.2). However, a comparison avoiding the use of the elastic coefficient ψ_i , that is, plotting the forces applied at the ends of the arms, again versus the strains in the central region, a good agreement is obtained between both methodologies. Now an equivalent linear response is obtained in both directions, while at an approximate load of 20 kN a non-linearity appears. Besides, the cross marks mean either failure (for experimental curves) or maximum load applied (for numerical results), observing a difference in the maximum stresses reached in the central zone according to the direction, both in the experimental estimate and in the numerical one, which reflects again the fact that the strength in x and y directions differs due to the stacking sequence observed also uniaxially for the $[0/90]_{NS}$ and $[90/0]_{NS}$.

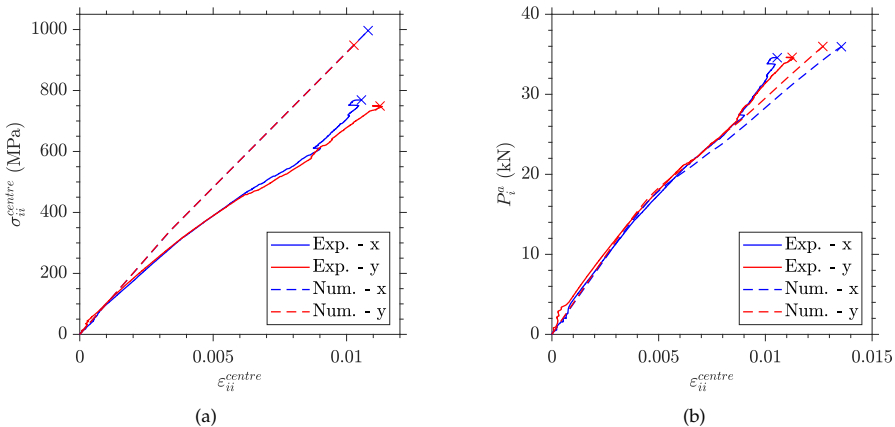


Figure 5.11: Numerical and experimental results for the biaxial tensile test of the cross-ply laminate: (a) Apparent stress-strain response in gauge zone and (b) Applied force against strains in tapered region.

Observing the experimental test via the images and strain contours recorded by the DIC system (Fig. 5.12), in all the experimental tests carried out with this config-

uration, a clear debonding is observed in the transition zone between the laminate of the arms and the tapered region. Although the photographs of the cameras do not have enough resolution to clearly illustrate this failure, the normal strain maps do depict the deformation concentration produced in the vicinity of this debonding (see Fig. 5.12b). Delaminations between 0° and 90° plies are associated with the interlaminar stresses that appear on the geometrical discontinuities of the tapered region, and which are much more relevant in the case of cross-ply laminates than the angle-ply sequences. This is due to the difference between stiffnesses in the loading direction between the plies principal material coordinate system aligned with loading directions. A deep analysis on the effect of interlaminar stress in the stepped transition is described in the work of Lamkanfi et al. [79].

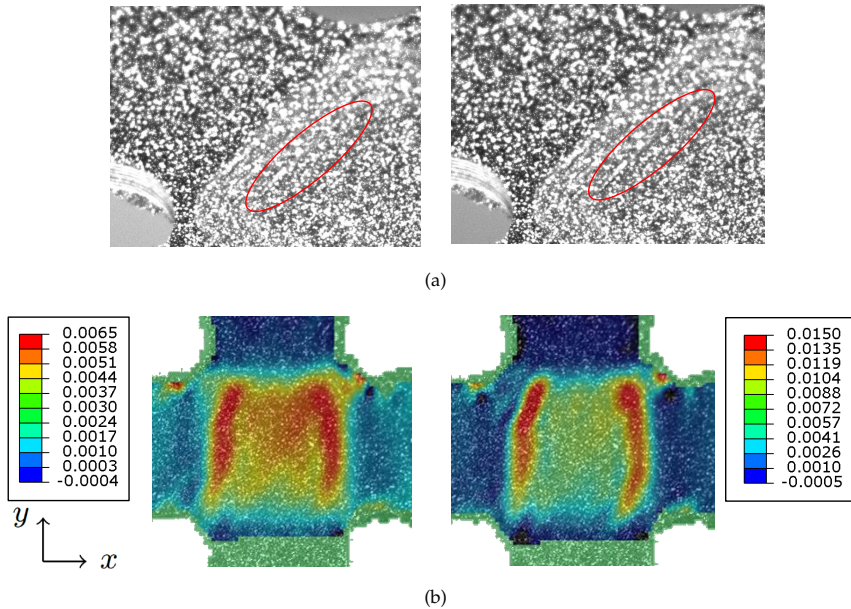


Figure 5.12: DIC observations of the biaxially loaded cross-ply laminate, previous (left) and after (right) the apparition of debonding in the stepped thickness transition: (a) Photographies and (b) ϵ_{xx} contour plots.

Despite not having used a numerical cohesive model, the fact that the simulations with the Hashin's damage model fit a force-strain curve similar to that produced experimentally by the damage of the interlaminar interface is associated with the gradual stiffness degradation in the matrix tensile damage mode, observing in the numerical maps (Fig. 5.13) that this mode leads to the strain concentration in the stepped region in a similar way to delamination in the experimental test.

Lastly, the observation of the specimen failure (Fig. 5.14) allows us to conclude

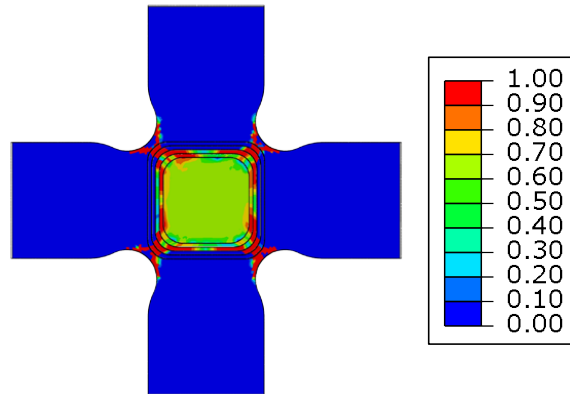


Figure 5.13: Numerical contour plot for the matrix tensile damage variable (d_{mt}) from the simulation of [0/90] biaxial tensile test. The represented state correspond to a load step higher than the experimental apparition of the debonding.

that the concentration of stresses in the vicinity of the filleted corners together with the damage caused by debonding in the stepped region are the mechanisms that promote the failure of the specimen, so that the measured maximum stress value cannot be taken as a reference of biaxial strength.

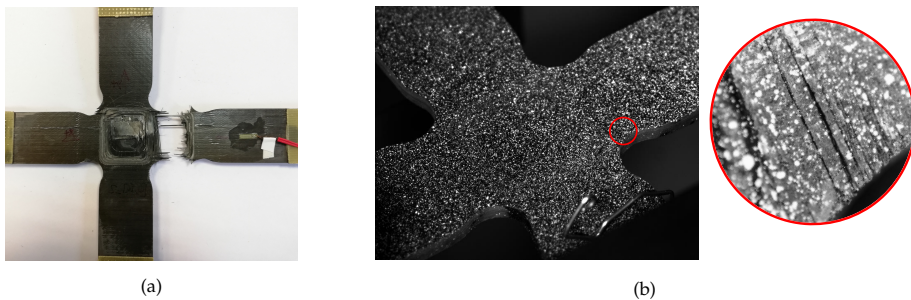


Figure 5.14: Failure of the cross-ply biaxially loaded specimen: (a) Specimen after tests and (b) initiation of matrix cracking at the corners.

5.3.2 $\pm 45^\circ$ laminate under Tensile-Tensile biaxial loading

Starting with the pure biaxial tensile case (namely T-T-A45-1), it can be foreseen that predominately uniaxial loaded arms are going to show pseudo-ductile behaviour, but the biaxially loaded zone is not expected to experiment non-linearities, as T-T loading do not produce apparent shear stresses/strains in principal directions.

Experimentally, a difference in the stress-strain behaviour in the gauge zone is recorded at the level of applied load which triggers the plateau of the pseudo-duc-

tility in the arms. This variation with regard to the numerical model is explained by the stress-measuring method in the central area. That is, the stress in the gauge zone is obtained through the numerical linear ratio between the force applied at the ends of the specimen and the force suffered by the central section. Then, it has been confirmed that the influence of the pseudo-ductility in the arms should be considered on the numerical ratio in order to find accurate measurements in the region biaxially tested. Fig. 5.15 depicts the experimental stress-strain response estimated for the biaxially loaded region of two tests that are only differentiated due to the position of the strain gauge rosette. As x and y strain measurements diverge depending on the position, a local effect is appearing on the biaxially loaded zone which can be explained due to the opposing sign reorientation of $+45^\circ$ and -45° plies. Nevertheless, if mean strain is computed, the both tests describe a similar slope, which is in agreement with the analytical estimation collected in Table 5.2.

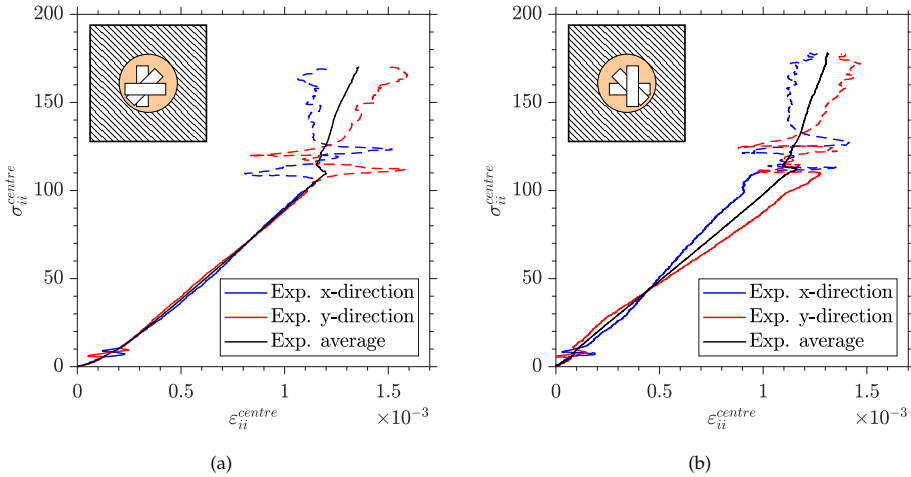


Figure 5.15: Biaxial stress-strain curves for T-T-A45-1: (a) Position A of strain gauges and (b) Position B of strain gauges. Dashed lines symbolise the elastic estimation for the centre stresses after initiation of non-linearities.

Also from the observation of the previous figure, the apparition of strain peaks at a small load level and around 110 – 130 MPa is noteworthy. In order to analyse this result, the experimental applied force curves in both loading directions for one of these tests are plotted in Fig. 5.16. The study of these curves reveals that, at the same load level than the previously commented strain peaks, small differences in force between both directions appear. Regarding the one with the lowest load level, this is believed to be related with small take-up of slack and alignment or seating of the specimen, as similarly described for other testing methodologies in standards [209], what is commonly named as *toe region*. This load non-linearities difficult the force synchronization between both directions during the initial loading steps.

More interesting is the load unbalance appearing around 63% of the maximum applied load in Fig. 5.16. This load level corresponds with the onset of non-linearities in the arms of the cruciform specimen. In other words, at this moment of the test, the uniaxial loaded arms are describing the high shear strain of the plateau stage. Therefore, load increase is apparently stopped, as macroscopic shear bands are evolving in the arms. This occurs up to point the delocalization of strains, once the arms reach the re-stiffening stage of the uniaxial stress-strain evolution observed in $\pm 45^\circ$ symmetrical laminates. Please note that above this stress level, dashed lines are plotted (in Fig. 5.15) in order to highlight that the values of experimental stress are estimations that may not represent the actual stress state.

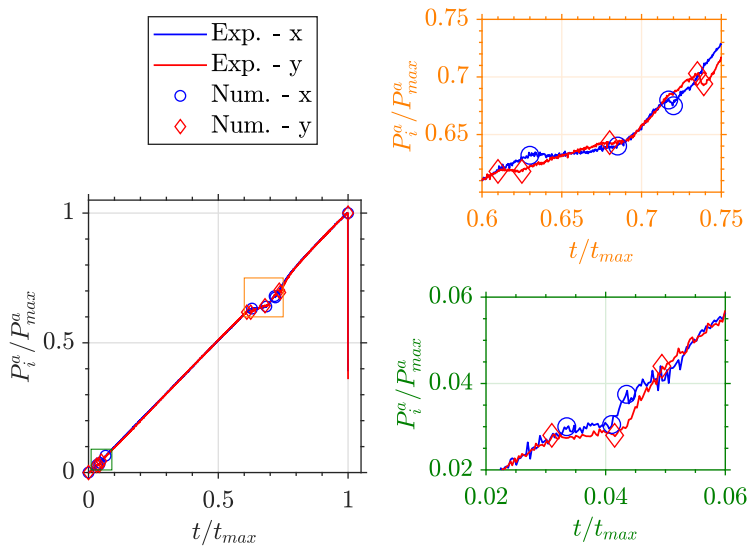


Figure 5.16: Normalized applied force-time plot for a pure T-T biaxial test showing small deviations in force regularization. Force data to virtualize the test is obtained from this plot.

In order to better visualize this non-linear effect, a simulation applying a force control scheme similar to the experimental curve is performed. This is done extracting force-time values of the Fig. 5.16, and defining a stepped (tabular) equivalent boundary conditions in the biaxial numerical model, including Hashin's PDM. The results of this numerical simulation are summarised in Fig. 5.17, where the stress-strain evolutions for the central tapered region of the cruciform specimen are plotted, together with the average experimental values for the same variables. Now the strain peaks observed in the Fig. 5.16 are quite well represented by the numerical simulation. The point of this comparison is to illustrate how the effect of the non-linearities in the arms of the specimen are reflected on the biaxial zone (and this is not only due to the elastic approximation with the parameter ψ).

Nevertheless, in any of the stress-strain figures previously plotted, the experi-

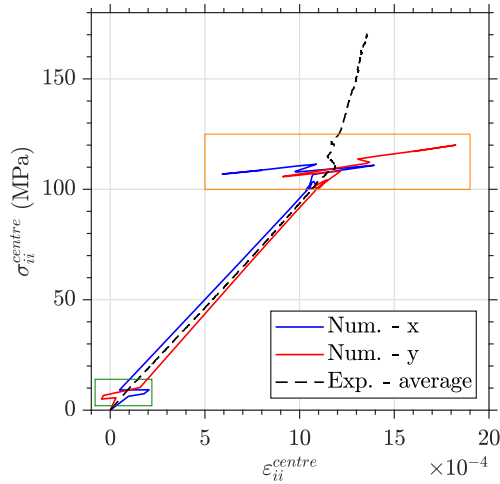


Figure 5.17: Stress-strain results from simulations for pure T-T biaxial test including force deviations. For easier comparison, experimental average stress-strain is also plotted. Green and orange rectangles allow comparison with Fig. 5.16.

mental average apparent stress-strain curve at the biaxially zone is almost linear, as it was expected beforehand. Actually, the numerical biaxial stress-strain response remains perfectly linear for any achieved loading ratio, as numerical damage initiation is never achieved at central region before failure.

Regarding the observation of the tested specimens, a crack initiated on the corner between arms (the stress/strain concentrator) propagates through the diagonal of the central zone. Specifically, through the diagonal in which the observation perpendicular to the crack always show a $[0/90]$ configuration (see Fig. 5.18). Again this breakage is easily understood by observing the stacking sequences effects associated with the $0/90$ laminate, so that the failure occurs more easily when the fibres of the outer layers are observed perpendicularly to the fracture surface.

Tensile-tensile ratios different to 1/1

After detailing the response observed in the pure biaxial test, the results observed for the $\pm 45^\circ$ submitted to other force ratios are described.

Starting with the most similar ratio, the T-T-A45-1.2 test, this allows a description similar to the analysis performed for the force deviations. Although force ratio is modified, the geometry A is still applied for comparison with the change of geometries described below. Fig. 5.19 depicts the experimental and numerical results. The Fig. 5.19a shows the experimental applied force, again depicting some initial

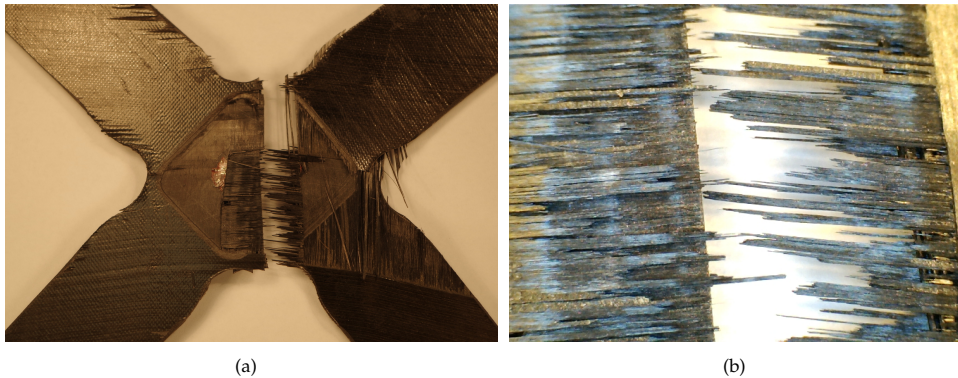


Figure 5.18: Failure of a T-T biaxially tested $\pm 45^\circ$ symmetrical laminate: (a) 1/1 ratio failure and (a) detail of fracture surface.

slight unbalances and a deceleration of force rate around the 63 % of maximum load, which again is related with the onset of the stress-strain plateau in the arms. Note that y -direction depicts an early drop of the force rate, as it expected due to the application of higher load in this direction. Besides, a numerical simulation is carried out assigning as input of the boundary conditions to maintain $P_y^a / P_x^a = 1.2$. The results from this simulation are plotted for comparison with experimental data in Fig. 5.19b. A good agreement of the results is highlighted. In this case, the high apparent Poisson's ratio of the $\pm 45^\circ$ symmetrical laminate ($\nu_{xy} = 0.81$) lead to compressive strains in the less loaded direction.

Observing the results of the biaxial simulations, it is verified that the initiation of the damage occurs firstly in the area of the arms next to the gauge zone, and this damage advances along the entire specimen's arm under tensile-uniaxial load. The laminate under biaxial loads, that is, the one of the central zone in the cruciform-shape specimen, does not reach in any point of the simulation values of damage initiation criteria close to 1, reason why it is verified that the laminate subjected to biaxial tension in two perpendicular directions does not suffer from the large-strain related to pseudo-ductility.

Following a similar procedure, the results of the tests T-T-B45-1.5 and T-T-C45-0.5 are now analysed. Firstly, a clarification must be noted regarding the experimentally applied force ratio. While 1.5 and 0.5 force ratios are pursued for these tests, respectively, the machine regulation software only allows the application of certain discrete force rates, therefore the most similar achievable ratios were studied experimentally (shown in Table 5.1). The outcome of numerical and experimental tests are gathered in Fig. 5.20. Once again, stress-strain curves in biaxial gauge zone are plotted, showing a very good correlation between numerical and experimental results. Note that this time strain gauge rosette measurements are utilised, therefore limiting

5.3. TENSILE-TENSILE BIAXIAL TESTS ON CRUCIFORM SPECIMENS

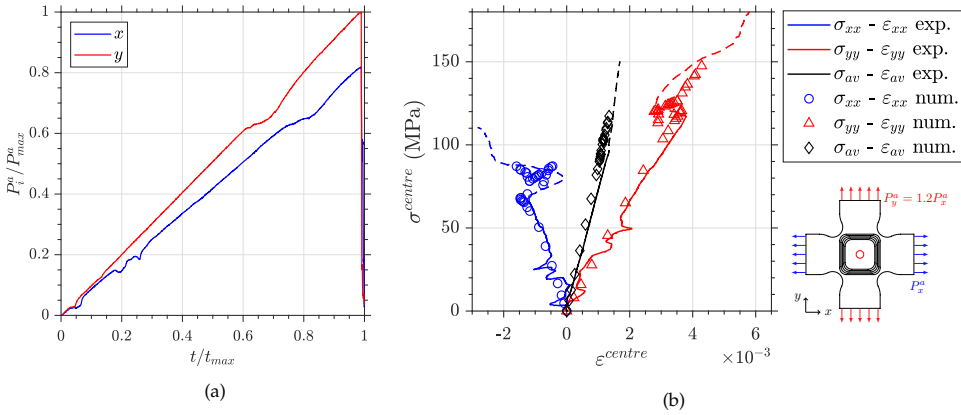


Figure 5.19: Biaxial **T-T** test over geometry *A* cruciform specimen under $P_y^a / P_x^a = 1.2/1$ (T-T-A45-1.2): (a) Force-time plot and (b) experimental and numerical stress-strain curves in gauge zone.

the experimental strain acquisition up to 2 %. In spite of applying load ratios quite different, the response obtained for both tests is very similar, which lead us to highlight that the relation between load ratios and corresponding biaxial stress ratios is not straightforward. In other words, these two configurations with different applied loading ratios and geometries have resulted in a quite similar central biaxial stress-strain ratios (see Fig. 5.9b), which can only be estimated before experimental test from numerical simulations.

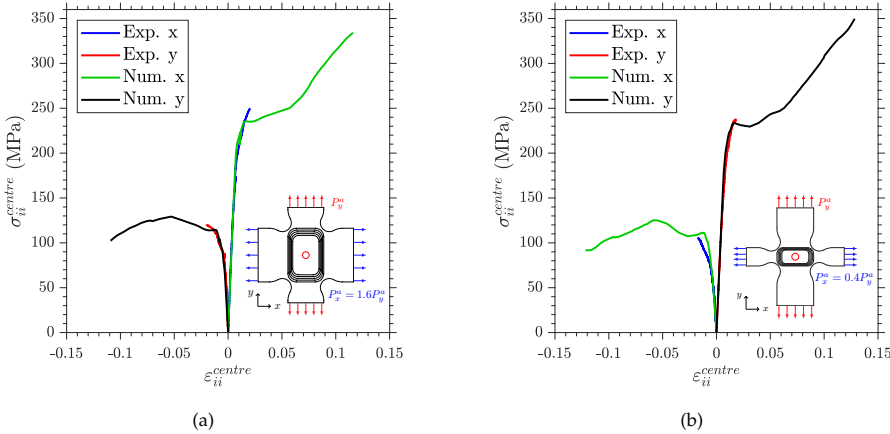


Figure 5.20: Numerical and experimental stress-strain responses for biaxially tensile tested laminates: (a) T-T-B45-1.5 and (b) T-T-C45-0.5.

Finally, in order to prove the effects of the specimen geometry on the failure mode, the pictures of tested specimens are shown in Fig. 5.21. Note that both specimens also depict similar failure modes, with a separation of the narrower arm due to a crack starting at the fillets and propagating at 45° . Again the biaxial strength

measured with these tests can only be used for comparative purposes. However, the most relevant outcomes are related with the previous discussion of the non-linear response and the geometrical effects.

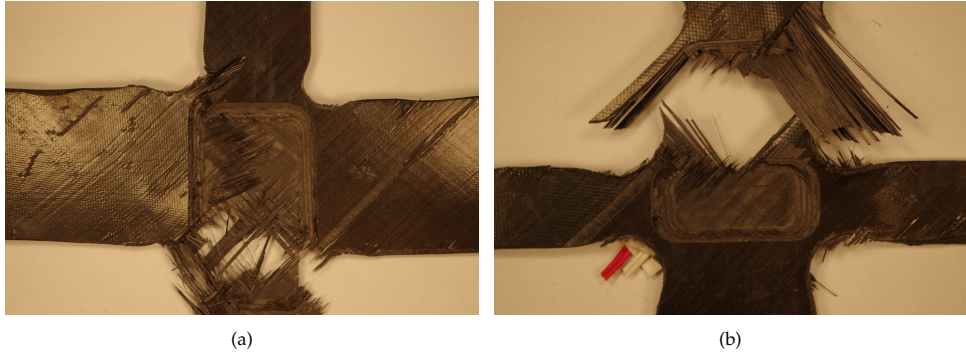


Figure 5.21: Failure of a T-T biaxially tested $\pm 45^\circ$ symmetrical laminate: (a) T-T-B45-1.5 and (b) T-T-C45-0.5.

Other angle-ply sequences under Tensile-Tensile biaxial loading

Continuing with the demonstration of the need to adapt the geometry of the specimen and the force ratio to the tested laminate, as well as to study the behaviour of stacking sequences which have not been previously analysed under biaxial loading, it is proposed to test the $[\pm 56.3]_{NS}$ laminate, in which fibres are aligned with the diagonals of the central zone.

This seemingly arbitrary angle-ply lay-up was chosen for its fibre orientation following the diagonals of the central zone of the geometry *B* specimen (Fig. 5.1b), in search of a suitable biaxial failure. Besides, this laminate no longer presents that equality of properties in the x and y directions. Although it is an orientation that differs only $\approx \pm 11^\circ$ from the previously detailed $\pm 45^\circ$ configuration, this small mismatch causes a very different behaviour in both directions, both in terms of elastic and resistant properties, such as reflected in the Table 3.4.

Three types of tests are performed on this laminate and described in Table 5.1. The first one (namely T-T-56-1) uses the original design ratio for geometry *B*, with a ratio close to 1.5/1, corresponding with the arm widths ratio. Subsequently, tests are carried out by trying to adjust the load ratio to the strength of the laminates in both directions, i.e. the laminates $[\pm 56.3]_{NS}$ and $[\pm 33.6]_{NS}$ (using uniaxially tensile strengths listed in Table 3.4):

$$\frac{S_u^t(\pm 33.7^\circ)}{S_u^t(\pm 56.3^\circ)} = 5.6 \quad (5.14)$$

Thus, we proceeded to apply a ratio $P_x^a/P_y^a = 1/6$ and $P_x^a/P_y^a = 1/8$, respectively in order to evaluate a test following the uniaxial strengths ratio (T-T-56-2) and a slightly higher one (T-T-56-3), in the opposite direction to the firstly proposed test. Please remind that deviation from these ratios is due to force control limitation to certain predefined rates. Examining Fig. 5.9c, we can realise that the asymptotic behaviour of the biaxial stress/strain ratios states causes the last two tests to differ very little. In Figs. 5.22 and 5.23 the numerical and experimental results are summarized for the biaxial tests performed on the laminate $[\pm 56.3]_s$, respectively collecting the measurements in the central area and in both arms. Note that the test T-T-56-2 is not represented due to the similarity with the T-T-56-3.

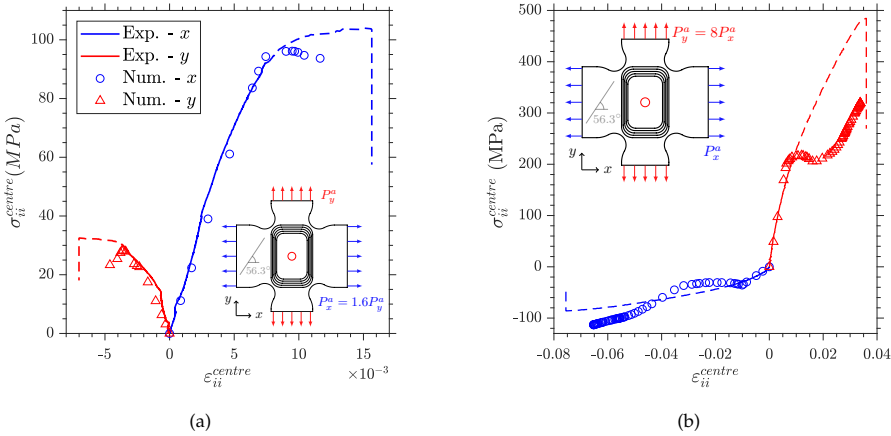


Figure 5.22: Experimental and numerical stress-strain plots at tapered region from biaxially tensile $[\pm 56.3]_s$ laminate: (a) T-T-56-1 and (b) T-T-56-3.

Detailing first the response in the central zone, a fairly good correlation is shown in the case of the lowest ratio (Fig. 5.22a), while higher ratios are generating a response for which simulations overestimates the loss of stiffness. Besides, the simulations capture quite accurately the initial behaviour and the initiation of nonlinearities. However, the evolution when the deformations become larger does not seem to fit with the experimental data, although it should be remembered that an elastic estimate of the stresses in the central area is being made for experimental data, using the Eq. 5.1, hence the dashed lines for non-linear evolution are plotted.

This idea is better understood by analysing the apparent response of the arms (Fig. 5.23), where experimental uniaxial curves have been included for an easier

comprehension of this discussion. It is observed how, as when applying the Hashin's damage model to the uniaxial tensile tests of the $\pm 56.3^\circ$ and $\pm 33.7^\circ$ laminates, the non-linear behaviour in these zones are poorly adjusted by numerical simulations, which may be reflected in the estimation of what is occurring in the biaxially loaded zone. Besides, it should be mentioned that the tests with higher P_x^a/P_y^a (Fig. 5.22b) collect a compressive $\sigma_{xx} - \varepsilon_{xx}$ evolution in the central zone, while no experimental evidence of the effect of uniaxial compressive loads was studied on these laminates.

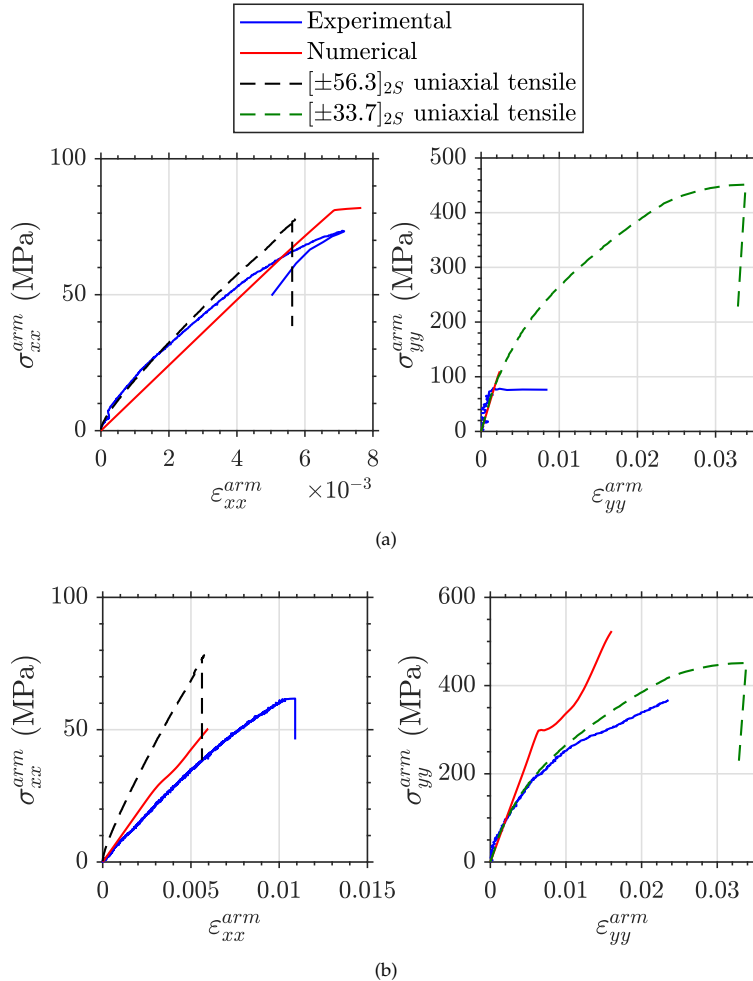


Figure 5.23: Experimental and numerical stress-strain plots at longitudinal direction of arms from biaxially tensile $[\pm 56.3]_S$ laminate: (a) T-T-56-1 and (b) T-T-56-3. Left figures represent x-direction arm and right figures represent y-direction arm.

Fig. 5.23 also allows us to observe the level of stress that both arms of the biaxial specimens are reaching with respect to the corresponding uniaxial tests. For instance, for the T-T-56-1 test, the y-direction, in which the laminate $[\pm 33.7]_{2S}$ is

observed at the arm, is well below the uniaxial ultimate strength. Therefore, failure in this biaxial specimen is dominated by the uniaxial behaviour of the laminate $[\pm 56.7]_{2S}$.

Finally, the fractographies for the extreme cases, i.e. T-T-56-1 and T-T-56-3, are shown in Fig. 5.24. These reflect the necessity of considering the geometry and force ratio which can be applied depending on the laminate. Note that the application of a stress ratio similar to the strength of both arms, altogether with the geometry of the gauge zone following the laminate orientation produces better results in terms of failure. Although these still may not be adequate for stress characterization due to concentrations, it is noteworthy that the stress-strain response of the material can be analysed up to large stress/strain when making this considerations.

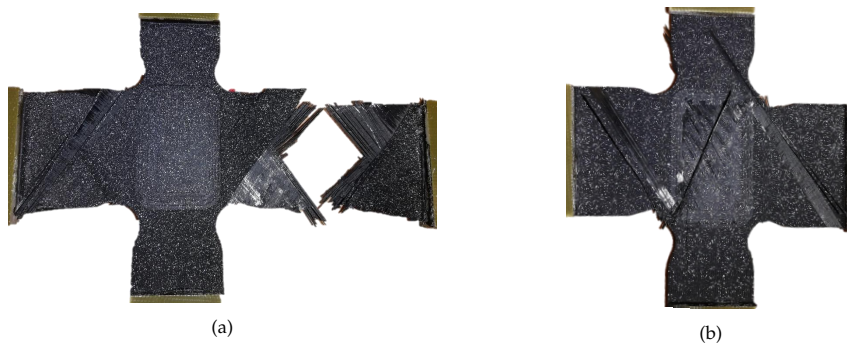


Figure 5.24: Photographies of biaxially tensile tested specimens of $[\pm 56.3]_S$ laminate: (a) T-T-56-1 and (b) T-T-56-3.

Similar conclusions can be drawn observing the experimental strain field obtained via DIC. Fig. 5.25 shows how there is a great concentration of strains in the arm near the corner for the ratio $P_x^a/P_y^a = 1.5/1$, while the ratio $1/8$ (similar to $1/6$) exhibits the concentration in the centre of the specimen, obtaining more homogeneous maps throughout the biaxial specimen. This allows us to emphasize that obtaining a certain biaxial state on a laminate entails very inadequate biaxial failure if the geometry and load ratio are not adjusted correctly.

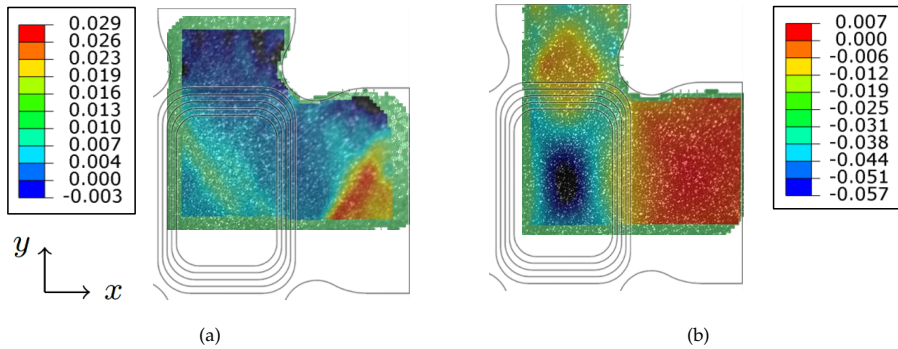


Figure 5.25: DIC contour plots for ε_{xx} under $P_x^d = 3$ kN: (a) T-T-56-1 and (b) T-T-56-3.

5.4 Analysis of the buckling initiation on biaxially compressed laminated plates

One of the conclusions drawn from the state of the art on biaxial testing is the lack of literature dealing with the issue of compressive loading on biaxial tests with cruciform specimens. Most of the documented research related to biaxial testing in cruciform specimens focuses on T-T cases (i.e. only tensile loads applied in both directions) [51, 77, 80, 87, 116, 210], avoiding as far as possible to involve the direct compression of the arms due to the problems of geometrical instability. Only some publications on metals and FRP composites [83, 92, 95, 96, 101, 102], present results related to load cases in quadrants II, III and IV of the biaxial plane, that is to say, involving at least one compressed direction. The reason for this seems the problem of obtaining an adequate failure mode, mainly due to the presence of instabilities. For this reason, a study of the buckling phenomenon is carried out in this section, which allows reconsidering the design of biaxial tests when there are compressive loads in at least one of the global directions.

5.4.1 Bending-twisting coupling effect on buckling critical load

Following a similar procedure to what has been done in Section 4.1, a theoretical framework [166, 211] will be presented in the first place, which will allow to explain the variation of the critical buckling load based on the flexural-torsional couplings. In this instance, the analytical formulation is firstly adapted to the case of a rectangular thin-plate simply supported on all four sides and subjected to biaxial loading (at least one compressive), as outlined in Fig. 5.26.

The deformation obtained due to buckling has a wavy (sinusoidal) 2D shape, which will vary depending on the dimensions of the plate and the rigidity of the laminate. Therefore, the perpendicular displacement to the plate is assumed an expression of the form of Eq. 5.15 [166].

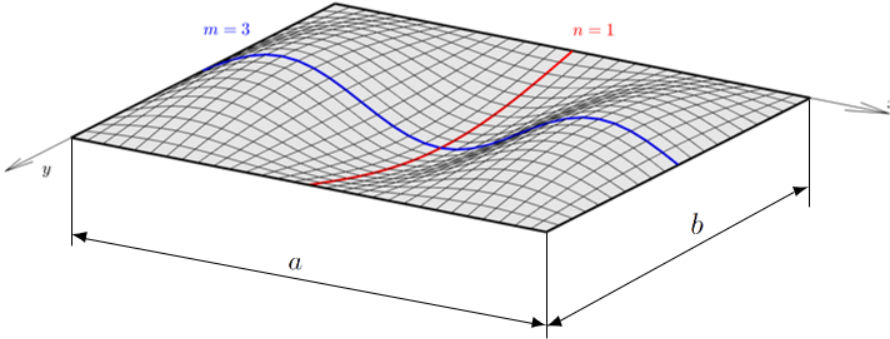


Figure 5.26: Schematization of a buckling mode for a in-plane biaxially loaded plate, representing the example of $m = 3$ and $n = 1$.

$$w = A_{mn} \sin \frac{m\pi x}{a} \sin \frac{n\pi y}{b} \quad (5.15)$$

where m and n are the number of buckling half-wavelengths in x and y directions respectively, and A_{mn} is an arbitrary amplitude coefficient. The Eq. 5.16 represents the equilibrium in differential form specifying for an angle-ply symmetrical laminate (of interest for this work).

$$\begin{aligned} D_{11}\partial_{xxxx}w + 4D_{16}\partial_{xxy}w + 2D_{16}\partial_{xxy}w + 2(D_{12} + 2D_{66})\partial_{xxy}w \\ + 4D_{26}\partial_{xyy}w + D_{22}\partial_{yyyy}w = H(\sigma_{xx}\partial_{xx}w + \sigma_{yy}\partial_{yy}w + \tau_{xy}\partial_{xy}w) \end{aligned} \quad (5.16)$$

Again, the appearance of D_{16} and D_{26} makes impossible to obtain a closed-form solution to the partial differential equation. However, if we consider the case of specially orthotropic laminated plates these terms are null and analytical solution for the differential equation (Eq. 5.17) are achievable. The last equation resembles the bending equilibrium 4.7, therefore it is likewise interesting to study the effect of D_{ratio} (defined in Eq. 4.5) on the critical buckling load.

$$\begin{aligned}
 D_{11}\partial_{xxx}w + 2(D_{12} + 2D_{66})\partial_{xyy}w + D_{22}\partial_{yyy}w \\
 = H(\sigma_{xx}\partial_{xx}w + \sigma_{yy}\partial_{yy}w + \tau_{xy}\partial_{xy}w)
 \end{aligned}
 \tag{5.17}$$

The Eq. 5.17 does have an analytical solution already collected in [166,211]. This approach can be performed similarly for a plate loaded in both directions, i.e. subjected to a compressive-compressive biaxial state, of interest for the design of the tests to be carried out in Section 5.3. The differential equilibrium equation particularised for specially orthotropic laminates (Eq. 5.18) lead to the solution expressed in Eq. 5.19.

$$\begin{aligned}
 D_{11}\partial_{xxx}w + 2(D_{12} + 2D_{66})\partial_{xyy}w + D_{22}\partial_{yyy}w \\
 = H(\sigma_{xx}\partial_{xx}w + \tau_{xy}\partial_{xy}w + \sigma_{yy}\partial_{yy}w)
 \end{aligned}
 \tag{5.18}$$

$$\begin{aligned}
 & \sigma_{xx}H\left(\frac{m}{a}\right)^2 + \sigma_{yy}H\left(\frac{n}{b}\right)^2 \\
 = \pi^2 \left[D_{11}\left(\frac{m}{a}\right)^2 + 2(D_{12} + 2D_{66})\left(\frac{n}{b}\right)^2 + D_{22}\left(\frac{n}{b}\right)^4\left(\frac{a}{m}\right)^2 \right]
 \end{aligned}
 \tag{5.19}$$

Consequently the aim of this section is to estimate the critical buckling load for different angle-ply laminates, which do not have a closed analytical solution (although there are some non-exact approximations).

Recurrently a “virtual testing” methodology is followed combined with the CLPT to find relations which allow estimating the critical load of laminates. On this occasion, numerical tests have been performed keeping the thickness constant and varying the number of layers. Moreover, the effect of elastic properties of the ply is investigated by randomly modifying the lamina properties to obtain a completely different laminate matrix. Table 5.4 collects the ply elastic in-plane properties required for simulations, denominate as “Modified properties”. Thus the effect of the coupling (depending on the number of plies) on the critical load is analysed, similarly to the semi-analytical work from other authors [212].

In Fig. 5.27 the results of this study are collected, where the values of D_{ij} have been estimated using the CLPT in the same way as for the Table 4.2, and the critical load comes from the solution of the eigenvalue buckling problem using Abaqus/

5.4. ANALYSIS OF THE BUCKLING INITIATION ON BIAXIALLY COMPRESSED LAMINATED PLATES

Table 5.4: Ply elastic properties for comparison in numerical models (named as “Modified properties”).

E_1 (GPa)	E_2 (GPa)	ν_{12}	G_{12} (GPa)
300.00	8.00	0.22	3.20

Standard. A $100 \times 100 \text{ mm}^2$ plane geometry is modelled consisting on shell elements S8R [213], simply-supporting and applying a unitary displacement in compressive direction in the four edges. The studied laminates (in Table 5.5) are defined internally to the element, defining a *Composite Layup*.

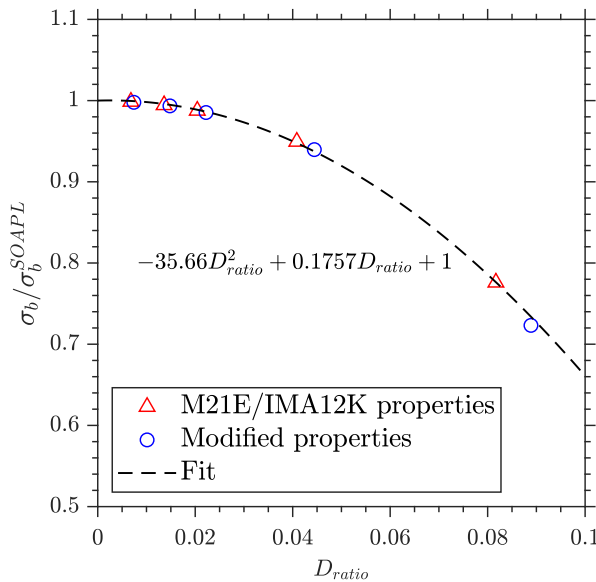


Figure 5.27: Buckling load regarding bending-twisting coupling ratio.

It is found that for a given geometry it is possible to find an analytical solution (in this case it has been made in the form of fitting due to the complexity of the partial differential equation governing this buckling phenomenon) that predicts the critical buckling stress. Furthermore, it is verified that the obtained ratio can be extrapolated to other materials with different stiffness. Nevertheless, it is pending for future works to study the possible extrapolation of this result to any plate size.

Once again the conclusion is analogous with what has already been stated in the Section 4.1 about the flexural modulus. The SOAPL produces the greatest critical buckling load in relation to any other stacking sequence with $+45^\circ$ and -45° plies. Another possible way to eliminate bending-twisting couplings would be with an antisymmetric laminate, but this would cause torsional-membrane couplings.

In consequence the SOAPL is an optimal angle-ply arrangement to increase stiff-

Table 5.5: Numerical results for flexural modulus estimation and bending stiffness values.

Laminate	D_{11} (Nm)	D_{16} (Nm)	D_{ratio}	$L \times w \times h$ (mm)	E_{flex} (GPa)
$[\pm 45^\circ]_5$	3.4924	1.9401	0.08169	300x5x1	17.915
				200x10x1	18.946
				30x10x1	24.315
$[\pm 45^\circ]_{4S}$	3.4924	0.485	0.02042	300x5x1	18.75
				200x10x1	20.019
				30x10x1	27.289
$[\pm 45^\circ]_{12S}$	3.4924	0.162	0.00681	300x5x1	18.783
				200x10x1	20.065
				30x10x1	27.432
SOAPL	3.4924	0	0	300x5x1	18.787
				200x10x1	20.071
				30x10x1	27.449

ness against transverse displacements, due to the minimization of flexion-torsion couplings. This outcome means that one of the advantages of thin-ply laminates, with smaller bending-twisting couplings due to lower layer thickness, can be achieved by thick-ply laminates with specially orthotropic sequences.

5.4.2 β -Coefficients approach for thin plates

In the previous section, analytical relations found in literature have been reviewed with the aim of estimating buckling critical loads and modes on symmetrical angle-ply thin plates subjected to simple BCs situations. Other recent studies have achieved semi-analytical solutions [167, 214–216] for more complex loading cases, but sometimes also limited to certain boundary conditions, geometries or specific laminate orientations.

In this section a new methodology (more details are found in the works [217, 218]) for the calculation of critical buckling loads on plates subjected to different BCs and multiaxial load states is summarised. This pursues obtaining a relatively simple approximation for buckling in the central region of cruciform specimen under compressive loading. It starts proposing an analytical-numerical model for isotropic materials, which is subsequently adapted to the study of $\pm 45^\circ$ symmetric laminates of interest for this Thesis.

The solutions of this model allow estimating the elastic stability of the biaxially loaded zone in the cruciform specimen, when considering an approximately rectangular geometry in the tapered region. This modelling serves as a calculation basis to guide the design of biaxial testing including compressive loads, which is reflected in the modification of the biaxial testing procedure [219] and includes the creation of a new biaxial anti-buckling fixture [217]. Moreover, the estimation capacity of these models is compared with the numerical analysis of the complete cruciform geometry.

The method of the β -coefficients is based on the traditional calculation of critical buckling load in slender beams with different BCs postulated by Euler, in which the critical load is computed by means of an effective buckling length. Proposing this same formulation for plates, the possibility of estimating the buckling load is achieved by obtaining the displacements of the first buckling modes on plates with different BCs and geometric ratios.

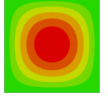
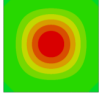
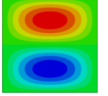
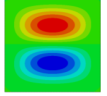
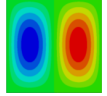
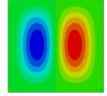
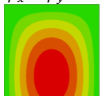
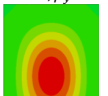
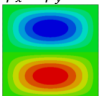
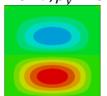
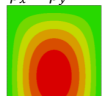
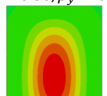
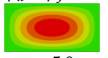
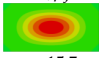
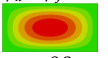
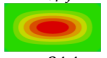
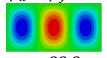
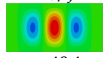
Table 5.6 collects the results obtained for isotropic plates, modifying the lateral BCs (simply supported or clamped) and the relations between the width and length of the plate. This affects the buckling modes obtained (defined by m and n , the half-waves in the x and y directions respectively, as schematised in Fig. 5.26).

The equation has been simplified by defining the term $\sigma_r = \frac{\pi^2 D}{Hd^2}$, where D is the flexural rigidity of an isotropic plate $\left(\frac{EH^3}{12(1-\nu^2)}\right)$. A good agreement between the numerical and analytical results is shown. The values of β seem reasonable. Taking as reference the value 1 for the simply-supported case, the case of clamped conditions results in $\beta < 1$ in any case. Furthermore, in several cases is close to 0.5, which is the value assigned for fixed-fixed beams in the Euler critical buckling load. It is recalled that β is a measure of the existing buckling length versus the total length, so that a clamped plate will have a shorter length fitting the sinusoidal modal shape than in the case of the supported one.

Turning to the case of orthotropic plates and specifically the $\pm 45^\circ$ symmetrical angle-ply laminates, analytical solutions for specially orthotropic plates (Eq. 5.19) allow to easily obtain the critical load and the mode in the case of a simply-supported rectangular plate under a biaxial load state, as shown in the Fig. 5.28.

Fig. 5.28a illustrates how a pure C-C biaxial state does not produce buckling modes other than $(m, n) = (1, 1)$, while in the T-C ($\sigma_{xx} = -\sigma_{yy}$) biaxial state (Fig. 5.28b) it is possible to expect different modes according to the geometric ratio of the plate. If for a same geometrical ratio there are different buckling loads, the one reported is the lowest one, i.e. the first buckling mode.

Table 5.6: Analytical and numerical estimations of the bifurcation stress and the corresponding buckling mode in isotropic rectangular thin-plates. The analytical methodology of the β -coefficients is utilised [218].

Geometry	C-C		T-C		C-T	
	$\sigma_c = \sigma_r \left(\frac{m^2}{\beta_x^2} + \frac{n^2}{\beta_y^2} \right)$		$\sigma_c = \sigma_r \frac{\left(\frac{m^2}{\beta_x^2} + \frac{n^2}{\beta_y^2} \right)^2}{\left(\frac{n^2}{\beta_y^2} - \frac{m^2}{\beta_x^2} \right)}$		$\sigma_c = \sigma_r \frac{\left(\frac{m^2}{\beta_x^2} + \frac{n^2}{\beta_y^2} \right)^2}{\left(\frac{m^2}{\beta_x^2} - \frac{n^2}{\beta_y^2} \right)}$	
	Simply Supported	Clamped	Simply Supported	Clamped	Simply Supported	Clamped
$b = a$	$m = n = 1$ $\beta_x = \beta_y = 1$  $\sigma_c = 2.0\sigma_r$	$m = n = 1$ $\beta_x = \beta_y = 0.61$  $\sigma_c = 5.3\sigma_r$	$m = 1, n = 2$ $\beta_x = \beta_y = 1$  $\sigma_c = 8.3\sigma_r$	$m = 1, n = 2$ $\beta_x = 0.72, \beta_y = 0.80$  $\sigma_c = 15.3\sigma_r$	$m = 2, n = 1$ $\beta_x = \beta_y = 1$  $\sigma_c = 8.3\sigma_r$	$m = 2, n = 1$ $\beta_x = 0.80, \beta_y = 0.72$  $\sigma_c = 15.3\sigma_r$
$b = 1.5a$	$m = n = 1$ $\beta_x = \beta_y = 1$  $\sigma_c = 1.4\sigma_r$	$m = n = 1$ $\beta_x = 0.61, \beta_y = 0.55$  $\sigma_c = 4.1\sigma_r$	$m = 1, n = 3$ $\beta_x = \beta_y = 1$  $\sigma_c = 8.3\sigma_r$	$m = 1, n = 3$ $\beta_x = 0.79, \beta_y = 0.92$  $\sigma_c = 12.8\sigma_r$	$m = n = 1$ $\beta_x = \beta_y = 1$  $\sigma_c = 3.7\sigma_r$	$m = n = 1$ $\beta_x = 0.50, \beta_y = 0.63$  $\sigma_c = 9.0\sigma_r$
$b = 0.5a$	$m = n = 1$ $\beta_x = \beta_y = 1$  $\sigma_c = 5.0\sigma_r$	$m = n = 1$ $\beta_x = 0.61, \beta_y = 0.55$  $\sigma_c = 15.7\sigma_r$	$m = n = 1$ $\beta_x = \beta_y = 1$  $\sigma_c = 8.3\sigma_r$	$m = n = 1$ $\beta_x = 0.66, \beta_y = 0.50$  $\sigma_c = 24.4\sigma_r$	$m = 3, n = 1$ $\beta_x = \beta_y = 1$  $\sigma_c = 33.8\sigma_r$	$m = 3, n = 1$ $\beta_x = 0.72, \beta_y = 0.81$  $\sigma_c = 49.4\sigma_r$

*The contour plots represent the normalized displacement perpendicular to the plane (red=1, green=0, blue=-1)

However, when it comes to clamped plates and tensile-compressive stress states, previous analytical solutions for the governing differential equation are not available. Nevertheless, results collected in Table 5.7 have been obtained with the proposed analytical-numerical method of β -coefficients. In this case, the $[\pm 45]_S$ stacking sequence has been modelled with orthotropic ply properties (Table 3.5). Only the square plate case has been represented because, as it will be discussed in the Section 5.3, it is only recommended to use this stacking sequence for the case of 1:1 stress ratio with the square tapered central region. Besides, the results of the C-T case have been omitted due to symmetry with the T-C in square plates. Again it shows how the case of the supported plates has values close to 1, but in this case slightly lower due to the presence of couplings.

In addition, the buckling modes observed in laminated plates with couplings have a distortion of the modal shape. In the case of C-C, instead of iso-displacement lines describing a circular shape, they represent something similar to an ellipse with the mayor axis parallel to the fibres at the outermost layer. A similar skewing of the deformed shapes is observed for T-C cases, with a deviation of the modes towards the fibre direction.

5.4. ANALYSIS OF THE BUCKLING INITIATION ON BIAXIALLY COMPRESSED LAMINATED PLATES

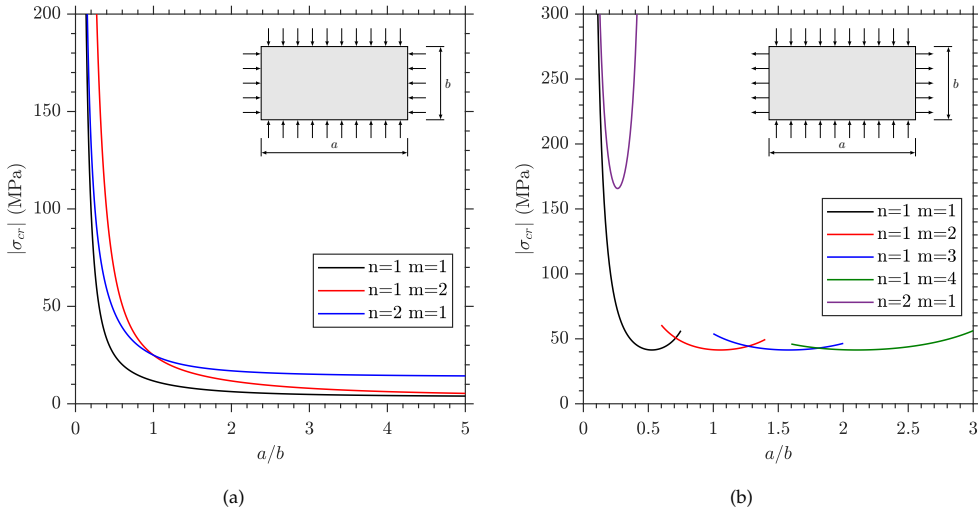


Figure 5.28: Buckling critical stress for a rectangular specially orthotropic plate under biaxial pure stress ($|\sigma_{xx}| = |\sigma_{yy}|$): (a) C-C and (b) T-C.

Table 5.7: Estimations of the bifurcation stress and the corresponding buckling mode in square thin-plates of a $[+45 - 45]_S$ laminate. The analytical methodology of the β -coefficients is utilised [218].

Laminate	C-C		T-C	
	Simply Supported	Clamped	Simply Supported	Clamped
[+45 -45] _S	$m = n = 1$ $\beta_x = \beta_y = 0.89$	$m = n = 1$ $\beta_x = \beta_y = 0.605$	$m = 1, n = 2$ $\beta_x = 0.93, \beta_y = 0.96$	$m = 1, n = 2$ $\beta_x = 0.75, \beta_y = 0.72$
	$\sigma_c = 2.5\sigma_r$	$\sigma_c = 5.5\sigma_r$	$\sigma_c = 9.4\sigma_r$	$\sigma_c = 15.2\sigma_r$

This fact is explained due to the difference in flexural stiffnesses at $+45^\circ$ and -45° (previously illustrated at Fig. 2.8) and the appearance of shear due to bending-twisting coupling. As the coupling is reduced, for example by increasing the number of layers (maintaining the thickness of the laminate so as not to affect the plate flexural rigidity), the deformation tends to mimic the buckling mode for the isotropic material. To compare this effect, the displacement maps of different laminates are shown in Fig. 5.29. Two extreme cases of laminates are depicted: the $[\pm 45]_S$ and the SOAPL which have the lowest and greatest similarity to the isotropic material, respectively. Once more this is related to what is explained in the 5.4.1 section about the effects of couplings.

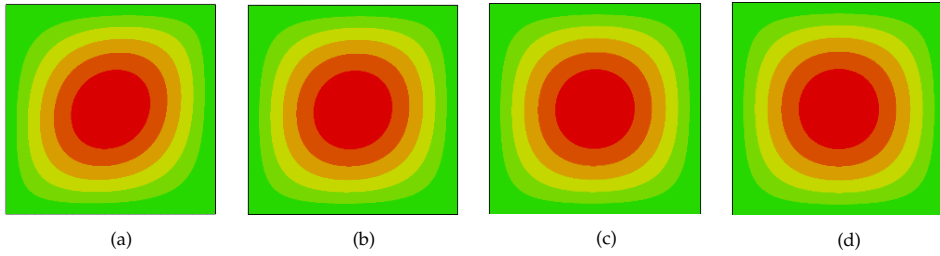


Figure 5.29: Buckling modes for different laminates with same geometry and BCs: (a) $[\pm 45]_{2S}$, (b) $[\pm 45]_{4S}$, (c) $[\pm 45]_{12S}$ and (d) $[-45/+45/-45/+45/-45/+45]_S$.

5.4.3 Buckling analysis of biaxially compressed cruciform specimens

The previous section developed the analytical methodology to assess the buckling initiation in rectangular plates under different loading and BCs. This results are utilised as a working basis to develop the buckling analysis of the full cruciform specimen, considering both the isotropic and orthotropic material behaviour.

The aim is to estimate the load and displacement applied to a cruciform specimen that causes the initiation of buckling instability. Angle-ply laminates composed $\pm 45^\circ$ laminae with 0.25 mm ply thickness are modelled with the material properties defined in Table 3.5, meshing with S8R shell elements and using the cruciform specimen geometries from previous works [77, 80, 208]. In the case of the arms subjected to compressive loading, their length is shortened to the point where the change of the arm section begins due to the fillet of the corners.

Additionally, the influence of the thickness reduction in the central area of the specimen is studied analysing different $[\pm 45]_{NS}$ laminates. The thickness of the laminate t_a is determined by the number of layers ($t_a = n \cdot 0.25$ (mm)), while the central zone is achieved by removing ply until obtaining the $[\pm 45]_S$ laminate, with thickness $t_c = 1$ mm.

Even though the experimental testing is performed with force control, the applied displacement is chosen as input in the numerical model. This is because of the need to introduce in-plane BCs to avoid zero pivot when forces are applied in the simulation. However, it could have been reproduced with loads whenever the buckling modal shape can be estimated and provided that it meets certain conditions of symmetry or antisymmetry, in any case limiting the obtained results. In this way, the results will be shown in terms on the critical load or the the critical displacement depending on the numerical model input.

Regarding the rest of the BCs, in a first model it is assumed that the compressed arms are simply supported at the ends, while the tensioned ones are clamped, reproducing the condition of the gripping system. A second model seeks to analyse the response of a possible anti-buckling fixture that prevents the perpendicular displacement of the outer faces of the specimen. Therefore, the out-of-plane displacement (δ_z) is only allowed in the tapered region (with dimensions of 22×22 mm), as contact or visual access to this region is required for strain data acquisition in the experimental test. Figure 5.30 depicts the aforementioned BCs, while the Table 5.8 collects the results obtained for the simulations modifying the ratio $t_r = t_a/t_c$ (always ≥ 1).

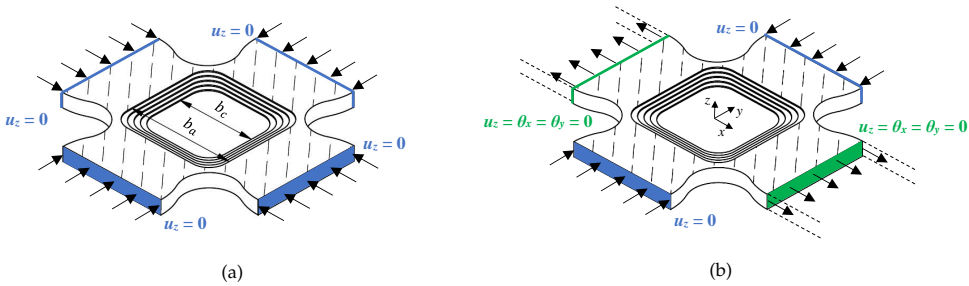


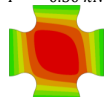
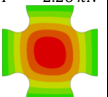
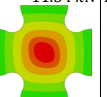
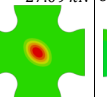
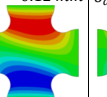
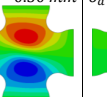
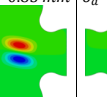
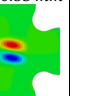
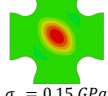
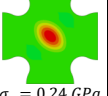
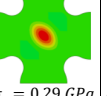
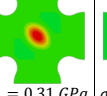
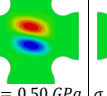
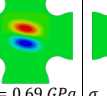
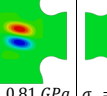
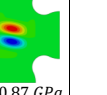
Figure 5.30: 3D schematic representation of the geometry, BCs and applied forces for the linear 2D buckling simulations on cruciform specimen: (a) C-C and (b) T-C. Dashed lines represent the u_z constrained faces supported for the anti-buckling jig.

The results shown in the Table 5.8 clearly demonstrate the effect of the use of an anti-buckling jig and the dependence on thicknesses ratio. If we analyse the cases without the fixture, it is clearly verified how the increase in the thicknesses ratio t_r results in the reduction of the half-wave lengths of the buckling modes. In other words, it produces a notable growth in the critical buckling load. This is easily acceptable to the relative change in flexural rigidity of the arms with respect to the central area associated with the increase in thickness.

If the influence of the fixture is analysed, the approximation of preventing perpendicular displacement to the plane (reminiscent of the basis of the anti-buckling fixtures proposed in standards [188] and research works [220]) has a stabilizing effect in all the cases analysed in this study. The buckling modes clarify how the jig confines the instability of the specimen to the central zone, preventing a global buckling of the specimen, in which the slenderness of the arms can lead to a premature instability.

Note the ratio $t_r = 8$ produces a result in which apparently the thickness-reduced laminate is found with BCs similar to a plate with the contour clamped. If a cost-effective solution is sought, in other words, reducing the number of layers required as much as possible, the use of a ratio $t_r = 4$ combined with the anti-buckling jig

Table 5.8: Numerical results of the bifurcation values, the corresponding buckling modes and the compressive stress in the central region in $\pm 45^\circ$ angle-ply laminates just before the instability [218].

Fixture	C-C				T-C			
	$t_r = 1$	$t_r = 2$	$t_r = 4$	$t_r = 8$	$t_r = 1$	$t_r = 2$	$t_r = 4$	$t_r = 8$
No	$P^a = 0.50 \text{ kN}$	$P^a = 2.26 \text{ kN}$	$P^a = 11.54 \text{ kN}$	$P^a = 27.09 \text{ kN}$	$\delta^a = 0.12 \text{ mm}$	$\delta_a = 0.50 \text{ mm}$	$\delta_a = 0.85 \text{ mm}$	$\delta_a = 0.85 \text{ mm}$
								
Yes	$\sigma_c = 0.01 \text{ GPa}$	$\sigma_c = 0.04 \text{ GPa}$	$\sigma_c = 0.17 \text{ GPa}$	$\sigma_c = 0.31 \text{ GPa}$	$\sigma_c = 0.07 \text{ GPa}$	$\sigma_c = 0.37 \text{ GPa}$	$\sigma_c = 0.76 \text{ GPa}$	$\sigma_c = 0.86 \text{ GPa}$
	$P^a = 7.85 \text{ kN}$	$P^a = 13.37 \text{ kN}$	$P^a = 19.37 \text{ kN}$	$F_a = 27.53 \text{ kN}$	$\delta_a = 0.92 \text{ mm}$	$\delta_a = 0.93 \text{ mm}$	$\delta_a = 0.90 \text{ mm}$	$\delta_a = 0.86 \text{ mm}$
Yes								
	$\sigma_c = 0.15 \text{ GPa}$	$\sigma_c = 0.24 \text{ GPa}$	$\sigma_c = 0.29 \text{ GPa}$	$\sigma_c = 0.31 \text{ GPa}$	$\sigma_c = 0.50 \text{ GPa}$	$\sigma_c = 0.69 \text{ GPa}$	$\sigma_c = 0.81 \text{ GPa}$	$\sigma_c = 0.87 \text{ GPa}$

lead to a response very close to case of $t_r = 8$, whose solution with and without fixture is practically the same. In [218], this comparison is studied in detail with the analytical results for the square plate, which allows a direct estimation of the specimen response using the β -coefficients model applied to a square plate of similar geometry to that of the tapered zone.

To conclude, when conducting the experimental testing the preferred configuration is the $t_r = 4$ combined with the use of an anti-buckling fixture that constraints the displacement perpendicular to the plane outside the biaxial gauge zone.

Finally, the closing result achieved with this analytical modelling is the representation of the elastic stability at the biaxially loaded zone in the cruciform specimen. This result is plotted in the $\sigma_{xx} - \sigma_{yy}$ normal stresses plane, and more specifically, in the three quadrants in which compressive stresses appear (Fig. 5.31). This approximation will serve to corroborate if in the proposed biaxial test the failure is reached before the strain bifurcation appear in the cruciform specimen. Besides, note that the critical buckling stress obtained may not represent the specimen failure, since the plate will continue to maintain a certain load-carrying capacity, known as post-buckling behaviour [166, 221]. Therefore, it is necessary to be clear about where post-buckling behaviour begins, in order to differentiate this stiffness loss mechanism from another due to the damage of the composite.

Consequently, the onset of the bifurcation is identified in experimental compressive tests via the use of strain measurement on both sides of the specimen, and/or the recording of out-of-plane displacement using the 3D DIC system. This procedure is used by other authors [222], proving how the buckling on a compressed plate generates an out-of-plane displacement, that can be also evidenced in a more precise way by the bifurcation of the strain measurement on both sides of the specimen.

Additionally, the analytical approach on the bifurcation onset depicted in Fig. 5.31 is the one obtained assuming the simply-supported isotropic material, modelled by the Eq. 5.20 [223]. This is performed in order to estimate a conservative buckling load, as the isotropic simply-supported approach produces the lowest values of critical loads in comparison with the orthotropic analysis. A linear relation between σ_{xx} and σ_{yy} is expressed in Eq. 5.20, depending on the buckling modes defined by m and n . In Fig. 5.31, the first buckling modes for the case of C-C, T-C and C-T biaxial loadings have been represented. Those correspond to $(m, n) = (1, 1), (1, 2), (2, 1)$, respectively.

$$\sigma_{xx} \left(\frac{m}{a}\right)^2 + \sigma_{yy} \left(\frac{n}{b}\right)^2 = \frac{\pi^2 D}{H} \left[\left(\frac{m}{a}\right)^2 + \left(\frac{n}{b}\right)^2 \right] \quad (5.20)$$

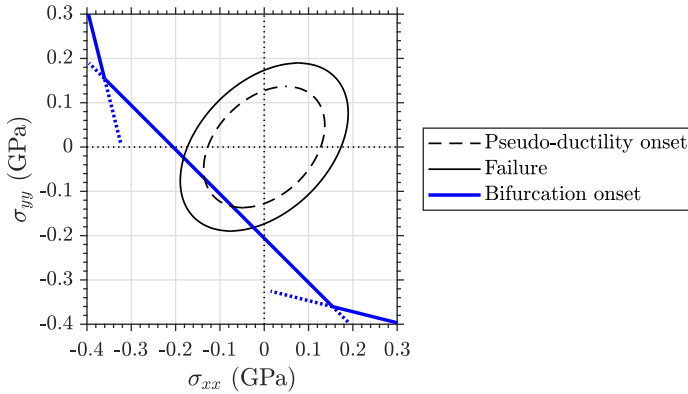


Figure 5.31: Region of elastic stability for a $[\pm 45]_S$ laminate, comprising at the upper part of the bifurcation curve, compared with the Tsai-Wu failure criterion in the biaxial plane [218].

Besides, Tsai-Wu failure criterion is computed for the laminate $\pm 45^\circ$ considering two different possibilities. First, the initiation of the non-linearities is estimated by means of the pseudo-ductility onset observed in uniaxial tests (this resembles a FPF criterion). Secondly, the criterion is applied to collect the final failure of the laminate. The averaged values applied for the calculation of the failure curve are summarized in Table 5.9

Table 5.9: $[\pm 45]_S$ averaged strengths obtained via uniaxial tensile and compressive characterization and biaxial T-T testing.

S_Y^t (MPa)	S_Y^c (MPa)	S_U^t (MPa)	S_U^c (MPa)	S_U^{T-T} (MPa)
124.23	130.73	182.37	164.78	174.10

where subscripts Y and U are used to denote yielding and ultimate strengths respectively. Note that the criterion is applied on the apparent response of the $\pm 45^\circ$

symmetrical laminate, which is allowed due to the invariance under rotation or re-definition of coordinates [166]. Besides, note that the previous table does not include a value of biaxial yielding, as it has been proven in previous section that biaxial tensile-tensile load does not lead to non-linearities. Nevertheless, in order to compute the criterion for the onset of non-linearity, the value of $S_Y^{T-T} = 107.7$ MPa is used. In other words, the dashed line in Fig. 5.31 for pure T-T and C-C represents only a theoretical estimation to close the envelope, not representative of an actual non-linearity onset.

Examining the Fig. 5.31, it can be concluded that, although the most conservative analytical approach for buckling has been considered, there are few biaxial ratios in which buckling is expected before non-linearities or failure criteria are reached. These ratios are limited to the compression-compression quadrant, most specifically to the ratios 0.53/1 to 1/1 during the linear elastic region, and expecting buckling before failure for the range between 0.13 and 0.53. Therefore, a special attention will be given to these biaxial C-C ratios when performing experimental testing.

5.5 $\pm 45^\circ$ laminate under Compressive-Compressive biaxial loading

This section aims to advise about the methodology and conditioning of the specimens to perform biaxial tests with cruciform specimens subjected to compressive loads, presenting a new anti-buckling biaxial fixture proposed for patent [224, 225], which postpones the instability in the specimen arms. The accessory prevents buckling by restricting off-plane displacements and it is applicable in both T-C and C-C loading scenarios. As far as the authors have been able to know, at least two other jigs with different characteristics can be found in bibliography [96, 101], but they are proposed for specific installation and configuration of the specimen.

The main requirement of the proposed fixture (shown in Fig. 5.32) was to prevent the arms of the cruciform specimen from destabilizing due to their buckling. Furthermore, a correct alignment must be achieved between the direction of the applied load and the axes of the arms to avoid the appearance of early or unexpected instabilities and to guarantee a pure biaxial load in the central region of the cruciform specimen. This is achieved by using an L-shaped base, which is fixed to the testing machine and assembled with the anti-buckling jig containing the cruciform specimen. Besides, the novel fixture has the advantage of being adjustable to most testing machines and geometries of cruciform specimens.

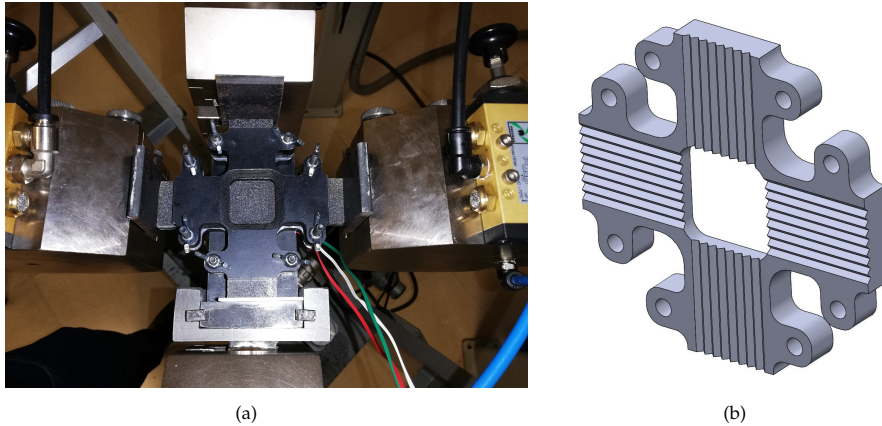


Figure 5.32: C-C biaxial testing: (a) Experimental facility including the fixture and (b) detail of the contact surface.

Fig. 5.32a shows the realization of a C-C biaxial test, in which the specimen follows the shape of geometry A (Fig. 5.1a), but reducing the arms length. It is verified that the window included in the anti-buckling fixture permits visualization of the strain state of the gauge zone using the DIC system, while the opposite face is instrumented with foil strain gauges. However, the presence of the anti-buckling tool and the tabs at the arms impedes the measurement of deformations in these regions. Note that the face of the fixture plates in contact with the specimen contains blunted ribs to reduce the friction between the specimen and the fixture (Fig. 5.32b).

A response comparable to the T-T test can be presumed since the uniaxially loaded arms are expected to suffer large deformations due to the non-linear strain induced by shear, while the centre should exhibit an apparent linear behaviour. In Fig. 5.33 the response in the central zone is shown, comparing the experimental outcomes and the simulation applying the Hashin's model. On the one hand, continuing the contrast with the T-T test, this one also shows the local effect at the gauges due to reorientation (as in Fig. 5.15). The strains recorded in the x and y directions differ, but nevertheless they present an average value which allows to compute an average stress-strain slope similar to the theoretical biaxial elastic apparent modulus under biaxial compression (72.98 GPa).

On the other hand, in this case an experimental non-linearity is appearing in the gauge zone, which is due to the onset of buckling in the central zone. This conclusion is based on the fact that the strains measured on both sides of the specimen through the different acquisition systems show a bifurcation point around 120 MPa. From this point, it is observed that the strain at the top face (green curve) moves to tensile values, while the bottom face (black line) depicts a shortening at a higher rate.

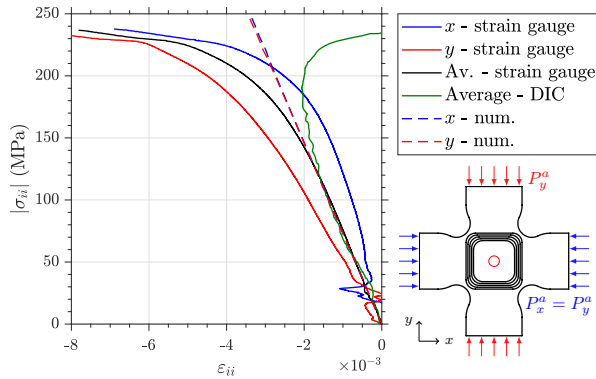


Figure 5.33: Stress-strain response in biaxially loaded zone of the C-C test, including numerical and experimental curves. DIC and strain gauge measurements in the central zone in both specimens are included.

Furthermore, the utilization of a 3D DIC system allows the measurement of the displacement perpendicular to the laminate mid-plane, while the software applied for postprocessing recreate the resultant 3D surface. Then, Fig. 5.34 depicts the z -displacement close to the failure of the specimen. Note that the displacement field agrees perfectly with the C-C buckling modal shape for the cruciform specimen applying the fixture (Table 5.8).

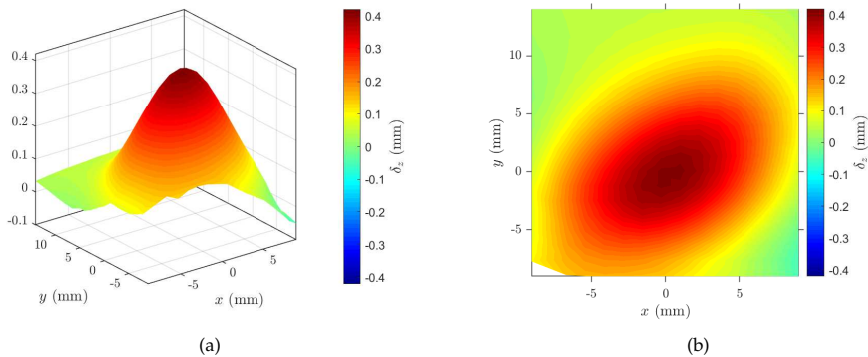


Figure 5.34: Out-of-plane displacement maps at the biaxially loaded zone obtained via DIC during C-C biaxial test of $[\pm 45]_S$ with anti-buckling jig: (a) 3D surface and (b) 2D representation.

Finally, Fig. 5.35 is included to illustrate the biaxial compressive failure mode obtained. Crack is obtained on the biaxially loaded zone, and the curvature of the top surface, as well as the crack patterns observed in Fig. 5.35b reveal that the failure is clearly induced by buckling, as typical kinking surface patterns are observed.

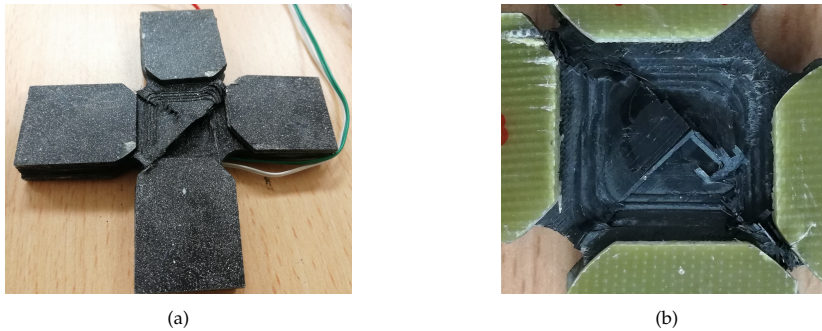


Figure 5.35: **C-C** biaxially tested $\pm 45^\circ$ symmetrical laminate, showing the buckling of the biaxially loaded zone.

5.6 Tensile-Compressive biaxial testing of $\pm 45^\circ$ laminate

In Section 5.2.1 it was commented how this test allows to obtain a state of pure in-plane shear. Another important advantage of this test is that, unlike the other biaxial cases studied, a significant reduction in stress concentration at corners is expected, which led us to assume that this test could be defined as a strength characterization methodology. To corroborate this hypothesis, the strain contour maps obtained by simulation in the elastic region of the material are compared with a similar load situation in the experimental test in Fig. 5.36. It should be noted that the test specimen used is based on the geometry *A* applied for **T-T** testing but the arms have been shortened in the compressed direction to reduce the possibility of buckling. Besides, Table 5.5 denoted that with a thickness-reduction of 4 (that is, with a cruciform specimen obtained by the central reduction of a laminate $[\pm 45]_{4S}$ up to $[\pm 45]_S$ in central region) the buckling bifurcation was anticipated highly above the laminate failure load (see Table 5.8). In addition, the arms of the specimen subjected to **T-C** are not expected to reach a sufficient level of stress to show non-linear behaviour.

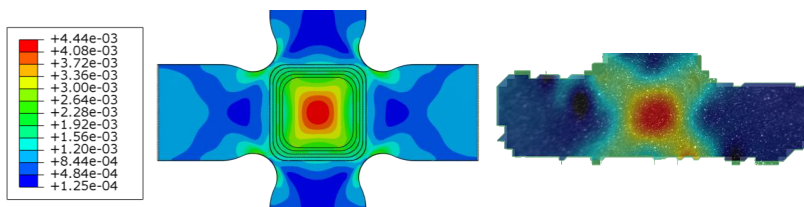


Figure 5.36: Comparison of ϵ_{xx} contours in the linear behaviour for the **T-C** biaxial test on $\pm 45^\circ$ laminate: numerical (left) and **DIC** (right)

The performance of this test without fixture favours the appearance of misalignment, so the effect of the anti-buckling jig as a tool to improve the stability of the specimen is tested. Note this reasoning is made for a thickness ratio $t_r = 4$, while smaller ratios are more needed of the anti-buckling accessory. Then, it was experimentally observed how the shear behaviour obtained by the T-C test leads to higher values of in-plane shear strength when using the anti-buckling fixture (Fig. 5.37). Therefore, even in the case of T-C where buckling is not expected to be the origin of non-linearities as in the case of C-C testing, the anti-buckling fixture is still effective in improving the results obtained in biaxial test in the presence of at least one compressive loading direction.

In addition, in-plane shear strength values are also higher than with the $\pm 45^\circ$ uniaxial tensile test (see Section 3.1.2), in which maximum shear stress in principal direction is combined with an equal value of normal stresses. On the other hand, the shear modulus obtained by both tests is similar, since this property should not be affected by a combined stress state, which allows validating the T-C test as an stiffness and strength characterization methodology.

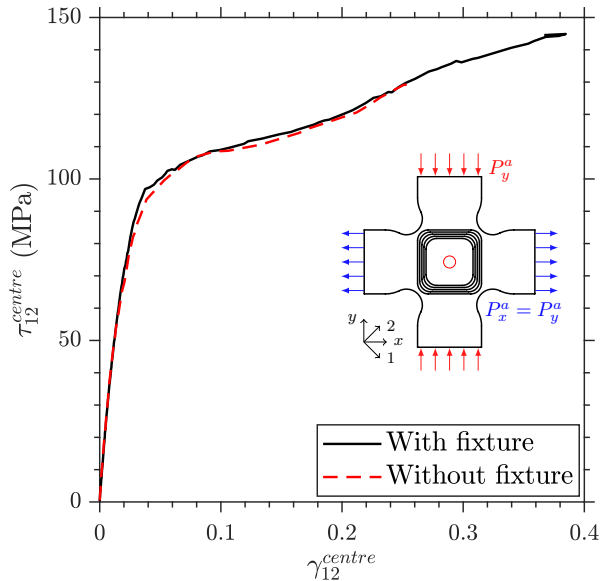


Figure 5.37: Shear response observed by means of T-C biaxial test with and without utilising the anti-buckling fixture. Both tests are performed for a $[\pm 45]_{4S}$ laminate, reduced to $[\pm 45]_S$ in the gauge section.

This outcome is also corroborated observing the deformation of the tested specimen, shown in Fig. 5.38. Note that the test without anti-buckling fixture resulted in a misalignment due to geometrical instabilities under compressive load. Analysing the failure modes, both methodologies reveal a high permanent shear strain on the

diagonal of the biaxially loaded zone, reflecting the capacity of high energy absorption related to the shear mode.

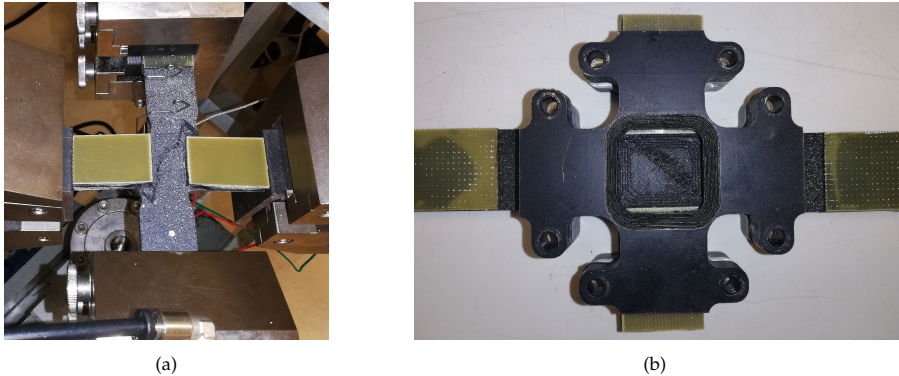


Figure 5.38: Failure of biaxially T-C tested $\pm 45^\circ$ symmetrical laminate: (a) due to misalignment of the cruciform specimen without the anti-buckling fixture and (b) adequate failure mode.

With regard to the Hashin's damage model, it is able to reproduce qualitatively the initiation of non-linear behaviour in the biaxially loaded area, describing the strain concentration in the neighbourhood of the diagonal (Fig. 5.39), while the estimated behaviour for the arms of the specimen subjected to uniaxial stress do not reach the values of damage initiation before the failure of the central zone. However, the numerical values obtained do not correctly reflect the high non-linear behaviour of the material experimentally observed. This may be explained because of the limitation of this model not allowing simultaneous consideration of the difference in tensile and compressive response existing in FRP composites.

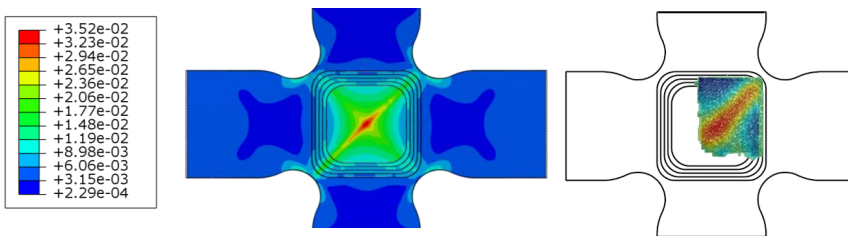


Figure 5.39: ϵ_{xx} strain contour plots obtained from simulation with Hashin's PDM and via DIC for T-C biaxial test after onset of non-linearities.

As a final step in the validation of this test, it is pending for future work to compare the results obtained with the standard characterization of in-plane shear by means of the Iosipescu, V-notched rail or similar standardized test.

5.7 Evaluation of internal damage via phased-array ultrasonic inspection

In this section the results for the inspection of biaxially tested specimens by means of the phased-array technique are depicted, in order to contrast the damage patterns observed in numerical simulations. For this purpose, the pure T-T, T-C and C-C biaxial ratios have been C-scanned for the $\pm 45^\circ$ laminates, looking for damage accumulation in the arms. Note that the tapered region is not observable due to geometrical restrictions which impede the adequate contact of the transducer with the specimen surface (due to the transducer is wider than the tapered region). Furthermore, the interest of the ultrasonic inspection is to find internal damage which are not optically visible.

A composition of the ultrasonic inspection and the numerical damage contours obtained with the Hashin's FEM analysis for the 1/1 biaxially tensile tested $\pm 45^\circ$ are depicted together for easier comparison in Fig. 5.40.

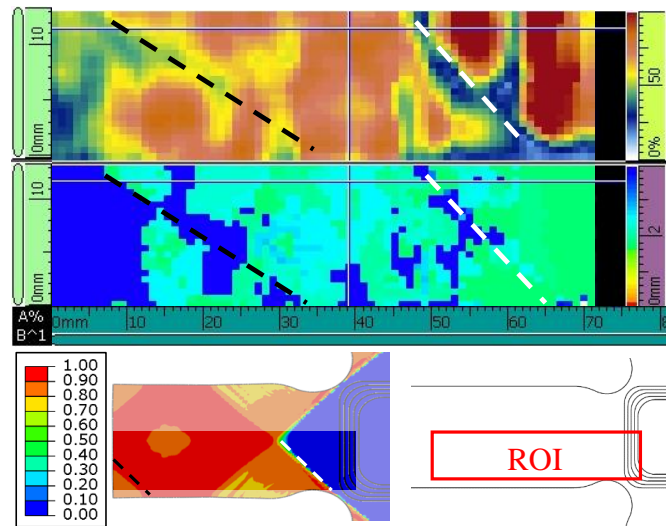


Figure 5.40: Phased-array inspection of the $\pm 45^\circ$ T-T cruciform specimen after 1/1 biaxial test (above), and numerical contour for matrix tensile damage variable d_m at a point close to maximum load (below). The inspected region (ROI) is schematized at the right side.

The thickness C-scan reveals the position and size of the damages thanks to the vertical and horizontal rules included in the image, while the colour refers to the depth with respect to the laminate surface (please take into account the colorbar at the right side to estimate the depth, which varies from zero to the 2mm thickness of the specimen's arm). Then, the dark blue color represents the undamaged material,

while the cyan and green marks reveals some internal debonding around the 1 mm depth, i.e. the $[\pm 45]_{2S}$ laminate mid-plane. More precisely, light green seems to refer to the interface $[+45 - 45 + 45 // - 45]_S$, while cyan marks could be related to the $[+45 - 45 + 45 - 45 - 45 // + 45 - 45 + 45]_T$, therefore the most internal plies are delaminating but not in the mid-plane, as it was expected due to the same orientation of the plies adjacent to the laminate mid-surface. A qualitative comparison of the numerical contour (bottom left image) with the C-Scan allow to see damage patterns similar in size and shape. In this case, amplitude C-Scan (top) allows better visualization, while some dashed lines are included to facilitate the observation of damage paths. Please obviate the rightmost area (starting at around 62 mm on the horizontal scale), which represents the central thickness reduction. Also note that horizontal and vertical dimensions in the C-Scan are not equally scaled, and therefore angles are not corresponding with actual ones.

The inspection of the tensile loaded arm in the T-C biaxial cruciform specimen reveals no damage (Fig. 5.41), as it is expected due to the concentration of strains and non-linearities in the biaxially loaded region.

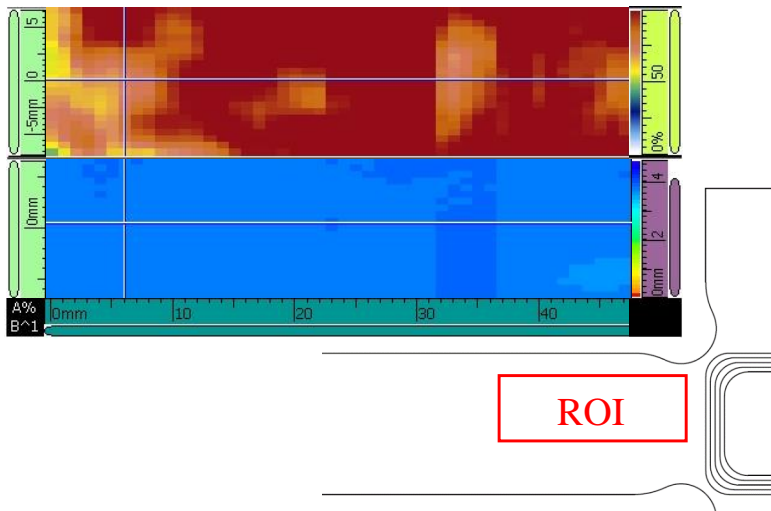


Figure 5.41: Phased-array inspection of the $\pm 45^\circ$ T-C cruciform specimen after biaxial test. The inspected region (ROI) is schematized at the right side.

A similar composition is now depicted for the C-C biaxial test of the $\pm 45^\circ$ lay-up, (after end-tabs removal). In this case, similarly to the T-T case, high accumulation of damage in the arms is expected from the previously analysed numerical and experimental results. Good agreement in the shape of the damage and position in depth (in this case around 2 mm, which represents the midplane of the 4 mm thick $[\pm 45]_{4S}$ laminate at the arms), obtaining in both cases a X-shaped damaged region. There-

fore, the capabilities of phased-array inspection to locate damage are demonstrated and the predicted numerical evolutions for the Hashin's PDM are corroborated with experimental evidences.

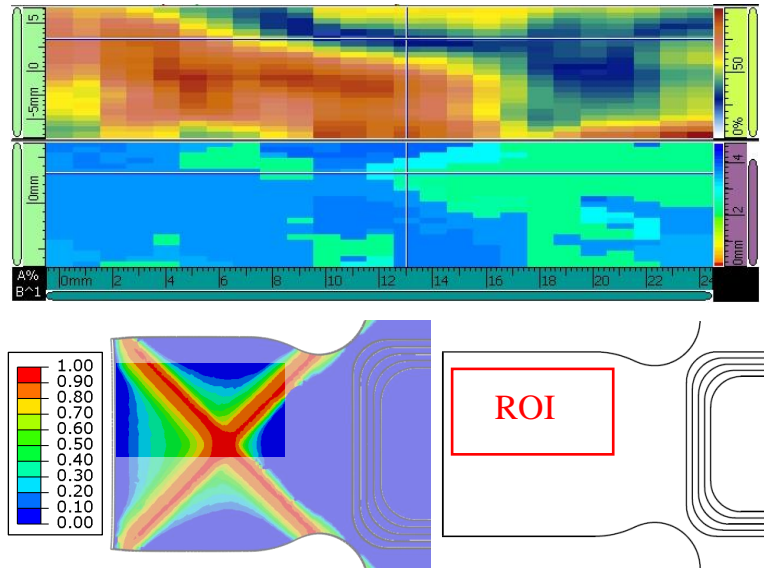


Figure 5.42: Phased-array inspection of the $\pm 45^\circ$ C-C cruciform specimen after biaxial test (above), and numerical contour for matrix compressive damage variable d_{mc} at a point close to maximum load (below). The inspected region (ROI) is schematized at the right side.

Chapter 6

Conclusions and future works

*“If we knew what it was we were doing,
it would not be called research, would it?”*

Albert Einstein

6.1 Conclusions

6.1.1 Uniaxial characterization and damage numerical modelling of laminates

The correct characterization of the properties of the ply in principal direction have been proven to intensively affect the numerical, analytical and experimental results of the rest of multiaxial loading scenarios analysed throughout this Thesis. While uniaxial tensile tests are common and easily achievable, compressive tests posed certain difficulties, mainly related to the buckling phenomenon. However, a bigger effort on the compressive testing campaign on preventing buckling and crushing of specimen resulted in an adequate characterization of the lamina properties under compression.

A more interesting discussion is aroused by the tensile and compressive uniaxial tests of angle-ply laminates, mainly those composed of $\pm 45^\circ$, in which the different degrees of non-linear effects associated with the so-called pseudo-ductility are measured and reported in detail. In this way, the damage and failure phenomena are understood in depth for different fibre orientations. Consequently, it is possible to discuss the application of different non-linear material models, which are correctly implemented in numerical simulations using software **FEM**. In addition, the proposed models base their applicability on that the necessary material parameters can be adjusted by means of the previously described uniaxial tests. Two **PDM** models based on mesomechanical stiffness reduction of the ply in principal directions are proposed. Both models have a phenomenological basis on the mechanical response

of UD FRP lamina.

On the one hand, it has been proven that the Hashin-Rotem strength-based failure criteria with four damage modes, implemented in the software Abaqus, allows to describe a wide range of tests with different phenomenology of damage initiation. In addition, the damage energy release rates of this model have been adapted to the shear-dominated large strain behaviour in angle-ply laminates, so that it is possible to estimate the quasi-static evolution of the non-linear response of different laminates. This damage modelling is fulfilled under the assumption of damage suppression through high shear strain energy absorption. However, this approach ignores the plasticity of the matrix, but offering a cost-effective approach based on the damaged energy release rates. Furthermore, it has even analysed the effect of different numerical modeling techniques, as well as the possibility of implementing the reorientation of the fibres in the numerical model.

On the other hand, Ladevèze's damage mesomodel allows to describe more carefully the phenomenology of shear-dominated behavior of the laminates studied. That is to say, the Ladevèze's model contemplates an evolution based on thermodynamic forces, simultaneously combined with a plasticity model that allows the high permanent deformation of the material to be collected. Through Load-Unload-Reload LUR tests, this model has been adjusted to accurately reproduce the stages of diffuse damage and start of permanent deformation for the studied laminates. However, a correct adjustment of this model to situations involving large deformations and high degradation of stiffness has not been achieved, proposing the possibility of making changes on the damage and yielding evolution law with the aim of collecting the full response of the material.

6.1.2 Bending and pseudo-ductility in angle-ply laminates

With regard to flexural loading, the possibility of obtaining an analytical model that collects the effects of bending-twisting coupling on angle-ply laminates has been demonstrated. In this way, the apparent flexural modulus reduction can be estimated through the closed analytical solution for specially orthotropic laminates, correcting this reference value with the coupling terms obtained by applying the CLPT. Through this model it is therefore possible to analyse the effects of ply-blocking on the flexural response of the ± 45 symmetrical laminate. It is also worth mentioning the discussion about the sometimes incorrect approach to the analysis of laminated structures as if they were beams when a laminated plate model is required.

Additionally, the pseudo-ductile behavior of two laminates with an aggregation

of $\pm 45^\circ$ plies is studied applying analytical models that consider the effect of the different tensile and compressive behavior of the FRP composites. By means of this novel methodology, in combination with the acquisition of full strain maps using DIC, it is possible to simultaneously detail the response under tension and compression generated by the bending moment in a three-point flexural test. Microscopic observations in combination with failure criteria allow clarification of the initiation and progression of the damage, as well as giving an explanation to the phenomenon of reorientation of the fibres. In addition, the analysis by means of the CLPT of these tests gives rise to the possibility of optimizing the stacking sequence with different arrangements of $\pm 45^\circ$ plies, so that the pseudo-ductile effects are maximized while reducing bending-twisting and curvature-membrane coupling terms.

6.1.3 Buckling in laminated plates and cruciform specimens

The lack of experimental data dealing with biaxial trials comprising compressive loads makes it necessary to first consider a careful analysis of elastic stability. In this regard, this Thesis has presented an analytical-numerical study of buckling on rectangular plates, which provides a simple approach to estimate the bifurcation point in both the case of isotropic and orthotropic materials. This solution makes possible to particularize for the laminate $[\pm 45]_{NS}$, due to its interest with respect to biaxial tests using cruciform specimens. A new methodology (β -coefficients technique) is described based on the approximation of the effective length for the calculation of the critical buckling load based on the boundary conditions of the plate. This methodology provides a solution to rectangular plates subjected to any tension/compression state in the two directions of the plane.

Similarly to the methodology described for the flexural response, the effect of bending-twisting couplings on the critical buckling load in laminates with layers at $\pm 45^\circ$ is reported, proposing relations to estimate this effect taking as reference the specially orthotropic laminates. These are numerically validated by linear buckling analysis.

The result of this study finally aims to ensure that buckling does not occur globally in the cruciform specimen. The eigenvalue simulations performed on different load cases and stacking sequences in cruciform specimens allow the development of a fixture which prevents displacement outside the biaxial gauge zone. It is proved that the idea of an anti-buckling jig allows to use specimens of reduced thickness with results equivalent in terms of bifurcation load to thick laminates.

6.1.4 Biaxial testing on cruciform specimens in FRP laminates

The main objective of this line of research was the development of an advanced methodology of biaxial testing which should include a correct approach of the stress-strain state of both the ply and the laminate, which inter alia involves the correct adaptation of the specimen geometry and the application of non-linear numerical models. Regarding the geometrical effects, in addition to the previously reported stress concentrations under **T-T** and **C-C**, it is necessary to ensure an adequate stress state throughout the specimen, which goes through an adaptation of the size of arms and a thickness reduction of the central section. When compressive loads are applied, it is necessary to deepen the appearance of geometric instabilities (buckling), at the level of the biaxial gauge zone and the complete stability of the specimen, demonstrating that the application of the anti-buckling fixture allows postponement of buckling and control its localized appearance. This fixture also helps in the correct alignment of the specimen within the loading application system.

The complexity of the damage and failure in **FRP** laminates with different orientations, particularly cross-ply and angle-ply, generates results with the presence of non-linear effects, associated both with diverse intralaminar damage mechanisms and with the location of permanent deformations or to the presence of interlaminar debondings. The application of the **DIC** technique together with the use of **PDM**-based numerical models has proven to be able to locate, explain and give a reasoned answer to all this complex phenomenology.

With respect to 0/90 symmetrical cross-ply laminate, it has been observed how the thickness reduction by means of a milled tapered region promotes the appearance of a debonding in the stepped transition from central zone to the arms' laminate, due to the great difference in behaviour between the in-plane principal directions 1 of the lamina. Hashin's numerical model should not fit this phenomenon due to the absence of cohesive elements between layers, although the gradual evolution of damage configured for the matrix produces a seemingly apparent result. It is demonstrated that the experimental observation of a non-linear evolution of applied force-strain in the centre is not due to the biaxial state but to this concentration of deformations in the vicinity of the debonding, while the behaviour of the actual biaxial 0/90 laminate under biaxial loading it is predominantly linear. The discussion concerning failure strengths pointed to avoid using these tests as biaxial strength characterisation, as failure is promoted by stress concentrations at filleted corners.

Particularizing the case of the **T-T** and **C-C** tests on $[\pm 45]_{NS}$ laminates, it is verified how the methodology developed has allowed us to isolate the effect of the large shear strain in the mainly uniaxially loaded arms from the linear elastic behaviour

of the area subjected to the pure biaxial state. The dataset of tests provided a new approach to the field of pseudo-ductility in angle-ply laminates, since to date no studies of in-plane multiaxial loads on laminates with this behavior were known by the author. In addition, a variety of loading ratios and fibre orientations in angle-ply laminates make possible to extend the vision on the pseudo-ductile effects under multiple biaxial loading states. This has been validated by accurately numerically modelling the stress-strain response of the reported laminates.

It is worth highlighting the succeed of uncommon tests in the literature, including biaxial compressive loads with outcomes detailed in a rigorous manner. Although the buckling phenomenon is still present, it is confined to the biaxially loaded area, and controlled by comparing the instrumentation of displacements and strains in contrast to the analytical-numerical models developed expressly for the analysis of any T-C and C-C biaxial state on $\pm 45^\circ$ laminates. In addition, the investigation of the T-C tests on laminates $[\pm 45^\circ]_{NS}$ is very remarkable due to the appearance of a pure shear state in the material principal directions. That is, the results of this test allow us to characterize the intralaminar shear behaviour avoiding the problem of other standardized shear tests in which undesired stress/strain components appear.

Finally, the optical and phased-array ultrasound inspection allows corroborating the analysis of the damage and failure performed in all cases of biaxial loading. The good agreement among the numerical damage patterns and the phased-array inspection is specially noteworthy.

6.2 Future research lines

The study of the mechanical multiaxial response and damage in fibre reinforced composites opens a vast field of research from the analytical, numerical and experimental methodologies. The realization of different tests on stacking sequences with different responses has allowed the author to deep into the knowledge of the structural complexity of continuous fibre laminates, establishing a basis for multiaxial characterization and basic numerical and analytical models for the knowledge of the response non-linear material, on which it is necessary to continue working in the future.

This section summarizes the research lines that are planned as a continuation of the work developed in this doctoral Thesis:

- Improvement of the numerical models applied in this Thesis. Specifically, the

possibility of including the effect of permanent deformations in the Hashin's damage model, as well as another plastic and/or damage law in the Ladevèze's model has been already discussed. In this way, it would be possible to obtain numerical models that capture with higher precision the non-linear behaviour exhibited by the angle-ply laminates. In addition, fibre reorientation has proven to be relevant to understand the experimental response of these laminates, with a significant re-stiffening effect after the large shear deformation. However, the reorientation approach carried out in this Thesis has not brought a substantial improvement of the numerical model, so it is necessary to explore alternative ways to correctly collect this effect. This could be done by developing numerical simulations at the microscale level, so as to deepen the behaviour of the constituents of the composite material, trying to accurately collect the phenomena of damage and permanent deformation in fibre reinforced materials. Finally, any of these computational models should result in the assortment of a large number of load cases, determining a global response of the laminate under any biaxial load state.

- The biaxial tests performed had the scope of the characterization of the quasi-static response of the material. However, this is only a first step of the possibilities contemplated for these testing methodology. For example, it would be possible to study the effect of geometric discontinuities (e.g. open-hole stress concentrators) or alternating dynamic loads which allow the assessment of multiaxial fatigue. A starting point, on which this thesis provides a greater basis, would be to perform biaxial Load-Unload-Reload tests, which allow an even more detailed description of the damage and permanent deformation. Thus, numerical models such as the Ladevèze's could be validated with certainty of the multiaxial response.
- Also from the experimental point of view, it would be possible to carry out load states outside those imposed in this Thesis, with ratios farther from 1/1, so that non-linear effects take greater relevance in the biaxially loaded area. It would be necessary to deepen the design of geometries and achievable ratios for each stacking sequence, based on the already performed T-T tests on $0/90$, $\pm 45^\circ$ and $\pm 56.3^\circ$ laminates, as well as the knowledge gained in the study of compressive loads. Biaxial tests can be proposed with new tools that completely prevent the buckling of the biaxially loaded zone, although it will be necessary to find solutions that continue to allow the strain measurement at the gauge zone. Similarly, any stacking sequence of interest could be proposed for testing and modelling.
- Complete the analytical theory of the effect of bending-twisting couplings on the buckling and flexural responses. It has been proved that the relation can

be fitted numerically, but it still necessary a deepest analytical modelling. Furthermore, it is possible to consider the optimization of lay-ups with different couplings and the application to practical cases of combined loads in which it is necessary to seek a balance of the different coupling terms against flexural stiffness and critical buckling load.

- The thorough study of biaxial loadings in cruciform specimens has allowed a detailed description of the possibilities and limitations of this testing methodology. Therefore, it is necessary to propose alternative multiaxial characterization methods. Among the existing possibilities, there is a great interest in describing the response to out-of-plane loads, both quasi-static and dynamic (impacts), which if applied on laminated plates would generate multiaxial states. Another possibility more aligned with the biaxial test would be to propose a triaxial test with a geometry similar to the cruciform but extrapolated to the third dimension. For this purpose, the most appropriate process would be to start with an isotropic material, detailing the characteristics of the specimen and the necessary fixtures to obtain and measure any triaxial stresses/strain state.

Bibliography

- [1] A.-S. Kaddour and M. J. Hinton, "Failure Criteria for Composites", in *Comprehensive Composite Materials II* (P. W. Beaumont and C. H. Zweben, eds.), pp. 573 – 600, Oxford: Elsevier, 2018.
- [2] S.-S. Yao, F.-L. Jin, K. Y. Rhee, D. Hui, and S.-J. Park, "Recent advances in carbon-fiber-reinforced thermoplastic composites: A review", *Composites Part B: Engineering*, vol. 142, pp. 241 – 250, 2018.
- [3] W. Tan, B. G. Falzon, M. Price, and H. Liu, "The role of material characterisation in the crush modelling of thermoplastic composite structures", *Composite Structures*, vol. 153, pp. 914 – 927, 2016.
- [4] V. Giurgiutiu, "Chapter 5 - damage and failure of aerospace composites", in *Structural Health Monitoring of Aerospace Composites* (V. Giurgiutiu, ed.), pp. 125 – 175, Oxford: Academic Press, 2016.
- [5] J. Halpin, *Primer on Composite Materials Analysis*. New York: CRC Press, 1992.
- [6] W.-P. Lin and H.-T. Hu, "Parametric study on the failure of fiber-reinforced composite laminates under biaxial tensile load", *Journal of Composite Materials*, vol. 36, no. 12, pp. 1481–1503, 2002.
- [7] "Defects and damage and their role in the failure of polymer composites", in *Failure Analysis and Fractography of Polymer Composites* (E. S. Greenhalgh, ed.), Woodhead Publishing Series in Composites Science and Engineering, pp. 356 – 440, Woodhead Publishing, 2009.
- [8] S. P. H. Skovsgaard, *Failure of composite materials by kink band formation*. PhD Thesis, Aarhus University, 2019.
- [9] J. D. Fuller and M. R. Wisnom, "Pseudo-ductility and damage suppression in thin ply CFRP angle-ply laminates", *Composites Part A: Applied Science and Manufacturing*, vol. 69, pp. 64–71, 2015.
- [10] J. D. Fuller, M. Jalalvand, and M. R. Wisnom, "Combining fibre rotation and fragmentation to achieve pseudo-ductile CFRP laminates", *Composite Structures*, vol. 142, pp. 155–166, 2016.
- [11] M. Fotouhi, M. Jalalvand, and M. R. Wisnom, "Notch insensitive orientation-dispersed pseudo-ductile thin-ply carbon/glass hybrid laminates", *Composites Part A: Applied Science and Manufacturing*, vol. 110, pp. 29–44, 2018.

-
- [12] X. Wu, J. D. Fuller, M. L. Longana, and M. R. Wisnom, "Reduced notch sensitivity in pseudo-ductile CFRP thin ply angle-ply laminates with central 0° plies", *Composites Part A: Applied Science and Manufacturing*, vol. 111, no. July 2017, pp. 62–72, 2018.
- [13] J. Chevalier, P. P. Camanho, F. Lani, and T. Pardoën, "Multi-scale characterization and modelling of the transverse compression response of unidirectional carbon fiber reinforced epoxy", *Composite Structures*, vol. 209, pp. 160–176, 2019.
- [14] E. Witten, V. Mathes, M. Sauer, and M. Kühnel, "Composites market report 2018: Market developments, trends, outlooks and challenges", Technical Report, AVK and CCEV, 2018.
- [15] S. Sihm, R. Y. Kim, K. Kawabe, and S. W. Tsai, "Experimental studies of thin-ply laminated composites", *Composites Science and Technology*, vol. 67, no. 6, pp. 996 – 1008, 2007.
- [16] H. Liu, B. G. Falzon, and J. P. Dear, "An experimental and numerical study on the crush behaviour of hybrid unidirectional/woven carbon-fibre reinforced composite laminates", *International Journal of Mechanical Sciences*, vol. 164, p. 105160, 2019.
- [17] ADS Advance, "A350 XWB flying test fleet doubles size". <https://www.adsadvance.co.uk/> (Accessed at 18/11/2019).
- [18] Northrop Grumman, "Orbital ATK Delivers 25,000th Boeing 787 Composite Part". <https://news.northropgrumman.com/news/features/orbital-atk-delivers-25-000th-boeing-787-composite-part> (Accessed at 18/11/2019).
- [19] ASTM D3518/D3518M-18, "Standard Test Method for In-Plane Shear Response of Polymer Matrix Composite Materials by Tensile Test of a $\pm 45^\circ$ Laminate", Standard, American Society for Testing and Materials, 2018.
- [20] M. R. Wisnom, "The effect of fibre rotation in $\pm 45^\circ$ tension tests on measured shear properties", *Composites*, vol. 26, no. 1, pp. 25–32, 1995.
- [21] C. T. Herakovich, R. D. Schroedter, A. Gasser, and L. Guitard, "Damage evolution in $[\pm 45]_s$ laminates with fiber rotation", *Composites Science and Technology*, vol. 60, no. 15, pp. 2781–2789, 2000.
- [22] W. Van Paeppegem, I. De Baere, and J. Degrieck, "Modelling the nonlinear shear stress-strain response of glass fibre-reinforced composites. Part II: Model development and finite element simulations", *Composites Science and Technology*, vol. 66, no. 10, pp. 1465–1478, 2006.

- [23] W. Van Paepegem, I. De Baere, and J. Degrieck, "Modelling the nonlinear shear stress-strain response of glass fibre-reinforced composites. Part I: Experimental results", *Composites Science and Technology*, vol. 66, no. 10, pp. 1455–1464, 2006.
- [24] F. Sket, R. Seltzer, J. M. Molina-Aldareguía, C. González, and J. Llorca, "Determination of damage micromechanisms and fracture resistance of glass fiber/epoxy cross-ply laminate by means of X-ray computed microtomography", *Composites Science and Technology*, vol. 72, no. 2, pp. 350–359, 2012.
- [25] F. Sket, M. Rodríguez-Hortalá, J. M. Molina-Aldareguía, J. Llorca, E. Maire, and G. Requena, "In situ tomographic investigation of damage development in $\pm 45^\circ$ carbon fibre reinforced laminates", *Materials Science and Technology*, vol. 31, no. 5, pp. 587–593, 2014.
- [26] F. Sket, A. Enfedaque, C. Alton, C. González, J. M. Molina-Aldareguia, and J. Llorca, "Automatic quantification of matrix cracking and fiber rotation by X-ray computed tomography in shear-deformed carbon fiber-reinforced laminates", *Composites Science and Technology*, vol. 90, pp. 129–138, 2014.
- [27] F. Sket, A. Enfedaque, C. Díaz López, C. González, J. Molina-Aldareguía, and J. Llorca, "X-ray computed tomography analysis of damage evolution in open hole carbon fiber-reinforced laminates subjected to in-plane shear", *Composites Science and Technology*, vol. 133, pp. 40–50, 2016.
- [28] E. Totry, J. M. Molina-Aldareguía, C. González, and J. Llorca, "Effect of fiber, matrix and interface properties on the in-plane shear deformation of carbon-fiber reinforced composites", *Composites Science and Technology*, vol. 70, no. 6, pp. 970–980, 2010.
- [29] J. D. Fuller and M. R. Wisnom, "Exploration of the potential for pseudo-ductility in thin ply CFRP angle-ply laminates via an analytical method", *Composites Science and Technology*, vol. 112, pp. 8–15, 2015.
- [30] W. Tan, F. Naya, L. Yang, T. Chang, B. G. Falzon, L. Zhan, J. M. Molina-Aldareguía, C. González, and J. Llorca, "The role of interfacial properties on the intralaminar and interlaminar damage behaviour of unidirectional composite laminates: Experimental characterization and multiscale modelling", *Composites Part B: Engineering*, vol. 138, pp. 206–221, 2018.
- [31] P. P. Camanho, C. G. Dávila, S. T. Pinho, L. Iannucci, and P. Robinson, "Prediction of in situ strengths and matrix cracking in composites under transverse tension and in-plane shear", *Composites Part A: Applied Science and Manufacturing*, vol. 37, no. 2, pp. 165–176, 2006.

- [32] M. Jalalvand, G. Czél, and M. R. Wisnom, "Damage analysis of pseudo-ductile thin-ply UD hybrid composites - A new analytical method", *Composites Part A: Applied Science and Manufacturing*, vol. 69, pp. 83–93, 2015.
- [33] University of Bristol and Imperial College London, "High Performance Ductile Composite Technology research project". <http://hiperduct.ac.uk/> (Accessed at 15/11/2019).
- [34] J. D. Fuller and M. R. Wisnom, "Ductility and pseudo-ductility of thin ply angle-ply CFRP laminates under quasi-static cyclic loading", *Composites Part A: Applied Science and Manufacturing*, vol. 107, pp. 31–38, 2018.
- [35] G. Czél, S. Pimenta, M. R. Wisnom, and P. Robinson, "Demonstration of pseudo-ductility in unidirectional discontinuous carbon fibre/epoxy prepreg composites", *Composites Science and Technology*, vol. 106, pp. 110–119, 2015.
- [36] S. Pimenta and P. Robinson, "An analytical shear-lag model for composites with "brick-and-mortar" architecture considering non-linear matrix response and failure", *Composites Science and Technology*, vol. 104, pp. 111 – 124, 2014.
- [37] F. De Luca, A. J. Clancy, N. R. Carrero, D. B. Anthony, H. G. De Luca, M. S. P. Shaffer, and A. Bismarck, "Increasing carbon fiber composite strength with a nanostructured "brick-and-mortar" interphase", *Materials Horizon*, vol. 5, pp. 668–674, 2018.
- [38] G. Czél and M. R. Wisnom, "Demonstration of pseudo-ductility in high performance glass/epoxy composites by hybridisation with thin-ply carbon prepreg", *Composites Part A: Applied Science and Manufacturing*, vol. 52, pp. 23 – 30, 2013.
- [39] M. Jalalvand, G. Czél, and M. R. Wisnom, "Parametric study of failure mechanisms and optimal configurations of pseudo-ductile thin-ply UD hybrid composites", *Composites Part A: Applied Science and Manufacturing*, vol. 74, pp. 123–131, 2015.
- [40] M. Fotouhi, M. Jalalvand, and M. R. Wisnom, "High performance quasi-isotropic thin-ply carbon/glass hybrid composites with pseudo-ductile behaviour in all fibre orientations", *Composites Science and Technology*, vol. 152, pp. 101–110, 2017.
- [41] M. Fotouhi, J. Fuller, M. Longana, M. Jalalvand, and M. R. Wisnom, "The high strain rate tension behaviour of pseudo-ductile high performance thin ply composites", *Composite Structures*, vol. 215, pp. 365–376, 2019.

- [42] G. Czél, T. Rev, M. Jalalvand, M. Fotouhi, M. L. Longana, O. J. Nixon-Pearson, and M. R. Wisnom, "Pseudo-ductility and reduced notch sensitivity in multi-directional all-carbon/epoxy thin-ply hybrid composites", *Composites Part A: Applied Science and Manufacturing*, vol. 104, pp. 151–164, 2018.
- [43] H. Cui, D. Thomson, A. Pellegrino, J. Wiegand, and N. Petrinic, "Effect of strain rate and fibre rotation on the in-plane shear response of $\pm 45^\circ$ laminates in tension and compression tests", *Composites Science and Technology*, vol. 135, pp. 106–115, 2016.
- [44] B. Fedulov, A. Fedorenko, A. Safonov, and E. Lomakin, "Nonlinear shear behavior and failure of composite materials under plane stress conditions", *Acta Mechanica*, vol. 228, no. 6, pp. 2033–2040, 2017.
- [45] F. Lagattu and M. Lafarie-Frenot, "Variation of peek matrix crystallinity in apc-2 composite subjected to large shearing deformations", *Composites Science and Technology*, vol. 60, no. 4, pp. 605 – 612, 2000.
- [46] J. Galiana, "Guías básicas para elección de material de útil de curado en autoclave para fabricar piezas de composite. CFRP vs INVAR36", *Materiales Compuestos*, vol. 3, no. 1, pp. 11–25, 2019.
- [47] S. Black, "Cruise-capable rotorcraft exploits the performance of composites". <https://www.compositesworld.com/> (Accessed at 18/11/2019), 2015.
- [48] H. Jia and H.-I. Yang, "Effect of shallow angles on compressive strength of biaxial and triaxial laminates", *SpringerPlus*, vol. 5, p. 2044, Nov 2016.
- [49] M. Quaresimin and P. Carraro, "4 - damage accumulation under multiaxial fatigue loading", in *Modeling Damage, Fatigue and Failure of Composite Materials* (R. Talreja and J. Varna, eds.), Woodhead Publishing Series in Composites Science and Engineering, pp. 61 – 83, Woodhead Publishing, 2016.
- [50] F. Mujika, "New considerations on the stress field in an off-axis tensile test", *Journal of Composite Materials*, vol. 39, no. 21, pp. 1909–1929, 2005.
- [51] A. Smits, D. Van Hemelrijck, T. P. Philippidis, and A. Cardon, "Design of a cruciform specimen for biaxial testing of fibre reinforced composite laminates", *Composites Science and Technology*, vol. 66, no. 7-8, pp. 964–975, 2006.
- [52] M. Hinton and P. Soden, "Predicting failure in composite laminates: the background to the exercise", *Composites Science and Technology*, vol. 58, no. 7, pp. 1001 – 1010, 1998.
- [53] M. J. Hinton, A.-S. Kaddour, and P. D. Soden, ""Evaluation of failure prediction in composite laminates: background to "part B" of the exercise"", *Composites Science and Technology*, vol. 62, no. 12, pp. 1481 – 1488, 2002.

- [54] P. D. Soden, M. J. Hinton, and A.-S. Kaddour, "Biaxial test results for strength and deformation of a range of E-glass and carbon fibre reinforced composite laminates. Failure exercise benchmark data", *Failure Criteria in Fibre-Reinforced-Polymer Composites*, vol. 62, pp. 52–96, 2004.
- [55] P. D. Soden, A.-S. Kaddour, and M. J. Hinton, "Recommendations for designers and researchers resulting from the World-Wide Failure Exercise", *Failure Criteria in Fibre-Reinforced-Polymer Composites*, vol. 64, pp. 1223–1251, 2004.
- [56] E. Shiratori and K. Ikegami, "A new biaxial tension testing machine with flat specimen", *Journal of the Society of Materials Science Japan*, vol. 16, pp. 433 – 439, 1967.
- [57] E. Shiratori and K. Ikegami, "Experimental study of the subsequent yield surface by using cross-shaped specimens", *Journal of the Mechanics and Physics of Solids*, vol. 16, no. 6, pp. 373–394, 1968.
- [58] M. Arcan, Z. Hashin, and A. Voloshin, "A method to produce uniform plane-stress states with applications to fiber-reinforced materials - A specially designed specimen yields material properties under pure shear or uniform plane-stress conditions", *Experimental Mechanics*, vol. 18, no. 4, pp. 141–146, 1978.
- [59] M. D. Monte, E. Moosbrugger, K. Jaschek, and M. Quaresimin, "Multiaxial fatigue of a short glass fibre reinforced polyamide 6.6 - fatigue and fracture behaviour", *International Journal of Fatigue*, vol. 32, no. 1, pp. 17 – 28, 2010. Fourth International Conference on Fatigue of Composites (ICFC4).
- [60] M. Quaresimin, L. Susmel, and R. Talreja, "Fatigue behaviour and life assessment of composite laminates under multiaxial loadings", *International Journal of Fatigue*, vol. 32, no. 1, pp. 2 – 16, 2010. Fourth International Conference on Fatigue of Composites (ICFC4).
- [61] M. Quaresimin and P. A. Carraro, "On the investigation of the biaxial fatigue behaviour of unidirectional composites", *Composites Part B: Engineering*, vol. 54, no. 1, pp. 200–208, 2013.
- [62] D. Cai, J. Tang, G. Zhou, X. Wang, C. Li, and V. V. Silberschmidt, "Failure analysis of plain woven glass/epoxy laminates: Comparison of off-axis and biaxial tension loadings", *Polymer Testing*, vol. 60, pp. 307–320, 2017.
- [63] J. S. Welsh and D. F. Adams, "Development of an electromechanical triaxial test facility for composite materials", *Experimental Mechanics*, vol. 40, no. 3, pp. 312–320, 2000.

- [64] A. Hannon and P. Tiernan, "A review of planar biaxial tensile test systems for sheet metal", *Journal of Materials Processing Technology*, vol. 198, no. 1-3, pp. 1–13, 2008.
- [65] A. Makris, C. Ramault, D. Van Hemelrijck, E. Lamkanfi, and W. Van Paepegem, "Biaxial failure envelopes for glass fibre reinforced composite laminates", in *Proceedings of the SEM Annual Conference*, (Albuquerque, USA), 2009.
- [66] A. Makinde, L. Thibodeau, and K. W. Neale, "Development of an apparatus for biaxial testing using cruciform specimens", *Experimental Mechanics*, vol. 32, no. 2, pp. 138–144, 1992.
- [67] G. Ferron and A. Makinde, "Design and development of a biaxial strength testing device", *Journal of Testing and Evaluation*, vol. 16, no. 3, pp. 253 – 256, 1988.
- [68] K. Buet-Gautier and P. Boisse, "Experimental analysis and modeling of biaxial mechanical behavior of woven composite reinforcements", *Experimental Mechanics*, vol. 41, no. 3, pp. 260–269, 2001.
- [69] N. Bhatnagar, R. Bhardwaj, P. Selvakumar, and M. Brieu, "Development of a biaxial tensile test fixture for reinforced thermoplastic composites", *Polymer Testing*, vol. 26, no. 2, pp. 154–161, 2007.
- [70] A. Barroso, E. Correa, J. Freire, M. D. Pérez, and F. París, "Biaxial Testing of Composites in Uniaxial Machines : Manufacturing of a Device , Analysis of the Specimen Geometry and Preliminary Experimental Results", in *15th European Conference on Composite Materials (ECCM15)*, (Venice, Italy), pp. 24–28, 2012.
- [71] A. Barroso, E. Correa, J. Freire, and F. París, "A Device for Biaxial Testing in Uniaxial Machines. Design, Manufacturing and Experimental Results Using Cruciform Specimens of Composite Materials", *Experimental Mechanics*, vol. 58, no. 1, pp. 49–53, 2018.
- [72] A. Smits, D. Van Hemelrijck, T. Philippidis, A. M. van Wingerde, and A. Cardon, "Study of the usability of various cruciform geometries for biaxial testing of fibre reinforced composites", in *XXI International Congress of Theoretical and Applied Mechanics*, (Warsaw, Poland), 2004.
- [73] C. Ramault and A. Makris, "Effect of tab design on the strain distribution of a biaxially loaded cruciform composite specimen", in *17th International Conference on Composite Materials (ICCM17) Proceedings*, (Edinburgh, United Kingdom), 2009.
- [74] C. Ramault, *Guidelines for biaxial testing of fibre reinforced composites using a cruciform specimen*. PhD Thesis, Vrije Universiteit Brussel, 2012.

- [75] E. Lamkanfi, W. Van Paepegem, and J. Degrieck, "Shape optimization of a cruciform geometry for biaxial testing of polymers", *Polymer Testing*, vol. 41, pp. 7–16, 2014.
- [76] E. Correa, A. Barroso, M. D. Pérez, and F. París, "Design for a cruciform coupon used for tensile biaxial transverse tests on composite materials", *Composites Science and Technology*, vol. 145, pp. 138–148, 2017.
- [77] M. C. Serna Moreno and J. J. López Cela, "Failure envelope under biaxial tensile loading for chopped glass-reinforced polyester composites", *Composites Science and Technology*, vol. 72, no. 1, pp. 91–96, 2011.
- [78] E. Lamkanfi, W. Van Paepegem, J. Degrieck, C. Ramault, A. Makris, and D. Van Hemelrijck, "Strain distribution in cruciform specimens subjected to biaxial loading conditions. Part 1: Two-dimensional versus three-dimensional finite element model", *Polymer Testing*, vol. 29, no. 1, pp. 7–13, 2010.
- [79] E. Lamkanfi, W. Van Paepegem, J. Degrieck, C. Ramault, A. Makris, and D. Van Hemelrijck, "Strain distribution in cruciform specimens subjected to biaxial loading conditions. Part 2: Influence of geometrical discontinuities", *Polymer Testing*, vol. 29, no. 1, pp. 132–138, 2010.
- [80] M. C. Serna Moreno, J. L. Martínez Vicente, and J. J. López Cela, "Failure strain and stress fields of a chopped glass-reinforced polyester under biaxial loading", *Composite Structures*, vol. 103, pp. 27–33, 2013.
- [81] J. Navarro-Zafra, J. L. Curiel-Sosa, and M. C. Serna Moreno, "Mixed-mode damage into a CGRP cruciform subjected to biaxial loading", *Composite Structures*, vol. 133, pp. 1093–1100, 2015.
- [82] J. Navarro-Zafra, J. L. Curiel-Sosa, and M. C. Serna Moreno, "Three-Dimensional Static and Dynamic Analysis of a Composite Cruciform Structure Subjected to Biaxial Loading: A Discontinuum Approach", *Applied Composite Materials*, vol. 23, no. 2, pp. 139–154, 2016.
- [83] M. C. Serna Moreno and J. L. Martínez Vicente, "In-plane shear failure properties of a chopped glass-reinforced polyester by means of traction-compression biaxial testing", *Composite Structures*, vol. 122, pp. 440–444, 2015.
- [84] T. Shi, W. Chen, C. Gao, J. Hu, B. Zhao, P. Wang, and M. Wang, "Biaxial strength determination of woven fabric composite for airship structural envelope based on novel specimens", *Composite Structures*, vol. 184, pp. 1126–1136, jan 2018.

- [85] H. Kumazawa and T. Takatoya, "Biaxial strength investigation of CFRP composite laminates by using cruciform specimens", in *Proceedings of the 17th International Conference on Composite Materials (ICCM-17)*, (Edinburgh, UK), 2009.
- [86] U. Kureemun, M. Ridha, and T. E. Tay, "Biaxial tensile-compressive loading of unnotched and open-hole carbon epoxy crossply laminates", *Journal of Composite Materials*, vol. 49, no. 23, pp. 2817–2837, 2015.
- [87] D. Van Hemelrijck, A. Makris, C. Ramault, E. Lamkanfi, W. Van Paepegem, and D. Lecompte, "Biaxial testing of fibre-reinforced composite laminates", *Proceedings of the Institution of Mechanical Engineers, Part L: Journal of Materials: Design and Applications*, vol. 222, no. 4, pp. 231–239, 2008.
- [88] M. C. Serna Moreno, J. J. López Cela, J. L. Martínez Vicente, and J. A. González Vecino, "Adhesively bonded joints as a dissipative energy mechanism under impact loading", *Applied Mathematical Modelling*, vol. 39, no. 12, pp. 3496–3505, 2015.
- [89] J. N. Périé, H. Leclerc, S. Roux, and F. Hild, "Digital image correlation and biaxial test on composite material for anisotropic damage law identification", *International Journal of Solids and Structures*, vol. 46, no. 11-12, pp. 2388–2396, 2009.
- [90] M. R. Gower and R. M. Shaw, "Towards a Planar Cruciform Specimen for Biaxial Characterisation of Polymer Matrix Composites", *Applied Mechanics and Materials*, vol. 24-25, pp. 115–120, 2010.
- [91] C. Ramault, A. Makris, D. Van Hemelrijck, E. Lamkanfi, and W. Van Paepegem, "Comparison of different techniques for strain monitoring of a biaxially loaded cruciform specimen", *Strain*, vol. 47, no. 2, pp. 210–217, 2011.
- [92] J. S. Welsh, J. S. Mayes, and A. C. Biskner, "2-D biaxial testing and failure predictions of IM7/977-2 carbon/epoxy quasi-isotropic laminates", *Composite Structures*, vol. 75, no. 1-4, pp. 60–66, 2006.
- [93] D. Lecompte, A. Smits, H. Sol, J. Vantomme, and D. Van Hemelrijck, "Mixed numerical-experimental technique for orthotropic parameter identification using biaxial tensile tests on cruciform specimens", *International Journal of Solids and Structures*, vol. 44, no. 5, pp. 1643–1656, 2007.
- [94] C. Williamson and J. Thatcher, "Investigation Into the Failure of Open Holes in Cfrp Laminates Under Biaxial Loading Conditions", *Experimental Analysis of Nano and Engineering Materials and Structures*, pp. 939–940, 2008.

- [95] Y. Huang, S. K. Ha, J. Koyanagi, J. D. D. Melo, H. Kumazawa, and I. Susuki, "Effects of an open hole on the biaxial strengths of composite laminates", *Journal of Composite Materials*, vol. 44, no. 20, pp. 2429–2445, 2010.
- [96] W. J. Vankan, B. H. A. H. Tijs, G. J. De Jong, H. C. De Frel, and N. K. Singh, "Strength of notched and un-notched thermoplastic composite laminate in biaxial tension and compression", *Journal of Composite Materials*, vol. 50, no. 25, pp. 3477–3500, 2016.
- [97] W. J. Vankan, B. H. A. H. Tijs, G. J. de Jong, H. C. de Frel, and N. K. Singh, "Strength of notched and un-notched thermoplastic composite laminate in biaxial tension and compression", Tech. Rep. NLR-TP-2015-019, Netherlands Aerospace Centre (NLR), 2017.
- [98] I. Susuki, "Strength properties of composite laminate under biaxial loadings", in *Proceedings of the 10th International Conference on Composite Materials (ICCM-10)*, (Canada), 1995.
- [99] Y. Qiao, A. A. Deleo, and M. Salviato, "A study on the multi-axial fatigue failure behavior of notched composite laminates", *Composites Part A: Applied Science and Manufacturing*, vol. 127, p. 105640, 2019.
- [100] T. Skinner, S. Datta, A. Chattopadhyay, and A. Hall, "Fatigue damage behavior in carbon fiber polymer composites under biaxial loading", *Composites Part B: Engineering*, vol. 174, p. 106942, 2019.
- [101] P. Hopgood, J. Cook, and A. Clarke, "Multi-axial testing of planar composite specimens", *12th International Conference on Composite Materials - ICCM12*, 1999.
- [102] M. A. Iadicola, A. A. Creuziger, and T. Foecke, "Advanced Biaxial Cruciform Testing at the NIST Center for Automotive Lightweighting Materials Sciences and Engineering Division National Institute of Standards and Technology", *SEM Annual Conference*, pp. 1–8, 2013.
- [103] J. Milner and T. Gnäupel-Herold, "Design of an Octo-Strain Specimen for Biaxial Tension Testing", in *13th International Manufacturing Science and Engineering Conference (MSEC2018)*, (Cincinnati, USA), 2018.
- [104] ZwickRoell, "Biaxial testing machines". <https://www.zwickroell.com/en/biaxial-testing-machines/cruciform-testing-machine> (Accessed at 28/10/2019).
- [105] MTS, "Planar Biaxial Test Systems". <https://www.mts.com/en/products/producttype/test-systems/load-frames-multiaxial/planar-biaxial/index.htm> (Accessed at 28/10/2019).

BIBLIOGRAPHY

- [106] Instron, “Biaxial Cruciform Test Systems”. <https://www.instron.us/products/testing-systems/dynamic-and-fatigue-systems/8800-cruciform> (Accessed at 28/10/2019).
- [107] ISO 16842:2014, “Metallic materials – Sheet and strip – Biaxial tensile testing method using a cruciform test piece”, Standard, International Organization for Standardization, 2014.
- [108] E. Petersen, R. G. Cuntze, and C. Hühne, “Experimental determination of material parameters in Cuntze’s Failure-Mode-Concept-based UD strength failure conditions”, *Composites Science and Technology*, vol. 134, pp. 12–25, 2016.
- [109] K. W. Gan, T. Laux, S. T. Taher, J. M. Dulieu-Barton, and O. T. Thomsen, “A novel fixture for determining the tension/compression-shear failure envelope of multidirectional composite laminates”, *Composite Structures*, vol. 184, no. October 2017, pp. 662–673, 2018.
- [110] T. Laux, K. W. Gan, J. M. Dulieu-Barton, and O. T. Thomsen, “A simple nonlinear constitutive model based on non-associative plasticity for UD composites: Development and calibration using a Modified Arcan Fixture”, *International Journal of Solids and Structures*, vol. 162, pp. 135–147, 2019.
- [111] P. Hao, I. U. Din, and S. Panier, “Development of Modified Arcan Fixture for biaxial loading response of fiber-reinforced composites”, *Polymer Testing*, vol. 80, p. 106148, 2019.
- [112] ISO 20337:2018, “Fibre-reinforced plastic composites - Shear test method using a shear frame for the determination of the in-plane shear stress/shear strain response and shear modulus”, Standard, International Organization for Standardization, 2018.
- [113] Grasse Zur Composite Testing, “Picture Frame Test According To DIN SPEC 4885 /DIN EN ISO 20337”. <https://grassezur.de/en/material-testing/shear-test/shear-test-din-spec-4885> (Accessed at 28/10/2019).
- [114] M. Mateen, D. R. Shankar, and M. M. Hussain, “A review on cruciform shaped frp composites laminates under biaxial testing”, *Materials Today: Proceedings*, vol. 5, no. 10, Part 1, pp. 20837 – 20841, 2018. International Conference on Smart Engineering Materials (ICSEM 2016), October 20-22, 2016.
- [115] C. Bisagni and C. Walters, “Experimental investigation of the damage propagation in composite specimens under biaxial loading”, *Composite Structures*, vol. 85, no. 4, pp. 293–310, 2008.

-
- [116] A. E. Antoniou, D. Van Hemelrijck, and T. P. Philippidis, "Failure prediction for a glass/epoxy cruciform specimen under static biaxial loading", *Composites Science and Technology*, vol. 70, no. 8, pp. 1232–1241, 2010.
- [117] S. Calloch and D. Marquis, "Triaxial tension-compression tests for multiaxial cyclic plasticity", *International journal of plasticity*, vol. 15, no. 5, pp. 521–549, 1999.
- [118] H. M. Deuschle and A. Puck, "Application of the Puck failure theory for fibre-reinforced composites under three-dimensional stress: Comparison with experimental results", *Journal of Composite Materials*, vol. 47, no. 6-7, pp. 827–846, 2013.
- [119] A. Comanici, V. Goanta, and P. D. Barsanescu, "Study of a Triaxial Specimen and a Review for the Triaxial Machines", in *Scientific Proceedings XII International Congress "Machines, Technologies, Materials"*, vol. 1, pp. 16–19, 2015.
- [120] J. Hu, W. Chen, Y. Li, C. Gao, T. Shi, and D. Yang, "A triaxial tensile machine for three-dimensional membrane components: Experimental investigations and numerical simulations", *Polymer Testing*, vol. 65, pp. 206–216, 2018.
- [121] J. S. Welsh and D. F. Adams, "Biaxial and Triaxial Failure Strengths of 6061-T6 Aluminum and AS4/3501-6 Carbon/Epoxy Laminates Obtained by Testing Thickness-Tapered Cruciform Specimens", *Journal of Composites, Technology and Research*, vol. 23, no. 2, pp. 111–121, 2001.
- [122] M. J. Hinton and A. Kaddour, "Triaxial test results for fibre-reinforced composites: The Second World-Wide Failure Exercise benchmark data", *Journal of Composite Materials*, vol. 47, no. 6-7, pp. 653–678, 2013.
- [123] A. Kaddour and M. Hinton, "Maturity of 3D failure criteria for fibre-reinforced composites: Comparison between theories and experiments: Part B of WWFE-II", *Journal of Composite Materials*, vol. 47, no. 6-7, pp. 925–966, 2013.
- [124] A. S. Kaddour and M. J. Hinton, "Triaxial Failure Criteria for Polymer Composites: Part (A) Of WWFE-II: Comparison between theories", in *18th International Conference on Composite Materials (ICCM-18) Proceedings*, (Jeju Island, Korea), 2011.
- [125] S. Pinho, *Modelling failure of laminated composites using physically-based failure models*. PhD Thesis, Imperial College London, 2005.
- [126] R. Hill, *The Mathematical Theory of Plasticity*. Oxford University Press, 1950.
- [127] S. W. Tsai, "Strength Theories of Filamentary Structures", in *Fundamental aspects of fiber reinforced plastic composites* (R. Schwartz and H. Schwartz, eds.), pp. 3–11, Wiley-Interscience, 1968.

- [128] S. W. Tsai and E. M. Wu, "A general theory of strength for anisotropic materials", *Journal of Composite Materials*, vol. 5, pp. 58–80, 1971.
- [129] ANSYS®, *Mechanical APDL Release 18.1 Documentation*.
- [130] Dassault Systèmes, *Abaqus 2019 Documentation*.
- [131] F. Mujika, N. Carbajal, A. Arrese, and I. Mondragon, "Determination of tensile and compressive moduli by flexural tests", *Polymer Testing*, vol. 25, no. 6, pp. 766–771, 2006.
- [132] M. C. Serna Moreno, A. Romero Gutiérrez, and J. L. Martínez Vicente, "Different response under tension and compression of unidirectional carbon fibre laminates in a three-point bending test", *Composite Structures*, vol. 136, pp. 706–711, 2016.
- [133] M. C. Serna Moreno, A. Romero Gutiérrez, and J. L. Martínez Vicente, "First flexural and interlaminar shear failure in symmetric cross-ply carbon-fibre laminates with different response under tension and compression", *Composite Structures*, vol. 146, pp. 62–68, 2016.
- [134] S. W. Tsai, "A survey of macroscopic failure criteria for composite materials", *Journal of Reinforced Plastic Composites*, vol. 3, pp. 40–62, 1971.
- [135] R. Narayanaswami and H. M. Adelman, "Evaluation of the tensor polynomial and hoffman strength theories for composite materials", *Journal of Composite Materials*, vol. 11, no. 4, pp. 366–377, 1977.
- [136] J. C. Suhling, *Constitutive Relations and Failure Predictions for Nonlinear Orthotropic Media*. University of Wisconsin, 1985.
- [137] Z. Hashin and A. Rotem, "A Fatigue Failure Criterion for Fiber Reinforced Materials", *Journal of Composite Materials*, vol. 7, no. 4, pp. 448–464, 1973.
- [138] Z. Hashin, "Failure criteria for unidirectional fibre composites", *ASME Journal of Applied Mechanics*, vol. 47, no. 2, pp. 329–334, 1980.
- [139] A. Puck and H. Schürmann, "Failure Analysis of FRP Laminates by Means of Physically Based Phenomenological Models", *Composites Science and Technology*, vol. 62, pp. 1633–1662, 2002.
- [140] A. Puck, J. Kopp, and M. Knops, "Guidelines for the determination of the parameters in Puck's action plane strength criterion", *Composites Science and Technology*, vol. 62, no. 3, pp. 371–378, 2002.
- [141] F. París, "A Study of Failure Criteria of Fibrous Composite Materials", Technical Report, NASA Langley Research Center, 2001.

-
- [142] S. Lauterbach, C. Balzani, and W. Wagner, "Failure analysis on shell-like composite laminates using the puck criteria", *Proceedings in Applied Mathematics and Mechanics*, vol. 9, no. 1, pp. 231–232, 2009.
- [143] A.-S. Kaddour, M. J. Hinton, P. A. Smith, and S. Li, "A comparison between the predictive capability of matrix cracking, damage and failure criteria for fibre reinforced composite laminates: Part A of the third world-wide failure exercise", *Journal of Composite Materials*, vol. 47, no. 20-21, pp. 2749–2779, 2013.
- [144] C. G. Dávila, N. Jaunky, and S. Goswami, "Failure Criteria for FRP Laminates in Plane Stress", in *44th AIAA/ASME/ASCE/AHS/ASC Structures, Structural Dynamics, and Materials Conference*, (Norfolk, USA), 2003.
- [145] C. G. Dávila, P. P. Camanho, and C. A. Rose, "Failure criteria for FRP laminates", *Journal of Composite Materials*, vol. 39, no. 4, pp. 323–345, 2005.
- [146] S. T. Pinho, C. G. Dávila, P. P. Camanho, L. Iannucci, and P. Robinson, "Failure Models and Criteria for FRP Under In-Plane or Three-Dimensional Stress States Including Shear Non-Linearity", Technical Report, NASA Langley Research Center, 2005.
- [147] S. T. Pinho, L. Iannucci, and P. Robinson, "Physically based failure models and criteria for laminated fibre-reinforced composites with emphasis on fibre kinking. Part II: FE implementation", *Composites Part A: Applied Science and Manufacturing*, vol. 37, no. 5, pp. 766–777, 2006.
- [148] S. T. Pinho, R. Darvizeh, P. Robinson, C. Schuecker, and P. P. Camanho, "Material and structural response of polymer-matrix fibre-reinforced composites", *Journal of Composite Materials*, vol. 46, no. 19-20, pp. 2313–2341, 2012.
- [149] S. T. Pinho, G. M. Vyas, and P. Robinson, "Material and structural response of polymer-matrix fibre-reinforced composites: Part B", *Journal of Composite Materials*, vol. 47, no. 6-7, pp. 679–696, 2013.
- [150] L. McCartney, "13 - microlevel approaches to modeling of damage in composite materials: Generalized plane strain analysis", in *Modeling Damage, Fatigue and Failure of Composite Materials* (R. Talreja and J. Varna, eds.), Woodhead Publishing Series in Composites Science and Engineering, pp. 289 – 327, Woodhead Publishing, 2016.
- [151] C. T. Herakovich, *Mechanics of Fibrous Composites*. Wiley, 1997.
- [152] O. Allix and F. Hild, *Continuum Damage Mechanics of Materials and Structures*. Oxford: Elsevier, 2002.

- [153] L. M. Kachanov, "On the life-time under creep conditions", *Bulletin of the Academy of Sciences of the USSR, Division of Technical Sciences*, vol. 8, pp. 26–31, 1958.
- [154] Y. N. Rabotnov, "On the equations of state for creep", in *Progress in Applied Mechanics: The Prager Anniversary Volume* (W. T. Koiter, ed.), p. 307, New York (USA): McMillan, 1963.
- [155] P. Ladevèze and E. Le Dantec, "Damage modelling of the elementary ply for laminated composites", *Composites Science and Technology*, vol. 43, no. 3, pp. 257–267, 1992.
- [156] P. Ladevèze, "Sur Une Théorie de l'Endommagement Anisotrope", Tech. Rep. 34, Laboratoire de Mécanique et Technologie, Cachan, France, 1983.
- [157] D. Garoz, F. A. Gilabert, R. D. B. Sevenois, S. W. Spronk, and W. Van Paepegem, "Material parameter identification of the elementary ply damage mesomodel using virtual micro-mechanical tests of a carbon fiber epoxy system", *Composite Structures*, vol. 181, pp. 391–404, 2017.
- [158] Siemens, *NX Nastran 11 Release Guide*.
- [159] G. Staab, *Laminar Composites*. Elsevier, 2nd ed., 2015.
- [160] J. Rouchon, "Certification of large airplane composite structures, recent progress and new trends in compliance philosophy", in *ICAS Proceedings 1990, 17th Congress of the International Council of the Aeronautical Sciences*, (Stockholm, Sweden), 1990.
- [161] Hexcel®, "HexPly® M21 DataSheet", Specification sheet, Available online at: <https://www.hexcel.com/Resources/DataSheets/Prepreg> (Accessed at 22/11/2019), 2015.
- [162] LaVision, "StrainMaster Digital Image Correlation Systems for Full Field Shape, Displacement and Strain". <https://www.lavision.de/en/products/strainmaster/> (Accessed at 22/11/2019).
- [163] N. Dubé, *Introduction to Phased Array Ultrasonic Technology Applications: Olympus Guideline*. Waltham, MA, USA: Olympus, 2004.
- [164] I. García-Moreno, M. A. Caminero, G. P. Rodríguez, and J. J. López-Cela, "Effect of Thermal Ageing on the Impact Damage Resistance and Tolerance of Carbon-Fibre-Reinforced Epoxy Laminates", *Polymers*, vol. 11, p. 160, 2019.
- [165] M. W. Hyer, *Stress Analysis of Fiber-Reinforced Composite Materials*. McGraw-Hill, 1998.

- [166] R. M. Jones, *Mechanics of Composite Materials*. Taylor & Francis, 2nd ed., 2002.
- [167] J. Reddy, *Mechanics of Laminated Composite Plates and Shells: Theory and Analysis, Second Edition*. CRC Press, 2nd ed., 2003.
- [168] M. C. Serna Moreno, S. Horta Muñoz, A. Romero Gutiérrez, C. Rappold, J. L. Martínez Vicente, P. A. Morales-Rodríguez, and J. J. López Cela, "Pseudo-ductility in flexural testing of symmetric $\pm 45^\circ$ angle-ply CFRP laminates", *Composites Science and Technology*, vol. 156, pp. 8–18, 2018.
- [169] P. P. Camanho and C. G. Dávila, "Mixed-Mode Decohesion Finite Elements for the Simulation of Delamination in Composite Materials", Technical Report, NASA Langley, 2002.
- [170] A. Matzenmiller, J. Lubliner, and R. Taylor, "A constitutive model for anisotropic damage in fiber-composites", *Mechanics of Materials*, vol. 20, no. 2, pp. 125 – 152, 1995.
- [171] A. Turon Travesa, *Simulation of Delamination Onset and Propagation Under Fatigue Loading Using Cohesive Zone Models*. PhD Thesis, Universitat de Girona, 2006.
- [172] Y. Yuan, S. Wang, H. Yang, X. Yao, and B. Liu, "Analysis of pseudo-ductility in thin-ply carbon fiber angle-ply laminates", *Composite Structures*, vol. 180, pp. 876–882, 2017.
- [173] P. Ladevèze and G. Lubineau, "On a damage mesomodel for laminates: micro-meso relationships, possibilities and limits", *Composites Science and Technology*, vol. 61, pp. 2149–2158, 2001.
- [174] P. Ladevèze and G. Lubineau, "On a damage mesomodel for laminates: Micromechanics basis and improvement", *Mechanics of Materials*, vol. 35, no. 8, pp. 763–775, 2003.
- [175] R. M. O'Higgins, C. T. McCarthy, and M. A. McCarthy, "Identification of damage and plasticity parameters for continuum damage mechanics modelling of carbon and glass fibre-reinforced composite materials", *Strain*, vol. 47, no. 1, pp. 105–115, 2011.
- [176] M. Q. Le, H. Bainier, D. Néron, C. Ha-Minh, and P. Ladevèze, "On matrix cracking and splits modeling in laminated composites", *Composites Part A: Applied Science and Manufacturing*, vol. 115, pp. 294–301, 2018.
- [177] R. D. B. Sevenois, *Models for Intraply Damage and Strength Prediction of Unidirectional and Woven Composites under Static and Fatigue Loading in Tension and Compression*. PhD Thesis, Ghent University, 2019.

- [178] W. Tan and B. G. Falzon, "Modelling the nonlinear behaviour and fracture process of AS4/PEKK thermoplastic composite under shear loading", *Composites Science and Technology*, vol. 126, pp. 60–77, 2016.
- [179] F. Naya, C. González, C. S. Lopes, S. Van der Veen, and F. Pons, "Computational micromechanics of the transverse and shear behavior of unidirectional fiber reinforced polymers including environmental effects", *Composites Part A: Applied Science and Manufacturing*, vol. 92, pp. 146–157, 2017.
- [180] P. Hartley, I. Pillinger, and C. E. Sturgess, eds., *Numerical Modelling of Material Deformation Processes*. Springer-Verlag London, 1992.
- [181] R. O. Eugenio Oñate, ed., *Computational Plasticity*. Luxembourg: Springer Netherlands, 2007.
- [182] ASTM D3039/D3039-17, "Standard Test Method for Tensile Properties of Polymer Matrix Composite Materials", Standard, American Society for Testing and Materials, 2017.
- [183] R. D. B. Sevenois, D. Garoz, E. Verboven, S. W. F. Spronk, F. A. Gilabert, M. Kersemans, L. Pyl, and W. Van Paepegem, "Multiscale approach for identification of transverse isotropic carbon fibre properties and prediction of woven elastic properties using ultrasonic identification", *Composites Science and Technology*, vol. 168, pp. 160–169, 2018.
- [184] M. A. Caminero, G. P. Rodríguez, J. M. Chacón, and I. García-Moreno, "Tensile and Flexural Damage Response of Symmetric Angle-Ply Carbon Fiber-Reinforced Epoxy Laminates: Non-Linear Response and Effects of Thickness and Ply-Stacking Sequence", *Polymer Composites*, pp. 1–13, 2019.
- [185] L. A. Carlsson, D. F. Adams, and R. B. Pipes, *Experimental Characterization of Advanced Composite Materials*. CRC Press, 4th ed., 2014.
- [186] A. Krasnobrizha, P. Rozycki, L. Gornet, and P. Cosson, "Hysteresis behaviour modelling of woven composite using a collaborative elastoplastic damage model with fractional derivatives", *Composite Structures*, vol. 158, pp. 101 – 111, 2016.
- [187] D. F. Adams, "Tabbed versus untabbed fiber-reinforced composite compression specimens", in *Composite Materials: Testing, Design, and Acceptance Criteria* (A. Zureick and A. Nettles, eds.), pp. 3 – 16, ASTM International, 2002.
- [188] ASTM D695-15, "Standard Test Method for Compressive Properties of Rigid Plastics", Standard, American Society for Testing and Materials, 2015.

- [189] ASTM D6641/D6641M-16e1, "Standard Test Method for Compressive Properties of Polymer Matrix Composite Materials Using a Combined Loading Compression (CLC) Test Fixture", Standard, American Society for Testing and Materials, 2016.
- [190] ISO 14126:1999, "Fibre-reinforced plastic composites – Determination of compressive properties in the in-plane direction", Standard, International Organization for Standardization, 1999.
- [191] ASTM D3410/D3410M-16, "Standard Test Method for Compressive Properties of Polymer Matrix Composite Materials with Unsupported Gage Section by Shear Loading", Standard, American Society for Testing and Materials, 2016.
- [192] Boeing Specification Support Standard BSS 7260, "Advanced Composite Compression Tests", Standard, The Boeing Company, 1988.
- [193] R. D. B. Sevenois, D. Garoz, F. A. Gilabert, C. Hochard, and W. Van Paepegem, "Influence of tab debonding on measured stiffness evolution in Compression-Compression and Tension-Compression fatigue testing of short gauge length coupons", *Composites Science and Technology*, vol. 180, pp. 1–13, 2019.
- [194] A. Barroso, J. C. Marín, V. Mantič, and F. París, "Eliminación de singularidades en ensayos estándar de materiales compuestos", *Materiales Compuestos*, vol. 2, no. 1, pp. 1–6, 2018.
- [195] D. O. Adams, "Comparative Testing to Assess the Equivalence of CEN and ASTM Test Methods for Composite Materials", Tech. Rep. DOT/FAA/AR-04/50, U.S. Department of Transportation, 2005.
- [196] E. J. Barbero, F. A. Cosso, R. Roman, and T. L. Weadon, "Determination of material parameters for Abaqus progressive damage analysis of E-glass epoxy laminates", *Composites Part B: Engineering*, vol. 46, pp. 211–220, 2013.
- [197] A. R. Conn, N. I. M. Gould, and P. L. Toint, *Trust Region Methods*. Society for Industrial and Applied Mathematics, 2000.
- [198] X. P. Morelle, J. Chevalier, C. Bailly, T. Pardoën, and F. Lani, "Mechanical characterization and modeling of the deformation and failure of the highly crosslinked RTM6 epoxy resin", *Mechanics of Time-Dependent Materials*, vol. 21, no. 3, pp. 419–454, 2017.
- [199] ASTM D7264/D7264M-15, "Standard test method for flexural properties of polymer matrix composite materials", Standard, American Society for Testing and Materials, 2015.

BIBLIOGRAPHY

- [200] M. A. Caminero, G. P. Rodríguez, and V. Muñoz, "Effect of stacking sequence on Charpy impact and flexural damage behavior of composite laminates", *Composite Structures*, vol. 136, pp. 345–357, 2016.
- [201] W. de Goeij, M. van Tooren, and A. Beukers, "Implementation of bending-torsion coupling in the design of a wind-turbine rotor-blade", *Applied Energy*, vol. 63, no. 3, pp. 191 – 207, 1999.
- [202] S. Guo, "Aeroelastic optimization of an aerobatic aircraft wing structure", *Aerospace Science and Technology*, vol. 11, no. 5, pp. 396 – 404, 2007.
- [203] C. B. York, "Unified approach to the characterization of coupled composite laminates: Benchmark configurations and special cases", *Journal of Aerospace Engineering*, vol. 23, no. 4, pp. 219–242, 2010.
- [204] C. B. York and S. F. M. de Almeida, "On extension-shearing bending-twisting coupled laminates", *Composite Structures*, vol. 164, pp. 10 – 22, 2017.
- [205] M. Meng, H. R. Le, M. J. Rizvi, and S. M. Grove, "The effects of unequal compressive/tensile moduli of composites", *Composite Structures*, vol. 126, pp. 207–215, 2015.
- [206] S. Horta Muñoz, M. C. Serna Moreno, J. M. González-Domínguez, P. Morales-Rodríguez, and E. Vázquez, "Experimental, Numerical, and Analytical Study on The Effect of Graphene Oxide in The Mechanical Properties of a Solvent-Free Reinforced Epoxy Resin", *Polymers*, vol. 11, no. 12, p. 2115, 2019.
- [207] N. Insausti, I. Adarraga, N. Carbajal, and F. Mujika, "Numerical assessment of the analytical models used to determine flexural and shear moduli in I-Beams when the tensile and compressive moduli are different", *Polymer Testing*, p. 106154, 2019.
- [208] M. C. Serna Moreno, J. L. Curiel-Sosa, J. Navarro-Zafra, J. L. Martínez Vicente, and J. J. López Cela, "Crack propagation in a chopped glass-reinforced composite under biaxial testing by means of XFEM", *Composite Structures*, vol. 119, pp. 264–271, 2014.
- [209] ASTM D638-14, "Standard Test Method for Tensile Properties of Plastics", Standard, American Society for Testing and Materials, 2014.
- [210] A. Makris, T. Vandenbergh, C. Ramault, D. Van Hemelrijck, E. Lamkanfi, and W. Van Paepegem, "Shape optimisation of a biaxially loaded cruciform specimen", *Polymer Testing*, vol. 29, no. 2, pp. 216–223, 2010.
- [211] A. W. Leissa, "Buckling of Laminated Composite Plates and Shell Panels", Technical Report, Flight Dynamics Laboratory.

- [212] J. Loughlan, "The influence of mechanical couplings on the compressive stability of anti-symmetric angle-ply laminates", *Composite Structures*, vol. 57, pp. 473–482, 2002.
- [213] S. Vummadisetti and S. Singh, "Buckling and postbuckling response of hybrid composite plates under uniaxial compressive loading", *Journal of Building Engineering*, vol. 27, p. 101002, 2020.
- [214] W. T. Koiter, *W. T. Koiter's Elastic Stability of Solids and Structures*. Cambridge University Press, 2008.
- [215] M. Kazemi, "A new exact semi-analytical solution for buckling analysis of laminated plates under biaxial compression", *Archive of Applied Mechanics*, vol. 85, pp. 1667–1677, Nov 2015.
- [216] A. Teter and Z. Kolakowski, "Influence of mechanical couplings on the buckling behaviour of thin-walled plates made of general laminates under compression", *Composite Structures*, vol. 166, pp. 68 – 76, 2017.
- [217] M. C. Serna Moreno and S. Horta Muñoz, "Dispositivo antipandeo para ensayos biaxiales con probetas cruciformes", in *XIII Congreso Nacional de Materiales Compuestos (MATCOMP'19)*, (Vigo, Spain), 2019.
- [218] M. C. Serna Moreno and S. Horta Muñoz, "Elastic stability in biaxial testing with cruciform specimens subjected to compressive loading", *Composites Structures*, vol. 234, p. 111697, 2020.
- [219] S. Horta Muñoz and M. C. Serna Moreno, "Ensayos biaxiales sobre probetas cruciformes de laminados CFRP ante presencia de cargas de compresión", in *XIII Congreso Nacional de Materiales Compuestos (MATCOMP'19)*, (Vigo, Spain), 2019.
- [220] M. Remacha, S. Sánchez Sáez, B. López Romano, and E. Barbero Pozuelo, "A new device for determining the compression after impact strength in thin laminates", *Composite Structures*, vol. 127, pp. 99 – 107, 2015.
- [221] S.-C. Han, S.-Y. Lee, and G. Rus, "Postbuckling analysis of laminated composite plates subjected to the combination of in-plane shear, compression and lateral loading", *International Journal of Solids and Structures*, vol. 43, no. 18, pp. 5713 – 5735, 2006.
- [222] N. Kharghani and C. G. Soares, "Experimental, numerical and analytical study of buckling of rectangular composite laminates", *European Journal of Mechanics - A/Solids*, vol. 79, p. 103869, 2020.
- [223] S. P. Timoshenko and J. M. Gere, *Theory of Elastic Stability*. McGraw-Hill, 2nd ed., 1985.

BIBLIOGRAPHY

- [224] M. C. Serna Moreno and S. Horta Muñoz, “Dispositivo para evitar pandeo en ensayos biaxiales de probetas cruciformes”, Spanish patent application number P 2018/109819, 2018.
- [225] M. C. Serna Moreno and S. Horta Muñoz, “Dispositivo para evitar pandeo en ensayos biaxiales de probetas cruciformes”, PCT/ES2019/070473 application, 2019.

Appendix A

Scientific production

A.1 Publications in peer-reviewed international journals indexed in the Journal Citation Reports

- María del Carmen Serna Moreno; Sergio Horta Muñoz. *Mechanical response of $\pm 45^\circ$ angle-ply CFRP plates under low-velocity impact and quasi-static indentation: influence of the multidirectional strain state*. Under review.
- Sergio Horta Muñoz; María del Carmen Serna Moreno; José Miguel González-Domínguez; Pablo Antonio Morales-Rodríguez, Ester Vázquez. *Experimental, Numerical, and Analytical Study on the Effect of Graphene Oxide in the Mechanical Properties of a Solvent-Free Reinforced Epoxy Resin*. *Polymers*. 11(12), 2115. 2019.
- María del Carmen Serna Moreno; Sergio Horta Muñoz. *Elastic stability in biaxial testing with cruciform specimens subjected to compressive loading*. *Composites Structures*. 234, pp. 111697. 2020.
- María del Carmen Serna Moreno; Sergio Horta Muñoz; Ana Romero Gutiérrez; Christophe Rappold; Juan Luis Martínez Vicente; Pablo Antonio Morales Rodríguez; Juan José López Cela. *Pseudo-ductility in flexural testing of symmetric $\pm 45^\circ$ angle-ply CFRP laminates*. *Composites Science and Technology*. 156, pp. 8 - 18. 2018.

A.2 Publications in national journals

- Sergio Horta Muñoz; María del Carmen Serna Moreno; José Miguel González Domínguez; Pablo Antonio Morales Rodríguez; Juan Luis Martínez Vicente; Ester Vázquez Fernández-Pacheco. *Fabricación y caracterización de materiales compuestos reforzados con óxido de grafeno*. *Materiales Compuestos*. 2 (4), pp. 22 - 25. 2018. ISSN 2531-0739.

- María del Carmen Serna Moreno; Ana Romero Gutiérrez; Juan Luis Martínez Vicente; Sergio Horta Muñoz; Pablo Antonio Morales Rodríguez; Christophe Rappold. *Flexión en materiales compuestos con distinta respuesta a tracción y a compresión*. *Materiales Compuestos*. 2 (4), pp. 1 - 4. 2018. ISSN 2531-0739.

A.3 Contributions to international conferences

- Sergio Horta Muñoz; María del Carmen Serna Moreno. *Characterization of the non-linear mechanical response of biaxially-tested angle-ply laminates*. 7th ECCOMAS Thematic Conference on The Mechanical Response of Composites (COMPOSITES 2019). Girona, 18-20/09/2019.
- María del Carmen Serna Moreno; Sergio Horta Muñoz; Ana Romero Gutiérrez; Christophe Rappold; Juan Luis Martínez Vicente; Pablo Antonio Morales Rodríguez; Juan José López Cela. *Pseudo-ductile response of $\pm 45^\circ$ CFRP submitted to flexural loading*. 18th European Conference on Composite Materials (ECCM18). Athens, 25-28/06/2018.
- Sergio Horta Muñoz, María del Carmen Serna Moreno. *Numerical modelling of the pseudo-ductility effect in $\pm 45^\circ$ angle-ply laminates under biaxial loading*. 18th European Conference on Composite Materials (ECCM18). Athens, 25-28/06/2018.
- Sergio Horta Muñoz; María del Carmen Serna Moreno; Juan Luis Martínez Vicente. *Experimental and numerical study of $\pm 45^\circ$ angle-ply CFRP laminates under tensile-tensile biaxial loads*. 20th International Conference on Composites Structures (ICCS20). Paris, 4-7/09/2017.
- Sergio Horta Muñoz; María del Carmen Serna Moreno; José Miguel González Domínguez; Pablo Antonio Morales Rodríguez; Juan Luis Martínez Vicente; Ester Vázquez. *Mechanical characterization of Graphene Oxide reinforced polymer composites*. 20th International Conference on Composites Structures (ICCS20). Paris, 4-7/09/2017.

A.4 Contributions to national conferences

- Sergio Horta Muñoz; María del Carmen Serna Moreno; David Garoz; Ruben D.B. Sevenois; Wim Van Paeppegem. *Modelado micromecánico de la evolución del*

daño en materiales compuestos reforzados con fibra. IX Jornada Doctoral de la Universidad de Castilla-La Mancha. 12/11/2019, Ciudad Real.

- Sergio Horta Muñoz; María del Carmen Serna Moreno. *Ensayos biaxiales sobre probetas cruciformes de laminados CFRP ante presencia de cargas de compresión.* XIII Congreso Nacional de Materiales Compuestos MATCOMP19. 03/07/2019, Vigo.
- María del Carmen Serna Moreno; Sergio Horta Muñoz. *Dispositivo antipandeo para ensayos biaxiales con probetas cruciformes.* XIII Congreso Nacional de Materiales Compuestos MATCOMP19. 03/07/2019, Vigo.
- Sergio Horta Muñoz; María del Carmen Serna Moreno. *Numerical assessment on the influence of pseudo-ductility in cruciform biaxial testing of fibre-reinforced composite materials.* XXII Reunión de Usuarios de SIMULIA. 14/11/2018, Madrid.
- Sergio Horta Muñoz; María del Carmen Serna Moreno; Juan Luis Martínez Vicente. *Estudio numérico, analítico y experimental de laminados angle-ply $\pm 45^\circ$ sometidos a cargas de tracción biaxial.* VII Jornada Doctoral de la Universidad de Castilla-La Mancha. 07/11/2017, Albacete.
- María del Carmen Serna Moreno; Ana Romero Gutiérrez; Juan Luis Martínez Vicente; Sergio Horta Muñoz; Pablo Antonio Morales Rodríguez; Christophe Rappold. *Flexión en materiales compuestos con distinta respuesta a tracción y a compresión.* XII Congreso Nacional de Materiales Compuestos MATCOMP 2017. 23/06/2017, San Sebastián.
- Sergio Horta Muñoz; María del Carmen Serna Moreno; José Miguel González Domínguez; Pablo Antonio Morales Rodríguez; Juan Luis Martínez Vicente; Ester Vázquez Fernández-Pacheco. *Fabricación y caracterización de materiales compuestos reforzados con óxido de grafeno.* XII Congreso Nacional de Materiales Compuestos MATCOMP 2017. 21/06/2017, San Sebastián.
- Sergio Horta Muñoz; María del Carmen Serna Moreno; Juan Luis Martínez Vicente; Miguel Ángel Caminero Torija. *Estudio biaxial de laminados reforzados con fibra de carbono (CFRP).* ANSYS Convergence 2015. 27/10/2015, Madrid.

A.5 Intellectual property

- María del Carmen Serna Moreno, Sergio Horta Muñoz. *Dispositivo para evitar pandeo en ensayos biaxiales de probetas cruciformes.* Spanish patent application number P 2018/109819.

- María del Carmen Serna Moreno, Sergio Horta Muñoz. *Dispositivo para evitar pandeo en ensayos biaxiales de probetas cruciformes*. Application PCT/ES2019/070473 for international extension of the spanish patent application through the Patent Cooperation Treaty.

A.6 Recognitions

- Finalist of the third edition of the contest “Tesis en tres Minutos” (Three Minutes Thesis, 3MT©) organized by UCLM. Albacete, June 7, 2019.
- AIRBUS Award for the best Master Thesis “Mechanical Behaviour of Graphene Oxide Reinforced Polymer Composites”. April 6, 2018.
- Award from Colegio Oficial de Graduados e Ingenieros Técnicos de Ciudad Real (COGITI) for the best Degree Thesis “Comportamiento multiaxial de laminados reforzados con fibra de carbono CFRP”. April 8, 2016.